MICROSTRUCTURAL AND PHOTUMINESCENCE CHARACTERISATION OF GERMANIUM AND SILICON-GERMANIUM NANOCRYSTALLINE MATERIALS

A thesis submitted in partial fulfilment of the requirements for the degree of

Doctor of Philosophy

of

De Montfort University

Giray Kartopu

Leicester, 2003

To my parents, to my sister, Emine,

and to her husband and my best friend, Faruk

Declaration of Originality

This is to certify that I am responsible for the work submitted in this thesis, that the original work is my own and is carried out, unless otherwise stated, by the author whilst studying in the Department of Applied Sciences (presently, the School of Molecular Sciences) at De Montfort University, Leicester, UK, and that neither the thesis nor any part of the original work contained therein has been submitted to this or any other institution for a higher degree.

Signed..... (G. KARTOPU)

Date.....19/06/2003....

Acknowledgements

I would like to express my sincere thanks to those who have made my research possible and fulfilling with their help and support.

First of all, I like to thank to my first supervisor, Prof. Sue C. Bayliss, for her continuous support, encouragement and guidance throughout the duration of my course. I also have to thank to my second supervisor Dr. Andrei V. Sapelkin for his involvement in this research and for the skills provided for the XAS study.

I am indebted to Renishaw plc for the provision of their micro-Raman spectroscopy facilities and to Dr. Tim Smith for his invaluable technical assistance.

I am also deeply grateful to my good friend and colleague Yasin Ekinci, Research Student at Max Planck Institute for Stroemungsforschung, Germany, for his fruitful discussions and the skills he provided for computer modelling of the Raman scattering spectra.

My genuine thanks should go to those researchers, who are our colleagues, all around the world... Prof. Rasit Turan, in the Department of Physics, METU, Ankara, Turkey, for preparation of ion-implanted samples and enlightening discussions on the data obtained from these samples; Dr. Vladimir Karavanskii, at the NSCG-Physics Institute, Russian Academy of Sciences, Moscow, Russia, for his involvement in the research with chemically-etched germanium, for his encouragements, and for the skilful hints provided for spectral analysis; Prof. Rolf E. Hummel, Department of Materials Science and Engineering, University of Florida, US, for providing us with their spark processed germanium samples for further analysis.

Also my special thanks go to both Dr. Nestor Capuj at ULL Tenerife, Spain, for -rather lengthy but- fruitful discussions, and to Prof. David Lockwood at National Research Council, Ottawa, Canada for his motivation and guidance in the beginning of my research activities, during their sabbatical/visits to our research group at the De Montfort University.

Last but not least, I have to address my very special thanks to those former research students at our research laboratory in De Montfort University, including Dr. Artem Starovoitov and Dr. Alex Parbukov, for their skilful and cheerful helps with the instruments, data analysis and in the research laboratories.

Finally, I am grateful to the Governors of De Montfort University providing both funding and the resources to allow this study to be accomplished.

Abstract

The discovery of the strong room temperature visible photoluminescence (PL) emission from porous Si in 1990 has been the catalyst for much of the recent study on the visible PL emitting semiconductor nanocrystalline materials. Silicon, an indirect bandgap semiconductor, in the form of nanoparticles is thought to emit strong visible light due to quantum confinement effects and, in the near future, will replace GaAs (and the other direct bandgap III-IV semiconductors) as for the light emitting devices such as lasers. On the other hand, mainly due to its much larger exciton Bohr radius, Ge, in the form of nanocrystals, is expected show more pronounced quantum confinement effects compared to Si nanocrystals. SiGe alloys also constitute a more attractive material than Si in terms of both industrial applications and fundamental research: the lifetime of the 'porous Si-like' PL of porous SiGe is observed to be approximately two orders of magnitude faster than that of porous Si. Moreover, the bandgap of Si-Ge alloys can be intentionally varied between those of pure Si and Ge via the alloy composition.

In this study, an investigation has been made of the microstructural properties of visible PL Group IV nanostructures (SiGe and Ge) that have been rather much less studied in the literature, for example, in comparison to Si nanocrystals. For the first time in the literature the confinement of phonons in SiGe nanocrystals has been shown, in anodised porous SiGe films, and variations in the film composition were estimated utilising Raman spectroscopy.

Methods such as stain etching, ion-implantation, and spark processing, were employed to synthesise Ge nanostructures. Particle sizes were usually estimated by modelling the Raman spectra in line with a phonon confinement model. Properties of 2-10 nm Ge nanostructures, ranging in structure from partially amorphous to crystalline, and in various environments, e.g. oxide matrices, were studied. Typical PL spectra were observed in the visible from these samples. These spectra were determined to be originating either due to Ge nanocrystals or other chemical origins, such as defects in GeO_xs or defects in host matrices (e.g. SiO_2, GeO_x). It is recommended that samples with a wider range of particle sizes must be prepared, preferably 'oxide-free', using the first two methods, and characterised optically from near UV to near IR in order to observe clearly the size dependence of the PL emission from Ge nanocrystals.

Table of Contents

INTRODUCTION

CHAPTER 1. INTRODUCTION TO GROUP IV SEMICONDUCTORS

CHAPTER 2. SILICON AND GERMANIUM NANOSTRUCTURES

CHAPTER 3. MATERIAL PREPERATION AND CHARACTERISATION TECHNIQUES

CHAPTER 4. RESULTS AND DISCUSSIONS

CHAPTER 5. CONCLUSIONS AND FUTURE WORK

INTRODUCTION

The discovery of visible, strong and room temperature photoluminescence (PL) from silicon (Si) nanocrystals opens new possibilities for the use of Group IV indirect-gap semiconductors as materials for optoelectronic applications such as light emitting diodes and display devices. Among the several forms of semiconductor nanostructures, porous silicon (PS) is the most studied material to date. On the other hand, visible luminescence from germanium (Ge)-based nanocrystals, for example, is much less well studied. For the Si nanocrystals, despite the continuing discussions, it has been recently become clear that both quantum confinement effects and surface states are likely to play a role in the visible PL from this material.

In this project, we aimed to study the structure of visible luminescent SiGe alloy and Ge nanostructures that have been studied rather much less in the literature. In particular, various methods, such as anodisation, chemical (or stain) etching, ion-implantation and subsequent annealing, and spark processing, have been utilised to synthesise and characterise Ge nanocrystals.

SiGe alloys have attracted much interest since the early 1970's due their adjustable bandgaps between those of bulk Si (1.17 eV) and Ge (0.67 eV). Moreover, the lifetime of the visible PL from porous SiGe (PSG) alloys, that is very similar to the orange PL of PS in air, has been reported by a few groups to be about two orders of magnitude faster than that of PS. These two effects might make PSG a more attractive material than PS in the future in terms of device applications. We observed that none of those studies on PSG

had actually studied in depth the microstructure (especially crystal size and type, and any alterations -if there are any- in the alloy composition from the starting substrate materials) of their PSG samples. Understanding and controlling of these effects are essential for any future applications of PSG material.

We prepared, therefore, a set of nanoporous SiGe films from molecular beam epitaxy-grown $Si_{0.87}Ge_{0.13}$ epilayers (on Si substrates) by anodisation, and examined extensively their microstructure, using micro-Raman spectroscopy and scanning electron microscopy, as a function of material preparation parameters. We have shown, for the first time, the confinement of phonons in SiGe alloy nanocrystals and estimated the particle sizes quantitatively, along with the compositional variations that took place in favour of Ge, as a function of sample preparation parameters. Yet our results are preliminary, since only one specific atomic composition (of the starting layers) was used to prepare PSG and the average particles sizes studied were relatively large (between 10 and 20 nm) and they could not be taken as responsible for the visible PL.

More recently there has been an increase in the number of studies on the visible PL from Ge nanostructures. This is because Ge nanocrystals are expected to show more pronounced quantum size effects than Si nanocrystals, especially due to a larger exciton Bohr radius (17.7 nm versus 4.9 nm). However, it is interesting that chemically prepared samples, and samples prepared by other techniques, such as co-sputtering and subsequent annealing, where there are Ge atoms in contact with O atoms, are mostly reported to show PL in the 2.1-2.3 eV range of the electromagnetic spectrum (other reported PL bands fall into the blue and orange/red wavelengths). These are summarized and tabulated at the end of Chapter 2.

Towards determination of the origin of the 2.1-2.3 eV (yellow-orange) PL, we prepared chemically-etched Ge by both anodisation and stain etching methods. Anodisation with HF solutions did not yield visible PL chemically-etched Ge samples, however visible PL (2.3 eV peak energy) was observed from stain-etched Ge samples. Ge nanocrystals were observed in one group of stain-etched samples produced using a novel etchant. The PL behaviour of these samples through annealing in different chemical environments, and that of other stain-etched Ge samples (containing no Ge nanostructures but merely germanium oxides) as well as crystalline GeO_2, made it possible to attribute the origin of the yellow-orange PL from these materials not to quantum confinement effects but to the luminescent defects in germanium oxides.

Preliminary nanocrystalline Ge samples were successfully fabricated by implantation of Ge ions at a range of doses into thermally-grown SiO_2 films and subsequent high temperature annealing (between 700 and 1050 °C). Structural and luminescent properties of these films were characterised using a wide range of techniques, including secondary ion mass spectrometry, transmission electron microscopy, micro-PL and -Raman spectroscopy, and PL spectroscopy. It has been observed that defect centres in the silicon oxide matrix or in germanium oxides can emit visible PL near 2.0-2.3 eV. Moreover, it was also well-demonstrated by using micro-PL and Raman spectroscopy that Ge ion-implanted and annealed SiO_2 films containing well-formed Ge nanocrystals exhibit non-negligible increases in the visible PL intensity in comparison to as-implanted and oxide-removed counterpart samples. Therefore, it was concluded that one cannot totally rule out the possibility that Ge nanocrystals might themselves emit or take a role in the visible luminescence.

Spark-processed semiconductors are expected to possess nanocrystals of the substrate material (with sizes between 2-10 nm), as known from the mostly studied spark-processed substance, the visible PL sp-Si. In recent years, visible PL from spark-processed Ge (sp-Ge) has also been reported. At room temperature the main PL peak of sp-Ge is situated near yellow-green (2.3 eV) having two shoulder peaks in the blue (3.0 eV) and orange (2.0 eV). To date the origins of these PL bands have not been comprehensively understood. There is a debate as to whether all or any of these PL bands originate due to defects in germanium oxides or Ge nanocrystals, or involve both. In addition, the microstructure of sp-Ge has not been studied in detail thus far. Specifically, no direct link has been made yet between the Ge nanocrystals (or any other chemical species in the films) and the visible PL.

In this study, our other objective was to investigate the microstructure of visible PL sp-Ge and correlate it with the (orange) PL emission using simultaneously performed micro-Raman and micro-PL spectroscopy. In order to provide direct comparison with the literature, several samples were prepared under equivalent conditions with those reported in the literature. It was found that the films are composed of mainly sub-stoichometric germanium oxides and elemental Ge (in the form of nano- or micro-crystals). Ge nanocrystals of sizes comparable to 6-7 nm were observed by the Raman spectra. It was suggested that the Ge crystals were embedded into thick germanium oxide layers, which showed structural inhomogeneities in terms of local structural configuration and stoichometry, across a single film or between the similarly prepared samples.

The micro-PL spectra, simultaneously taken with the micro-Raman spectra, in the orange PL band enabled us to determine unambiguously that this PL band did not involve any kind of Ge-Ge bonded material, i.e. Ge nanocrystals, but presumably Ge-O bonded material. It has been established by this study that this rather unique technique (i.e. simultaneous micro-Raman and micro-PL spectroscopy) pose great advantages in determining the material type (or the simple chemistry) responsible for the PL, provided that the nature of the material allowed the observation of differences between such spectra. Since the sp-Ge films showed such a behavior indeed, we find it favourable to propose that the microstructure of sp-Ge films would enable one also to study the origin of the other PL bands (blue and yellow-green) using the same method but different excitation energies.

Finally, as a concluding remark, it is strongly recommended that, in order to study the size dependence of the PL emission of Ge nanocrystals, nanocrystalline samples with a wider range of particle sizes must be prepared, preferably as oxide-free as possible, and optically characterised, especially with PL and bandgap measurements, throughout from near IR to near UV.

CHAPTER 1. INTRODUCTION TO GROUP IV SEMICONDUCTORS

1.1 THE BAND THEORY OF SOLIDS

The energy band structure of a solid determines whether it is an insulator, a conductor or a semiconductor. The existence of electron energy bands in solids makes it possible to understand the most varying property of solids, namely their electrical resistivity: a value of 1.7×10^{-8} Ω m for the dc electrical resistivity of copper, a good conductor, is more than 25 powers of ten smaller than the value of 7.5×10^{17} Ω m for the electrical resistivity of quartz which is a good insulator.

The electrical and optical behavior of a solid is governed by its energy bands, the gaps between them, and the extent to which they are filled by electrons. Materials with electrical resistivity lying in the range of 10^{-5}-10^{7} Ω m can be classified as semiconductors [1]. A semiconductor has an energy gap between zero and 3 electron volts (eV) for electronic excitations from its valence band to the conduction band (that is, its fundamental bandgap), whereas a metal or semimetal has a zero bandgap and an insulator has a bandgap of larger than 3 eV.

The origin of the energy bands in terms of the periodicity a crystal lattice imposes on the motion of the electrons is explained by the solution of the Schrödinger equation for

the Kronig-Penney model, which was suggested in early 1930's [2]. The key assumption of the Kronig-Penney model is that the solution of the Schrödinger equation is a Bloch function, which takes into account the periodicity of the lattice. A detailed explanation can be found in any of the standard textbooks [3-5].

1.2 SEMICONDUCTORS

Many different chemicals can be semiconductors, including both elements and binary compounds. The semiconducting elements silicon, germanium and tin, from column IV of the periodic table, have the diamond crystal structure (see 1.2.2). The diamond form of carbon is more properly classified as an insulator owing to its bandgap of ~ 5.5 eV. Silicon and germanium are the technologically most important semiconducting elements. Red phosphorus, boron, selenium, and tellurium are the other semiconducting elements, and these have complex crystal structures.

Semiconducting compounds are generally formed by the elements from columns III and V of the periodic table, III-Vs, or from columns II and VI of the periodic table, II-VIs. There are also many more complicated semiconducting compounds, such as oxides and organics.

1.2.1 Effects of Doping and Temperature on Resistivity

An *intrinsic semiconductor* is one in which the semiconducting properties are due to the pure material itself. In such semiconductors, conduction band electrons only come from

formerly occupied valence band levels, leaving holes behind them. In an *extrinsic semiconductor*, impurities contribute a significant fraction of the conduction band electrons or valence band holes. An extrinsic semiconductor is called *n-type* or *p-type* according to whether the dominant carriers are electrons or holes respectively. In n-type semiconductors, impurity atoms are called *donors* as they can give up electrons to the conduction band, and impurity atoms in p-type semiconductors are called *acceptors* as they accept electrons from the valence band, leaving holes in the band.

The resistivity of an extrinsic semiconductor is much lower than for its intrinsic state. This is because it is far easier to excite a hole into the valence band from an acceptor level or an electron into the conduction band from a donor level, than it is to excite an electron across the entire energy gap from valence to conduction band. This can be better understood from Fig. 1.1 where the resistivity of antimony doped Ge (n-type) is plotted versus the inverse of temperature for a variety of impurity concentrations. As the concentration of donors increases the resistivity (or the conductivity) decreases (increases). It can be also deduced from Fig. 1.1 that for most doping concentrations the electrical resistivity of a semiconductor decreases with rising temperature, opposite to the behavior for metals.

Specimen	Donor Concentration (cm^{-3})
1	5.3×10^{14}
2	9.3×10^{14}
5	1.6×10^{15}
7	2.3×10^{15}
8	3.0×10^{15}
10	5.2×10^{15}
12	8.5×10^{15}
15	1.3×10^{16}
17	2.4×10^{16}
18	3.5×10^{16}
20	4.5×10^{16}
21	5.5×10^{16}
22	6.4×10^{16}
23	7.4×10^{16}
24	8.4×10^{16}
25	1.2×10^{17}
26	1.3×10^{17}
27	2.7×10^{17}
29	9.5×10^{17}

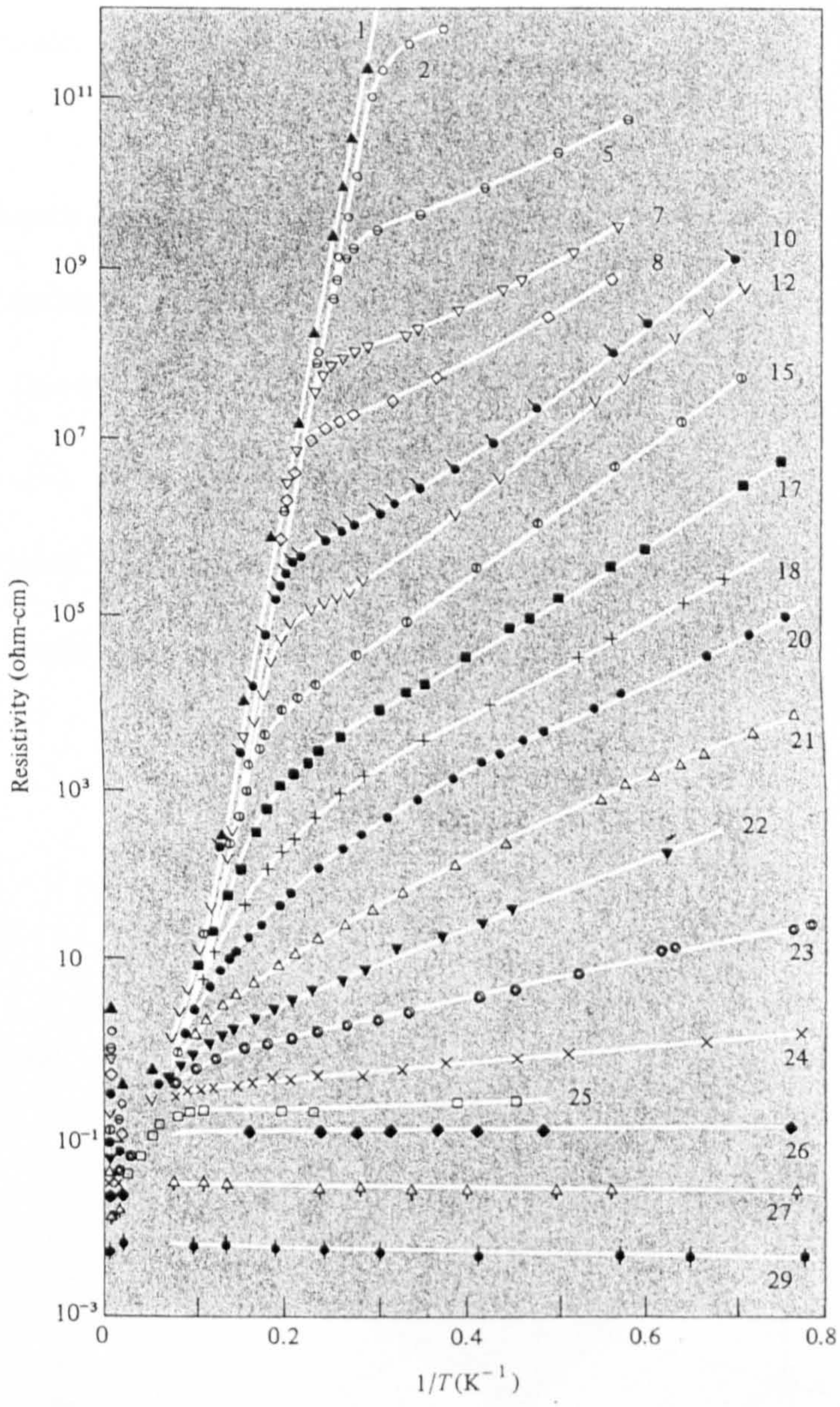

Figure 1.1 The resistivity of antimony-doped Ge as a function of 1/T for several impurity concentrations [1].

1.2.2 Diamond Crystal Structure

Semiconductors can be in the crystalline state, that is in an ordered state exhibiting a perfectly regular 3-D arrangement of atoms, or in the amorphous state, that is in a

chemically or statically disordered state. Crystalline structures can be described in terms of translational, rotational, and reflection symmetries.

Primitive lattice vectors can be chosen for a given crystalline array of atoms so that the *direct lattice* can be obtained by translating a point by multiples of the primitive lattice vectors. The lattice for diamond is face-centred-cubic (FCC) with a basis of two atoms, one at (0,0,0), the other at (¼,¼,¼). Diamond can be viewed as the result of 2 interpenetrating FCC lattices displaced from each other by one quarter of the cube diagonal distance. In Fig. 1.2 the diamond structure and FCC lattice with its primitive lattice vectors are given.

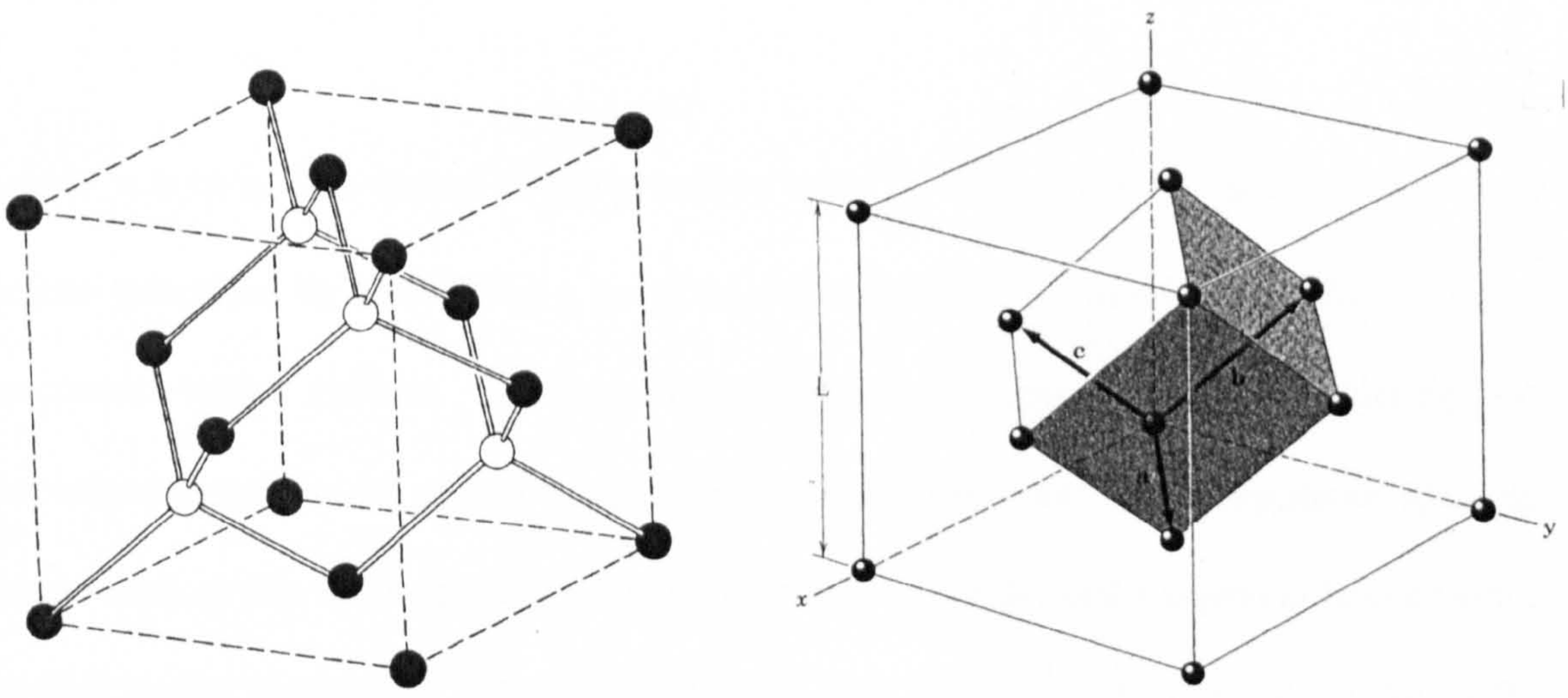

(a) (b)

Figure 1.2 (a) The diamond structure. For clarity atoms inside the cube are un-shaded. **(b)** The lattice for the diamond structure, i.e. the FCC lattice, with a set of primitive lattice vectors.

Numbers specifying the size of a unit cell (a single parameter (L) in cubic crystals) are called *lattice* constants. Si and Ge are two important examples of elements crystallising in

the diamond structure with lattice constants 5.43 Å and 5.66 Å, respectively. Each atom in diamond has 4 tetrahedrally-arranged nearest neighbors and 12 second and 12 third nearest neighbors. These are the first three *coordination numbers* for the diamond structure.

1.2.3 Reciprocal Lattice and Brillouin Zone

In three dimensions, if $\mathbf{a}$, $\mathbf{b}$, and $\mathbf{c}$ are a set of primitive vectors for a direct lattice, then the *reciprocal lattice* can be generated by the three *primitive reciprocal lattice vectors*, $\mathbf{p}$, $\mathbf{q}$, and $\mathbf{r}$, given by

$$\mathbf{p} = 2\pi \frac{\mathbf{b} \times \mathbf{c}}{\mathbf{a}.\mathbf{b} \times \mathbf{c}} \qquad \mathbf{q} = 2\pi \frac{\mathbf{c} \times \mathbf{a}}{\mathbf{a}.\mathbf{b} \times \mathbf{c}} \qquad \mathbf{r} = 2\pi \frac{\mathbf{a} \times \mathbf{b}}{\mathbf{a}.\mathbf{b} \times \mathbf{c}} \tag{1.1}$$

where $\mathbf{a}.\mathbf{b} \times \mathbf{c}$ is the volume of the primitive cell [1]. The reciprocal lattice is the set of points generated by translating a point of wavevector $\mathbf{k}$ by multiples of the primitive reciprocal lattice vectors. The reciprocal lattice is a compact way of tabulating two important properties of crystal planes, that is their slopes and their interplanar spacing. *Miller indices* of a lattice plane are the coordinates of the shortest reciprocal lattice vector normal to that plane, thus for example a plane with Miller indices (*hkl*) is normal to the reciprocal lattice vector $\mathbf{G} = h\mathbf{p} + k\mathbf{q} + l\mathbf{r}$. Secondly, the length of the vector $\mathbf{G}(hkl)$ is $2\pi / \mathrm{d}(hkl)$ where d is the separation of the planes (hkl).

The *first Brillouin zone* (BZ) is the smallest volume entirely enclosed by planes perpendicularly bisecting the reciprocal lattice vectors. The reciprocal lattice for the FCC

lattice is a truncated octahedron and the first BZ for the FCC lattice is as given in Fig. 1.3.

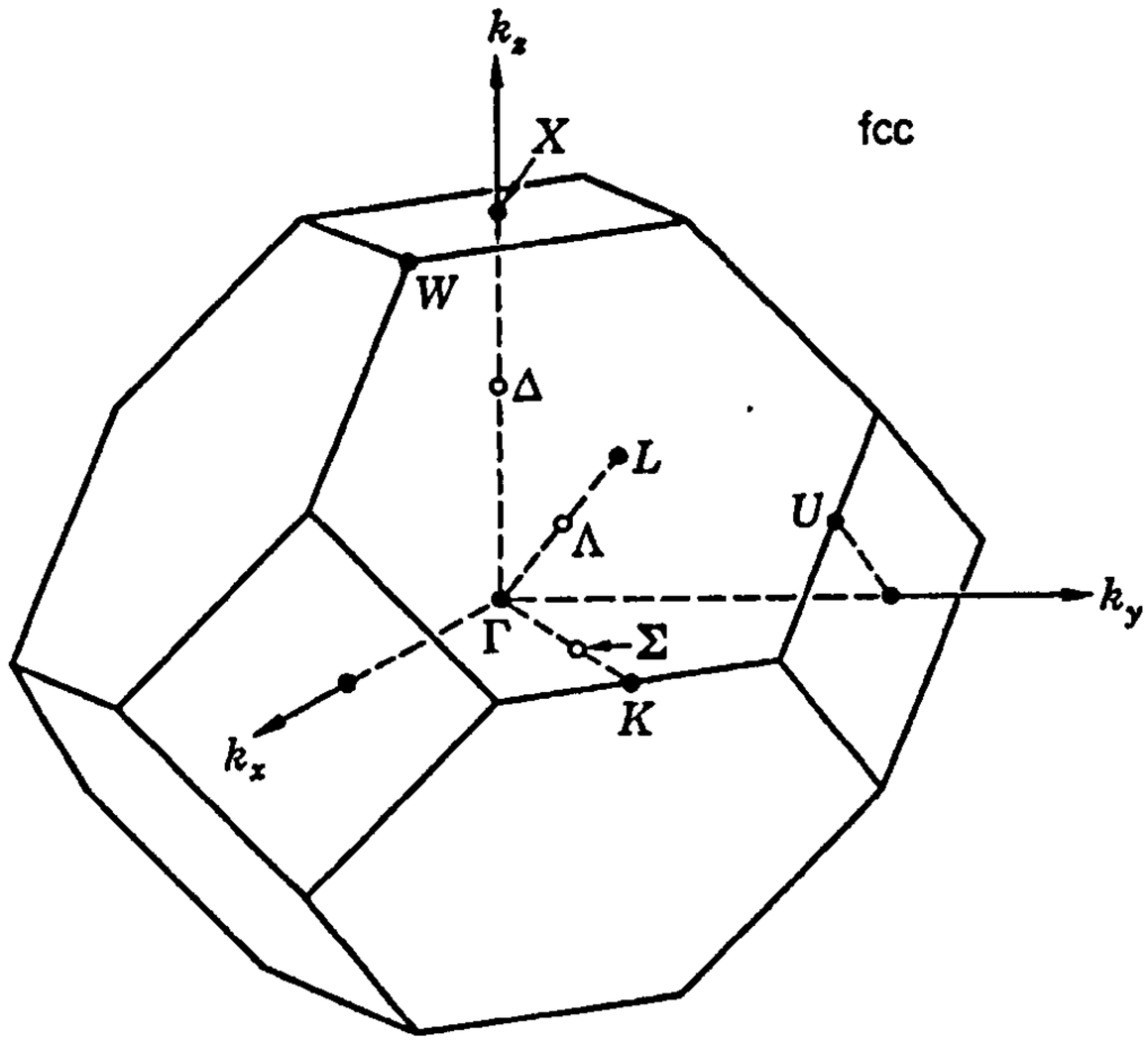

Figure 1.3 Brillouin zone of the FCC lattices with the standard labels of the symmetry points and axes indicated [6].

The BZ is highly symmetrical due to the symmetry from the direct lattice and hence the crystal. In Fig. 1.3 high symmetry points on the surfaces and lines inside the BZ are labeled using some letters. The three high-symmetry directions [100], [110], and [111] in the first BZ of the FCC are denoted by:

[100] direction: $\Gamma-\Delta\rightarrow X$

[111] direction: $\Gamma-\Lambda\rightarrow L$

[110] direction: $\Gamma-\Sigma\rightarrow K$.

Points and axes in the reciprocal lattice space which transform to each other under symmetry operations are said to be equivalent. For example the eight hexagonal faces including the L points in the first BZ of the FCC lattice (Fig. 1.3) are equivalent and can be transformed into one another by 90° rotations. Therefore, it is necessary to calculate the energies of the electron at only one of the eight equivalent hexagonal faces containing the L point to completely describe the band structure in all faces.

1.2.4 Direct and Indirect Bandgaps

If the locations of the maximum valence band energy and the minimum conduction band energy correspond in **k**-space the semiconductor is said to be a *direct* bandgap semiconductor, and if they do not correspond in **k**-space the semiconductor is *indirect*. It is clear from Fig. 1.4 that GaAs is a direct bandgap semiconductor and both Ge and Si are indirect bandgap semiconductors.

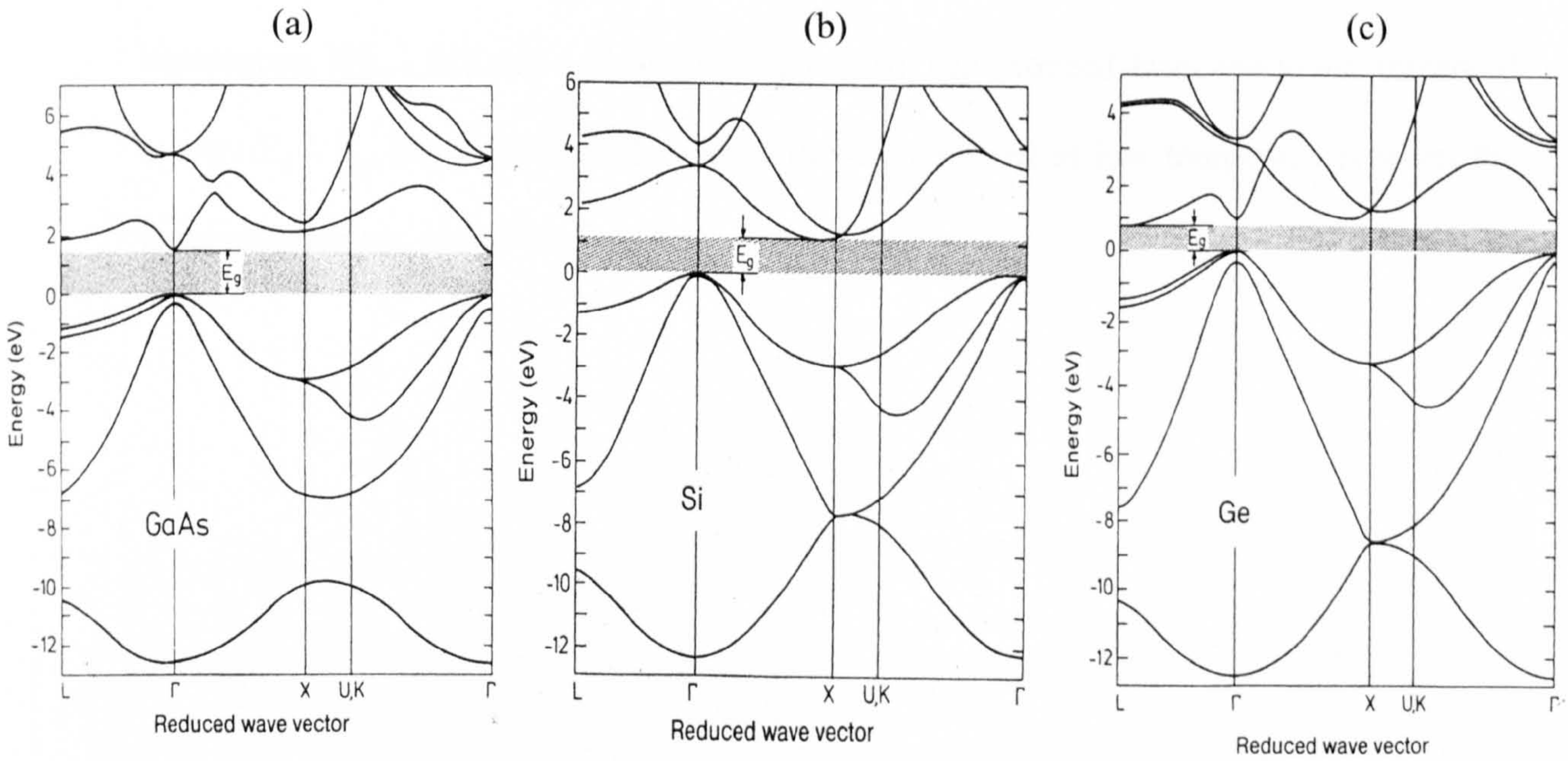

Figure 1.4 Electronic band structures of (**a**) GaAs (direct bandgap), (**b**) Si and (**c**) Ge (indirect bandgaps) [7].

Minimum energy transitions are vertical (in **k**-space) for a direct bandgap material whereas indirect bandgap materials undergo a non-vertical transition as sketched in Fig. 1.5. In other words in a direct bandgap material photon of energy equal to the energy difference between that of the valence band maximum and conduction band minimum can excite an electron from the top of the filled band directly to one of the states at the bottom of the conduction band. Any photon with energy larger than this value (E_g) can participate in a direct transition; the free electrons and holes so produced share the excess energy in such a manner that they have the same value of **k**. However, non-vertical transitions in an indirect bandgap material occur via an intermediate virtual state, whereby photon absorption is accompanied by either the creation or annihilation of a lattice vibrational phonon to achieve the momentum conservation. This model requires a minimum photon energy of $E_g + E_p$ for an indirect transition which creates an electron-hole pair and a phonon of energy E_p and momentum $\hbar(\mathbf{k_c} - \mathbf{k_v})$, a process which takes place at any temperature ($\mathbf{k_c}$ and $\mathbf{k_v}$ are the wavevectors of the conduction and valence band extrema locations, respectively). The alternative process, in which a phonon of momentum $\hbar(\mathbf{k_c} - \mathbf{k_v})$ and a photon are absorbed, can proceed from the lower threshold energy $E_g - E_p$, but such a mechanism will be attenuated at low temperatures when the required phonons are no longer readily available.

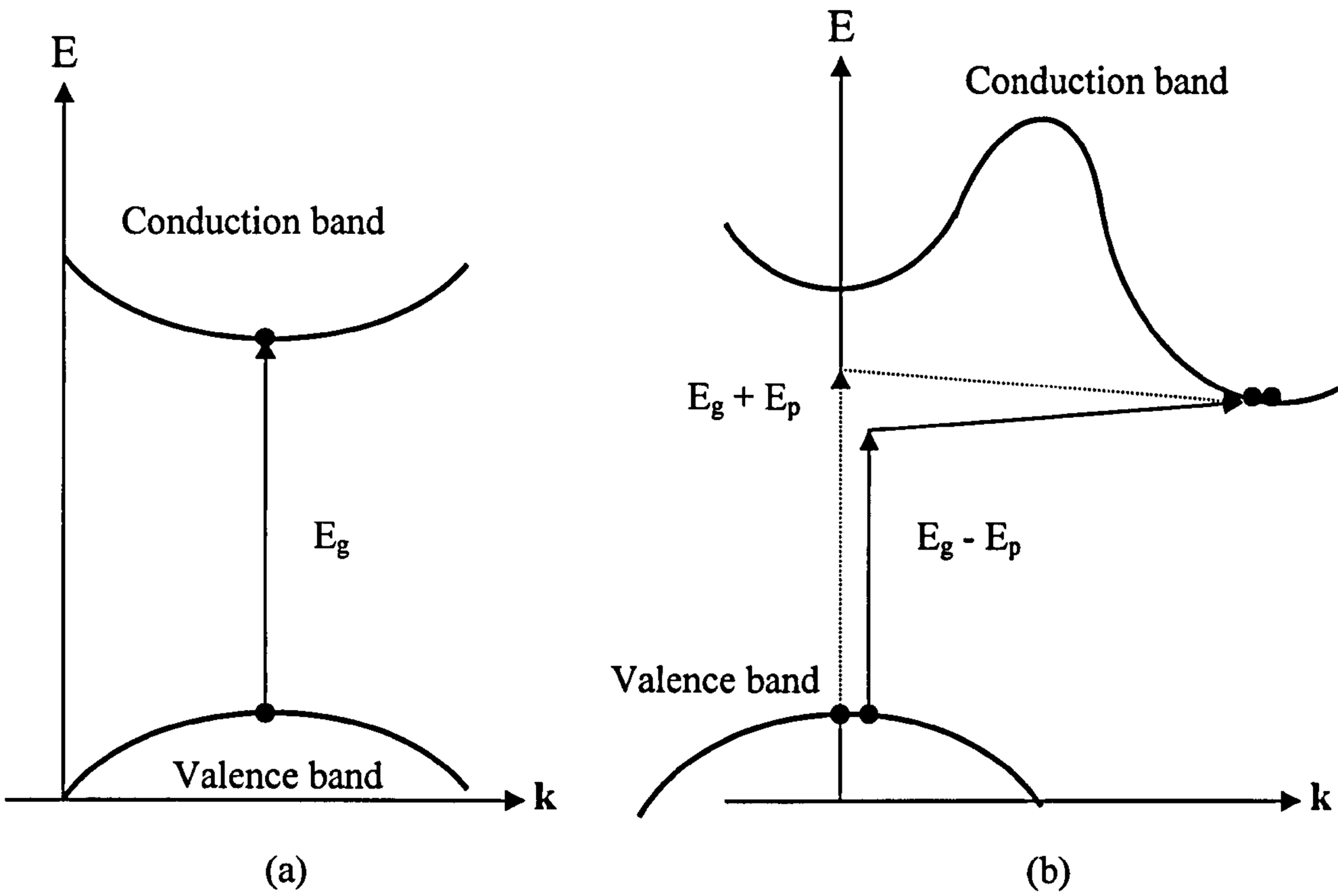

Figure 1.5 (a) Direct transition and (b) indirect transition in semiconductors

1.2.5 Impurity States and Band-Tailing

When an impurity atom is introduced in a lattice, if it replaces a host atom it is called a *substitutional impurity*, and if it occupies an interstitial state it is termed an *interstitial impurity*. Defects involving such impurity atoms are referred to as *extrinsic defects*.

Most defects are electrically active. Defects which can contribute free electrons to the host crystal are donors, and those which can contribute holes (i.e. remove free electrons) are acceptors. Substitutional Group-V atoms such as Sb, P and As are examples of donors in Si, having one more valence electron than the Si atoms they replace. Examples of acceptors in Si are substitutional Group-III atoms such as B, In, and Al. When a substitutional impurity atom, however, has the same valence as the host atom it is called

an *isoelectronic impurity*. Isoelectronic impurities can behave as donors or acceptors or remain electrically inactive [8].

The extra electron of the donor is attracted most strongly to the positive charge of the impurity nucleus. However, this attractive potential is not equal to that of an isolated impurity nucleus since it will be screened by the remaining valence and core electrons of the impurity atom, and more importantly, by all the valence electrons of the neighboring host atoms. Therefore, the extra valence electron in the impurity atom is only loosely bound to the impurity atom. In the case of an acceptor, such as an In atom replacing a Si atom, there is a deficiency of the valence electron when the acceptor bonds with its four nearest-neighbor atoms. Instead of regarding an acceptor atom as short of a valence electron, it can be thought as having an 'extra hole' which is loosely bound to its negatively charged nucleus [8].

The loosely bound donor electron can be ionised easily by thermal or electrical excitations: the ionisation energy from the ground state to the conduction band is usually less than 0.1 eV [9]. When the electron of the donor is in the conduction band, it is essentially free; thus its ground state (i.e. the donor level) is one ionisation energy below the conduction band. Likely, the acceptor level is one ionisation or binding energy above the valence band (Fig. 1.6).

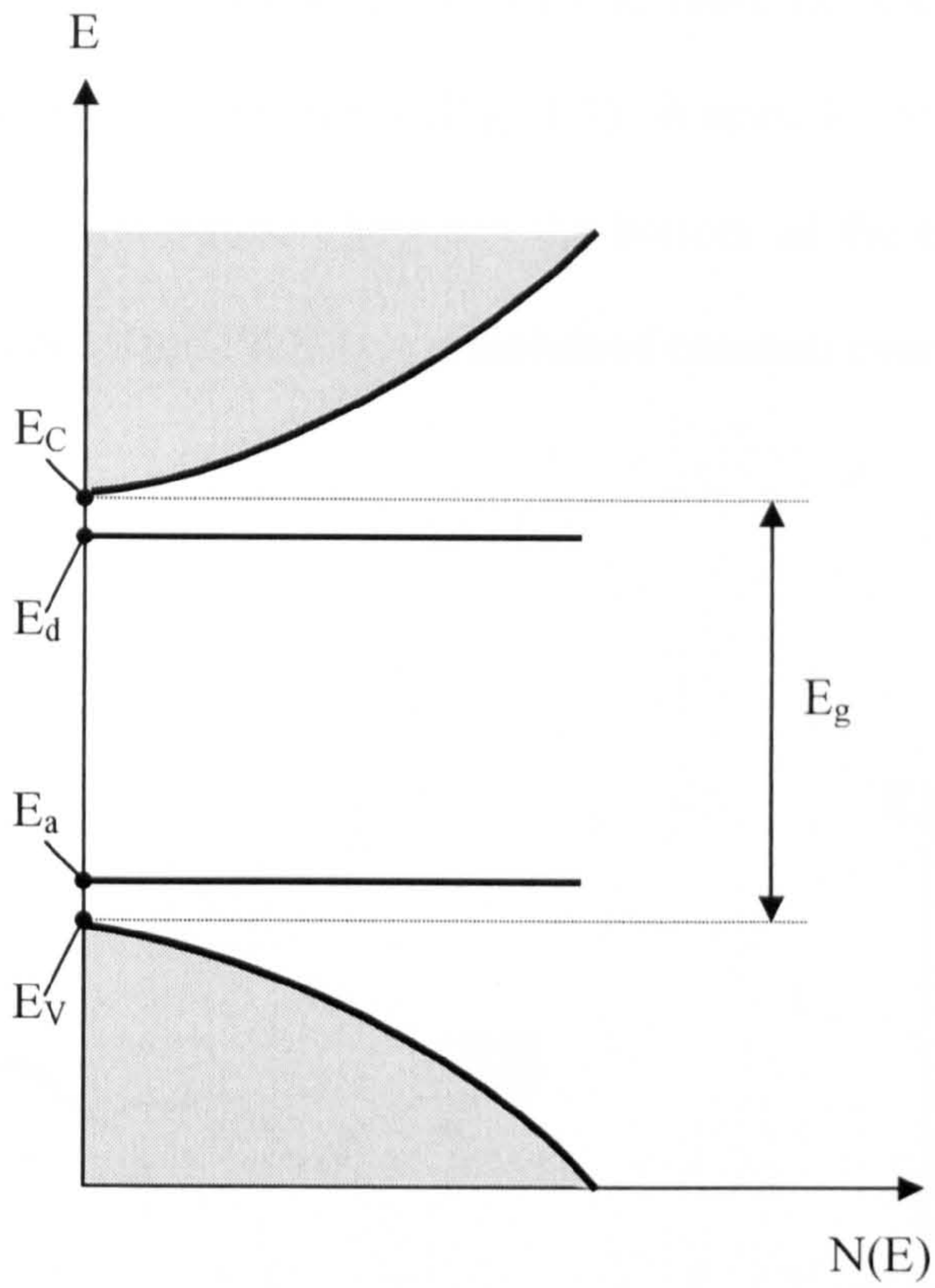

Figure 1.6 Schematic Electron Energy Level density N(E) for semiconductor containing, both donor and acceptor impurities. The donor levels E_d and acceptor levels E_a are generally close to the conduction band and valence band, respectively.

The electron wave functions at the impurity level begin to overlap when the impurity concentration is increased. As a result, the potential of each level changes slightly which leads to the formation of a band of states in the region of overlap. As the impurity concentration is increased further, the impurity band broadens and a tail of states is formed, extending the bands into the energy gap.

Band-tailing occurs also due to the Coulombic attraction of the conduction electrons and repulsion of valence holes by the ionised donors (acceptors act conversely). Donors are inhomogeneously distributed in the host crystal. Depending on the local population of

the impurities, the (Coulombic) interaction will be more or less strong for higher and lower population densities, respectively (Fig. 1.7). It must be noted, however, that the local energy gap (i.e. the separation between the bottom of the conduction band (C.B.) and the top of the valence band (V.B.)) is maintained constant everywhere.

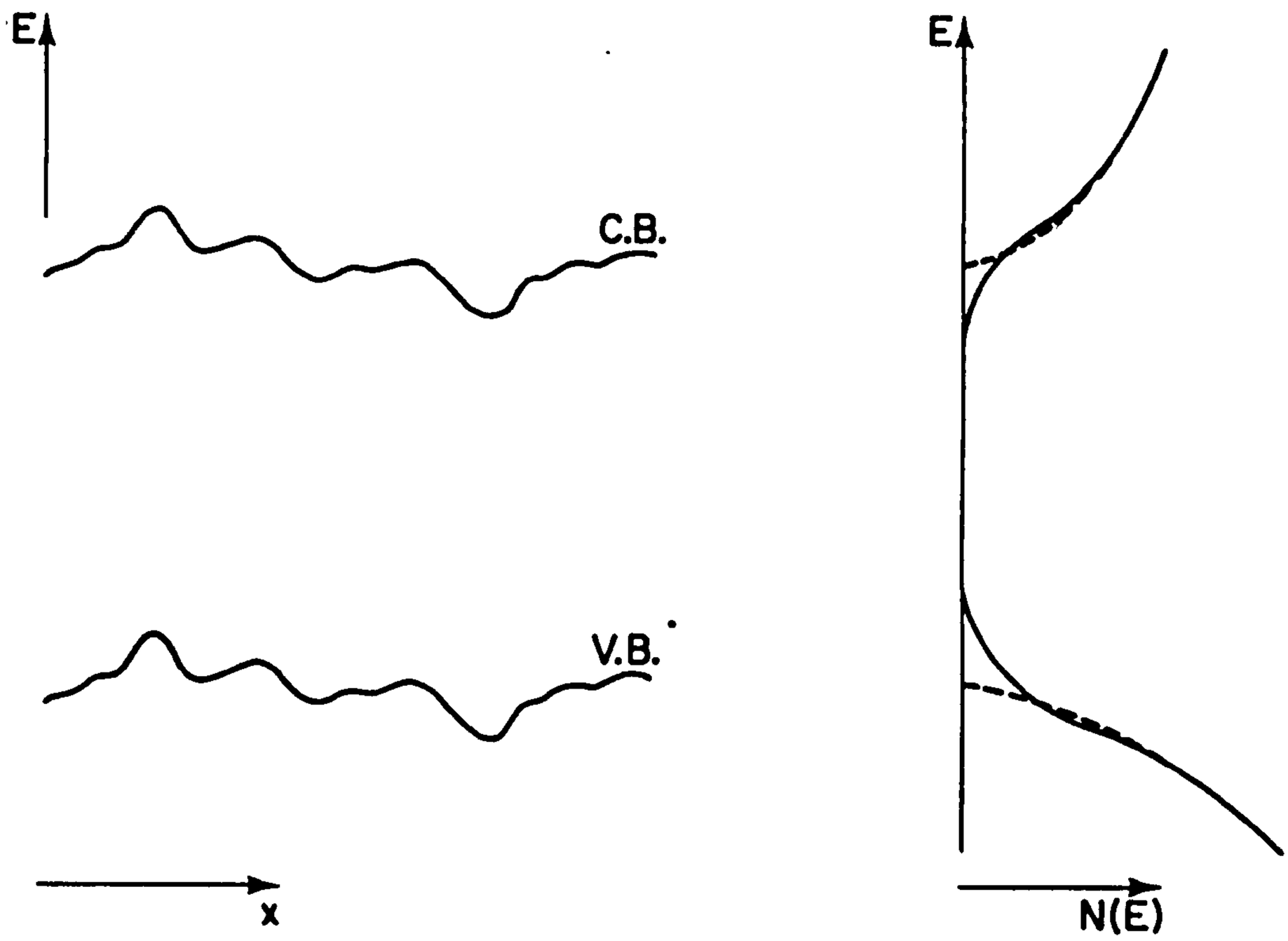

Figure 1.7 (a) Perturbation of the band edges by Coulomb interaction with inhomogeneously distributed impurities. (b) Tailing of the states into the energy gap, as a consequence of (a). Dashed lines denote the distribution of states in the unperturbed case [9].

1.2.6 Amorphous (Non-Crystalline) Semiconductors

Semiconductors that do not possess long-range order or periodicity characteristic of a crystalline semiconductor are referred to as *non-crystalline* or *amorphous*. Amorphous

semiconductors can be glasses, rapidly quenched melts and layers evaporated onto cold substrates.

There are close structural similarities between crystalline and amorphous semiconductors, particularly in respect of nearest neighbors, because the same chemical bonds and forces hold both types of solids together. Amorphous semiconductors have well-defined bond lengths, bond angles and nearest-neighbor coordination close to those found in crystalline semiconductors. However, there still remain many problems with the description of amorphous semiconductors. One of them is the absence of simplifications associated with periodicity. Another one, making the concept of amorphous state ill-defined, is that the transition from existing short-range order to 'non-existent' long-range order can occur in a variety of ways. The range of local order existing depends, anyway, on the material and the condition of its formation.

Therefore it is convenient to characterise the static structure of amorphous semiconductors by certain geometrical factors such as the angle between nearest-neighbor bonds or the bond lengths. These parameters are regarded as statistical variables. Due to the strength of the covalent bond, there is only a small (less than 1 %) variation in the bond length, while the bond angles can fluctuate by as much as 10^{o} [10]. Thus, for example, in a material such as amorphous silicon (a-Si), the silicon atoms still sit at the centre of the tetrahedron, but this tetrahedron is not quite regular.

The simplest defect in an amorphous semiconductor is a broken or unsatisfied bond (a *dangling bond*), resulting for example in a 3-fold coordinated atom for a covalently bonded amorphous semiconductor such as a-Ge, a-Si, etc. [Such a defect is not feasible in

a crystalline semiconductor like c-Ge; each atom is surrounded tedrahedrally by four other atoms so that a missing atom results in four dangling bonds and these may reconstruct]. Single dangling bonds are due to the randomness in the structure of the amorphous semiconductor.

Amorphous semiconductors can also contain voids up to 10 nm in size which may be considered as an aggregate of a number of vacancies. Such voids are the major source of dangling bonds as their surfaces will contain them in abundance.

An 'ideal' amorphous semiconductor can be defined as a random network with no long range order but an excellent short range order. This requires the semiconductor contain no structural defects (such as voids) or dangling bonds. Examples nearest to this ideal are amorphous films of Ge and Si prepared by vacuum evaporation onto a cool substrate. For example, a-Ge with a density of 97 % of that for a Ge crystal can be deposited as a film. Such a film has a nearest-neighbor coordination of 4 just as the Ge crystal and very few voids.

The intrinsic gap E_i (as measured optically) is slightly smaller for an ideal amorphous Ge or Si film than in the corresponding crystal. Amorphous layers of greater disorder show a gap which is smaller or less distinct. The conventional density of states for a semiconductor crystal, the expected density of states for the same solid as an ideal amorphous semiconductor and as a much more disordered amorphous semiconductor are shown in Figure 1.8. In part (a), a few 'pockets' of localised states within the intrinsic gap (E_c - E_v) corresponding with impurities and native flaws which perturb the periodicity are shown. Conduction and valence bands are still denoted in part (b), although now a

continuum of density of states is shown extending downwards from E_c and upwards from E_v, towards the centre of the gap.

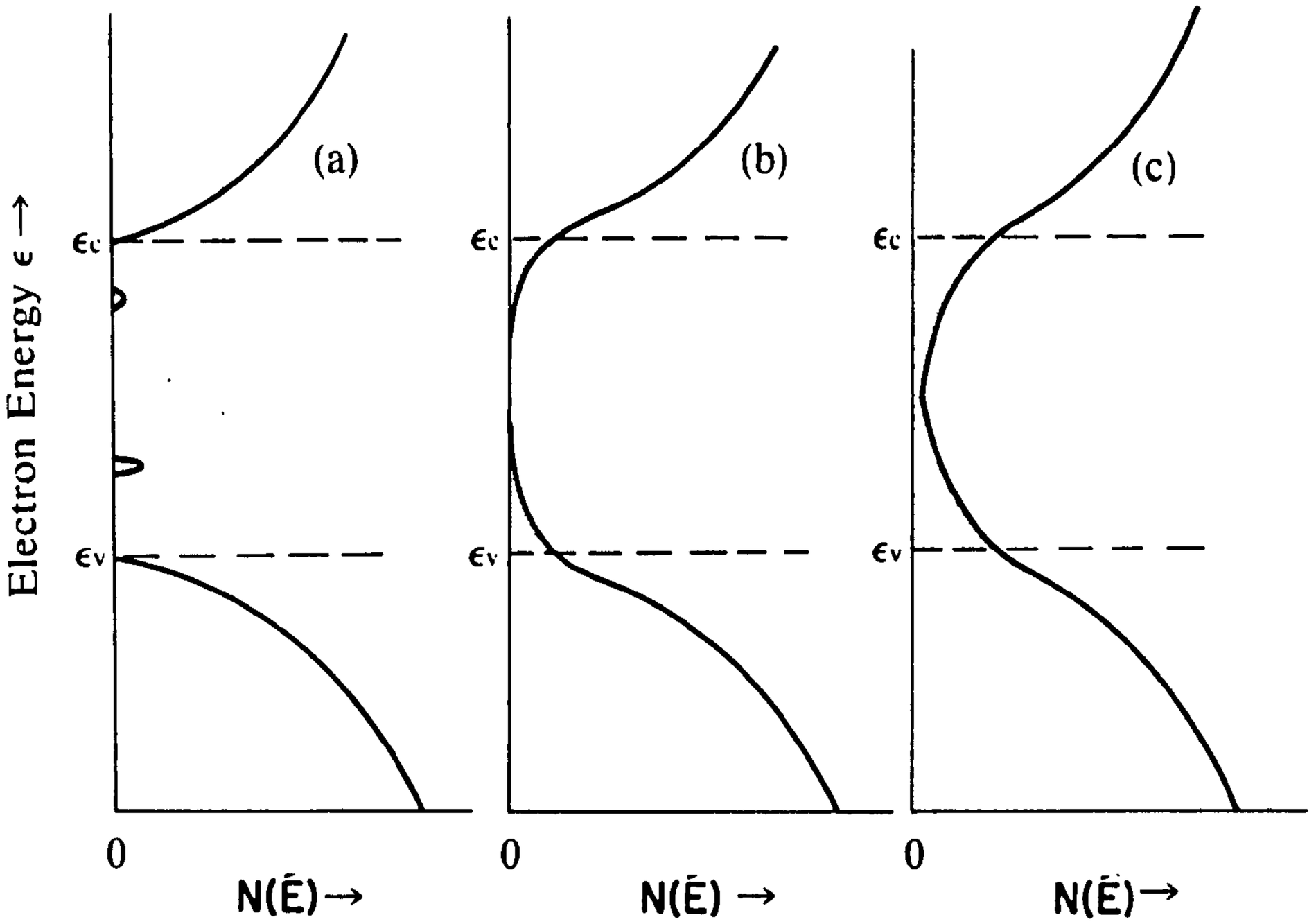

Figure 1.8 Density of states versus energy for (**a**) a crystalline semiconductor, (**b**) the same semiconductor as an 'ideal' amorphous semiconductor and (**c**) the same material as a much more disordered amorphous solid [11].

Band-tailing is inevitable even for a very high quality (or ideal) amorphous semiconductor film because it has a random network which tends to possess high strain energy and this must be reduced by creation of a number of defects in the structure. For the semiconductor in part (c), the strong disorder due to the imperfect short range order leads to substantial exponential tails of the densities of states for both conduction and valence bands which cover the whole forbidden gap. They are inevitably divided into

'donor-like' and 'acceptor-like' states which will be equal in number owing to the 'self-compensating' effect of the disorder. These states also contain empty localised states which serve as 'traps' for electrons and holes. Dangling bonds form states especially in the centre of the gap. Doping of such a semiconductor is unlikely to change the behaviour shown in part (c), because the valence requirements of the impurity atoms are met by changing the local coordination.

1.3 LUMINESCENCE

In section 1.2.4, we discussed the fundamental absorption of an electron, i.e. the transition of an excited-electron from the top of the valence band to the bottom of the conduction band, in both direct- and indirect-gap semiconductors. However, beside the band-to-band transitions, there are several others an electron can make, such as transitions between impurities and bands, between subbands, or as free carriers within a band. Absorption by an exciton is also possible when the excited electron forms a pair with a hole due to Coulomb attraction. Such an exciton will have energy states near the conduction band and a binding energy lower than either the donor or acceptor binding energies. The easiest way to measure the bandgap structure of a semiconductor is probably through a measurement of its *absorption* spectrum. In the absorption process, a photon of certain energy is removed from the incident beam on exciting an electron from a lower-energy state to a higher-energy state. The absorption process is therefore characteristic of the sample.

Luminescence is, on the other hand, an optical phenomenon that involves emission of characteristic *radiation* from the sample. For emission of radiation, initially the electrons and holes have to be excited by some external means. Luminescence can be excited in a variety of ways; for example, by injection of electrons and holes via an external current, known as *electroluminescence*, with electron beams (*cathodoluminescence*) or photons (*photoluminescence*), or by heating up the sample (*thermoluminescence*). Secondly, in most cases the excited electrons and holes thermalise among themselves (i.e. relax towards nearby potential minima) and reach quasi-thermal equilibrium in a time short compared to the time it takes electrons and holes to recombine. Finally, the thermalised electron-hole pairs recombine radiatively, producing spontaneous emission. The recombination energy, however, can also be released without the emission of photons; this is called *non-radiative recombination*.

1.3.1 Radiative Transitions

Fundamental transitions in a semiconductor are those occurring at or near the band edges, namely band-to-band (i.e. conduction band to valence band) or excitonic transitions. The occurrence probabilities of these transitions in a semiconductor are highly temperature dependent. The other main transitions involve impurities and so are dependent on the dopant level and temperature. As examples, transitions from a donor level to valence band or to an acceptor level and from conduction band to an acceptor level will also be summarised below.

1.3.1.a Conduction-Band-to-Valence-Band

In a perfect semiconductor electron-hole pairs thermalise and accumulate at the conduction and valence band extrema. The free carriers can then recombine radiatively in a band-to-band transition.

In a direct-bandgap semiconductor, momentum-conserving transitions connect states having the same **k**-values (Fig. 1.9.a). Accordingly, the emission has a low-energy threshold at $h\upsilon = E_g$. As the excitation rate increases and/or as the temperature increases, states deeper in the conduction band become filled, permitting emission at higher photon energies. In the emission spectrum, therefore, the low-energy edge is abruptly cut-off at $h\upsilon = E_g$, while a temperature-dependent high-energy tail characterises the free-carrier recombination. Direct-bandgap semiconductors are strong emitters of bandgap radiation and so are important materials for lasers and light emitting diodes (LEDs).

In an indirect-bandgap semiconductor, all the occupied upper states nominally connect to all the empty states. They are not efficient emitters: momentum conservation requires electron-hole pairs to recombine radiatively only by phonon-assisted transitions (Fig. 1.9.b), and hence the probability of these transitions is smaller than for competing non-radiative processes. Phonon emission is the most likely intermediate process. An optical transition assisted by phonon emission occurs at a lower photon energy than the bandgap energy, $h\upsilon_{min} = E_g - E_p$; whereas a higher energy of at least $E_g + E_p$ is required for the phonon absorption. Emission with phonon absorption is not such a favourable process; the number of available phonons rapidly decreases at lower temperatures and a photon with energy $h\upsilon = E_g + E_p$ can in fact readily be reabsorbed by the semiconductor.

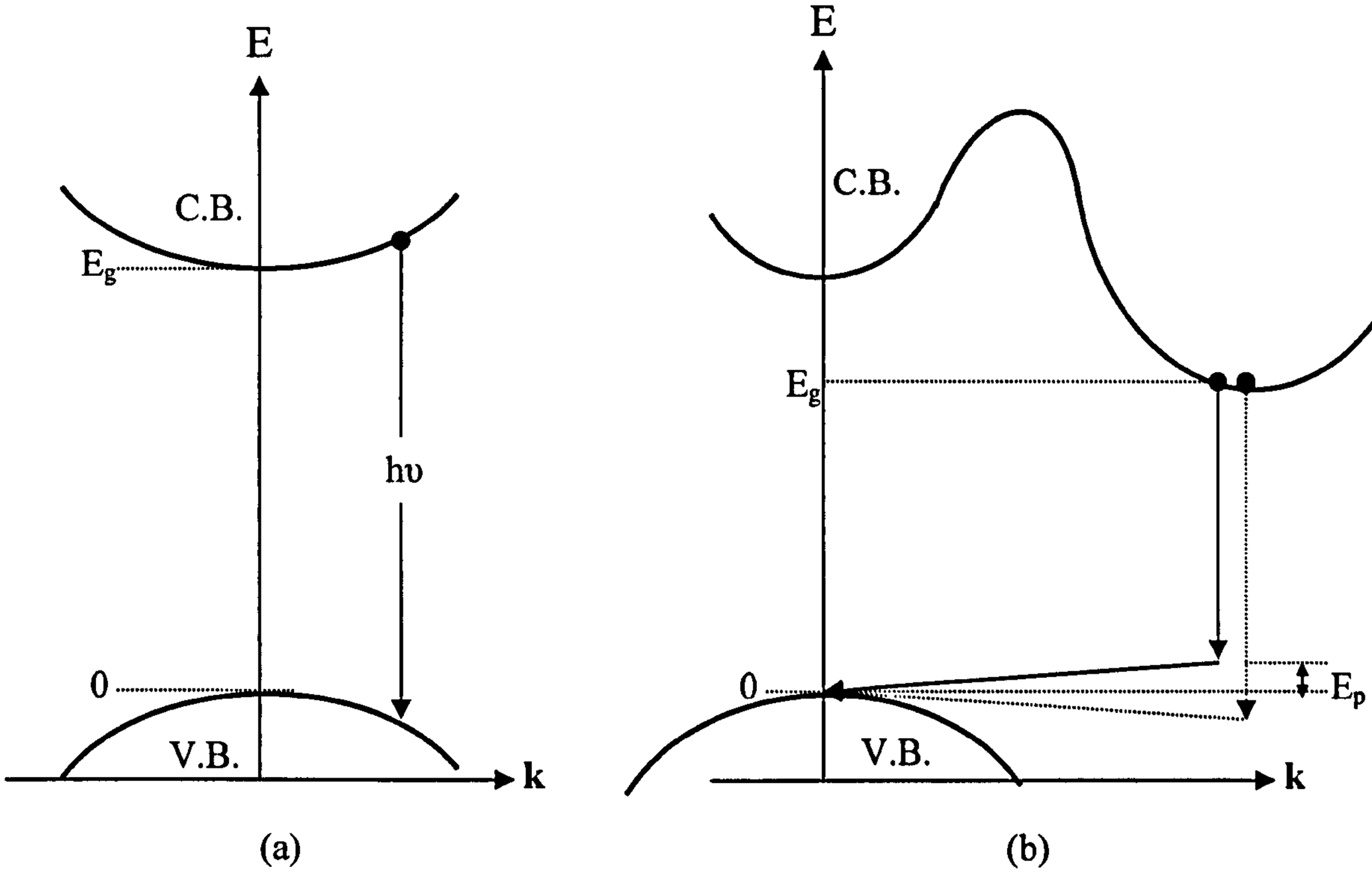

Figure 1.9 Band-to-band (**a**) direct and (**b**) indirect radiative transitions.

1.3.1.b Excitonic

In photoluminescence (PL) experiments on high purity and high quality semiconductors at very low temperatures, exciton states represent lowest-energy states for the photo-excited electron and hole pairs. On the other hand, at elevated temperatures such that $k_BT > E_x$ (k_B = Boltzman constant; E_x = ionisation energy for the exciton) and when the semiconductor crystal is less pure or less perfect, the local fields tend to break up the exciton into free carriers, which then can recombine radiatively in a band-to-band transition.

When excitons recombine a characteristic narrow spectral line is emitted. While in a direct-gap semiconductor the energy of the emitted photon simply equals to $h\upsilon = E_g - E_x$

(Fig. 1.10.a), in an indirect-gap semiconductor, since momentum conservation requires a phonon to be emitted (Fig. 1.10.b), this energy is $h\upsilon = E_g - E_x - E_p$ (E_p is the energy of the phonon involved).

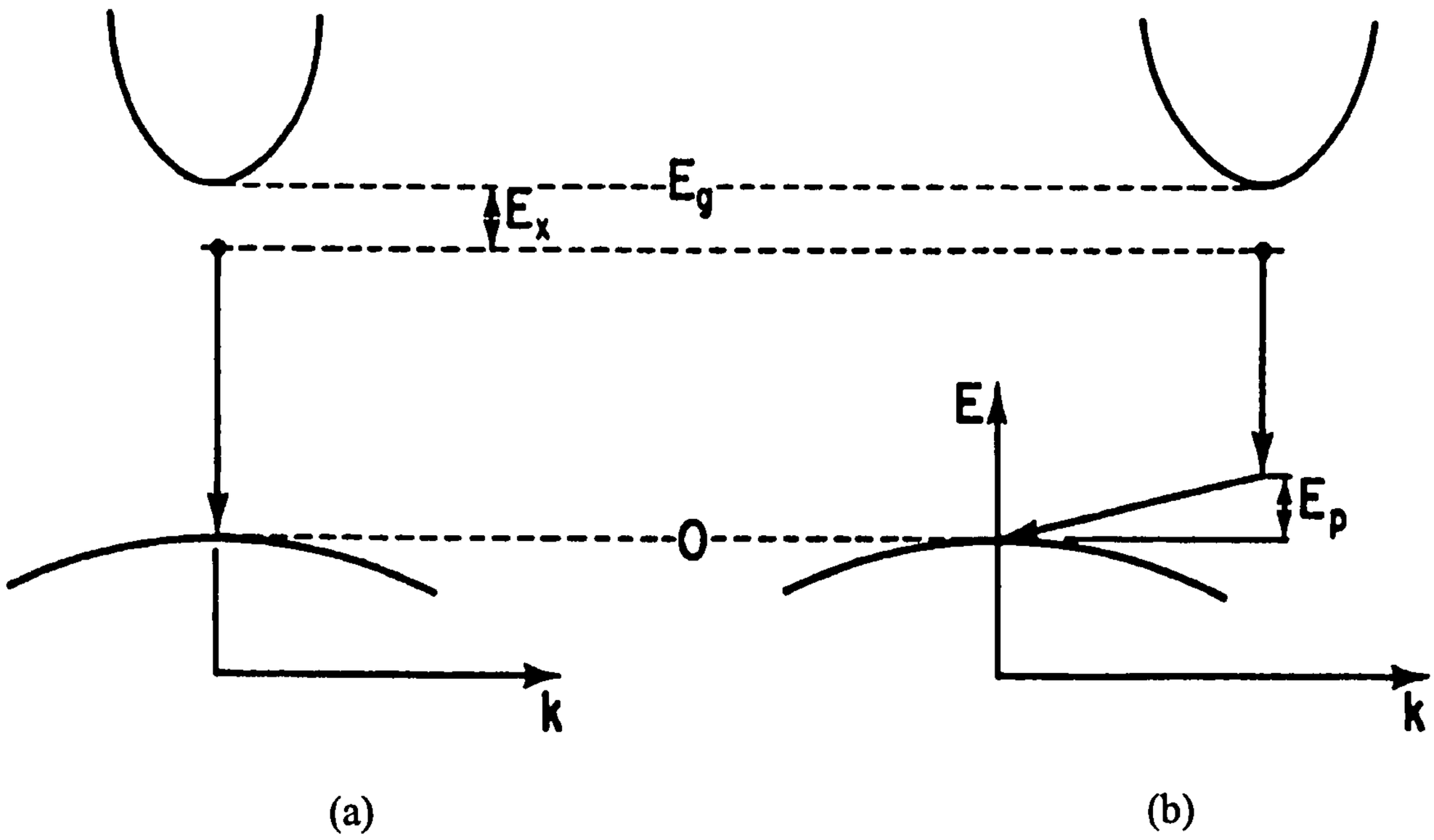

Figure 1.10 Exciton recombination in (**a**) direct- and (**b**) indirect-gap semiconductors [9].

Excitons can be either 'free' or bound to impurity atoms. Often, both free and bound excitons occur simultaneously in the same material. Figure 1.11 gives the emission spectrum of excitons in Si. Lines at A, B, D, and E are due to free excitons, whereas line C is attributed to an excitonic complex consisting of a hole bound by two electrons to a phosphorus ion [12]. The main PL line at D, shifted by ~ 70 meV from the bandgap energy (1.17 eV), is produced by the emission of a transverse optical (TO)-phonon, the line at E is produced by the emission of a transverse acoustical (TA)-phonon, and the

lines at A and B are produced by the emission of two phonons. The no-phonon (NP) transition, which is hardly recognisable in Fig. 1.11, is at lower energy than the bandgap energy by ~ 11 meV, which corresponds to the binding energy of excitons in Si [13].

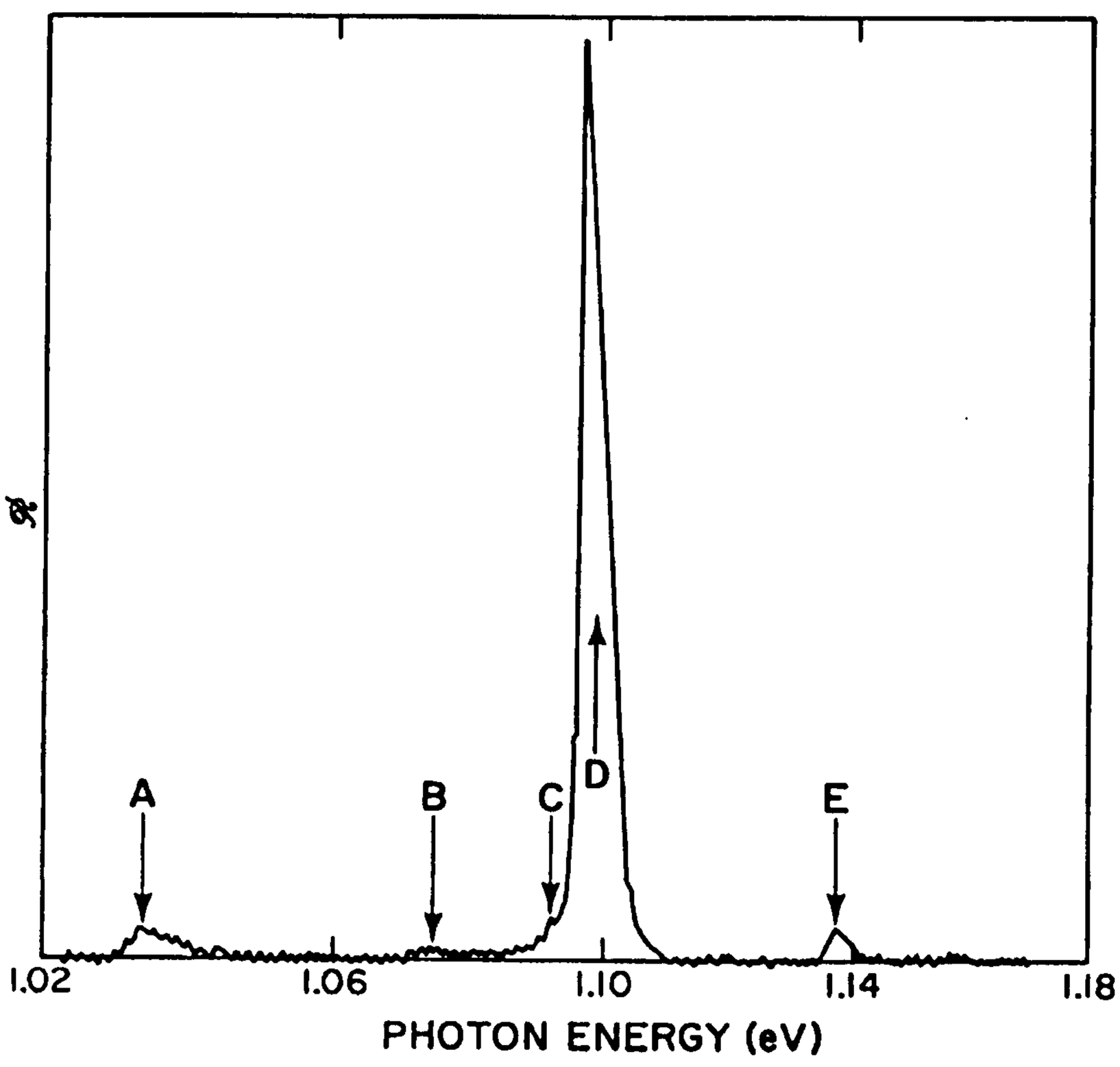

Figure 1.11 PL spectrum for a Si crystal containing 2 x 10^{14} phosphorus atoms per cm^3, at low temperature (18 K) [12].

1.3.1.c Between an Impurity Level and a Band

In a semiconductor, the transition of an electron from the conduction band to an acceptor state or a transition from a donor to the valence band can cause the emission of a

photon $h\upsilon = E_g - E_i$ for direct transitions and $h\upsilon = E_g - E_i - E_p$ if the transition is indirect (E_i = ionisation energy of the impurity; E_p = the energy of the phonon involved). In order to observe such radiative transitions experimentally, the semiconductor should have a relatively low concentration of impurities, and also the temperatures must be low such that $k_BT << E_i$. When the impurity concentration is large enough to form an impurity band which merges with the nearest intrinsic band, it results in a very broad emission spectrum and the interpretation of the process become less certain. On the other hand, for the purer materials, the dominant process may be the exciton recombination, whose signature is its very narrow emission spectrum.

1.3.1.d Donor to Acceptor

A semiconductor is said to be *compensated* if it contains both donors and acceptors. Such a semiconductor can emit photons with energy $h\upsilon = E_g - E_A - E_D + e^2/(\varepsilon\, r)$ provided that the combination of the donor and acceptor ionisation energies (i.e. $E_D + E_A$) is not very small. The term $e^2/(\varepsilon\, r)$ arises from the Coulomb interaction between the donor and acceptor that modifies their binding energies, where ε is the dielectric constant of the material and r is the distance between the donor-acceptor pair. A transition between distant pairs is assisted by tunnelling processes and hence it is less probable than a transition between nearer pairs. Examples of donor-acceptor transitions are found in GaP [14]. In Si, Ge, GaAs, and other semiconductors where $E_D + E_A$ is small, theoretically only distant pairs can contribute to the emission spectrum since the Coulomb-interaction term drives the donor and acceptor levels beyond the intrinsic band edges for nearer pairs. Therefore, donor-acceptor transitions are extremely difficult to observe from these semiconductors.

1.3.2 Non-Radiative Recombination Processes

In addition to the radiative recombination processes, the photo-excited pairs can also recombine non-radiatively. In fact, in many semiconductors the dominant process is the non-radiative recombination. States like defect levels inside the forbidden gap of a semiconductor are known as *radiative recombination centres* when they host electrons and holes which recombine radiatively; otherwise they are referred to as *non-radiative traps* or *luminescence killers*. Several radiationless transitions can occur in a semiconductor: for example, in the Auger effect, surface recombination, phonon emission, etc.

In the Auger effect, the excited electron immediately transfers its energy to another electron before returning to its ground state without emitting a photon; the second electron dissipates this energy by emitting phonons. It is evident that any process dependent on carrier-carrier interaction should become more intense as the carrier concentration increases.

A crystal lattice is strongly perturbed at the crystal surface, where many dangling bonds are produced. These dangling bonds can absorb impurities from the ambient which form a high concentration of shallow and deep levels in the forbidden gap, called *surface states*. Surface states may act as recombination centres. If a uniform distribution of states can be assumed for these levels, then the recombination of electron-hole pairs within a diffusion length from the surface will be readily non-radiative.

Localised defects, such as metallic inclusions, impurity precipitates, and local strains, inside a semiconductor can also produce a continuum of states inside the energy gap.

Such a microscopic defect could induce a deformation potential barrier (of height E_{ac}) around it. Then, only 'hot' carriers with sufficient energy to overcome this barrier, i.e. $k_B T_e > E_{ac}$, can recombine at this centre. For example, transitions involving either copper centres or defects in Ge have a *thermal-activation energy* $E_{ac} = 0.14$ eV [9].

Therefore, luminescence intensity from a semiconductor quenches by increasing the temperature as this will increase the non-radiative transitions.

Large luminescence efficiency is obtained when the non-radiative recombination rate is smaller than the radiative recombination rate. The efficiency is defined by

$$\mu = \frac{\tau_{nonrad}}{\tau_{nonrad} + \tau_{rad}} \tag{1.2}$$

where μ is the quantum efficiency, τ_{nonrad} is the non-radiative lifetime and τ_{rad} is the radiative lifetime.

1.4 SILICON AND GERMANIUM LIGHT EMISSION

In direct-gap semiconductors such as GaAs the electrons and the holes are located at the same point in the BZ. Thus these semiconductors emit photons having energy equal to the bandgap energy and a momentum that is negligible. Under these conditions, the radiative recombination rate is large and the radiative lifetime is short, typically of the

order of a few nanoseconds. The efficiency of direct gap III-V semiconductor compounds such as GaAs exceeds 1 % at room temperature and 10 % at cryogenic temperatures.

In Si and Ge, holes and electrons are found at different locations in the BZ as they are indirect-gap semiconductors. Therefore, recombination by emission of a single photon is (generally) not possible. Photon emission is possible only if another particle, such as a phonon, capable of carrying a large momentum is involved. Participation of a third particle in addition to the electron and the hole makes the rate of the radiative transition process substantially lower and the radiative lifetime is typically in the millisecond regime. Therefore, as it follows from Eq. 1.2, the efficiency drops by several orders of magnitude compared to the efficiency of direct gap semiconductors. At room temperature the efficiency of c-Si is usually of the order of 10^{-4}-10^{-5} % [15], which makes it unattractive for light emitting devices.

It is unfortunate that two different semiconductors are at the heart of the two basic devices: Si for transistors and GaAs (or other III-V semiconductors) for lasers. A goal for electronics technologies is creation of both types of devices using the same material, and in particular Si [16].

Driven by this reason, there has been much research to improve the luminescence efficiency of Si, and Si-based alloys, with the strategy of increasing radiative rate or decreasing the non-radiative rate. These initially included the use of Si-Ge superlattices or alloys [16] and isoelectronic impurities [17].

1.4.1 Silicon-Germanium Alloys and Superlattices

It was predicted that BZ folding in atomic layer superlattices could result in a direct bandgap structure. For example, it was theoretically shown for Si that the minimum in the conduction band can be folded back into the BZ centre and this would increase the transition probability [18]. It would however still be several orders of magnitude below that of GaAs. Furthermore, at low temperature no-phonon contribution luminescence bands were obtained from Si_mGe_n superlattices (m and n are the number of monolayers of Si and Ge) at infrared region of the electromagnetic spectrum, however the photoluminescence and the electroluminescence are essentially quenched at room temperature [19].

Alloying of Ge or C with Si allows 'engineering' of the electronic band structure, where the energy gap can be varied with alloy composition and strain [20]. It is expected that the energy gap of the alloy will assume a value intermediate between the gaps of the two pure semiconductors and vary in proportion to the composition. Si and Ge form a solid solution, $Si_{1-x}Ge_x$, and they are continuously miscible over the whole compositional range $0<x<1$ [21]. Figure 1.12 shows the variation of the energy gap of the Si-Ge alloys with the composition. With increasing Si concentration, the <111> valleys of Ge move to higher energies faster than the <100> valleys (see Fig. 1.4 for reference). The two sets of valleys have the same potential energy when (1-x) is ~ 0.15. Thus, as the composition is further changed in favour of Si, the bandgap enlargement slows down since the movement of the <100> valleys will start determining it. It is also noteworthy that the energy gap of the alloy does not vary with linearly with composition. This non-linearity may be explained with band-tailing due to the random perturbation of the lattice by the minority atoms (e.g. Ge atoms on Si site or vice versa).

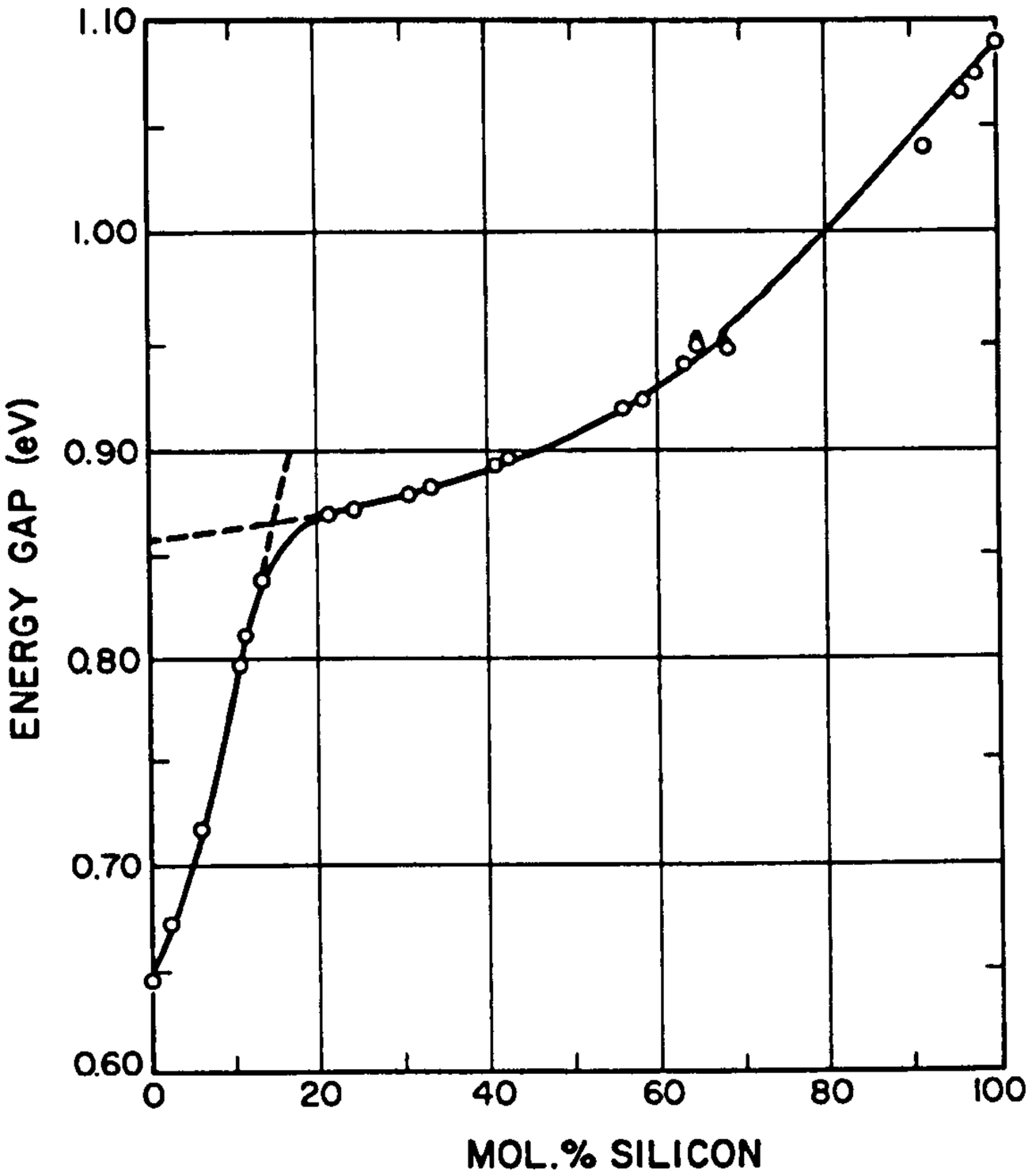

Figure 1.12 Composition dependence of energy gap in Si-Ge alloys at room temperature [21].

Photoluminescence and electroluminescence have been observed from $Si_{1-x}Ge_x$ alloys with increased intensity compared with Si. However, the light emitting devices made from these materials also suffer from low efficiency at room temperature [22].

1.4.2 Enhanced Light Emission from Nanostructured Silicon

The search for an efficient light emitting form of Si has been renewed with the observation of efficient, visible and room temperature luminescence from *porous Si* (PS) [23]. This observation opened a new information era. Since then several other forms of Si have been studied, such as nanocrystals, superlattices, impurity centres in Si, etc. [16]. In

the next chapter, we will deal with Si (and Ge) nanostructures, with more emphasis on PS.

1.5 LIGHT SCATTERING

When the light is travelling through a medium, as well as a part of it being absorbed or reflected, a very small fraction of it is scattered, in all directions, by the inhomogeneities inside the medium. These inhomogeneities can be either static or dynamic. Defects such as dislocations in a crystal are examples of static scatterers which scatter the light elastically (*Rayleigh scattering*). In Rayleigh scattering, the scattered light is strong and has the same frequency as the incident beam (υ_i). Fluctuations in the density of the medium that are associated with the atomic vibrations are examples of dynamic scatterers which scatter the light inelastically (*Raman scattering* or *Brillouin scattering*). In semiconductors, there are sets of oscillators with which phonons can interact, namely the optical and acoustical modes of lattice vibration. The interaction of light with optical phonons is known as Raman scattering, while the interaction with the acoustical phonons results in Brillouin scattering.

1.5.1 Raman Scattering

In Raman scattering (RS) spectroscopy, scattered light is observed as a result of irradiating the sample by UV-visible light. Momentum and energy are conserved in the scattering process. The scattered light is very weak (~ 10^{-5} of the incident beam [23]) and has frequencies either $\upsilon_i + \upsilon_{ph}$ (*anti-Stokes lines*) or $\upsilon_i - \upsilon_{ph}$ (*Stokes lines*). In the Stokes-

shifted scattering the incident photon excites a phonon; hence the energy of the photon re-emitted by the semiconductor is reduced. In contrast, in the anti-Stokes-shifted scattering, a more energetic phonon is emitted since it absorbs a phonon from the semiconductor which was already in an excited state. Therefore, in Raman spectroscopy the phonon frequency υ_{ph} is measured as a shift from the incident beam frequency υ_i, which is referred to as *the Raman shift*. Stokes lines are stronger than the anti-Stokes lines under normal conditions, yet both give the same information. Thus, it is customary to measure only the Stokes side of the spectrum. Today RS has become one of the standard spectroscopic tools in the study of the semiconductors.

1.5.2 The Raman Selection Rule in Bulk Semiconductors

In the RS of bulk crystalline semiconductors a selection rule is imposed by momentum conservation. As the interaction involves two photons and one phonon, the momentum of the phonon is restricted to small values, extending to at most twice the momentum of a photon ($\hbar k_l$). Suppose that a visible laser with λ=500 nm is used to excite RS in a semiconductor. The maximum wavevector transfer then will be

$$2 \times k_l = 4\pi / \lambda \approx 2 \times 10^5 \text{ cm}^{-1},$$

which is approximately $1/10^3$ of the size of the BZ ($2\pi/a \approx 10^8$ cm^{-1}, a being the lattice spacing and of the order of 0.5 nm). Thus, the one-phonon RS probes only phonons near the BZ-centre (i.e. around $\mathbf{k} = 0$). This yields the so-called ***k** = 0 selection rule*. In disordered systems such as amorphous and nanocrystalline semiconductors this selection rule is not so rigorous. We will see these examples later. Figure 1.13 gives the one-phonon Raman spectrum of c-Ge at room temperature. The main peak at 300 cm^{-1}

corresponds to the zone-centre optical phonons (TO and LO modes are degenerate at the zone-centre for crystals having the diamond structure). The other peak at ~ 580 cm^{-1} with small amplitude is due to the second-order Raman scattering, where two phonons are involved in the inelastic scattering of the 514.5 nm photon.

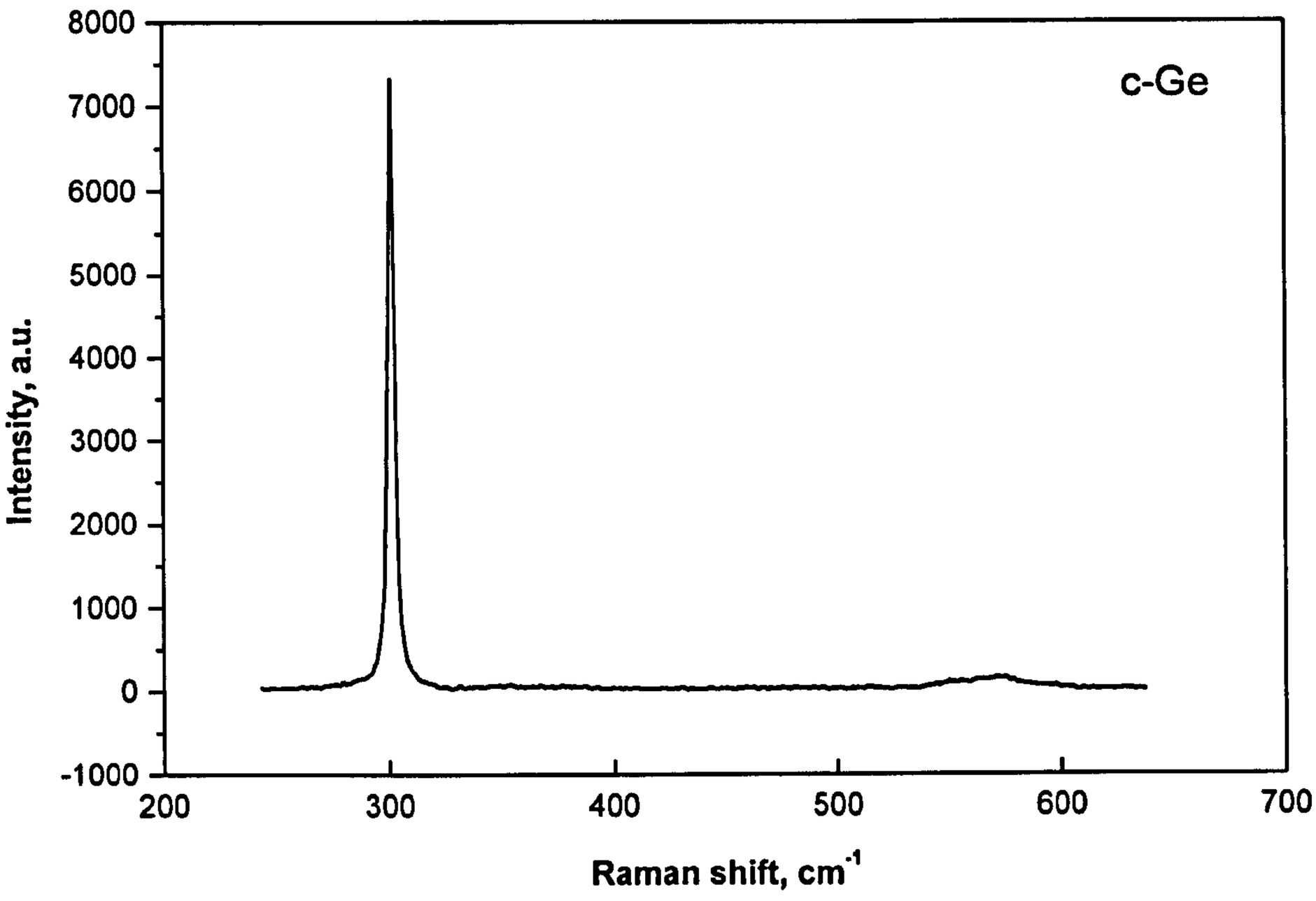

Figure 1.13 Raman spectrum of Ge crystal at room temperature (λ_{ec} = 514.5 nm).

1.6 REFERENCES

[1] N.W. Ashcroft and N.M. Mermin, *Solid State Physics*, Int.Ed., Saunders College Publishing (1976).

[2] L. Kronig and W.J. Penney, *Proc. Roy. Soc., London*, **A130**, 499 (1930).

[3] C. Kittel, *Introduction to Solid State Physics,* 7th Ed., John & Sons, New York (1996).

[4] D.B. Beard and G.B. Beard, *Quantum Mechanics: Principles and Applications,* Allyn & Bacon, Boston (1970).

[5] K. Seeger, *Semiconductor Physics*, Springer-Verlag, Wien (1973).

[6] C. Kittel, *Introduction to Solid State Physics,* 4th Ed., John & Sons, New York (1971).

[7] H. Ibach and H. Luth, *Solid-State Physics*, Springer-Verlag, Berlin Heidelberg (1990).

[8] P.Y. Yu and M. Cardona, *Fundamentals of Semiconductors*, Springer-Verlag, Berlin (1996).

[8] J. Pankove, *Optical Processes in Semiconductors*, Prentice-Hall (1971).

[9] T. E. Jenkins, *Semiconductor Science*, Prentice-Hall (1995).

[10] J.S. Blakemore, *Solid State Physics*, 2nd Ed., Cambridge University Press, New Jersey (1985).

[11] J.R. Haynes, M. Lax, and W.F. Flood, *Intern. Conf. on Physics of Semiconductors, Prague*, 1960, Acad. of Sciences, Prague (1961).

[12] L. Tybeskov, MRS Bulletin/April, 33 (1998).

[13] D.G. Thomas, M. Gershenzon, and F.A. Trumbore, *Phys. Rev.*, **133**, A269 (1964).

[14] S.S. Iyer and Y.H. Xie, *Science*, **260**, 40 (1993).

[15] D.J. Lockwood, *Light Emission in Silicon, Semiconductors and Semimetals*, Vol. 49, Academic, New York (1997).

[16] P.L. Bradfield, T.G. Brown, and D.G. Hall, *Appl. Phys. Lett.*, **55**, 100 (1989).

[17] U. Gnutzman, and A. Clausecker, *Appl. Phys.* **3**, 9 (1974).

[18] U. Menczigar, G. Abstreiter, J. Olajos, H.G. Grimmeis, H. Kibbel, H. Presting and E. Kasper, *Phys. Rev. B*, **47**, 4099 (1992).

[19] T.P. Pearsall, *Prog. Quant. Opt.*, **18**, 97 (1994).

[20] R. Braunstein, A.R. Moore, and F. Herman, *Phys. Rev.*, **109**, 695 (1958).

[21] (a) Q. Mi, X. Xiao, J.C. Sturm, L.C. Lenchyshyn, and M.L.W. Thewalt, *Appl. Phys.Lett.*, **60**, 3177 (1992); (b) H. Presting, T. Zinke, A. Splett, H. Kibbel, and M. Jaros, *Appl. Phys. Lett.*, **69**, 2376 (1996).

[22] L.T. Canham, *Appl. Phys. Lett.*, **57**, 1046 (1990).

[23] J.R. Ferraro, K. Nakamoto, *Introductory Raman Spectroscopy*, Academic Press, San Diego (1995).

CHAPTER 2. SILICON AND GERMANIUM NANOSTRUCTURES

In today's age of tailor-made materials, more complex structures having unique physical properties are produced. Nanometer-sized crystalline semiconductors, often called nanocrystals, are notable examples of such structures. Nanocrystals are intermediate materials between the limits of small molecules and bulk crystals.

Interest in nanostructures of Si or Ge stems from the effects of confinement on carrier wavefunctions. It is predicted that these effects become observable when the nanoparticle diameter is less than the size of the free exciton (electron-hole pair) Bohr radius (4.9 nm in bulk c-Si) [1]. *Quantum confinement* (QC) of carriers within the nanocrystallite is expected firstly to increase the electron-hole wavefunction overlap, resulting in partial breaking of the optical selection rules and allowing increased light emission efficiency, and secondly to shift the radiative emission peak to higher energies. Indeed, absorption measurements on porous Si (PS) showed the enlargement of the PS bandgap due to QC [2], and this was correlated with presence of quantum wires of diameters smaller than 5 nm. In addition to the QC effect, spatial localisation of excitons in Si nanocrystals, which prevents them from reaching luminescence killing centres, is also used to explain the efficient light emission from Si nanocrystals.

The discovery of room temperature visible luminescence from Si nanocrystals opens new possibilities for the use of Group IV indirect-gap semiconductors as materials for optoelectronic applications such as LEDs and display devices. Among the several forms of Si (or other semiconductor) nanostructures, PS is the most studied material to date.

Porous Si has the highest *external quantum efficiency* (EQE) with an order of magnitude higher than that of the other Si-based materials; nevertheless, this value is still an order of magnitude lower than that of typical III-V-based LEDs [3]. Visible luminescence from Ge nanocrystals is much less well studied and was first observed in samples prepared by the co-sputtering method [4][5].

In the following sections of this chapter, we will present the most recent understanding of PS and Si and Ge nanoparticles fabricated by other methods.

2.1 POROUS SILICON

It was not until 1990 that it was found that PS can emit strong visible and tuneable PL at room temperature [6], although PS was discovered back in 1956 by Uhlir while performing experiments on electropolishing of Si using an HF acid-containing electrolyte [7]. Fundamental differences between this material and its corresponding bulk crystalline form promise a wide range of properties. For example, PS has shown that Si in a nanocrystalline form has long-term potential as an optical, optoelectronic and biomedical material [8]. Yet its properties are very 'structure-specific' since they are a sensitive function of many parameters like porosity, size distribution, degree of oxidation, etc.

2.1.1 Fabrication and Processing

Porous silicon is usually formed by electro-chemical etching (*anodisation*) or chemical etching (*stain etching*) of Si in HF solutions (we will discuss only the first one here). A schematic diagram of a type of anodisation cell widely used for producing PS is shown in Fig. 2.1. The Si wafer acts as the anode and the cathode is made of a HF-resistant and conductive material (e.g. platinum). The cell body is usually made of Teflon since it is a highly acid-resistant material. There are some other types of cell designs used, such as the double-tank cell, lateral anodisation cell, etc. [3]. In the De Montfort University-Silicon Laboratory, we mostly use lateral anodisation geometry, with a selection of lateral front panels with differently sized-apertures.

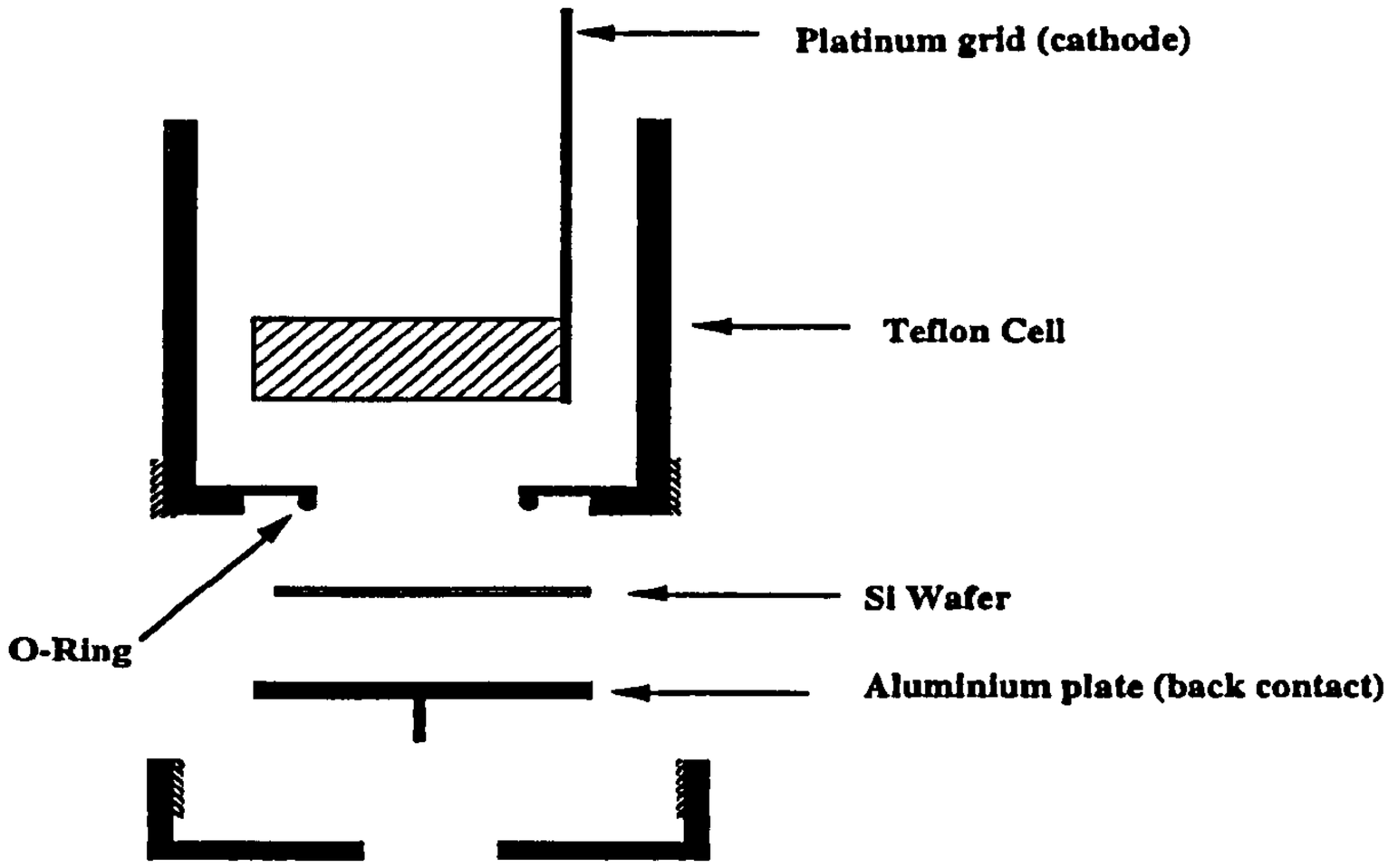

Figure 2.1 Cross-sectional view of a conventional single-tank cell [8].

During the anodisation reaction there is hydrogen evolution. In pure aqueous solutions bubbles can stick on the Si surface, reducing the amount of wetted surface, thus it is customary to add pure ethanol to the solution to increase the surface wettability. It is only

under anodic polarisation that Si dissolves. The dissolution is obtained controlling either the current or the potential. Generally, it is desirable to work with constant current (when producing a single porous layer), since this allows one to control porosity, thickness and reproducibility of the PS layer [3].

Porous silicon formation occurs only at low anodic overpotentials, which leads to the formation of a disordered web of pores, which propagates in depth. As a result, Si nanocrystals of some nanometer size are left in the inter-pore regions. At high anodic overpotentials the surface electropolishes and under cathodic polarisation, Si is stable, i.e. it does not dissolve, and so, in both these cases Si retains its smooth and planar morphology.

After completing the formation of PS by anodisation, the next step is the drying of the PS layers. This is a critical process, especially for PS of high porosities, since as the electrolyte evaporates out of the pores, a systematic cracking of the porous layer occurs due to the large capillary stress associated with the liquid-vapor interface [9]. Various different methods have been developed to reduce the capillary stress, such as pentane drying, ethanol drying, nitrogen blow drying, freeze drying, slow evaporation rates and supercritical drying (see for example [10]).

2.1.1.a The Theory of Porous Si Formation

A dissolution scheme for Si proposed by Lehmann and Gösele [2] is shown in Fig. 2.2.

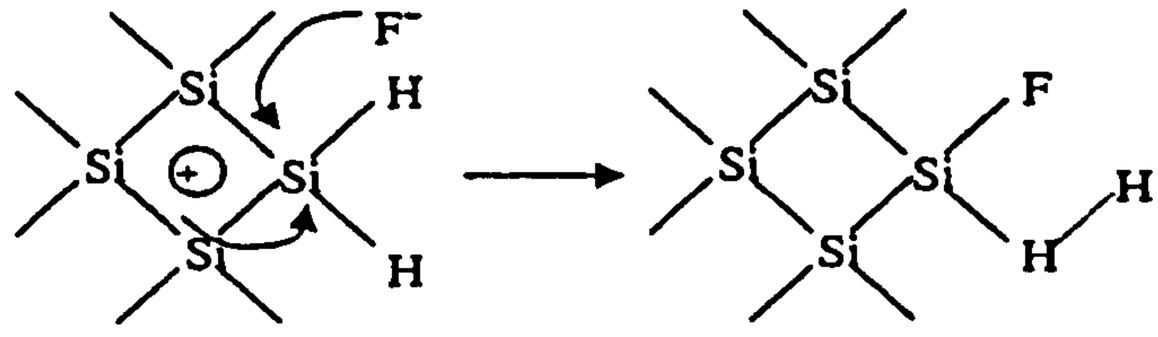

Hole injection and attack on a Si-H bond by a fluoride ion

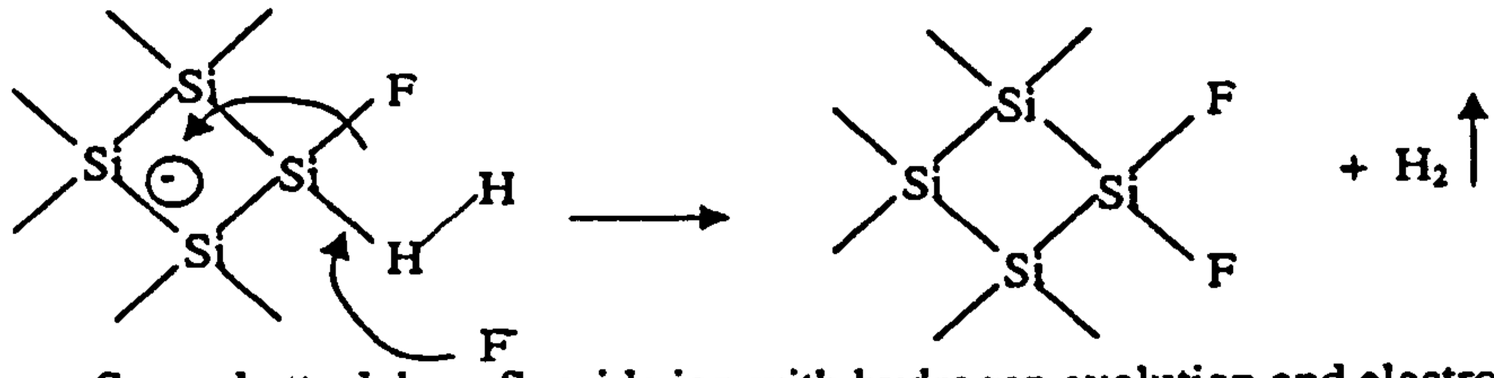

Second attack by a fluoride ion with hydrogen evolution and electron injection into the substrate

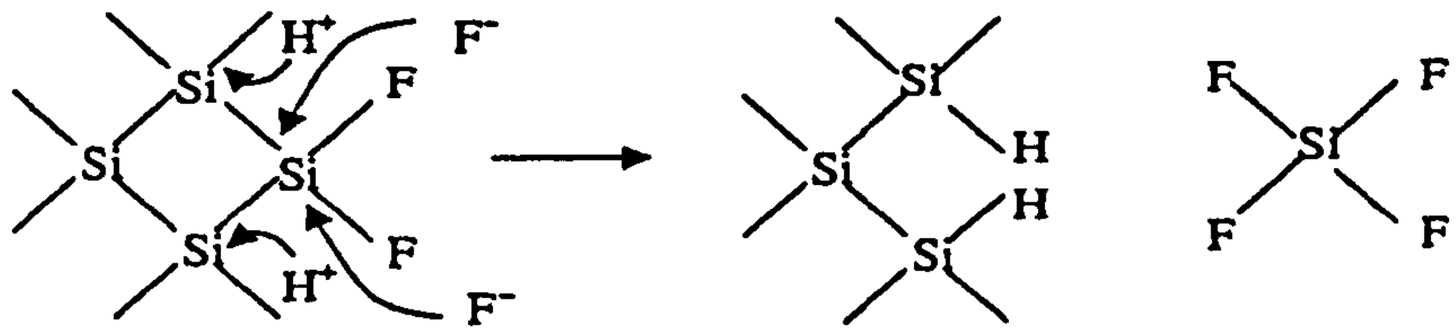

HF attack to the Si-Si backbonds. The remaining Si surface atoms are bonded to the H atoms and a silicon tetrafluoride molecule is produced

The silicon tetrafluoride reacts with two HF molecules to give H_2SiF_6 and then ionizes.

Figure 2.2 Silicon dissolution scheme proposed by Lehmann and Gösele [2].

According to this widely accepted theory, the global semi-reactions during the pore formation can be written as

$$Si + 6HF \rightarrow H_2SiF_6 + H_2 + 2H^+ + 2e^-. \qquad (2.1)$$

During the pore formation one hydrogen molecule evolve for every Si atom dissolved and the final product for Si in HF is H_2SiF_6 or some of its ionised forms [2][3]. It is widely accepted that holes are required for pore formation. For the etching of n-type and high resistivity substrates, holes can be supplied by suitable light assistance during the process. Figure 2.2 shows that the Si hydride bonds passivate the Si surface unless a hole is available. Various spectroscopic techniques (e.g. infrared absorption spectroscopy) have suggested the presence of Si-H surface bonds during PS formation [11]. For example the infrared absorption spectrum for a fresh PS sample, as given in Fig. 2.3, can depict clearly the features assigned to Si hydride bonds formed on the PS surface.

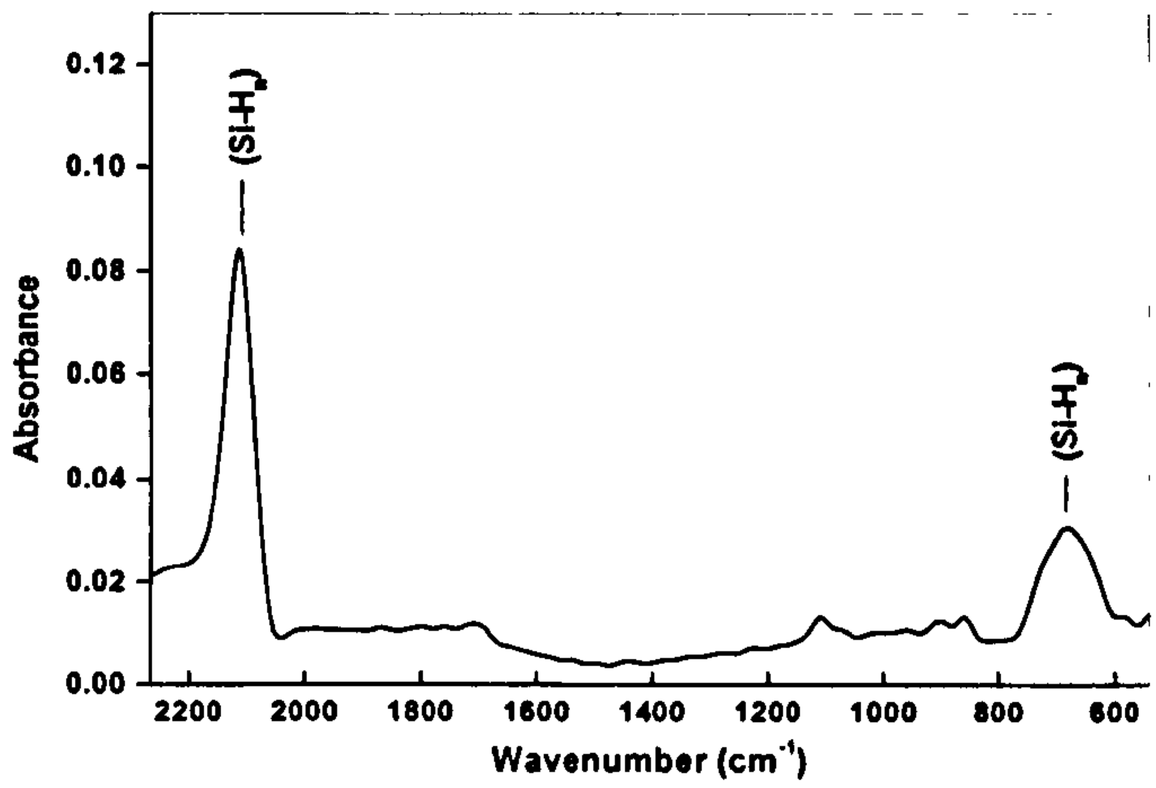

Figure 2.3 Infrared absorption spectrum of a fresh PS sample. P-type, 1-7 Ω cm resistivity Si (100) is anodised for 10 min. with a current density of 25 mA cm^{-2} in room light and at room temperature.

2.1.1.b Factors Determining The Material Properties

Anodisation conditions determine most of the properties of PS, such as porosity, thickness, pore diameter, and microstructure. Porosity is usually described as the fraction of the 'void' within the porous layer. It can be determined by gravimetric measurements using the following equation

$$P(\%) = \frac{m_1 - m_2}{m_1 - m_3} \tag{2.2}$$

where m_1 is the mass of the unetched wafer, m_2 is the mass of the wafer after anodisation and m_3 is the mass of the wafer after a rapid dissolution of the PS layer in a suitable solution, such as 3 % KOH [3]. Using the measured values m_1 and m_2 only, it is also possible to determine theoretically the thickness of the PS layer according to the following equation

$$d = \frac{m_1 - m_2}{\rho S} \tag{2.3}$$

where S is the etched surface area and ρ is the density of bulk Si [3].

It follows from Fig. 2.4.a that porosity decreases with increasing HF concentration for a given current density (for both n- and p-type Si [8]) and that porosity increases with increasing current density for a given HF concentration (for p-type Si [8]). For heavily n-type (n^+) doped Si Fig. 2.4.b shows that the porosity goes through a minimum at a current density of around 20 mA cm^{-2}, but the porosity increases at both higher or smaller current densities. Finally, for a given HF concentration and current density, porosity

increases with etching time (especially in lightly doped Si [8]): the longer the etching time, the higher the mass of the chemically dissolved PS (and thus the thicker the porous layer).

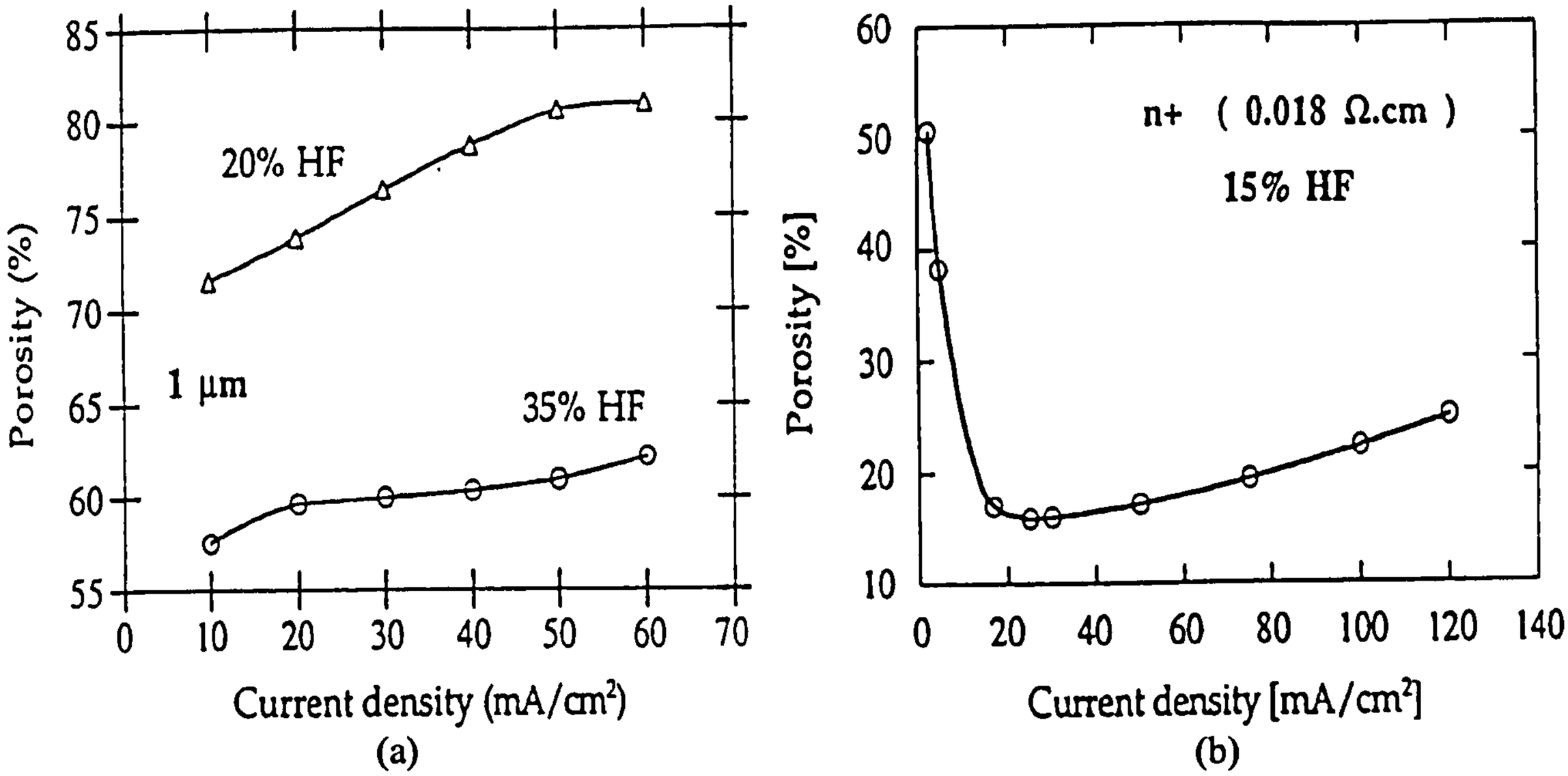

Figure 2.4 Porosity as a function of current density (**a**) for two different HF concentrations and lightly doped p-type substrate (~1 Ω cm) with a porous layer thickness of 1 µm and (**b**) for a highly doped n-type substrate (0.018 Ω cm) and HF concentration of 15 % (from [8]).

2.1.2 Structure

Beginning with the first proposals that PS constituted a nanostructure [2][6] there has been a continuous effort to establish the 'skeleton' size within the material. Since then the determination of phase, shape, dimensionality and size of the nanoparticles has become a central issue due to the basic requirement to understand to what extent the QC effects control properties (such as the optical absorption and luminescence properties) of

nanostructured materials. This is, however, not a simple task in PS, since it is a highly interconnected material with complex and varied morphology [9].

For direct imaging of structures smaller than 5 nm different microscopy techniques such as transmission electron microscopy (TEM), high-resolution scanning electron microscopy (HRSEM), atomic force microscopy (AFM), and scanning tunnelling microscopy (STM) have been used. To determine the average nanostructure size a variety of optical techniques such as Raman scattering, x-ray diffraction (XRD), small-angle x-ray spectroscopy (SAXS), extended X-ray absorption fine structure (EXAFS) have been employed to obtain quantitative data. A compilation of early reports are compared in Table I (from [9]). Clearly, there is a general agreement that visible luminescing PS has high concentrations of 1-4 nm objects. But, a considerable divergence of opinions also exists as to the precise size and shape that correspond to the specific wavelengths of emission; this is, for example, very apparent among those two EXAFS works ([17] and [18]) [9].

Table I. Techniques applied to estimating skeleton size in luminescent porous Si (adapted from [9]).

Characteristic technique used	Method of Extracting size	Spectral location and wavelength of PL peak	Dominant structural component responsible	Reference
TEM	Imaging of thinned sections	Near IR (810-855 nm)	2-3 nm quantum wires	Cullis, 1991 [12]
STM	Imaging of surface features	Red (675 nm)	1-5 nm protrusions	Dumas, 1993 [13]
RAMAN	Modelling of size dependent vibrational frequencies	Red (635 nm)	2.5-3.0 nm quantum dots	Sui, 1992 [14]
SAXS	Modelling of size dependent scattering processes	PL spectrum not shown	2.5 nm interconnected nanocrystals	Vezin, 1992 [15]
XRD	Modelling of size dependent diffraction peak broadening	Yellow-red (590-775nm)	3-4 nm interconnected nanocrystals	Lehmann, 1993 [16]
EXAFS	Size estimation via EXAFS-derived average coordination number for Si	Near IR (830 nm) Red (640 nm) Red (690 nm) Yellow (580 nm) Green (520 nm)	5 nm quantum dots 1.3 nm quantum dots 2.2 nm quantum wires 1.9 nm quantum wires 1.3 nm quantum wires	Schuppler, 1994 [17] Zhang, 1996 [18]

Porous Si samples are inhomogeneous in the sense that they have broad distributions of crystallite size and shape, surface roughness, and fluctuation of surface stoichometry [19]. In particular, vertical inhomogeneity in the porous layer, which is a consequence of the PS formation mechanism, plays an important role in determining the luminescence properties of PS. The top of the layer is in the etching solution longer than the rest of the

layer and the crystals are therefore expected to be smaller at the top of the layer. Indeed, this depth dependence of nanocrystal size has been demonstrated by microprobe Raman spectroscopy studies [20][21]; to exemplify, results of Mariotto *et al.* [21] are given in Fig. 2.5. It was also shown by these studies that both amorphous and (nano)crystalline Si phases exist at any depth within the porous layers, which can be seen in Fig. 2.5.b.

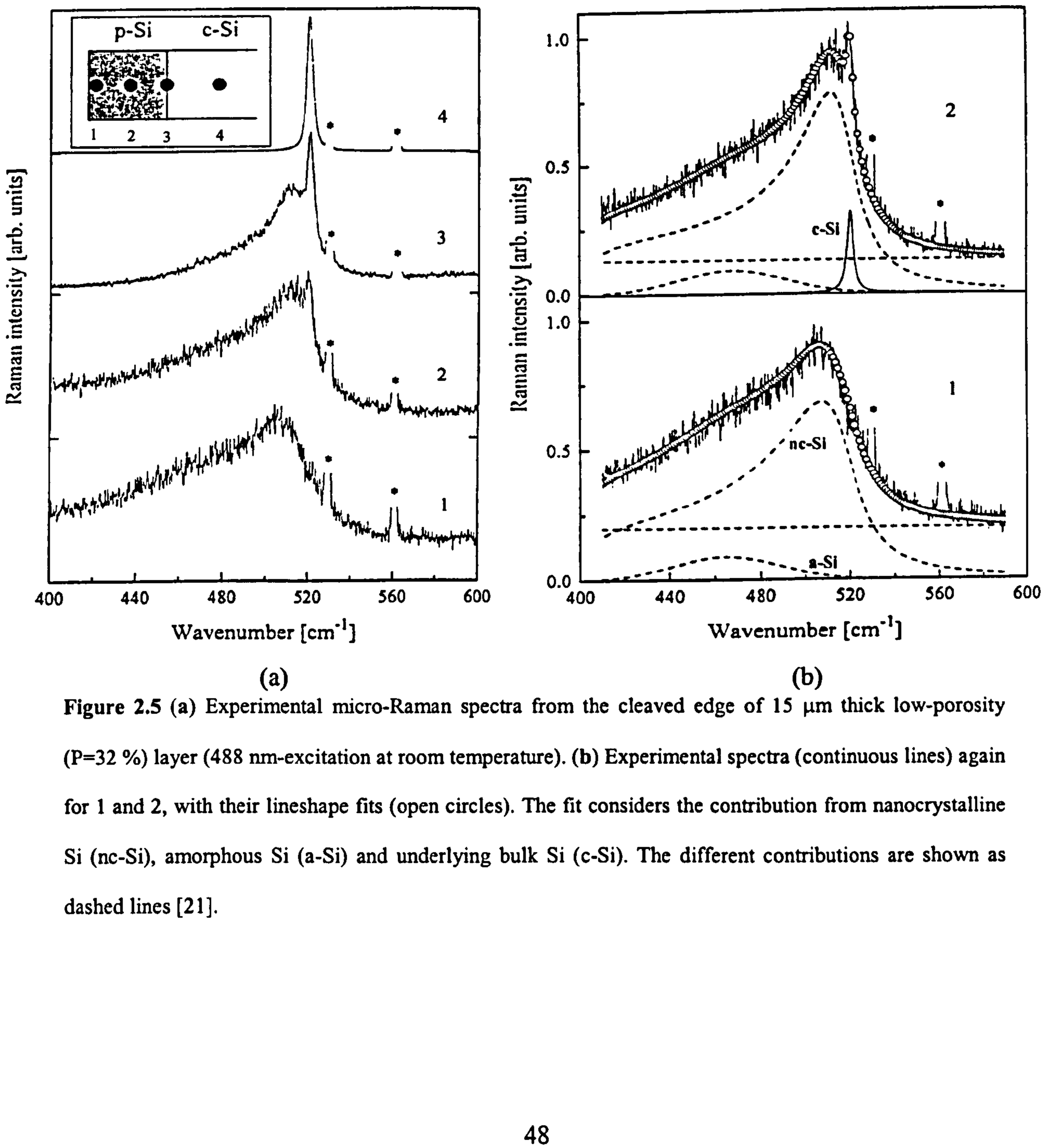

Figure 2.5 (a) Experimental micro-Raman spectra from the cleaved edge of 15 μm thick low-porosity (P=32 %) layer (488 nm-excitation at room temperature). (b) Experimental spectra (continuous lines) again for 1 and 2, with their lineshape fits (open circles). The fit considers the contribution from nanocrystalline Si (nc-Si), amorphous Si (a-Si) and underlying bulk Si (c-Si). The different contributions are shown as dashed lines [21].

2.1.3 Bandgap and Photoluminescence

Different propositions have been made to explain the PL emission from PS by various researchers, such as quantum confinement (QC) [22-24], surface states [25], defects in the oxide [26], specific chemical species [27][28], etc. Based on the similarities between vibrational properties (established with IR and Raman spectroscopies) and PL properties of PS and siloxane ($Si_6O_3H_6$), Brandt *et al.*[27] proposed that the visible light emission from PS is not an intrinsic property of (nano)crystalline Si (QC effects) and that its origin is related to siloxane derivatives present in PS. Nevertheless, siloxanes were soon after ruled out as the luminescing species in PS, since samples which had been oxidised by rapid thermal annealing at and above 700 °C (and with 'no detectable Si hydride bonds') proved to exhibit strong, red luminescence [29].

From the theoretical point of view the PL mechanism involves a complicated sequence of physical processes such as relaxation processes (thermalisation), excitonic interactions, impurity scattering, etc. [30] (see also section 3 in Ch. 1). Different computational techniques have been used to investigate the electronic properties of 'confined' Si structures [31-34]. All the calculations performed on confined Si structures give a similar picture: the QC effect causes widening of the Si bandgap from the near-infrared (1.12 eV ≈ 1100 nm) to-and-beyond the visible region.

Therefore, it is widely accepted that the PL is pushed into the visible for crystallite sizes below 5 nm, following the bandgap opening, as a result of QC. On the other hand, it has been reported by several groups that when the crystallite size decreases to a few nanometers, the PL in air does not increase much beyond ~ 600 nm. This observation does not coincide with the QC theory; as can be seen from Fig. 2.6, observed PL energies

for PS (or Si nanocrystallites in an oxide) are consistently lower than the theoretical optical gaps [35]. Nevertheless, the optical absorption is characteristic of QC effects of the crystallite.

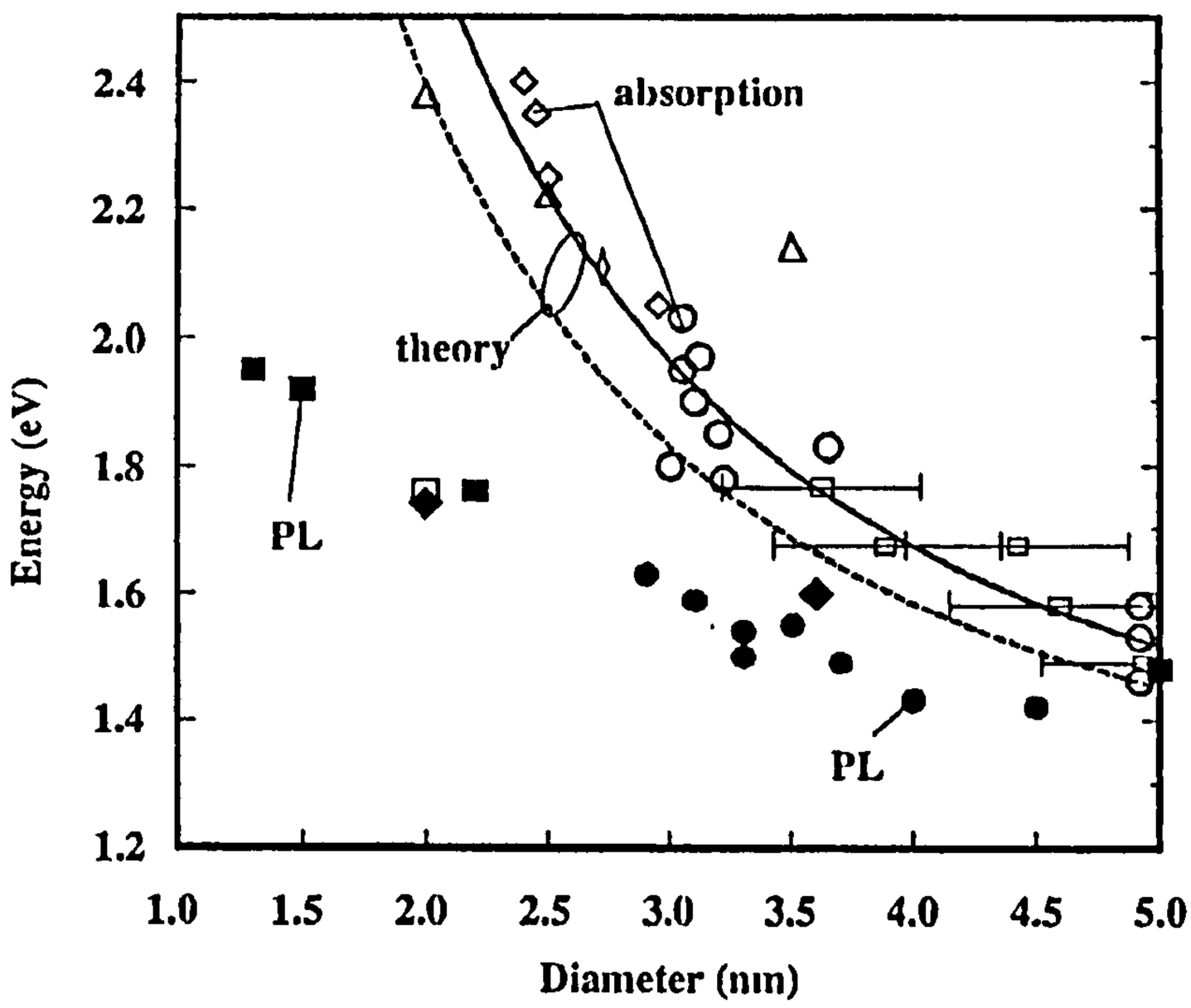

Figure 2.6 Comparison of a compilation of experimental optical gaps of PS samples and Si nanocrystallites [17, 36, 37] obtained from PL energies (filled symbols and the symbols with error bars) and optical absorption (unfilled symbols) with calculated optical gap values - with (dashed line) and without (full line) excitonic correction [35].

As can be seen from Fig. 2.6, tunability of the PL from PS seems to be limited. Fresh PS samples, in fact, show a variety of colors in luminescence (e.g. [18]); however, after air exposure, PS usually shows orange / red luminescence. Wolkin *et al.* prepared a set of PS samples emitting blue, green, yellow, orange and red luminescence in only vacuum or

Ar or pure H environments (Fig. 2.7.a) [38]. When the samples were exposed to air or transferred to a pure O environment an immediate red-shift was observed for the blue and green emitting samples, that is for the high porosity samples (Fig. 2.7.b and c). They monitored the chemical coverage of these samples by infrared spectroscopy which showed a trend for the replacement of the surface hydrides ($Si\text{-}H_{1\text{-}3}$ peaks at 2100 and 664 cm^{-1}) with oxygen (Si-O-Si feature at 1070 cm^{-1}) starting immediately after the air exposure (Fig. 2.7.d). They also noticed (Fig. 2.7.c and d) that the PL energy for the blue and green emitting samples stabilised, along with the surface chemical coverage (Si-O-Si and Si-O-H (850 cm^{-1}) peaks did not change significantly), after 200 minutes of air exposure. However, no change in the PL energy of yellow, orange and red emitting samples was observed with air exposure (even after 24 hours) (Fig. 2.7.b). The authors concluded that the recombination mechanism in oxidised nanocrystallites of sizes <3 nm is different from that in hydrogen passivated nanocrystallites of the same size and suggested that the red-shift upon oxidation can be related to recombination involving a trapped electron or exciton in the Si=O bonds at nanocrystal surfaces [38].

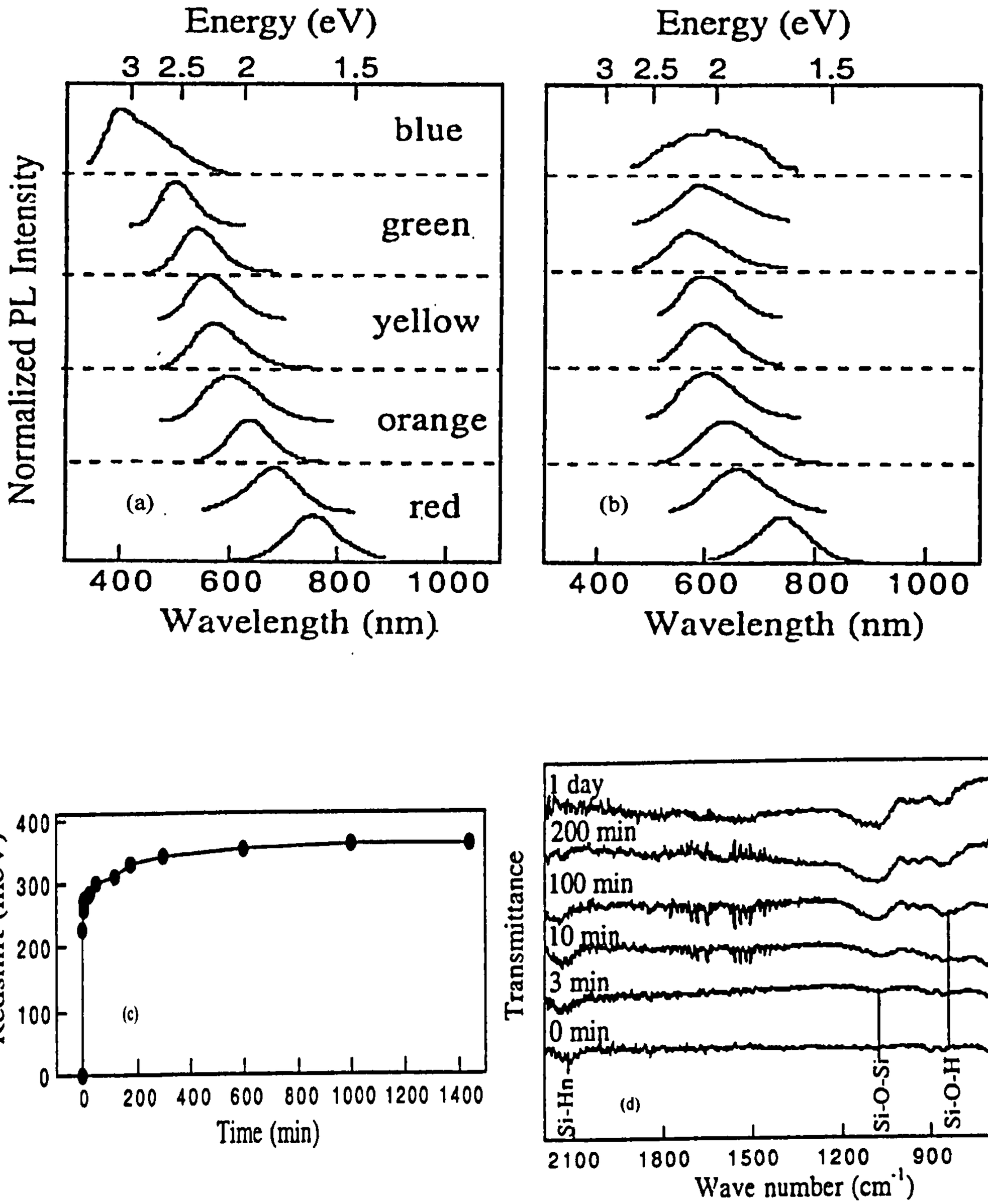

Figure 2.7 Room temperature PL from different porosity samples of (**a**) fresh PS (kept in Ar ambience) and (**b**) air-exposed PS (for 24 h). (**c**) The red-shift of the PL and (**d**) the evolution of the IR spectra for a blue-green emitting sample as a function of air-exposure time [38].

These observations indicate that although the bandgap of Si nanocrystals widens by QC and PL energy increases with decreasing sizes, surface passivation also plays an important role in the PL mechanism, especially for very small sizes. In fact, calculations of Allan, Deleure and Lannoo [37] have shown that luminescence in Si nanocrystallites can be due to excitons trapped at the surface which is passivated by hydrogen or silicon oxide.

Contrary to the observations above, thermal oxidation of the PS surface has been shown to produce 'blue' PL [36] which becomes intense only after strong oxidation and has much faster decay than the typical red PL. Strong oxidation implies that a large fraction of the volume of Si nanocrystals has been transformed into SiO_2, thus the average size of any c-Si remnants can be as small as ~ 1 nm [40]. For the origin of this blue PL, there are different models considered, such as band-to-band recombination in small c-Si core regions [41], emission from the oxide or due to surface states [40].

Actually, the theory suggests that for a size comparable to ~ 1 nm, the bandgap should approach 3 eV [42] and both phonon-assisted and pure (no-phonon) radiative transitions with high recombination rates and characteristic lifetimes in the nanosecond regime should dominate the emission spectra [43]. Therefore, the model of [41] seems to be consistent to explain the blue PL. However, this model lacks an explanation for the experiments which demonstrated quenching of the blue PL after exposing the oxidised PS to chemicals (for example, Fig. 2.8 shows the experiment of Rehm *et al.* [44]). The c-Si remnants are surrounded by a thick oxide layer, so the blue PL should be insensitive to the chemical environment. Therefore, the second model [40] which suggests that the blue PL in oxidised PS originate from the oxide surrounding the Si remnants or from the

Si-SiO_2 interface (or even from the species present at the surface of the oxide) gains some weight against the preceding model.

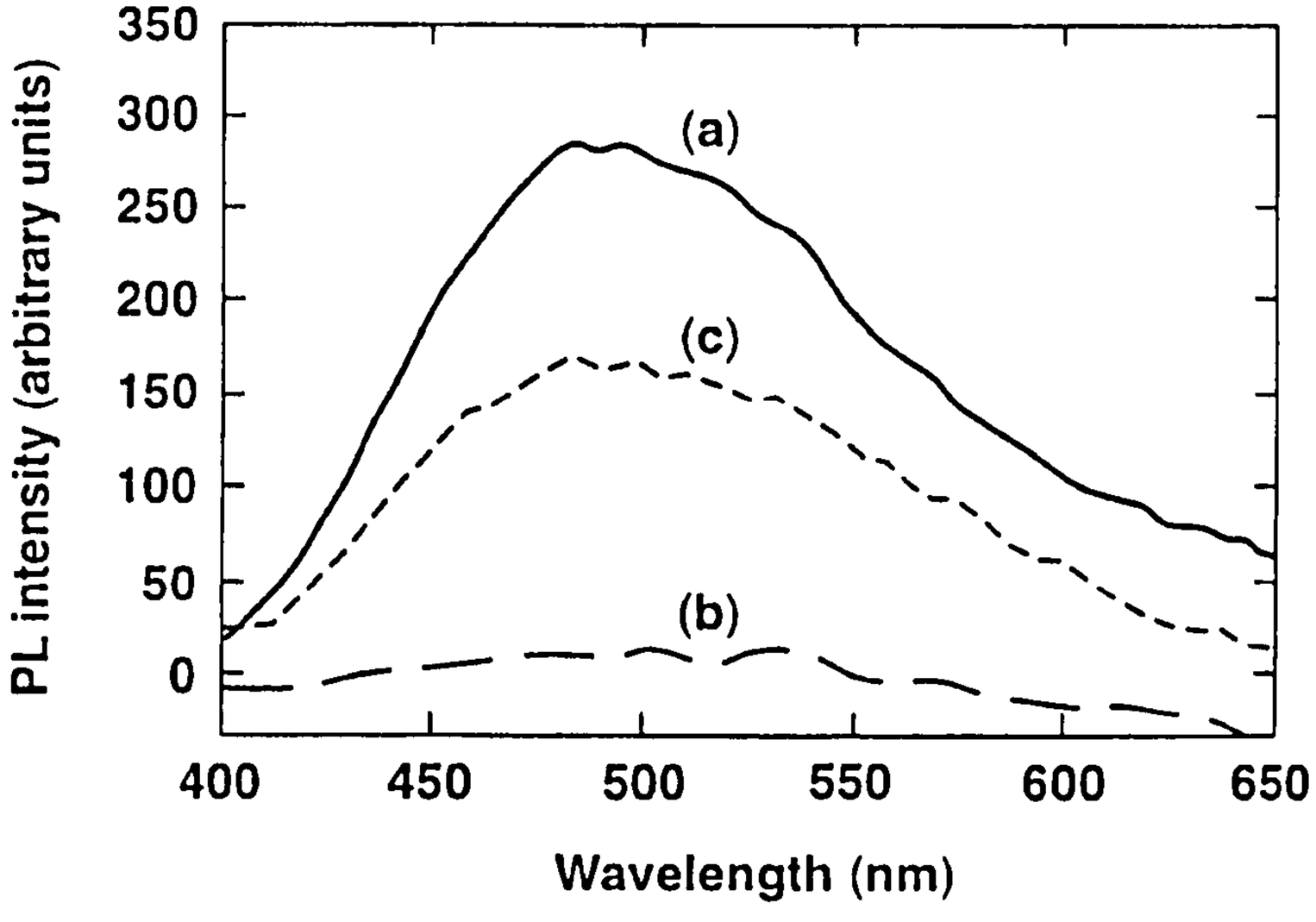

Figure 2.8 PL quenching of thermally oxidised PS. Spectra taken **(a)** before, **(b)** immediately after and **(c)** one day after, the methanol-exposure. PL intensity recovers after most of the methanol has evaporated [44].

To conclude, as 'partially' discussed above, it can be said that the experimental data reveal a complex situation probably characteristic of several radiative channels in PS, and that most probably the QC and surface states are the two of those channels.

2.1.4 Electroluminescence

Electroluminescence was observed in PS shortly after the observation of visible, room temperature PL in a solid-state device (a PS LED) [45]. A typical PS LED consists of a

transparent or a semitransparent contact (e.g. metal, indium-tin-oxide or conducting polymers) and a 1-10 μm thick PS layer on a c-Si substrate (n- or p-type) [45-47].

The stability (lifetime) and the power efficiency of most PS LEDs are relatively poor. The *power efficiency* of a LED is calculated from the ratio of the number of photons emitted in the hemisphere to the power (V x I) dissipated in the device. The best value achieved for the PS LED power efficiency until 1999 was below 0.1 % [48]. The reported stabilities for PS LEDs were as low as 10 min (for example [49]). Haneman and Yuan [50] explained the reason why the intensity of EL is much lower than the PL intensity as follows. In bulk Si, the non-radiative defects (including impurities) are easily accessed by carriers at considerable distances, due to high velocities and lifetimes. However, in nanostuctured materials like PS, each defect has the strongest effect only on the carriers in that nanoparticle and this factor is different for PL and EL. In PL, there is little or no driving force and no requirement for carriers to pass between nanocrystals, hence recombination can take place in the individual nanocrystals, being effected only from the defects present in that particle. However in EL, carriers have to pass through the material, i.e. pass from particle to particle, so that there is more likelihood of encountering defects, with an unknown loss of intensity.

The cause of the low stability of PS LEDs is usually related to poor surface passivation provided by the Si-H bonds: Si-H bonds that passivate the Si nanocrystal surfaces are very fragile and can be easily broken by exposure to light, air, large electric fields and moderate temperatures [38][51][52]. For example, Loni *et al.* [53] showed that the efficiency of their PS LEDs degrades within minutes in air, but in hours in vacuum. Instead, for example, the fragile Si-H bonds can be intentionally replaced by stronger

Si-O bonds and this way the non-radiative defects can be kept to a minimum [54]. Indeed, this way it is found that simple semitransparent metal / partially oxidised PS / c-Si LEDs were stable for over 100 hours of continuous operation [54]. However, these devices were relatively inefficient with power efficiencies below 0.01 %.

Recently (in 1999) a continuous wavelength power efficiency of 0.2 % has been obtained by Gelloz and Koshida [55] for a PS LED with a set of optimised preparation parameters. To our knowledge this value is still the highest for a PS based LED obtained to date. In their device, a superficial low porosity layer formed on the optically active porous layer is anodically oxidised (at 0 °C). The efficiency of this device is shown in Fig. 2.9, along with data for the same device without the superficial low porosity layer and without the anodic oxidation treatment.

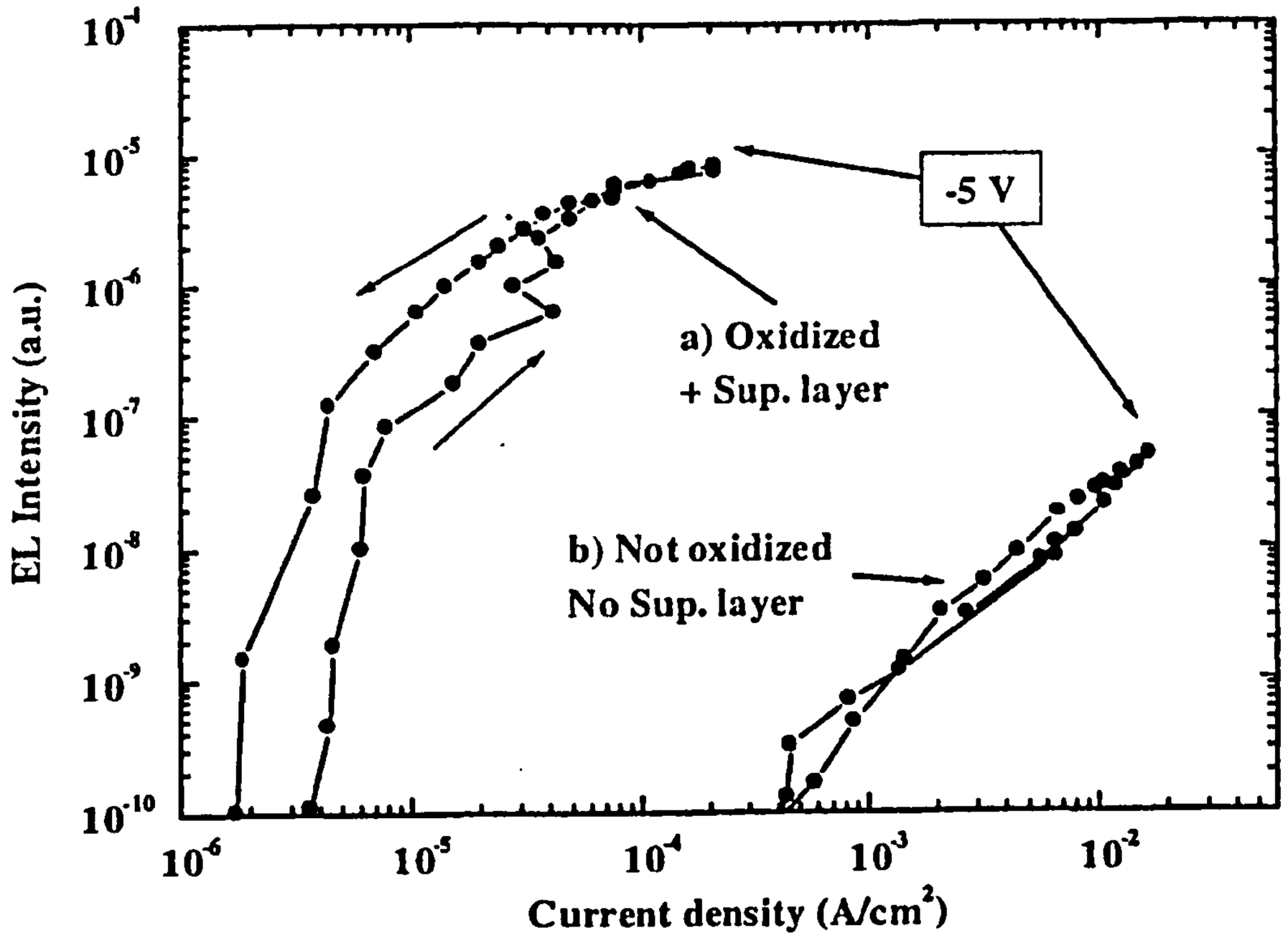

Figure 2.9 EL intensity versus current density for a PS LED (formed at 0 °C from a n^+-type c-Si substrate) (**a**) with and (**b**) without an anodically-oxidised superficial low porosity layer on the optically active porous layer. Arrows show the progress of the scan [55].

Obviously, it is not possible to mention here about all of the tremendous research activities into the physical and chemical characteristics of PS. Many more aspects can be found in any of the recent books and reviews devoted to this subject (e.g. [3][9][56]).

2.2 SILICON AND GERMANIUM NANOCRYSTALS

Semiconductor nanostructures can be produced by a variety of techniques. While some of these techniques are very-large-scale integration (VLSI)-compatible techniques some

are used (or just 'invented') for the fundamental research of nanocrystals (mainly Si nanocrystals). We will present below a few of these techniques which have come into focus during this study.

2.2.1 Ion Implantation and Sputtering

Ion implantation and sputtering are both VLSI-compatible techniques. Nanocrystals of Si trapped in various matrices prepared by one of these techniques thus form an attractive system for device fabrication when compared to PS (anodisation of Si to produce PS is not VLSI-compatible). They also include the advantage of having increased surface stability and material rigidity in comparison to PS.

2.2.1.a Si Nanocrystals in SiO_2 Matrices

Ion implantation results in a Gaussian-like implantation profile similar to that given in Fig. 2.10. In order to form Si nanocrystals by ion implantation, high doses of Si ions (Si^+) are generally implanted into a thermally grown SiO_2 film, and this is followed by a high-temperature anneal. The excess Si, introduced by ion implantation, forms small precipitates during annealing. Doses up to and around 10^{17} cm^{-2} and ion energies in the range of 25-200 keV are used to produce atomic concentrations of excess Si at a level of a few percent [57][58]. With this technique, it is possible to have independent control over the concentration and depth of the implanted impurity, and to control the size of the nanocrystals by adjusting the parameters of implantation (dose, temperature) and annealing (temperature, time, ambience).

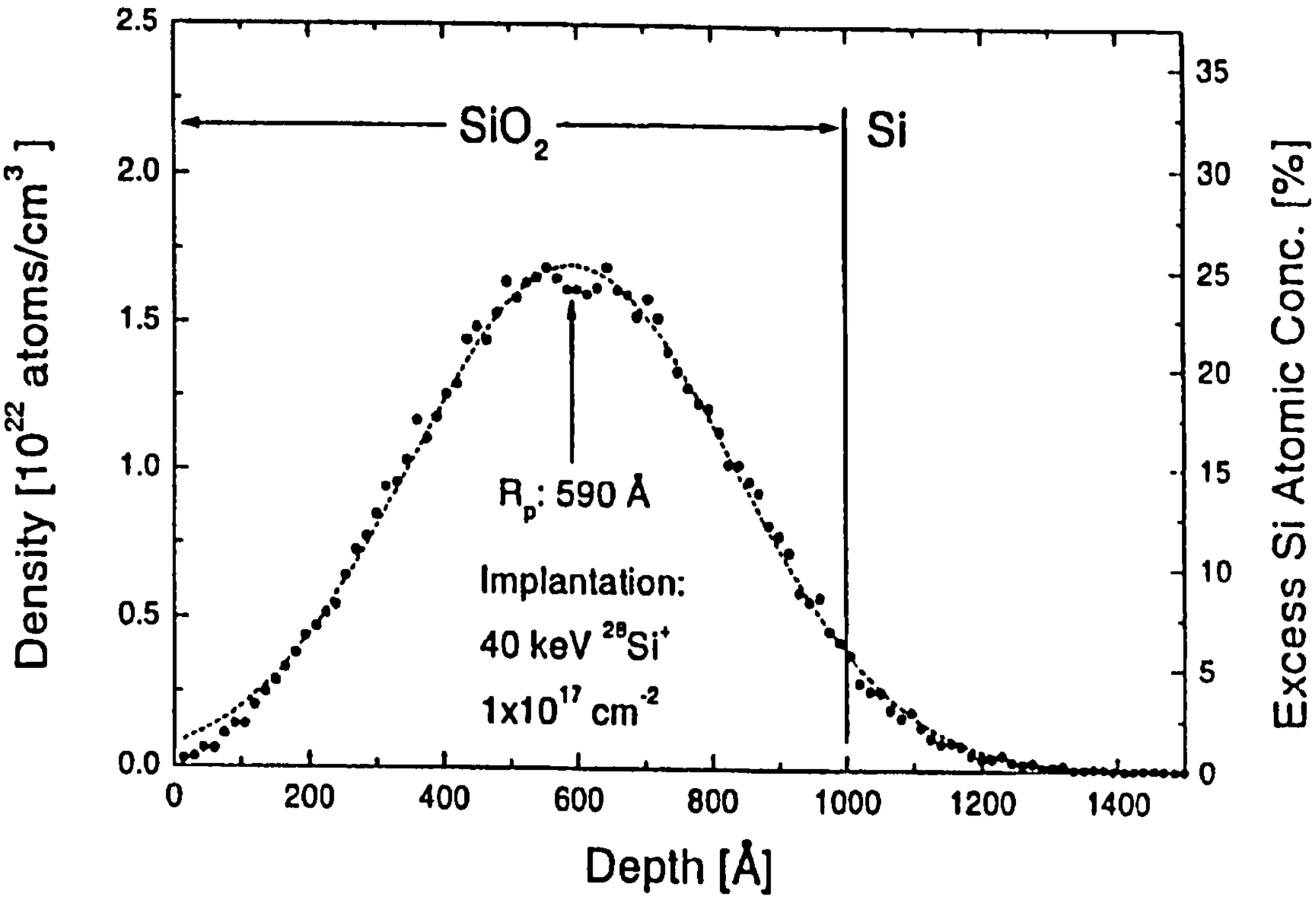

Figure 2.10 TRIM implantation profile of 40 keV Si atoms in a 1000 Å SiO_2 layer on Si [58].

The main drawback of ion implantation is the requirement of implanting high doses of ions in order to produce excess impurity concentrations of several atomic percent. In most cases the implanted species are expected to form the light-emitting material itself. Another disadvantage of the technique is that it also produces radiation damage in the host matrice (in this case SiO_2). In this sense, sputtering is more favorable, although it is somewhat less controllable.

In sputtering, Si nanoparticles in SiO_2 are usually obtained by RF magnetron co-sputtering of Si and SiO_2 in argon or oxygen plasmas at various deposition temperatures (up to a few hundred degrees Celsius) and annealing at high temperatures. To control the excess Si concentration, Si chips of the required areal density are positioned on the SiO_2 target (e.g. [59]). The film is generally deposited onto a transparent substrate such as

quartz or on a c-Si substrate and usually has a thickness ranging between several hundreds to a few thousand nanometers. Properties of the nanocrystals can be controlled by altering the sputtering conditions, e.g. substrate temperature, gas type and concentration, or the annealing conditions such as those cited above.

2.2.1.a.1 Photoluminescence

As-implanted samples generally show a weak green or blue PL [58][60]. A stable PL can be produced after a high temperature anneal. Annealed samples are generally reported to exhibit a broad PL band peaked in the red [60][61]. Many groups have studied PL from Si^+-implanted SiO_2 films in order to elucidate mechanism(s) of the observed PL. For example, Min *et al.* reported that there are in fact two detectable PL bands (at ~ 600 nm and ~ 800 nm) from their post-annealed Si^+-implanted SiO_2 films [62]. They suggested that one of these bands was related to surface-defects, as it was present even in samples implanted with only Xe^+, and the other can be correlated to the Si nanocrystals. The former band is located at around 600 nm and has a short lifetime (<100 ns), whereas the other has a lifetime of 630 μs. In Si^+-implanted samples, only the first band disappears after a deuterium implantation (this is supposed to increase the level of surface passivation of nanocrystals). Ghislotti *et al.* demonstrated more clearly the differences between defect- and nanocrystal-related PL by using the time-gated PL spectra (Fig. 2.11) [63]. The top spectrum shows the PL band near 600 nm with a short decaytime of ~ 100 ns, which is less than that predicted for nanocrystals with sizes corresponding to these wavelengths [43]. In contrast, the nanocrystal related PL band at 700-900 nm exhibits long decaytimes (hundreds of μs).

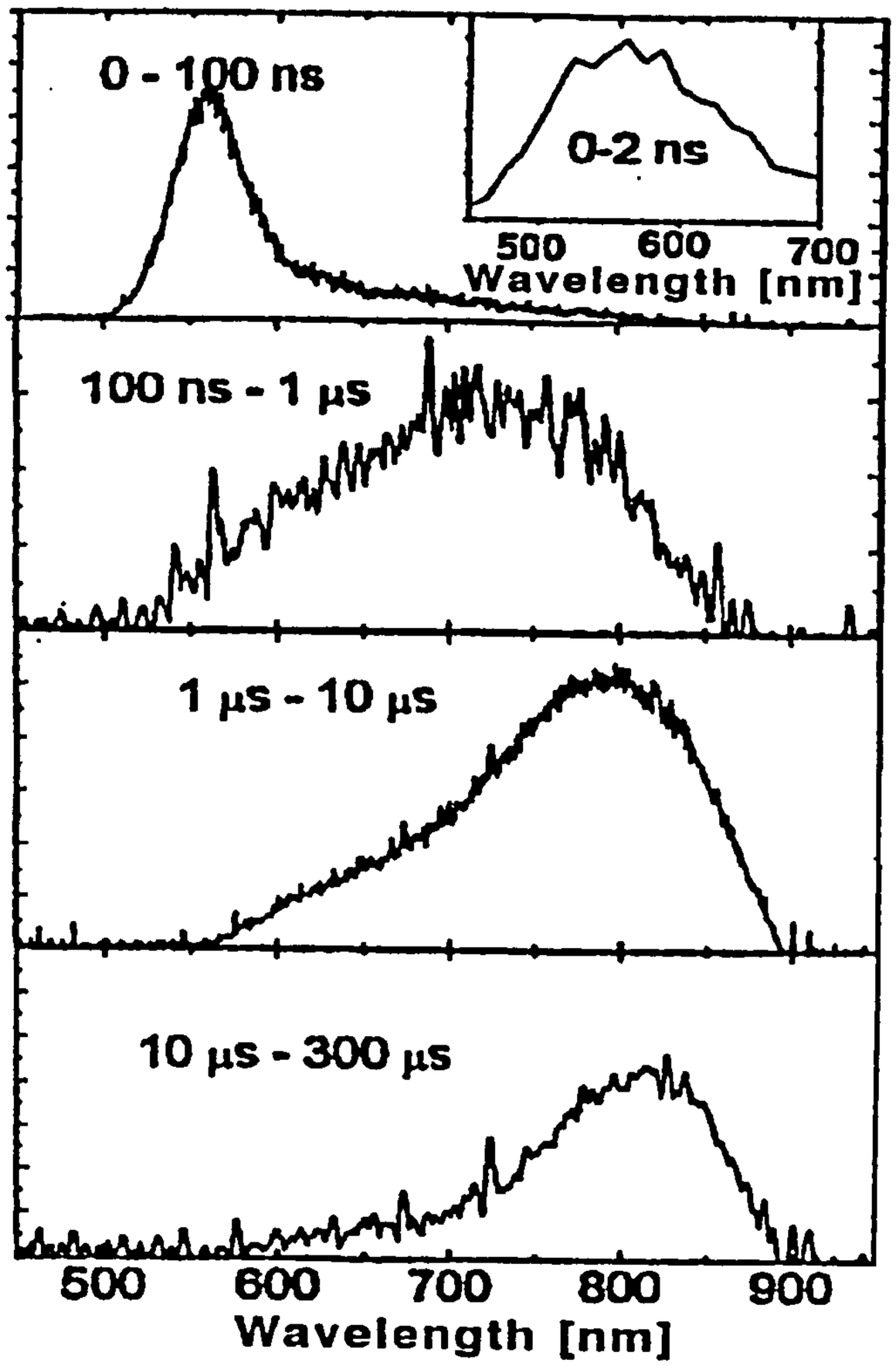

Figure 2.11 Time-gated PL spectra of 2 x 10^{17} cm^{-2} fluence implant after annealing at 1000 ^{0}C in Ar gas atmosphere for 30 min. The inset refers to a nanosecond-resolved time-gated spectrum [63].

The red PL band is usually reported to be size independent from ion-implanted and post-annealed SiO_2 films (nanocrystalline Si / SiO_2). In order to explain size independence of the red PL, Kanemitsu *et al.* suggested a model that still involved the QC effect [64]. According to this famous model, absorption of photons leads to the generation of excitons which are confined in Si nanocrystals, whilst the emission of the photons takes place at the interface between Si nanocrystals and the SiO_2 matrix due to an oxygen-modified surface state on the nanocrystals [19][64]. This model is used by

others to explain successfully, for example, the independence of the PL energy on the excitation energy or the annealing time [57].

As-grown films of Si/SiO_2 composites prepared by co-sputtering usually show a green PL [65]. The difference of these films from the as-implanted films of Si^+/SiO_2 composites is that 'nanoclusters' of Si at very small sizes (~ 1 nm) are already present in the co-sputtered films; whereas for the ion-implanted films precipitates of Si (i.e. 'nanocrystals') can only be formed after a high temperature anneal. Therefore, it is expected that the PL behaviour of the sputtered films should not change profoundly (except the intensity) after annealing at a high-temperature (that is when the small Si nanoclusters are grown into larger nanocrystals). However, after annealing anomalous PL behaviours are reported by some groups (e.g. see [65]); also the reported PL energies show quite big variations for the annealed films (from near UV to blue [66], green to yellow [65][67], red to near IR [59][68]). Besides, these PL energies are also reported to be size independent (except the near IR PL reported by Takeoka *et al.* [68]).

2.2.1.a.2 Electroluminescence

Si nanocrystals produced by both sputtering or ion-implantation in SiO_2 matrices are stable and compatible with VLSI processing technology, however, electrical injection throughout an isolating oxide seems to be a major obstacle for EL applications [69]. Nevertheless, it is suggested that for high nanocrystal densities carriers may traverse the oxide by 'hopping' on nanocrystals or by thermally-activated tunnelling [70]. In order to obtain efficient EL, in principle, two different approaches have been suggested [58]: a thick oxide and a high voltage, or an ultra-thin oxide and a low voltage.

Fig. 2.12 shows a schematic cross-section of a nanocrystal-based LED produced by Lalic and Linnros [61] with ion-implantation and using the latter method. For the preparation of this device, high doses of Si ions were implanted into a thin SiO_2 layer and nanocrystals were formed at 1100 ^{o}C. A polycrystalline-Si layer was deposited, followed by metallisation using an Au contact on part of the emitter area. They observed stable and visible EL (1.9 eV-1.6 eV) at low voltages (<10 V) from this device, although it suffered from low EL intensity (more than an order of magnitude weaker than a PS LED at the same bias, prepared by the same authors [71]) and quantum efficiency.

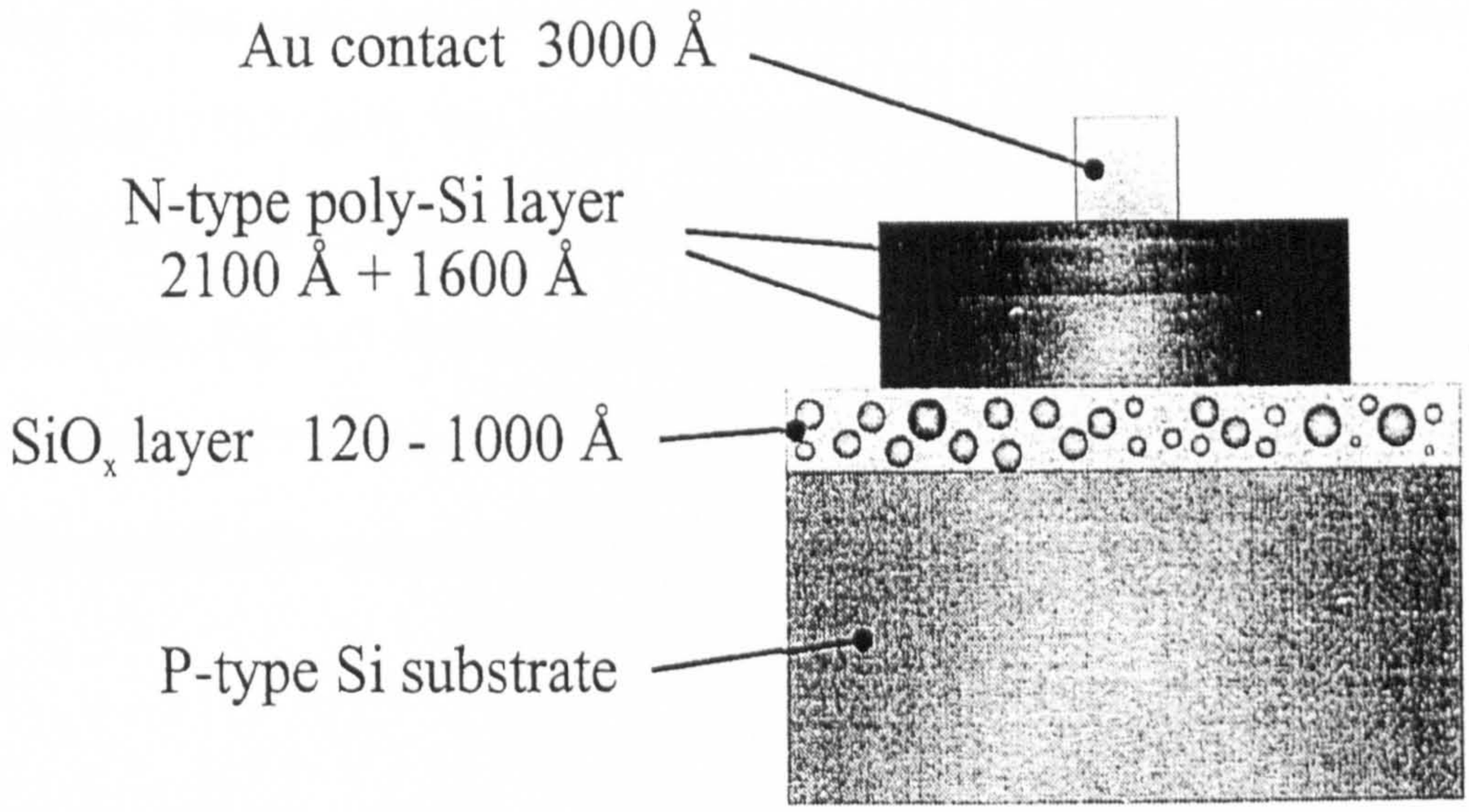

Figure 2.12 Schematic diagram of a nanocrystal LED structure [61].

2.2.1.b Ge Nanocrystals in SiO_2 Matrices

Germanium nanocrystals have been prepared by many different methods, including co-sputtering [4,5][72,73] and ion implantation [74-76]. Although not as successful as these techniques in terms of producing Ge nanocrystals, porosification of c-Ge by anodisation or stain-etching, in a similar manner to PS preparation, has also been tried by several groups [77-80] to prepare light-emitting nanocrystals of Ge.

Both RF magnetron co-sputtering of Ge and SiO_2 [4,5][72,73] and implantation of Ge ions into SiO_2 [74-76] followed by annealing at high temperatures have been found to be a convenient way to prepare Ge nanocrystals in SiO_2. X-ray photoelectron spectroscopy (XPS) data showed that GeO_2, GeO and Ge exist in the as-deposited or as-implanted films and that most germanium oxides decompose into Ge nanocrystals after thermal annealing [73][75][81]. The crystallinity and the size of Ge nanocrystals were mainly studied by Raman spectroscopy [4,5][72][74] and high-resolution TEM [72][73][75]. As an example, Fig. 2.13 shows a sharp TEM picture for a Ge nanocrystal of size ~ 15 nm [73]. XPS and FTIR spectroscopy indicated that amorphous GeO_2 and GeO were formed at the surface of Ge nanocrystals [19].

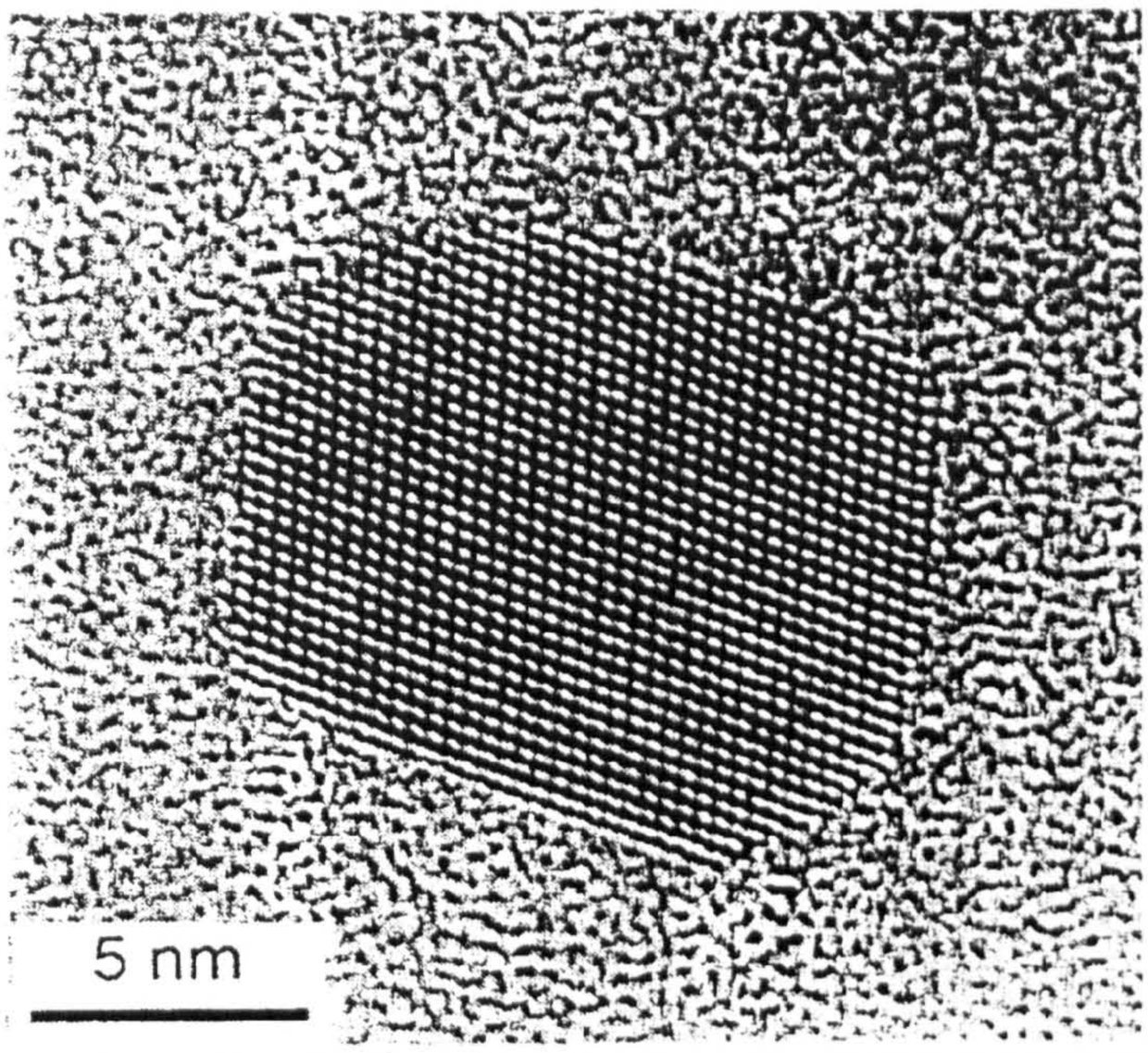

Figure 2.13 High resolution-TEM image of a high-quality Ge nanocrystal with size 15 nm [73]. (For other TEM images of Ge crystal sizes smaller than 5 nm see Fig. 9 of Maeda (1995) [73]).

2.2.1.b.1 Photoluminescence

Table II provides a summary of the PL studies from Ge (and GeO_2) nanocrystals in the literature. In most cases nanocrystals were prepared as embedded in a SiO_2 matrix.

Table II. Summary of a selection of papers published on PL from Ge (and GeO_2^*) nanocrystals (Abbreviations: NC: nanocrystal; PLE: Photoluminescence excitation; T: temperature; abs.: absorption; RTA: Rapid thermal annealing; rec.: recombination).

Preparation method	Estimated NC size (nm)	λ_{exc} of PL (eV / nm)	PL energy (eV)	PLE / abs. energy (eV)	PL decaytime (ns)	Attributed origin(s) for PL	Ref.
RF magnetron co-sputtering and high T annealing (Ge NCs in SiO_2)	4 – 14	2.54 / 488	2.2–2.3	-	1	Direct-gap recombination in NCs ≤4 nm	[5]
	2 – 6	2.54	2.1–2.3 (main) and 1.6–1.8 (weaker)	-	1	QC is likely, but can't explain fast PL decay	[73]
		3.81 / 325	3.1 (only as-deposited)				
	3.7	2.54	2.25 (broad) or 2.3, 2.2 and 2.0 (deconvoluted)	2.35 & onset of abs. starts at ~ 2.4	1	Direct-gap properties & excitons at NC surface couples to GeO_x stretching vibrations	[81]
RF magnetron co-sputtering and RTA (Ge NCs in SiO_2)	2 – 8	2.54	2.2–2.3	-	-	QC of excitons in NCs	[82]
DC magnetron sputtering and high T annealing (Ge or GeO_2 NCs in a-SiO_x)	1.5 – 25 or 25 $^*(GeO_2)$	3.81	3.1 (main), 2.2 (weak) and 1.8 (weak)	3.4 (given for only Ge NCs)	1	Ge/O related defect either on NC surfaces or in the matrice	[83], [84]
		2.81 / 441	2.2				
DC magnetron sputtering and high T annealing (Ge NCs in $Si_xGe_yO_z$)	< 4	3.81	3.0	-	-	Defects at the surface of NCs or in SiO_x matrice	[85]
		2.81	2.3				
Ion implantation and high T annealing (Ge NCs in SiO_2)	2 – 7 ($2x10^{16}$ cm^{-2})	2.71 / 458	1.8 (also for as-implanted)	-	<< 100 ns (system resolution)	Irradiation induced defects in SiO_2 network	[76]
	4 – 6 ($1x10^{16}$ cm^{-2})	4.99 / 248	2.1 and 1.6 (also for as-implanted)	2.4 and >4.2 bands (related to direct gap abs.)	-	1.6 eV PL -rec.s on NC surfaces & 2.1 eV PL - related to both NCs and oxygen-deficient centers in SiO_2 network	[74]
	no NCs ($1x10^{15}$ cm^{-2})		2.1 (main) and 1.6 (weak)	5 (sharp)		Implantation induced-defects in SiO_2 network	
	5 ($1.8x10^{17}$ cm^{-2})	2.54	0.95 (at 13 °K)	-	-	Direct gap rec.s in Ge NCs	[86]
Cluster-beam evaporation technique	4 – 40	3.96 / 313	2.8 (only photo-oxidised samples)	-	-	Defect centers in GeO_x	[87]
Lithography (plasma dry etching)	(no size given) planar quantum structure	2.41 / 514	1.7–1.9	-	-	Direct bandgap luminescence due to quantum size effects	[88]

Although there are various PL energies (blue, yellowish-green, red, and near IR) reported to date from Ge nanocrystals in SiO_2 (Table II), one of the possible explanations used for the observed PL is QC [5][73,74][81,82][86,88]. The other explanations usually involve defects in the network of SiO_2 matrice [74,76][83-85] and/or at the surface of nanocrystals [74,81][83-85], or defect centers in GeO_x [83,84,87]. There is no appreciable size dependence of PL in any of these data; however, depending on the excitation wavelength the PL energy shows variations. Usually the blue PL band (3.1 eV-2.8 eV) is observed when the PL is excited in the near UV, and when the excitation wavelength is longer than the blue wavelengths the other PL bands (i.e. 2.1-2.3 eV, 1.6-1.9 eV, and 0.9 eV bands) are observed. Nevertheless, the most commonly reported PL band from Ge (and GeO_2) nanocrystals is the broad yellowish-green band located between 2.1-2.3 eV [4,5,73,81-84,89-92].

Since the direct gap in Ge is close to the indirect gap (ΔE = 0.12 eV at 300 K), it is expected that Ge nanocrystals would exhibit a direct-gap semiconductor nature [5][74,81][86,88]. Besides, effects of the QC are expected to appear more profoundly in Ge nanocrystals than in Si nanocrystals since the exciton Bohr radius is larger in Ge (17.7 nm in bulk Ge versus 4.9 nm in bulk Si) [4][73]. Therefore, some groups suggested that the direct-transitions E_0, E_1 (0.88 and 2.25 eV, respectively, at 10 K [93]) and even E_2 (4.5 eV [93]) in Ge should play an important role in the absorption and PL excitation processes in Ge nanocrystals [74][81]. Although the PL spectra are 'size-insensitive' in terms of peak energy and typically have decaytimes ~ 1 ns, these groups also use this presumption to explain the PL mechanism; they suggest that while the photon absorption generates excitons in the nanocrystals, radiative recombination takes place via the surface (defect) states caused by germanium oxides on the surface of Ge nanocrystals.

Nevertheless, Ye *et al.* also account for the defects in the SiO_2 network as the origin of the PL [74]. Indeed some defects in silicon and germanium oxides can act as recombination centers. For example, 1.8 eV and 1.9 eV PL bands attributed to the non-bridging oxygen hole centers (NBOHCs or dangling oxygen bonds) were reported in γ (gama)-irradiated glassy GeO_2 and SiO_2, respectively [94]; a self-trapped exciton related PL at ~ 2.2 eV was reported from c-GeO_2 [95]; a PL band at ~ 3 eV due to oxygen-deficiency related defects was reported from glassy GeO_2 [96]. Additionally, at high energies for example, an excitation band at 4.3 eV associated with Ge *E'* ($_3O{\equiv}Ge{\bullet}$) defects was reported by Skuja *et al.* from Ge doped silica glass [97].

2.2.2 Spark-Processing

Although it was later going to be established that the structure and optical properties of spark-processed Si (sp-Si) are quite different from those of PS [98], spark-processing of Si was initially introduced as a new (or rather a 'novel') way of preparing PS [99]. Nevertheless, it is demonstrated that this technique is also capable of producing Si nanocrystals; but in sp-Si an amorphous silicon oxide (or possibly an amorphous silicon oxynitride) matrix surrounds the Si nanocrystals (see Fig. 2.14.a) [98]. In terms of the microstructure (Fig. 2.14.b and c), sp-Si is characterised by heavily indented and fine-structured columns, and sp-Si samples can be relatively thick films (typically between 5 and 300 μm) depending on the sparking conditions such as spark intensity or frequency and total sparking time [98].

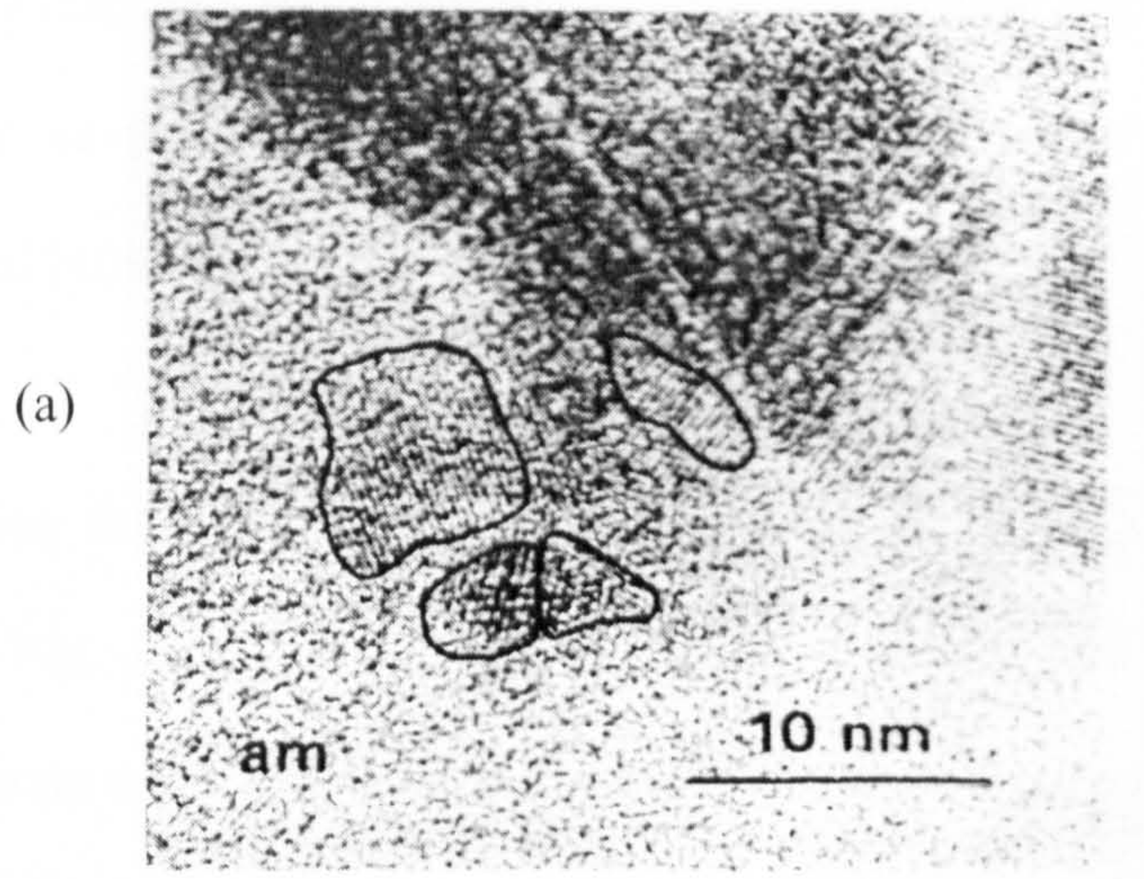

(a)

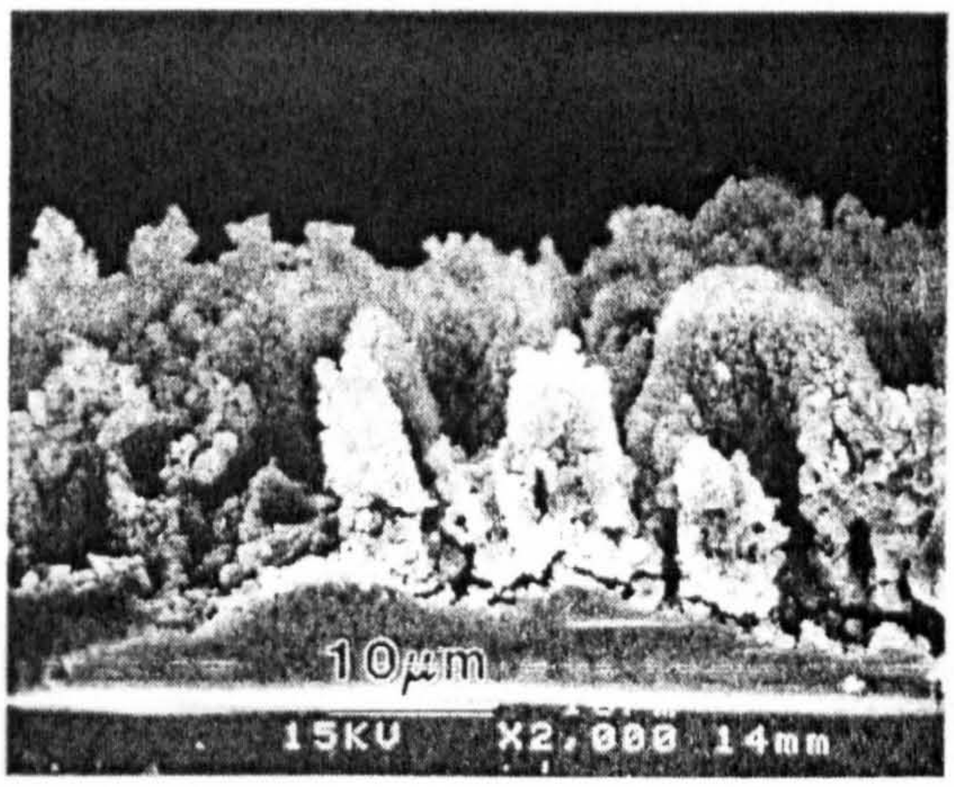

(b)

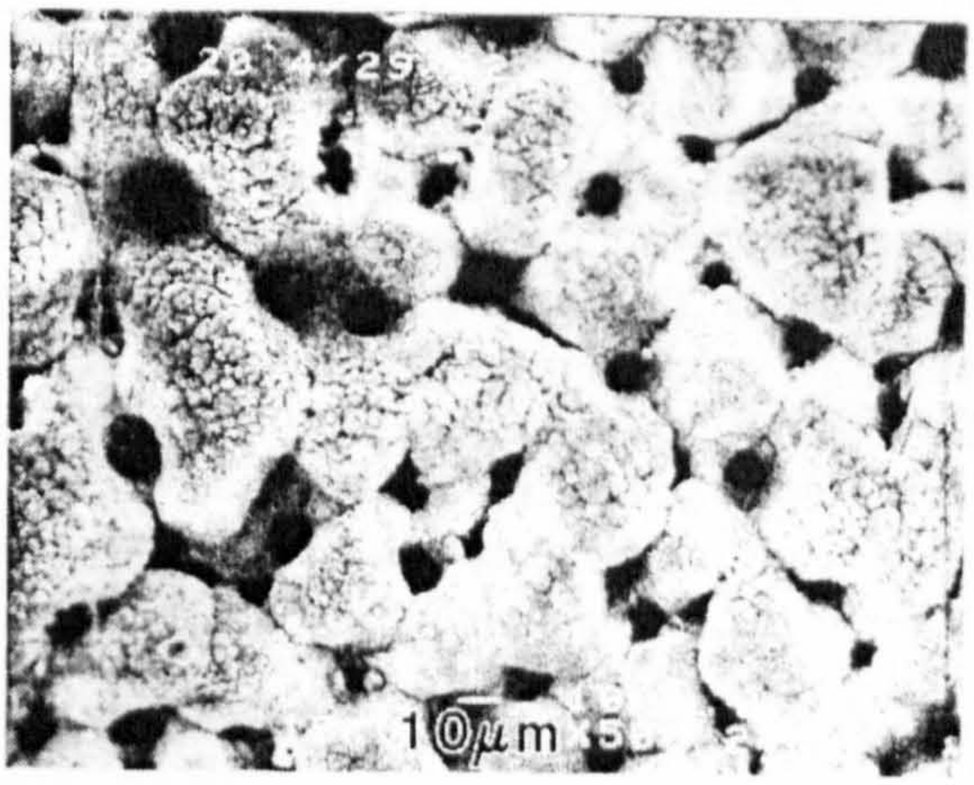

(c)

Figure 2.14 Micro-images of sp-Si (produced in flowing air): (**a**) high-resolution TEM image (some single crystalline nanoparticles are encircled); (**b**) SEM cross-sectional and (**c**) SEM plan views [98].

In order to produce typical visible-luminescing sp-Si samples a high frequency (several kHz), high voltage (several thousands volts) and low average current (several mA) electric pulses are applied to a Si substrate (cathode) by a counterelectrode (anode), which is usually a metal tip (e.g. tungsten wire) or a piece of a Si wafer, from approximately 1 mm distance. The resulting product is a greyish-looking circular layer

(~ 2 mm in diameter) which is surrounded by a light-brown halo (in plan view). The PL energy and intensity can be varied by preparation parameters such as the substrate temperature and the environment (air, nitrogen, oxygen, or CO_2, etc.) in which the sparking is conducted [100].

The mechanism for the formation of nanocrystalline particles and microstructures similar to those in Fig. 2.14 is explained usually as follows. The high voltage used between the Si substrate and the counterelectrode tip causes ionisation of the surrounding gas. The gas ions (such as nitrogen or oxygen) accelerate towards the substrate surface, and as a result some areas of the Si undergo localised flash evaporation. During off-times of the applied voltage the Si vapor re-deposits on the free surface, and in the meantime the remaining Si substrate forms a native oxide (or a nitride or an oxynitride). This causes the formation of randomly-oriented nanocrystallites of Si (like those seen in Fig. 2.14.a) which are embedded into an amorphous matrix [98].

The intensity and energy of the sp-Si PL are extremely stable (e.g. against annealing, UV illumination, HF etching) [100] and the PL energy is completely tunable through all wavelengths from near UV to near IR (depending on the gas environment used during the spark-process) [100]. Figure 2.15 provides a comparison of a set of PL spectra for Si spark-processed in different environments (stagnant/flowing air, oxygen, nitrogen, and various ratios of oxygen and nitrogen). Although the origin(s) of these spectra are not satisfactorily explained so far, based on these spectra themselves and on the other findings on the optical properties (e.g. PL decaytime) of sp-Si [101], it is arguably suggested that some possibilities can be ruled out as the origin(s) of the different PL emissions. For example, it is suggested that the UV/blue and green PL bands for sp-Si

prepared in air cannot be related to radiative transitions in silicon oxides or silicon nitrides since these bands are absent in samples prepared in pure oxygen or nitrogen, respectively [100] (Fig. 2.15).

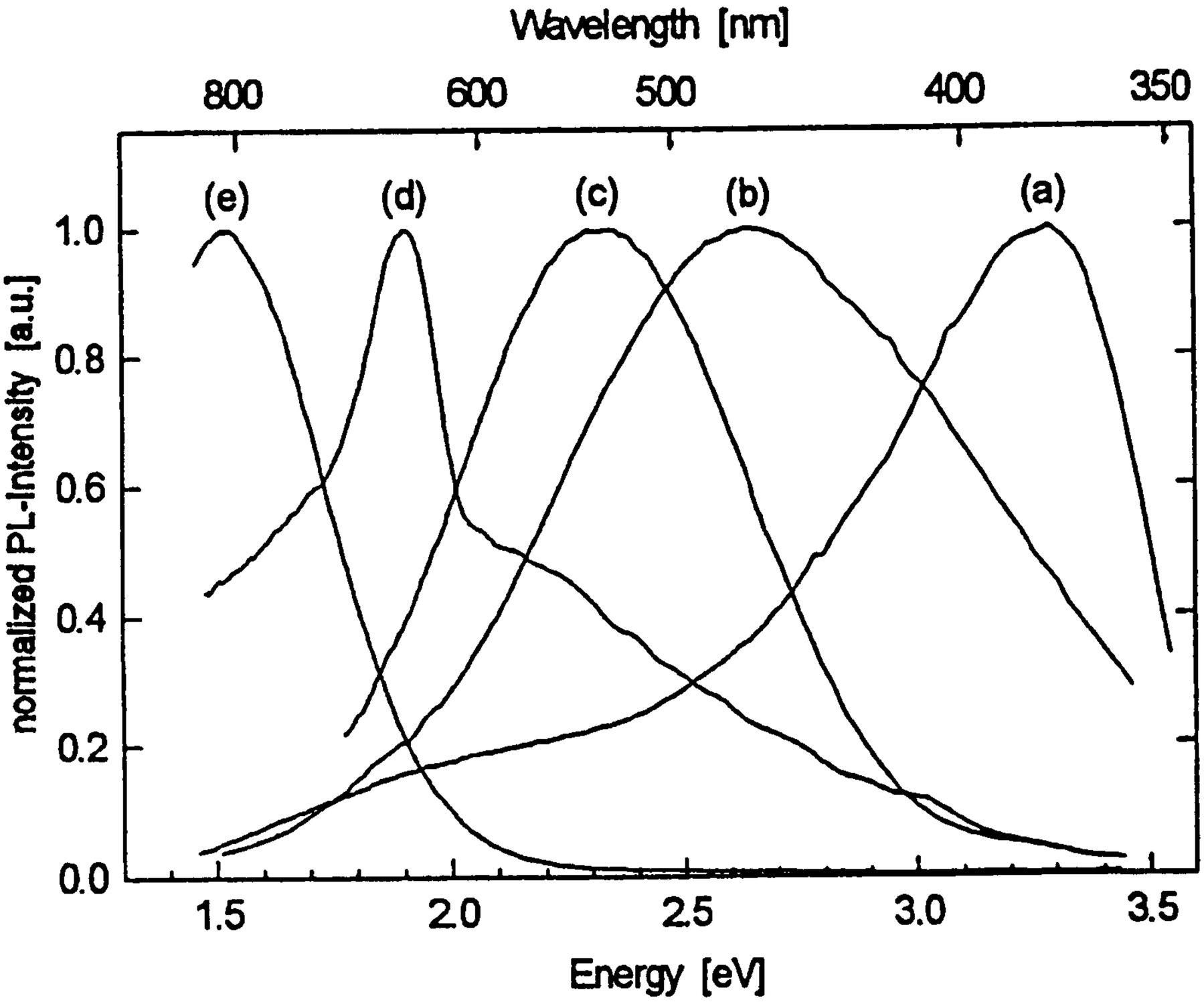

Figure 2.15 Normalised PL spectra for sp-Si prepared in **(a)** flowing air or in a 1:1 oxygen/nitrogen mixture, **(b)** pure oxygen and subjected to low pressure, **(c)** stagnant air or in nitrogen/oxygen atmospheres with volume ratios of >3:1 or <1:3, **(d)** pure oxygen, and **(e)** oxygen and annealed in oxygen at 850 °C [100].

Further, in a comparative study of blue/violet emitting sp-Si (peak 410 nm) with bluish-green emitting dry-oxidised PS (peak around 460-480 nm) [101] it is suggested that they derive their PL from somewhat different mechanisms, which was deduced from the differences in some optical properties. Among these are difference in emitted-color, a larger stability against UV laser illumination or HF etching of sp-Si, different decaytimes (nanoseconds for sp-Si versus microseconds for PS), and different IR vibrational spectra [101][102].

Finally, it has been demonstrated that 'virtually' all semiconducting and semimetallic materials can be spark-processed to yield strong, visible and room temperature PL [103]. Among these materials sp-Ge is of particular importance in this study. We will discuss the visible PL from sp-Ge (also according to our data) later.

2.3 REFERENCES

[1] A.G. Cullis, L.T. Canham, and P.D.J. Calcott, *J. Appl. Phys.*, **82**, 909 (1997), and reference therein.

[2] V. Lehmann and U. Gösele, *Appl. Phys.* **58**, 856 (1991).

[3] L. Pavesi and V. Mulloni, *Societa Italiana di Fisica, Proceedings of the ISP-Course CXLI*, 87, IOS Press (1999).

[4] Y. Maeda, N. Tsukamoto, Y. Yazawa, Y. Kanemitsu, and Masumoto, *Appl. Phys.Lett.*, **59**, 3168 (1991).

[5] Y. Kanemitsu, H. Uto, Y. Masumoto, and Y. Maeda, *Appl. Phys. Lett.*, **61**, 2187 (1992).

[6] L.T. Canham, *Appl. Phys. Lett.*, **57**, 1046 (1990).

[7] A. Uhlir, *Bell Syst. Tech. J.*, **35**, 333 (1956).

[8] A. Halimaoui, in L.T. Canham, *Properties of Porous Silicon*, IEE INSPEC, The Institution of Electrical Engineers, London (1997).

[9] L.T. Canham, *Properties of Porous Silicon*, IEE INSPEC, The Institution of Electrical Engineers, London (1997).

[10] L.T. Canham, A.G. Cullis, C. Pickering, O.D. Dosser, T.I. Cox, and T.P Lynch, *Nature*, **368**, 133 (1994).

[11] (a) A. Venkateswara, F. Ozanam, and J.N. Chazalviel, *J. Electrochem. Soc.*, **138**, 533 (1991);

(b) L.M. Peter, D.J. Blackwood, and S. Pons, *Phys. Rev. Lett.*, **62**, 308 (1989).

[12] A.G. Cullis, L.T. Canham, *Nature*, **353**, 335 (1991).

[13] Ph. Dumas *et al.*, *Europhys. Lett.*, **23(3)**, 197 (1993)

[14] Z. Sui, P.P. Leong, I.P. Herman, G.S. Higashi, and H. Temkin, *Appl.Phys.Lett.*, **60(17)**, 2086 (1992).

[15] V. Vezin, P.Gaudeau, A. Naudon, A. Halimaoui, and G. Bomchil, *Appl.Phys.Lett.*, **60(21)**, 2625 (1992).

[16] V. Lehmann, B. Jobst, T. Muschik, A. Kux, and V. Petrova-Koch, *Jpn. J. Appl.Phys.*, **32(5A)**, 2095 (1993).

[17] S. Schuppler, S.L. Freidman, M.A. Markus, D.L. Adler, Y.H. Xie, F.M. Ross, T.D. Harris, W.L. Brown, Y.J. Chabal, L.E. Brus, and P.H. Citrin, *Phys. Rev. Lett.*, **72**, 2648 (1994).

[18] Q. Zhang and S.C. Bayliss, *J. Appl.Phys*, **79(3)**, 1351 (1996).

[19] Y. Kanemitsu, in D.J. Lockwood (Ed.), *Light Emission in Silicon, Semiconductors and Semimetals*, Vol. 49, Academic, New York (1997).

[20] K. Inoue, O. Matsuda, K. Maehashi, H. Nakashima, and K. Murase, *Jpn.J. Appl. Phys.*, **31**, L997 (1992).

[21] G. Mariotto, F. Ziglio, and F.L.J. Freire, *J.Non-Cryst. Solids*, **192&193**, 253 (1995).

[22] J.P. Proot, C. Deleure, and G.Allan, *Appl. Phys. Lett.*, **61**, 1948 (1992).

[23] J.C. Vial, A. Bsiesy, F. Gaspard, R. Hérino, M. Lugeon, F. Muller, R. Romenstain, and R.M. Macfarlane, *Phys. Rev. B.*, **95**, 14171 (1992).

[24] P.D.Calcott, K. J. Nash, L.T. Canham, M.J. Kane, and D. Brumhead, *J. Phys.Condens. Matter*, **5**, L91 (1993).

[25] F.Koch, V. Petrova-Koch, T. Muschik, *J. Lumin.*, **57**, 271 (1993).

[26] S.M. Prokes, O.J. Glembocky, V.M. Bermudez, R. Kaplan, L.E. Friedersdorf, and P.C. Searson, *Phys. Rev. B*, **45**, 13788 (1992).

[27] M.S. Brandt, D.H. Fuchs, M. Stutzman, J. Weber, and M. Cardona, *Solid State Commun.*, **81**, 307 (1992).

[28] H. Tamura, M. Ruckschloss, T. Wirschem, and S. Veprek, *Thin Solid Films*, **255**, 92 (1995).

[29] V. Petrova-Koch, T. Muschik, A. Kux, B.K. Meyer, F. Koch, and V. Lehmann, *Appl. Phys. Lett.*, **61**, 943 (1992).

[30] S. Oscini, C.M. Bertoni, M. Biagini, A. Lugli, G. Roma, and O. Bisi, *Thin Solid Films*, **297**, 154 (1997).

[31] T. Takagahara and K. Takeda, *Phys. Rev.* B, **46**, 15578 (1992).

[32] C. Deleure, G. Allan, and M. Lannoo, *Phys. Rev. B*, **48**, 11024 (1993).

[33] P. Deak, M. Rosenbauer, M. Stutzman, J. Weber, and M.S. Brandt, *Phys. Rev. Lett.*, **69**, 2531 (1992).

[34] A.J. Read, R.J. Needs, K.J. Nash, L.T. Canham, P.D.J. Calcott, and A. Qteish, *Phys.Rev. Lett.*, **69**, 1232 (1992).

[35] C. Deleure, G. Allan, and M. Lannoo, *J. Lumin.*, **80**, 65 (1999).

[36] D.J. Lockwood, *Solid State Commun.*, **92**, 101 (1994).

[37] M. Ebrecht, B. Kohn, F. Hulsken, M.A. Laguna, and V. Paillard, *Phys. Rev. B*, **56**, 6958 (1997).

[38] M.V. Wolkin, J. Jorne, P.M. Fauchet, G. Allan and C. Deleure, *Phys. Rev. Lett*, **82**, 197 (1999).

[39] G. Allan, C. Deleure, and M. Lannoo, *Phys. Rev.Lett.*, **76**, 2961 (1996).

[40] P.M. Fauchet, in D.J. Lockwood (Ed.), *Light Emission in Silicon, Semiconductors and Semimetals*, Vol. 49, Academic, New York (1997).

[41] J.F. Harvey, H. Shen, R.A Lux, M. Dutta, J. Pamulapati, and R. Tsu, *Mat. Res. Soc.Symp. Proc.*, **256**, 175 (1992).

[42] B. Delley, and E.F. Steigmeier, *Phys. Rev.B*, **48 (15)**, 11024 (1993); L.W. Wang and A. Zunger, *J. Chem. Phys.*, **100**, 2394 (1994).

[43] M.S. Hybertsen, *Phys. Rev. Lett.*,**72**, 1514 (1994).

[44] J.M. Rehm, G. L. McLendon, L. Tsybeskov, and P.M. Fauchet, *Appl. Phys. Lett.*, **66**, 3669 (1995).

[45] A. Richter, P. Steiner, F. Kozlowski, and W. Lang, *IEEE Elec. Dev. Lett.*, **12**, 691(1991).

[46] N. Koshida and H. Koyama, *Appl. Phys. Lett.*, **60**, 347 (1992); N. Koshida, H. Koyama, Y. Yamamoto, and G.J. Cullis, *Appl. Phys. Lett.*, **63**, 2655 (1993).

[47] N.M. Kalkhoran, F. Namavar, and H.P. Maruska, *Mat. Res. Soc. Symp. Proc.*, **256**, 84 (1992).

[48] B. Gelloz, T. Nakagawa, and N. Koshida, *Mat. Res. Soc. Symp. Proc.*, **536**, 15 (1998).

[49] A.J. Simons, T.I. Cox, A. Loni, L.T. Canham and R. Blacker, *Thin Solid Films*, **297**, 281 (1997).

[50] D. Haneman, J.Yuan, *Appl. Surf. Sci.*, **113-114**, 103 (1997).

[51] M.B. Robinson, A.C. Dillon, D.R. Haynes, and S.M. George, *Appl. Phys. Lett.*, **61**, 414 (1992).

[52] R.T. Collins, M.A. Tischler, and J.A. Stathis, *Appl. Phys. Lett.*, **61**, 1649 (1992).

[53] A. Loni, A.J. Simons, T.I. Cox, P.D.J. Calcott, and L.T. Canham, *Electron. Lett.*, **31**, 1228 (1995).

[54] L. Tsybeskov, L.P. Duttagupta, and P.M. Fauchet, *Solid State Commun.*, **95**, 429 (1995).

[55] B. Gelloz and N. Koshida, *Electrochemical Society Proceedings*, Vol 99-22, 27(1999).

[56] D.J. Lockwood, *Light Emission in Silicon, Semiconductors and Semimetals*, Vol. 49, Academic, New York (1997).

[57] T. S. Iwayama, D. E. Hole, and P.D. Townsend, *J. Lumin.*, **80**, 235 (1999).

[58] J. Linnros, Societa Italiana di Fisica, Proceedings of the ISP-Course CXLI, 47, IOS Press (1999).

[59] S. Charvet, R. Madelon, R. Rizk, B. Garrido, O. G. Verona, M. Lopez, A. P. Rodriguez, and J.R. Morante, *J. Lumin.*, **80**, 241 (1999).

[60] S. Cheylan, N. B. Manson, and R. G. Elliman, *J. Lumin.*, **80**, 213 (1999).

[61] T.S. Iwayama, M. Ohshima, T. Niimi, S. Nakao, K. Saitoh, T. Fujita, N. Itoh, *J. Phys.: Condens. Matter*, **5**, L375 (1993).

[62] K.S. Min, K.V. Shcheglov, C.M. Yang, H.A. Atwater, M.L. Brongersma, and A. Polman, *Appl. Phys. Lett.*, **69**, 2033 (1996).

[63] G. Ghislotti, B. Nielsen, P. A. Kumar, K.G. Lynn, A. Gambhir, L.F.D. Mauro, and C.E. Bottani, *J. Appl. Phys.*, **79**, 8660 (1996).

[64] Y. Kanemitsu, T. Ogawa, K. I Shiraishi, and S. Takeda, *Phys. Rev. B*, **48**, 4883 (1993).

[65] V. G. Baru, A. P. Chernushish, V.A. Luzanov, G.V. Stepanov, L.Y. Zakharov, K.P. O'Donnell, I.V. Bradley, and N.N. Melnik, *Appl. Phys. Lett.*, **69 (27)**, 4148 (1996).

[66] Q. Zhang, S.C. Bayliss, A.A. Ajili, D.A. Hutt, and P. Harris, *Nucl. Instr. and Meth. In Phys. Res. B*, **97**, 329 (1995)

[67] S. Hayashi, M. Kataoka, and K. Yamamoto, *Jpn. J. Appl. Phys.*, **32**, L274 (1993).

[68] S. Takeoka, M. Fujii, and S. Hayashi, *Phys. Rev. B*, **62(24)**, 16820 (2000).

[69] N. Lalic and J. Linnros, *J. Lumin.*, **80**, 263 (1999).

[70] M. Fujii, O. Mamezaki, S. Hayashi, and K. Yamamoto, *J. Appl. Phys.*, **83**, 1507 (1998).

[71] N. Lalic, J. Linnross, *J. Appl. Phys.*, **80**, 5971 (1996).

[72] M. Fujii, S. Hayashi, and K. Yamamoto, *Appl. Phys. Lett.*, **57(25)**, 2692 (1990); M. Fujii, S. Hayashi, and K. Yamamoto, *Jpn. J. Appl. Phys.*, **30(4)**, 687 (1991).

[73] Y. Maeda, *Phys. Rev. B*, **51(3)**,1658 (1995).

[74] Y.H.Ye, J.Y. Zhang, X.M. Bao, X.L. Tan, and L.F. Chen, *Appl. Phys. A*, **67**, 213 (1998).

[75] H.B. Kim,K.H. Chae, C.N. Wang, J.Y. Jeong, M.S. Oh, S. Im, and J.H. Song, *J. Lumin.*, **80**, 241 (1999).

[76] K.S. Min, K.V. Shcheglov, C.M. Yang, H.A. Atwater, M.L. Brongersma, and A. Polman, *Appl. Phys. Lett.*, **68(18)**, 2511 (1996).

[77] S. Miyazaki, K. Sakamoto, K. Shiba, and M. Hirose, *Thin Solid Films*, **255**, 99 (1995).

[78] M. Sendova-Vassileva, N. Tzenov, D. Dimova-Malinovska, M. Rosenbauer, M. Stutzman, and K.V. Josepovits, *Thin Solid Films*, **255**, 282 (1995).

[79] S. Bayliss, Q. Zhang, and P. Harris, *Appl. Surf. Sci.*, **102**, 390 (1996).

[80] S.S. Chang and R.E. Hummel, *J. Lumin.*, **86**, 33 (2000).

[81] S. Okamoto, and Y. Kanemitsu, *Phys. Rev. B*, **54(23)**, 16421 (1996).

[82] W.K. Choi, S. Kanakaraju, Z.X. Shen, and W.S. Li, *Appl. Surf. Sci.*, **144-145**, 697 (1999).

[83] M. Zacharias, and P.M. Fauchet, *Appl. Phys.Lett.*, **71(3)**, 380 (1997).

[84] M. Zacharias, and P.M. Fauchet, *J. Non-Cryst. Solids*, **227-230**, 1058 (1998).

[85] M. Zacharias, R. Weigand, B. Dietrich, F. Stolze, J. Blasing, P. Veit, T. Drusedau, and J. Christen, *J. Appl. Phys.*, **81(5)**, 2334 (1997).

[86] Y. Kanemitsu, K. Masuda, M. Yamamoto, K. Kajiyama, and T. Kushida, *J. Lumin.*, **87-89**, 457 (2000).

[87] S. Sato, S. Nozaki, H. Morisaki, and M. Iwase, *Appl. Phys.Lett.*, **66(23)**, 3176 (1995).

[88] R. Venkatasubramanian, D.P. Malta, M.L. Timmons, and J.A. Hutchby, *Appl. Phys.Lett.*, **59(13)**, 1603 (1991).

[89] D.C. Paine, C. Caragianis, T.Y. Kim, Y. Shigesato, and T. Ishakara, *Appl. Phys. Lett.*, **62**, 2842 (1993).

[90] (a) M. Nogami, and Y. Abe, *Appl. Phys. Lett.*, **65**, 2545 (1994); (b) A. Saito, and T. Suemoto, *Phys. Rev. B*, **56(4)**, R1688 (1997).

[91] V. Craciun, C.B. Leborgne, E.J. Nicholls, and I.W. Boyd, *Appl. Phys. Lett.*, **69**, 1506 (1996).

[92] M. Zacharias, R. Weigand, J. Blasing, and J. Christen, EMRS Proceedings, **452**, 117 (1997).

[93] D.E. Aspnes, *Phys. Rev. B*, **12**, 2297 (1975).

[94] L. Skuja, H. Hosono, M. Mizuguchi, B. Gutler, and A. Silin, *J. Lumin*, **87-89**, 699 (2000).

[95] A.N. Trukhin, *J. Non-Cryst. Solids*, **189**, 1 (1995).

[96] L. Skuja, *Phys. Stat. Sol. A*, **114**, 731 (1989).

[97] L. Skuja, *J. Non-Crys. Solids*, **149**, 77 (1992).

[98] R.E. Hummel, M.H. Ludwig, *J. Lumin.*, **68**, 69 (1996).

[99] R.E. Hummel, S.S. Chang, *Appl. Phys. Lett.*, **61 (16)**, 1965 (1992)

[100] M.H. Ludwig, A. Austin, and R.E. Hummel, M*at. Res. Soc. Symp. Proc.*, **452**, 153 (1997).

[101] R.E. Hummel, M.H. Ludwig, S.S. Chang, P.M. Fauchet, J.V. Vandyshev, L. Tsybeskov, *Solid State Commun.*, **95 (8)**, 553 (1995).

[102] R.E. Hummel, M.H. Ludwig, S.S. Chang, and G. LaTorre, *Thin Solid Films*, **255**, 219 (1995).

[103] M.H. Ludwig, R.E. Hummel, and M. Stora, *Thin Solid Films.*, **255**, 103 (1995).

CHAPTER 3. MATERIAL PREPERATION AND CHARACTERISATION TECHNIQUES

3.1 POROUS $Si_{1-x}Ge_x$

3.1.1 Introduction

$Si_{1-x}Ge_x$ alloys have attracted much interest since the early 1970's due to their band-gaps being variable between those of bulk Si and Ge via so-called 'band-structure engineering' [1][2]. After the observation of strong visible luminescence from porous Si (PS) [3], several groups attempted to prepare porous $Si_{1-x}Ge_x$ with visible luminescence, either by anodisation [4,5] or stain etching [6,7]. Schoisswohl *et al.* reported that the spectral shape of PL emission from porous SiGe is not different from that of porous Si, except for being slightly red-shifted [5]. On the other hand, the porous SiGe (PSG) film PL lifetime was measured to be ~ 100 times faster than that of PS [8-10]. The latter observation makes PSG a more attractive material than PS for both fundamental research and industry. However none of the studies of $Si_{1-x}Ge_x$ were on the microstructure of the samples, but instead only discussed the PL properties in comparison to those of PS, and generally in line with the quantum confinement (QC) effect (e.g. [3,4,9]).

Recently $Si_{1-x}Ge_x$ nanocrystals have been successfully prepared in insulating matrices of SiO_2 by Takeoka *et al.*, using RF co-sputtering and post-annealing techniques [11]. They

studied the size and nature of the nanocrystals from high-resolution TEM micrographs and the corresponding electron diffraction patterns, and estimated their compositions using Rutherford backscattering spectroscopy (RBS). RBS results on the composition were supported with Raman scattering experiments. PL emission from $Si_{1-x}Ge_x$ samples containing nanocrystals as small as 4 nm was observed in the near infrared, between 1.2-1.4 eV, very different from the visible luminescence observable from PSG [4-9]. Furthermore, the PL lifetime was several microseconds, in contrast to published PL lifetimes for PSG [8,9].

In this study, we investigated the microstructure of porous $Si_{1-x}Ge_x$ samples prepared by anodisation. Using Raman spectra we have determined both compositional variations with respect to those of the starting alloys and the size of SiGe nanocrystals, as a function of etching time. This has given insight into the mechanism of etching of $Si_{1-x}Ge_x$ alloys and to the resulting porous structure, both of which are likely to be crucial in determining the optical properties of the porous $Si_{1-x}Ge_x$ material.

3.1.2 Growth of Initial SiGe layers

Starting $Si_{1-x}Ge_x$ materials were prepared with molecular beam epitaxy (MBE) using a VG Semicon V90S system in the Department of Physics of the University of Warwick.

MBE is one of the standard methods used for the epitaxial growth of semiconductors. It is essentially a thermally controlled evaporation process taking place in an ultra-high vacuum (down to a pressure about 10^{-10} torr [12]) apparatus. MBE occurs by molecular flow where elements or compounds of the to-be-grown semiconductor(s) are heated in crucibles to generate 'neutral' atomic or molecular beams which are directed on to a

heated substrate. The particles in the molecular flow do not interact with each other physically or chemically before their arrival at the substrate on which they will be grown. The slow growth rate (about one atomic layer per second) of MBE allows sufficient control over the type and amount of material deposited and changing composition across an atomic layer.

Substrates used in this study consisted of a fully-relaxed, undoped, 1 μm-thick $Si_{0.87}Ge_{0.13}$ alloy layer (top layer) on a 0.2 μm-thick, undoped Si buffer layer, both grown at 550 °C, on an n^+-type Si wafer. Thickness and Ge content (x) of the alloy were determined from X-ray diffraction rocking curves (giving composition x accurate to ± 0.01 (= 1%)) following the production of the layers [13].

3.1.3 Anodisation

Anodisation of the wafers was performed using a mixture of 48 % HF and absolute ethanol in 1:1 volume ratio (resulting in a final HF concentration of 25 %) in a lateral etching cell. The etch area was 0.5 cm^2. While the current density was fixed to 22 mA cm^{-2} for all the porous SiGe samples, the etching time was varied between 2-20 minutes in order to produce a set of samples with different porosities. To enhance the etching of 'undoped' samples a 250 W tungsten lamp was held ~ 20 cm above the etching cell [14].

3.1.4 Characterisation of the Films

3.1.4.a Micro-Raman

A Renishaw RM series microRaman spectrometer (Fig. 3.1) operating with a 514.5 nm Ar^+ laser was used for the investigation of the structure of the porous films. The beam diameter was focused to 1 μm on the sample surface and scattered light was collected with a CCD camera on the head of the microscope. The laser power was 1 mW on the sample for all measurements. The resolution of this system was 1 cm^{-1}. Micro-optical images of the sample surface enabled positioning of the laser spot on the desired area of the sample.

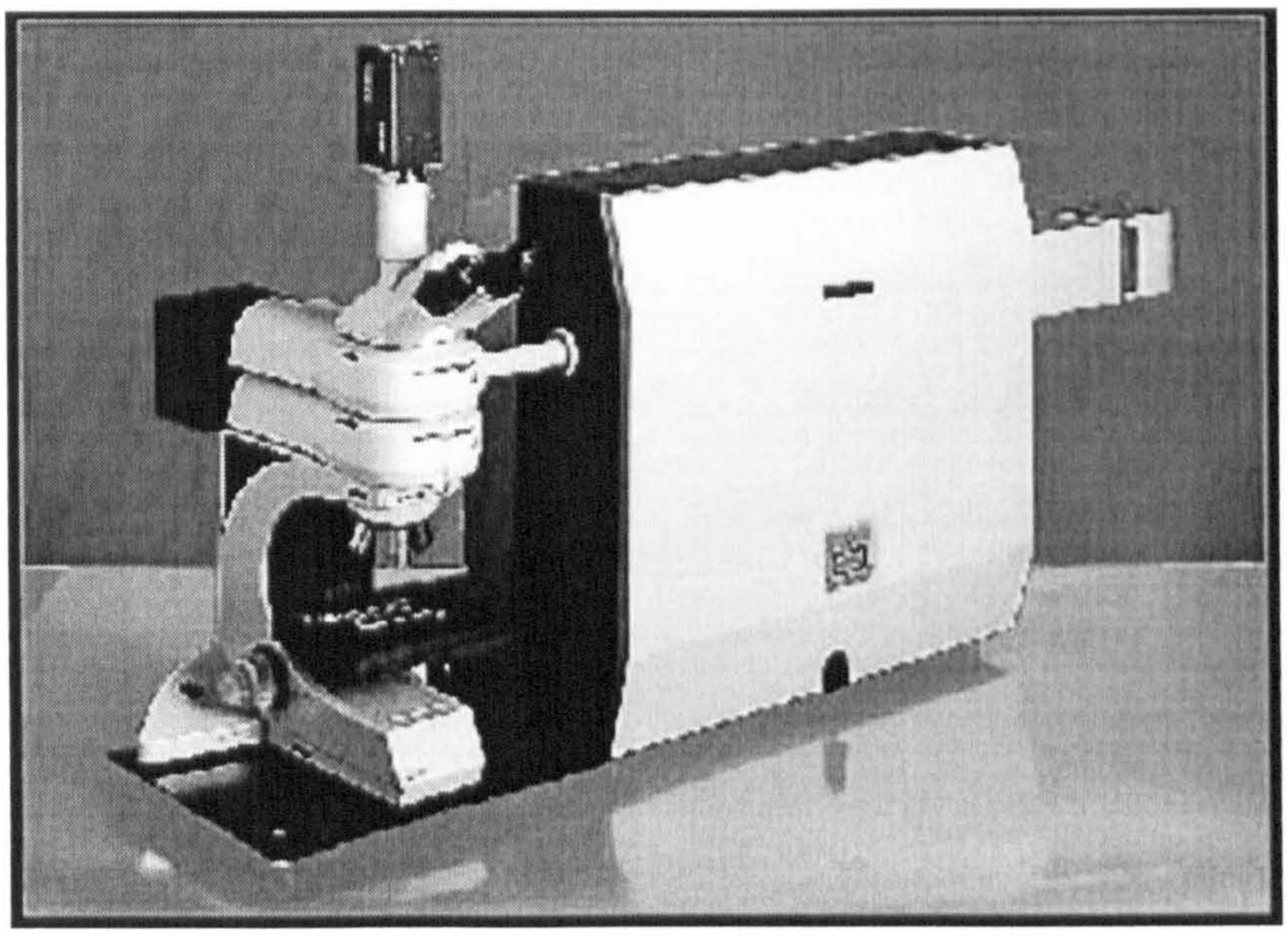

Figure 3.1 An image of the Renishaw RM series microRaman spectrometer used in this study.

3.1.4.a.1 Raman Modelling

The theory of the confinement of phonons in small semiconductor nanocrystals suggests that for less than a critical crystal size the Raman lineshape should show some definite modifications, such as peak-frequency shifting, peak-broadening, and increasing peak asymmetry, from that of its bulk spectrum. The reason for these alterations is the partial breakdown of the $\mathbf{q} = 0$ selection rule due to the spatial confinement of the phonons in a finite volume [15][16]. A phonon can no longer be described by a plane wave, as it is for the bulk crystal, but instead by a wave packet spatially confined inside the nanocrystal. A finite particle L size would bring about an uncertainty in wavevector on the order of $\pm 2\pi/L$, which will be larger for smaller crystal sizes. In an infinite (bulk) crystal, uncertainty is 0, and as only the phonons near the zone centre can contribute to the first-order Raman spectrum, the Raman peak will be rather sharp. If the phonon dispersion curves are not flat near $\mathbf{q} = 0$, then, for nanocrystals, the spectral features will shift, broaden, and become asymmetric by the phonon confinement.

In order to explain the size dependant spectral changes observed in the PSG Raman spectra in this study we calculated the Raman lineshape using the following integral given for the first-order Raman spectrum I(w) for nanocrystals by Campbell and Fauchet [16]

$$I(\omega) = \int \frac{d^3q \left|C(0,\mathbf{q})\right|^2}{\left[\omega - \omega(\mathbf{q})\right]^2 + \left(\frac{\Gamma_0}{2}\right)^2} \tag{3.1}$$

where $C(0,\mathbf{q})$ is a Fourier transform of a phonon confinement function; $\mathbf{q}$ is expressed in units of $2\pi/a_{si}$; $\omega(\mathbf{q})$ is the phonon dispersion curve; and Γ_0 is the natural (bulk) linewidth. The integral is taken over the entire Brillouin zone. With $|C(0,\mathbf{q})|^2 \approx \exp[-q^2L^2/4]$ [17],

$\Gamma_0 = 4.9\ cm^{-1}$ and $a_{si} = 0.548$ nm for Si, the calculated peak frequency and linewidth as a function of crystallite size are plotted in Fig. 3.2. As seen from both curves, the critical diameter is about 20 nm at which the above-mentioned changes become observable for Si. Theoretically either of the relations given in Fig. 3.2.a or Fig. 3.2.b can be used to estimate the crystallite size. However, usually this is not the case, since the peak frequency shift does not only result from phonon confinement. Therefore, care must be taken in interpreting the Raman spectral changes. The calculated and measured Raman spectra for a selection of sizes will be given later.

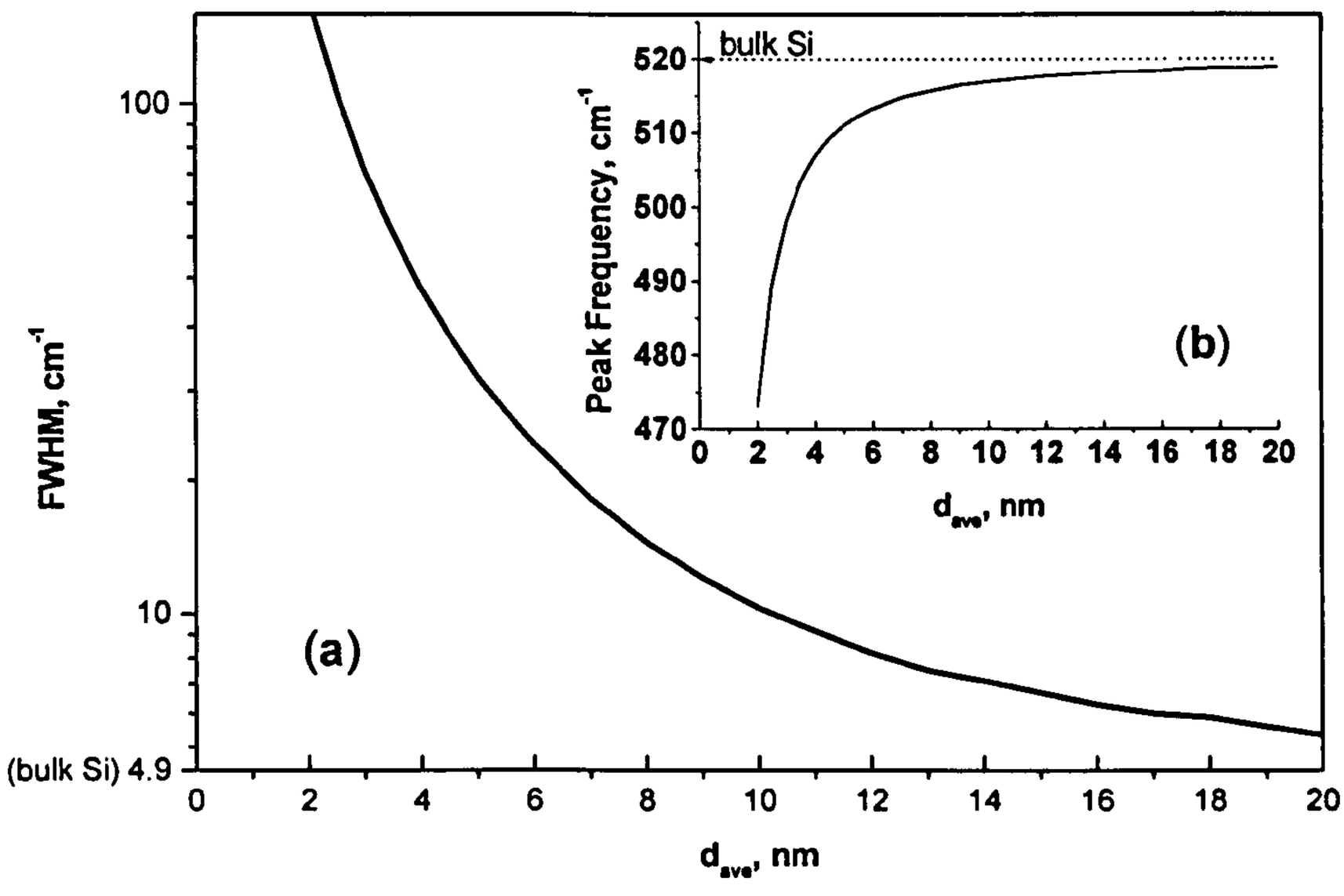

Fig. 3.2 The calculated (**a**) linewidth (FWHM) and (**b**) peak frequency as a function of Si crystal size (d_{ave}). Corresponding bulk Si values are indicated.

3.1.4.b High-Resolution SEM

Scanning electron microscopy (SEM) is performed by scanning a focussed probe across the surface of the sample to be studied. The interaction of the primary electron beam with the surface is accompanied by the formation of a flux of secondary, back-scattered electrons. Secondary electrons emitted from the vicinity of the impact area of the primary electron beam are typically detected by a photomultiplier system in order to produce images. The more electrons a particular region emits, the brighter the image at that point.

We obtained micro-images of the samples using a LEO 1530VP high-resolution field emission gun scanning electron microscope (also known as FEGSEM) in order to check whether a nanoporous structure has really formed from such high resistivity layers. The resolution of the HR-SEM system used was 1 nm at 20 keV accelerating voltage (and 2.1 nm at 1 keV).

Figure 3.3 shows the thickness of the initial SiGe layer as 1 μm. This result is in good agreement with that determined from the x-ray analysis [13]. Micro-images of the PSG samples will be given and discussed later.

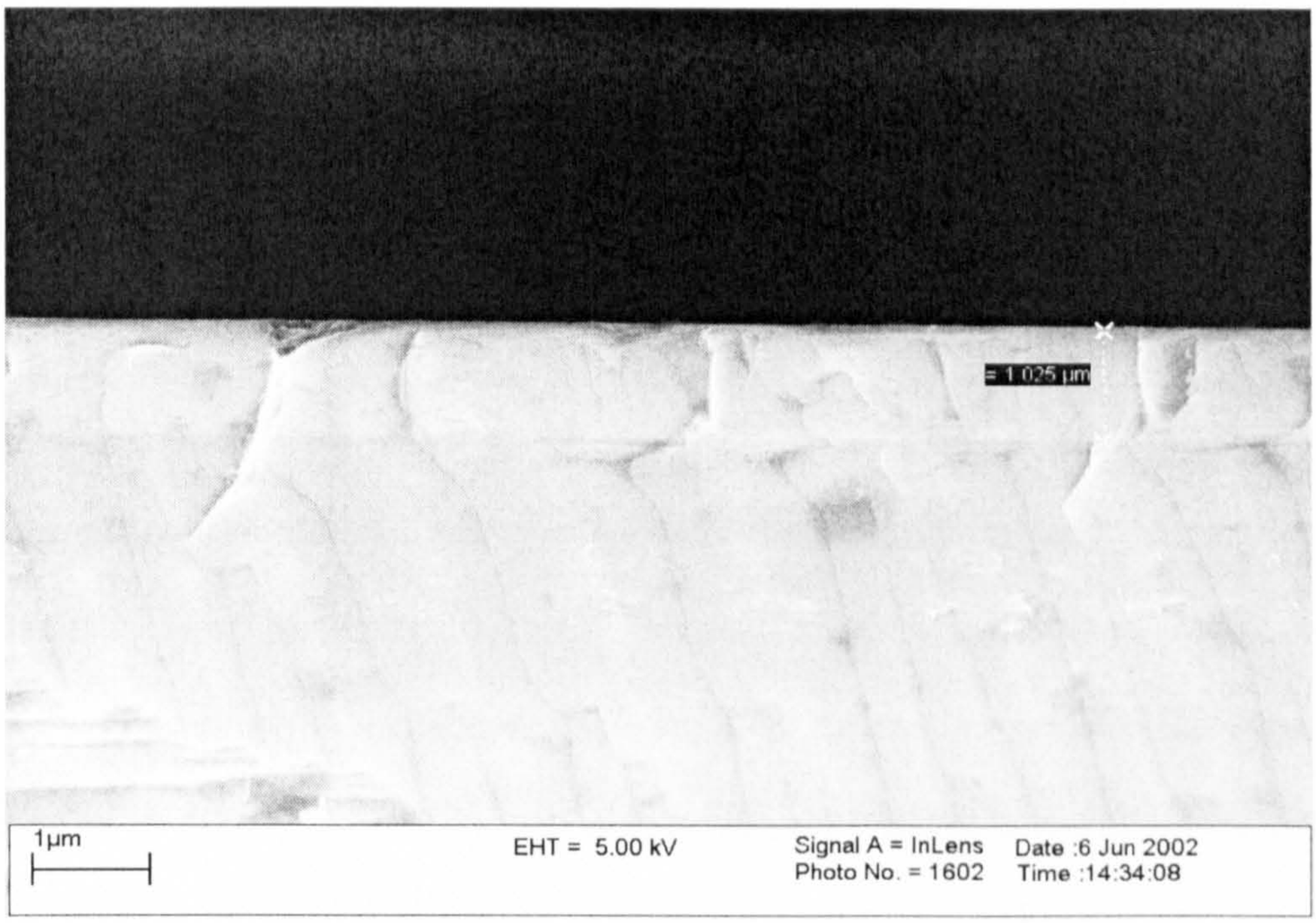

Figure 3.3 An SEM image of the starting MBE-$Si_{0.87}Ge_{0.13}$ epilayer on Si. The inset marker shows 1.025 µm for the thickness of the epilayer.

3.1.4.c PL

For PL measurements on PSG samples 120 mW He-Cd 442 nm cw excitation was used with a single-grating SPEX 270M spectrograph and a Hamamatsu R2949 photomultiplier (PMT) tube.

3.2 STAIN ETCHED Ge

3.2.1 Introduction

The observation of bright, room-temperature, visible PL from PS by Canham [3] has been the catalyst for much of the recent interest in luminescent group IV nanostructures. Though much of this initial interest was aimed at visible luminescent nanostructured Si more recently there has been increasing interest in Ge nanostructures. For these latter studies co-sputtering has been the most common method to prepare Ge (and GeO_2) nanocrystals in a SiO_2 matrix, due to its convenience [18-22]. Several groups have also tried to prepare porous germanium containing visible luminescing Ge nanocrystals similar to PS, either by anodisation [23-26] or stain-etching methods [26]. It is interesting that chemically prepared samples, and samples prepared by other techniques where there are Ge atoms in contact with O atoms, are reported to show PL in the 2.1-2.3 eV range of the spectrum [19-22][27-32]. Towards determination of the origin of the 2.1-2.3 eV PL, we prepared chemically-etched Ge by both anodisation and stain etching methods. Anodisation with HF solutions did not yield visible PL chemically-etched Ge samples (see the following section), however visible PL (2.3 eV peak energy) was observed from stain-etched Ge samples. In this study, we will present the results from the study of PL from 2 types of stain-etched Ge (SG): Type I-SG prepared following the method of [26]; Type II-SG prepared using an HF based solution ($HF:H_3PO_4:H_2O_2$) with a new method [33]. The material displaying the greatest luminescence was prepared using a H_2O_2:HF solution (Type I-SG), though the obtained structure was found by Raman spectroscopy to be far from the nanocrystalline nature observed in PS. On the other hand, Type II-SG

proved to contain Ge nanocrystals at sizes 8-9 nm in diameter when annealed at a low-temperature in H environment, but yielded a weaker PL.

3.2.1.a Anodised Ge

We started our investigation to prepare luminescent porous Ge samples using HF solutions for the anodisation of Ge similar to those in [24-26]. The etchant mostly employed was the conventional HF:ethanol:water solution used to fabricate PS [34] at a 1:2:1 volume ratio. Various different etching conditions (etching time, current density) have been tried on different resistivity (100) and (111) Ge substrates.

We observed some weak visible PL emission (bluish-green to orange-red) with an UV laser excitation from a number of (porous) layers produced. An example spectrum is reproduced in Fig. 3.4. However, the light emission was discernible only from a few dot-like isolated emission centres on the porous layers (sizes of the centres were comparable to the tip of a needle). SEM analysis of these samples revealed a 'macroporous' structure (similar to that typically seen in PS prepared using lightly n-type doped Si) in most of the samples (Fig. 3.5.a). The SEM system (see sec. 3.2.3.d) also enabled us to characterise the samples using cathodoluminescence (CL) and energy-dispersive x-ray (EDX) analysis using the same SEM configuration. In order to gain a deeper understanding about nature of the luminescent centres, we studied the surface of the photoluminescent samples extensively with cathodoluminescence (CL) and the chemistry of the luminescent centres by energy-dispersive x-ray (EDX) probing. The results were so surprising since we did not find any inclusion of Ge atoms in any of those luminescent species. Instead we found that these species were formations of the contaminant atoms/molecules adsorbed by the material surface, perhaps either from the electrolyte,

during anodisation, or from the atmosphere, after drying during storage of the samples. Among the atoms found were mainly F, Al, O (and, on one occasion, even Ga atoms). An example image of a cathodoluminescing centre formed by the contaminants on the material surface is shown in Fig. 3.5.b.

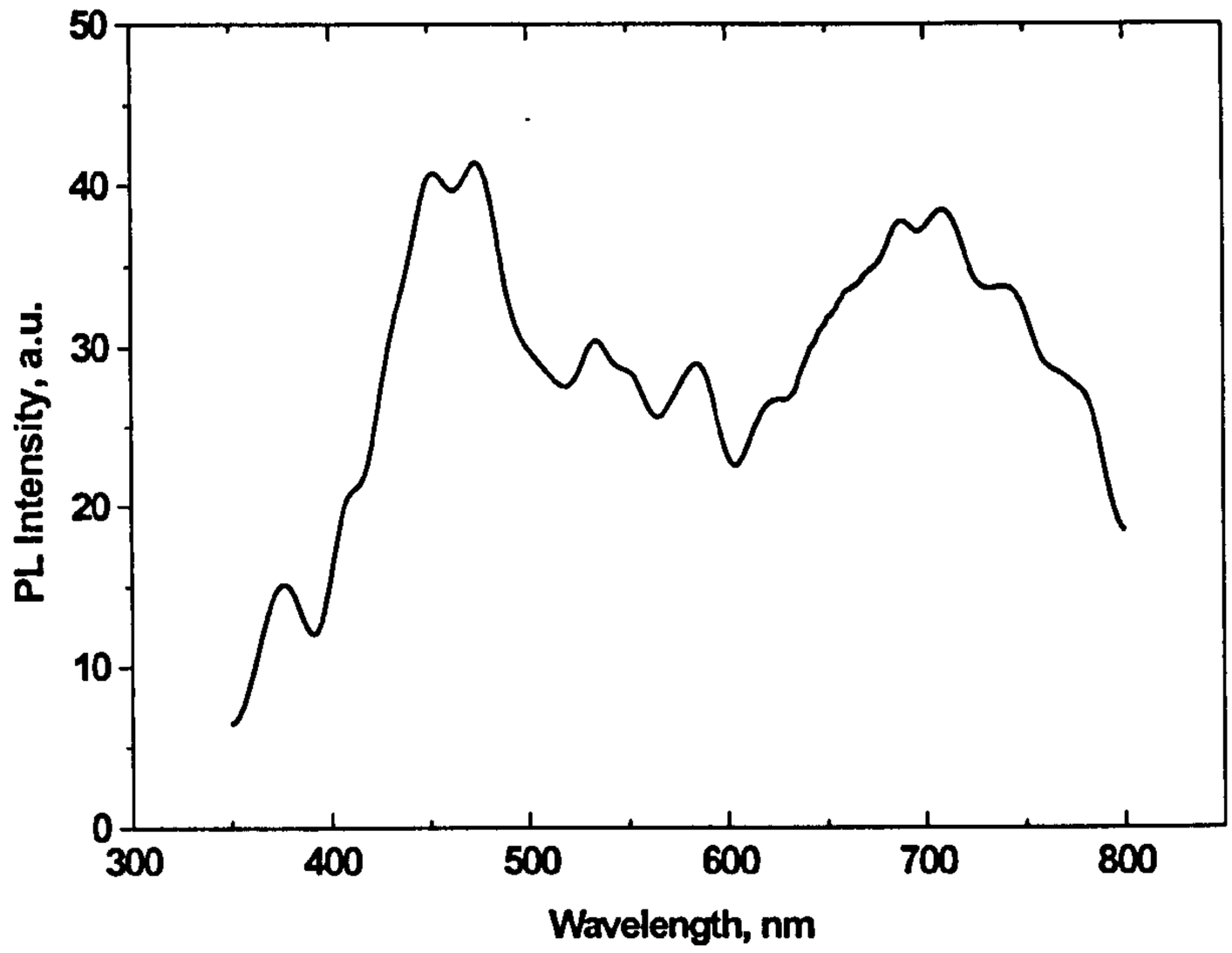

Figure 3.4 A visible PL spectrum recorded from a luminescent centre (possibly due to contaminants) on an anodically-etched Ge layer (j = 450 mA cm^{-2}, t = 7 min, and 15 min chemical etching in solution).

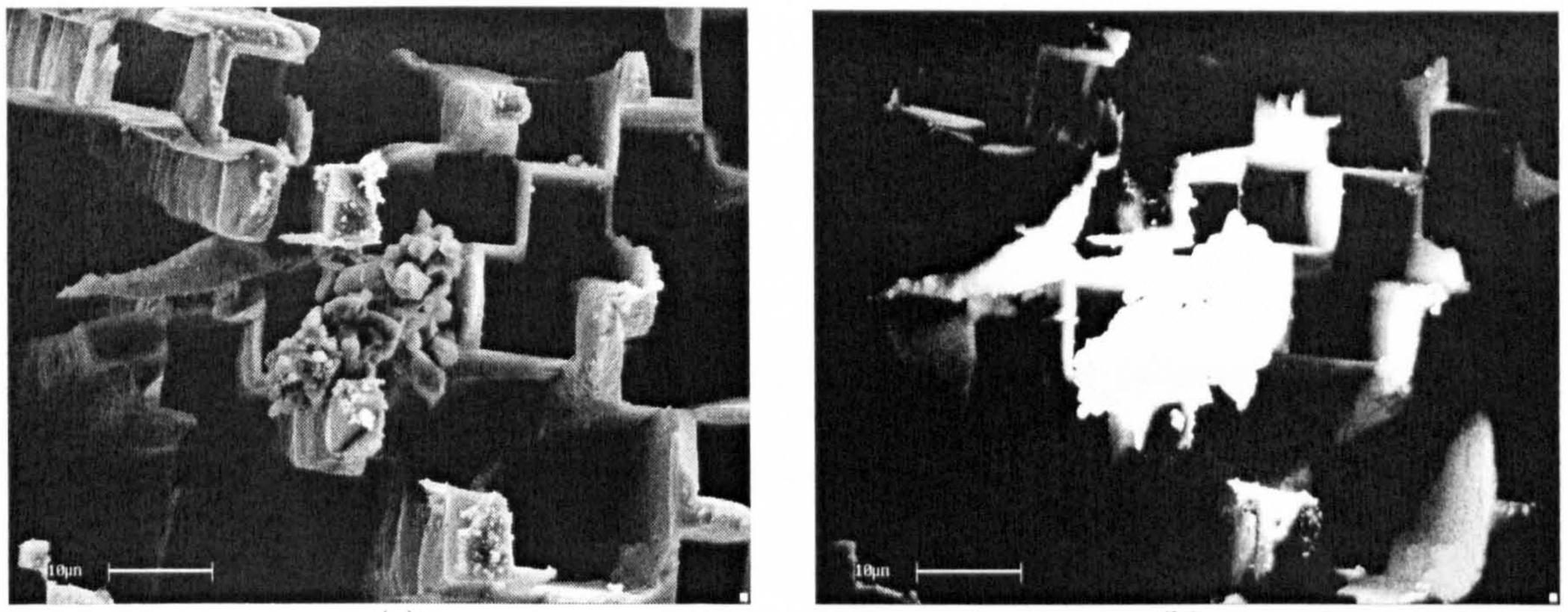

(a) (b)

Figure 3.5 (**a**) An SEM image of an anodically-etched Ge showing the formation of macropores as well as an contaminant object adsorbed by the surface (near the centre). (**b**) Strong CL emission from the surface involving the contaminant object. (Internal scales denote 10 μm).

On the other hand, reliable and reproducible results were obtained from visible PL stain-etched Ge samples (see the introduction). Therefore, we terminated our research with anodisation at this point.

3.2.2 Stain-Etching

Chemically-etched Ge samples were prepared by stain-etching n-type Ge (111) wafers with resistivity 4.6 Ω cm. Type I-SG was prepared in a solution of H_2O_2:HF at 50:1 volume ratio under 250 W tungsten lamp illumination. Type II-SG was prepared in $HF:H_3PO_4:H_2O_2$ at 34:17:1 volume ratio for 3 hours under room light. For Type I, ~ 1.5 cm x 1.5 cm pieces of Ge wafer were treated for 5-10 min in solution and dried in air. This was repeated several times (as described [26]) and resulted in a white layer with some colorful patches on the surface. The white layer was mechanically unstable and was easily removed when scraped or the samples were washed in hot water, leading to PL

quenching. An unstable white layer has also been reported in anodically-etched [24] and stain-etched [26] Ge, as well as in oxidised a-Ge:H (hydrogenated amorphous Ge) prepared using plasma enhanced chemical vapor deposition (PECVD) [35].

Removal of the white layer with washing in water and the subsequent PL quenching has also been reported previously [26,35]. Chen *et al.* [35] argued that the white layer was oxidised Ge, as GeO_x is soluble in water. Here we use XANES, Raman, FTIR and EDX to characterise the composition of the samples.

3.2.2.a Annealing

To remove strain and improve crystallinity, some samples of the second group (Type II-SG) were annealed either in an H atmosphere or in air at a relatively low temperature (600 °C) for a period of 30 min.

3.2.3 Characterisation of the Films

3.2.3.a X-ray absorption Near Edge Structure (XANES)

X-ray absorption spectroscopy (XAS) is an atom-specific structural probe, which can be a sensitive probe of the local coordination of atoms. In other words, the local structure of a given type of atom can be examined by this technique. For the studied element, the absorption edge (or the absorption threshold) energy E_o is the energy needed to excite a core level electron, usually from the K-edge, to the vacuum level. In the x-ray absorption spectrum, the absorption edge is characterised by a discontinuous increase in the x-ray

absorption coefficient at an energy E corresponding to the absorption threshold E_o. On the high energy side of the absorption edge region, the x-ray absorption coefficient exhibits small oscillations known as EXAFS (Extended X-ray Absorption Fine Structure) for energies ~ 100 eV beyond the edge and XANES (X-ray Absorption Near-Edge Structure) for energies closer to the edge. The post-edge fine structure of EXAFS or XANES arises not from direct absorption processes, but from what can be viewed as an internal diffraction phenomenon. When a photon of energy slightly higher than threshold is absorbed by an atom a photoelectron is ejected. The photoelectron wave propagates outwards to infinity if the absorbing atom is isolated. However, if some other atoms surround the absorbing atom, the outgoing photoelectron wave will be back-scattered (diffracted) and back-scattered waves will interfere with the outgoing waves.

X-ray absorption spectroscopy (XAS) was used as an atom-specific structural probe to obtain information on the local coordination of atoms in the chemically-etched Ge layers. The near-edge structure (XANES) is the x-ray absorption up to ~ 50 eV above the particular absorption edge. Germanium K-edge Total Electron Yield XANES data (TEY-XANES) for Type I- and Type II-SG, and transmission-XANES data for crystalline GeO_2 powder, were collected on beamline 9.2 at CCLRC Daresbury Laboratory (DL), using a water-cooled, harmonic rejecting double-crystal Si (220) monochromator. A detailed description of station 9.2 is available on the DL website [36].

3.2.3.b Raman

Raman measurements were carried out in back-scattering configuration either with a Renishaw RM series Raman microscope (shown in Fig. 3.1), using a 514.5 nm Ar^+ laser

excitation source (for Type I-SG samples, c-Ge and commercial GeO_2 crystalline powder), or a Jobin-Yvon (JY) U1000 monochromator equipped with a 488 nm Ar^+ laser excitation source (for Type II-SG samples). All of the Raman measurements were performed at room temperature.

3.2.3.c PL

For PL measurements on Type I-SG and GeO_2, 120 mW He-Cd 442 nm cw excitation was used with a single-grating SPEX 270M spectrograph and a Hamamatsu R2949 photomultiplier (PMT) tube. PL of Type II-SG samples was taken with the Raman JY system. All of the PL measurements were performed at room temperature.

3.2.3.d SEM

SEM measurements were carried out on Type I-SG samples using a LEICA S430 microscope with a 7.5 keV, 10 pA beam.

3.3 Ge NANOCRYSTALS IN SiO_2

3.3.1 Introduction

To date a number of approaches have been employed to synthesise Ge nanocrystals [19-22][27-32]. One of the techniques for nanocrystal fabrication involves ion-implantation followed by a thermal annealing at high temperatures. This technique is most promising because of the possibility to control the projectile depth profile of the implanted ions and the growth and size of the nanocrystals by simply altering one or more of the preparation parameters such as the ion dose, the kinetic energy of the ions, or the annealing temperature. It is considered that embedding semiconductor nanocrystals into a SiO_2 matrix is quite advantageous for device applications, due to the mechanical and chemical stability of the composite [37]. In addition, SiO_2 is a well-characterised material known to passivate semiconductor surfaces [38] and has widely been used in silicon devices and integrated circuits [39].

In this study we aimed to fabricate luminescent Ge nanocrystals in SiO_2 matrices by ion-implantation and post-annealing techniques. Samples prepared using different doses of Ge ions were characterised before and after annealing using techniques such as SIMS, TEM, PL, and Raman scattering. Preliminary results obtained so far in this investigation will be summarised in this thesis.

3.3.2 Oxide Growth

There are several methods available to grow silicon dioxide such as thermal oxidation, electrolysis, vacuum deposition and plasma oxidation [40]. The basic process involves

sharing of valence electrons between oxygen and silicon, in other words the Si-O bond is covalent. By thermal oxidation, one can produce reproducible and chemically stable films of SiO_2 directly on a Si substrate. The growth is carried out in a reactor typically at temperatures between 900-1200 °C. The chemical reactions describing the thermal oxidation of Si in oxygen (*dry oxidation*) or water steam (*wet oxidation*) are given [40] as

$$Si\ (solid) + O_2 \rightarrow SiO_2\ (solid) \quad (dry\ oxide) \tag{3.2}$$

$$Si\ (solid) + 2H_2O \rightarrow SiO_2\ (solid) + 2H_2 \quad (wet\ oxide). \tag{3.3}$$

In thermal oxidation, oxidation proceeds by the diffusion of the oxidising species through the oxide to the Si-SiO_2 interface, where the oxidation reaction occurs [40]. Thus, during the reaction, as the volume of the oxide expands, the Si-SiO_2 interface moves into the Si. The oxide growth with H_2O is much more rapid (~ 10 times) than with dry oxygen, due to the higher solubility and diffusion rate of H_2O in SiO_2. Although there are growth rate and associated thickness problems with dry oxidation, the quality of the oxide produced is better (for example, it provides a structure which is less porous to impurities).

The SiO_2 films used in this study for the implantation of Ge ions were grown with either dry or wet oxidation of Si. 100 nm thick films were grown using the first method on c-Si substrates, whereas for the growth of thicker films (≥200 nm) the second method was preferred.

3.3.3 Ion-Implantation

Ion-implantation has long been used conventionally for doping semiconductors as an alternative technique to diffusion methods [12]. In ion-implantation, the semiconductor is bombarded with high-speed positively charged ions. The depth of the implanted ion depends strongly on its energy. Most ion-implantation sources operate in the energy region 30-200 keV (or in the 0.2-2.5 MeV high-energy range) [12].

A schematic diagram of a typical ion implanter is shown in Fig. 3.6. Ions from the ion source are accelerated through an analyser magnet in which, due to the field strength, only the ions with the desired mass can pass through the exit slit. This beam is then collimated via the help of quadrupole lenses before being focused on the semiconductor target. Doping uniformity across the target is achieved by the *X* and *Y* scan-plates which scan the ions in the beam in a raster pattern over the whole area of the target.

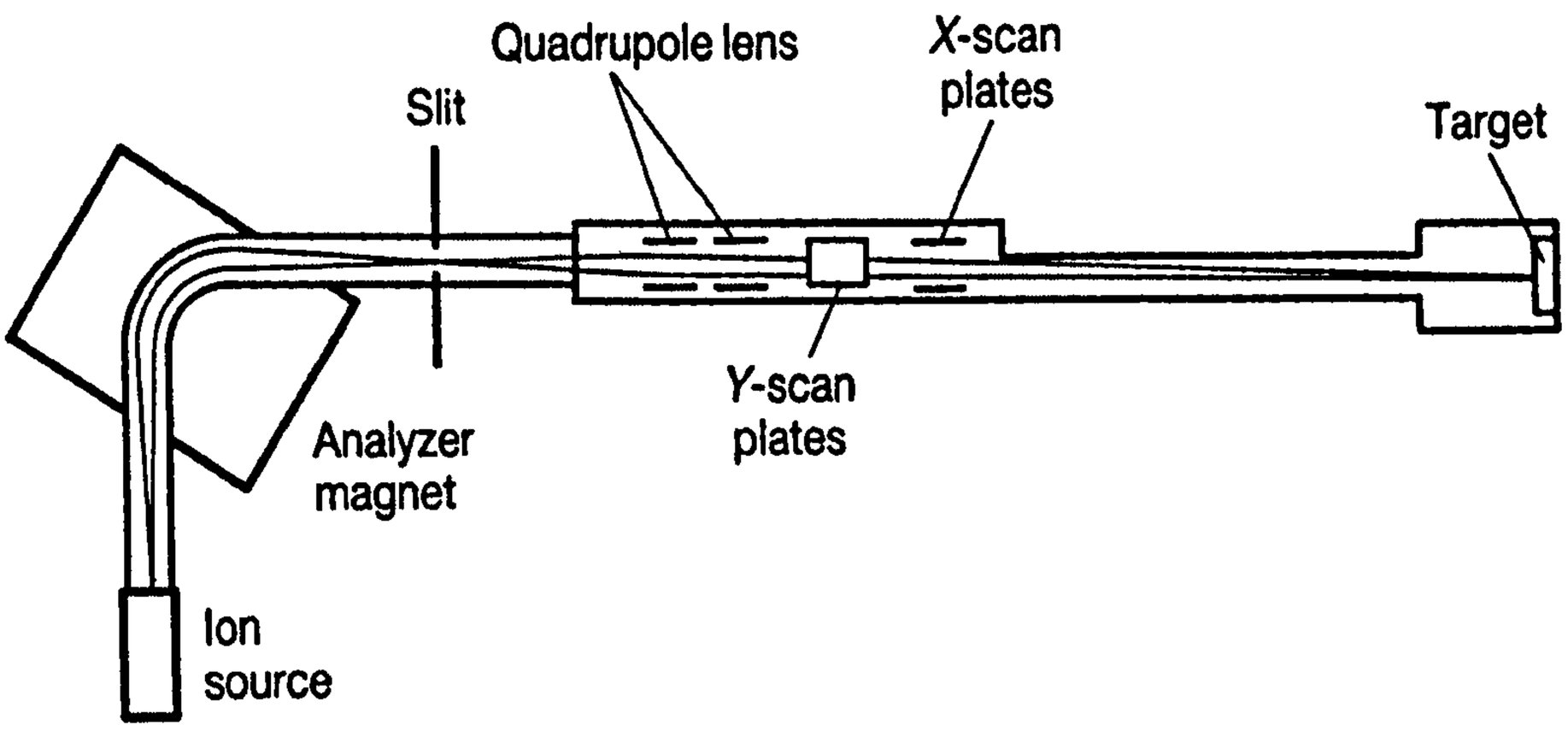

Figure 3.6 Schematic diagram of an ion implanter [12].

When energetic ions reach the target surface, they penetrate the surface and slow down, losing energy mainly via excitation of electrons (or electronic collisions) and nuclear collisions. Figure 3.7 shows a typical path of an ion in a semiconductor. The path is initially straight, but, later, it zigzags until the ion comes to rest. In the first part, an ion loses energy due to electronic collisions, whereas in the latter nuclear collisions dominate. *Ion range* (R) is the total distance travelled by the ion and is usually divided into two components: the distance (R_p) travelled along the axis of incidence and the distance ($R_\perp$) travelled along the axis perpendicular to the axis of incidence. These are known as the *projected range* and the *perpendicular range*, respectively.

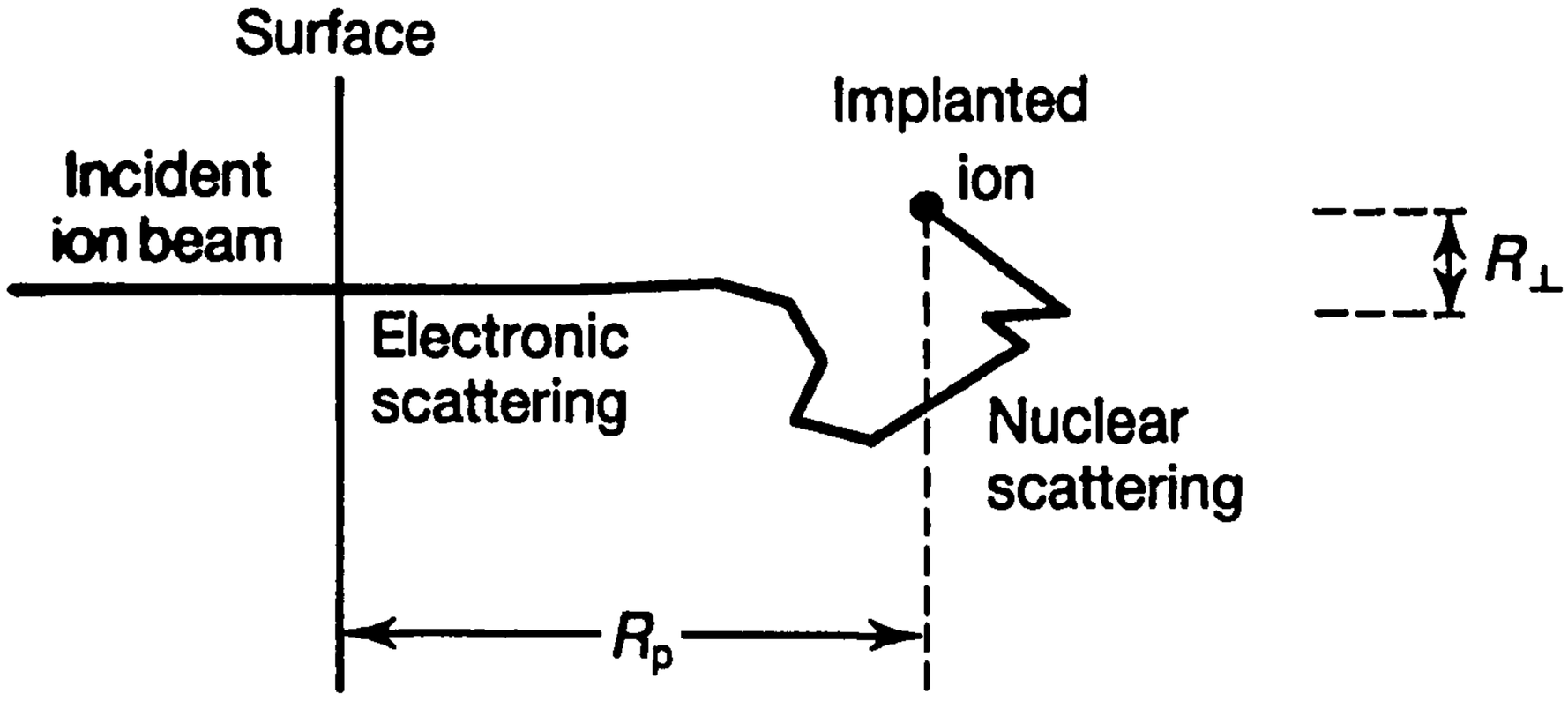

Figure 3.7 The path of an ion in a semiconductor as it loses energy and slows down [12].

Since the number of collisions per unit length and the energy loss per collision are random variables, the ions of the same mass and energy will have a range distribution. For example, the range distributions for amorphous semiconductors are Gaussian

functions. For this function, the concentration of ions n(x) that stop at distance x along the axis of incidence will be given by

$$n(x) = n_0 \cdot \exp\left(\frac{-(x-R_p)^2}{2 \cdot \Delta R_p^{\,2}}\right) \tag{3.4}$$

where n_0 is the peak concentration at $x = R_p$, and ΔR_p is the standard deviation of R_p and known as the *range straggle* [40]. If the total dose is N_{inc}, then the integration of Eq. 3.4 gives an expression for the peak concentration [40]

$$n_0 = \frac{N_{inc}}{\sqrt{2\pi}\,\Delta R_p} \cong \frac{0.4 \cdot N_{inc}}{\Delta R_p} \,. \tag{3.5}$$

Ge ion implantation of the SiO_2 films was performed using a Varian DF4 ion-implanter in the Department of Physics of the Middle East Technical University, Ankara, Turkey. This system had an operating energy range between 0-200 keV and contained 3 diffusion pumps to evaporate into the system. The gas used as the source of Ge ions was GeF_4. Ge ions of doses $7x10^{15}$, $3x10^{16}$ and $1x10^{17}$ cm^{-2} were implanted into 200 nm and 100 nm thick films of SiO_2 at an energy of 100 keV and at room temperature. At this energy, the peak concentration of the implanted ions was lying ~ 70 nm from the surface, as determined by the Ge secondary ion mass spectrometry (SIMS) profiles (see Fig. 3.8).

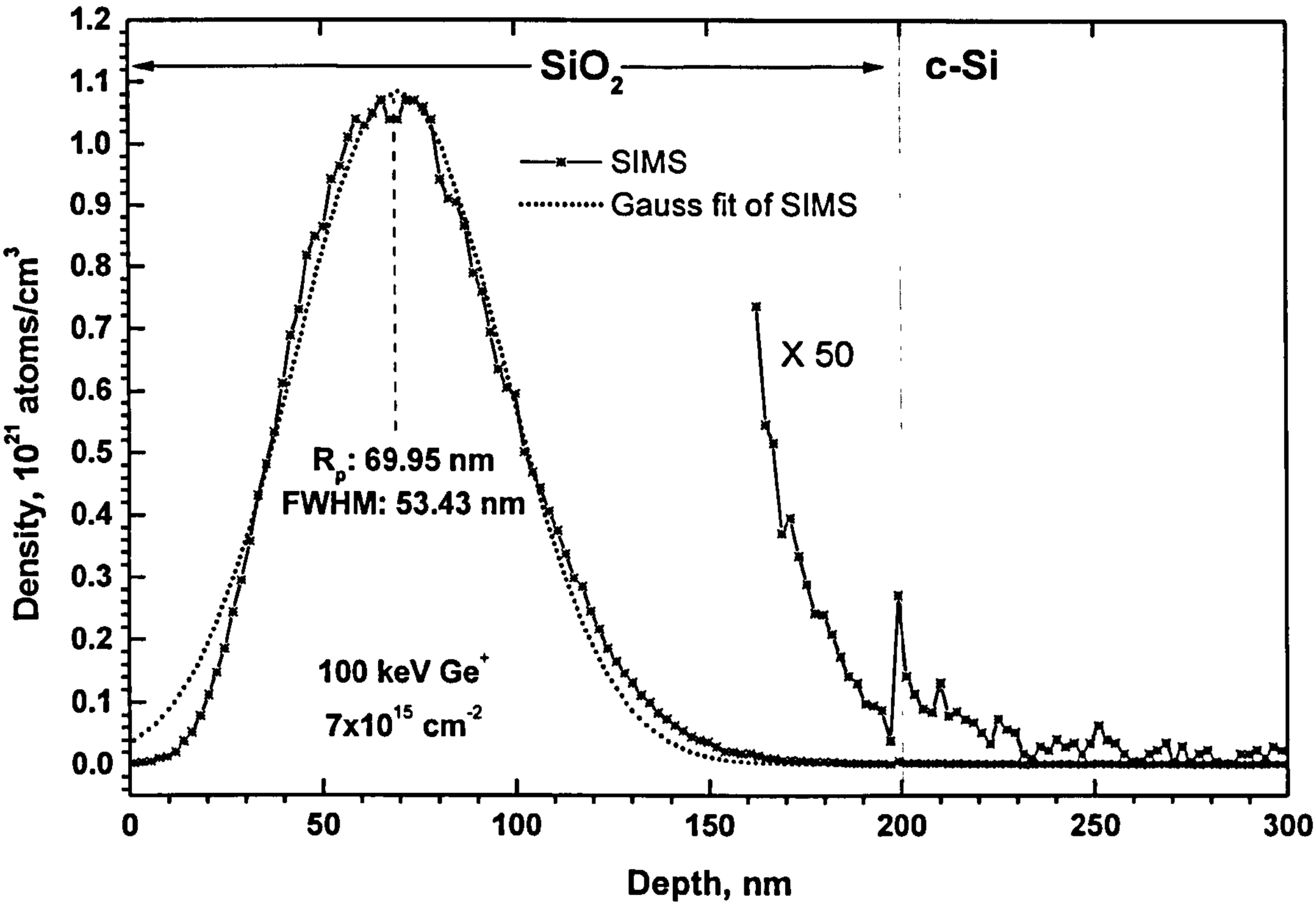

Figure 3.8 SIMS implantation profile of 100 keV Ge^+ in a 200 nm SiO_2 film on Si (line+star). Gaussian fit (short dots) of the curve gives the projected range (R_p) as ~ 70 nm and the full width at half maximum (FWHM) as ~ 53 nm. The enlarged (50X) part of the experimental curve on the right confirms the oxide thickness, i.e. as 200 nm (notice the abrupt stoppage edge of ions at the Si surface).

In Fig. 3.8, by taking the half-width-at-half-maximum (HWHM) of the Gaussian peak, i.e. ~ $27x10^{-7}$ cm, as the range straggle (ΔR_p), and given that the total ion dose is $7x10^{15}$ cm^{-2}, we can calculate the peak concentration (n_0) as $1.05x10^{21}$ ions cm^{-3}. This value is in good agreement with the experimental value of $1.09x10^{21}$ ions cm^{-3}. Further, using the calculated value of n_0 and by taking the R_p as 70 nm, the ion concentration can be estimated using Eq. 3.4, for example, at x = 33 nm from the surface as $3.83x10^{20}$ ions cm^{-3}. At this depth, the SIMS data give n(33 nm) = $4.20x10^{20}$ ions cm^{-3}, which is also in good agreement with its corresponding calculated value.

3.3.4 Annealing

Since the binding energy of a lattice site is only 10-20 eV [40], with the energies employed in ion-implantation, enough energy can be transferred to the atoms in the target to displace them and make them travel through the target. Each implanted ion can displace hundreds or thousands of stationary atoms in the target [12] and these newly-generated target atoms with some kinetic energy can cause further displacements in the target. Eventually, an initial crystal structure, for example, can change into a highly-disordered state (i.e. amorphous state) as a result of ion-implantation. Therefore, if implantation is aimed as a doping mechanism for a semiconductor to improve its conductivity, then the ion damage has to be repaired and electrically inactive ions, sitting on interstitial sites, have to be moved on to the lattice sites by an additional process. Annealing (heating) of such a semiconductor at high temperature can overcome these problems. Annealing can restore the crystallinity of the semiconductor and provide sufficient thermal energy for the implanted ions to move on to lattice sites where they become electrically active.

Moreover, if the ion-implantation is performed to synthesise nanocrystals of the implanted impurity (embedded in the target (host) material), rather than to increase the conductivity of the target, again, annealing becomes a necessary step to be taken. Annealing causes a diffusion of the scattered ions through the target as well as repairing the damage in the host lattice. However, annealing also smears out any intended impurity profiles as it causes a re-distribution of the implanted ions.

After Ge^+ implantation we annealed the SiO_2 films in a conventional furnace, in dry N_2 ambient (gas flow rate = 3 l min^{-1}), at temperatures between 700-1050 °C, and for a

period of 45 min or 60 min. Table I provides a specification of the samples prepared and studied in this investigation.

Table I. Preparation conditions for Ge^+ implanted SiO_2 films on Si: |ion energy is 100 keV for all the samples.| |d_{ox}: oxide thickness; T_a: annealing temperature; t_a: annealing time.|

Ion Dose (cm^{-2})	d_{ox} (nm)	T_a (^oC)	t_a (min)	annealing atmosphere
$7x10^{15}$	100	1050	45	N_2
$7x10^{15}$	200	1050	45	N_2
$3x10^{16}$	200	700, 900, 1050	45	N_2
$1x10^{17}$	200	900	45	N_2
$1x10^{17}$	250	800	60	N_2

3.3.5 Characterisation

3.3.5.a Raman

Raman scattering spectra of the films were obtained before and after annealing, in back-scattering configuration with a Renishaw RM series Raman microscope (shown in Fig. 3.1), using a 514.5 nm Ar^+ laser excitation source. All of the measurements were carried out at room temperature, using a total laser power of either 4 or 0.4 mW (on the sample). The beam diameter was 1 μm on the sample surface and scattered light was collected with a CCD camera on the head of the microscope. The spectral resolution was 1 cm^{-1}.

3.3.5.b PL

PL measurements were carried out in the visible region at room temperature (300 K) for the as-implanted and annealed films. The spectra were excited using the 488 nm line of an Ar^+ laser and recorded using a photomultiplier tube. Whereas a liquid-nitrogen cooled Ge photodiode was used to collect the PL in the near IR region from the samples implanted with dose of $7x10^{15}$ cm^{-2} at 300 K and 100 K in a temperature-controlled He cryostat.

3.3.5.c SIMS

When an energetic ion beam is incident on a semiconductor, atoms near the surface may receive enough energy to be ejected (sputtered) from the surface. A small fraction of the sputtered species will be ionised. This process is known as *secondary ion emission* and secondary ion mass spectrometry (SIMS) is based upon the detection of these ions. In SIMS, ions are analysed using a mass spectrometer. In today's SIMS systems, the sputtering is usually performed in an argon [40] or oxygen [41] plasma so that the ionisation of the neutral particles can be accomplished after ejection, thus minimising the matrix effects and increasing the uniformity of the sensitivity for various species.

SIMS has various applications such as dopant and impurity depth profiling, surface analysis, and microanalysis. During the SIMS analysis the sample surface is slowly sputtered away. Continuous analysis produces information as a function of depth (depth profile), known as *dynamic* sputtering. *Static* sputtering uses extremely low ion current and energy and it is usually used to obtain information from nearly undisturbed surface

monolayers [12]. Focusing the primary ion beam to a diameter on a scale of a micron [41] on the surface allows the microanalysis of a sample.

In dynamic SIMS, a focused ion beam is raster-scanned over an area greater than approximately 5 times its diameter [12]. This results in a crater with a flat bottom, revealing successive layers of the sample. The intensity of the sputtered ions is measured first as a function of the sputtering time. Using a profilometer the depth of the crater is determined and then the time axis is converted into depth. Secondary ions are extracted from the sample as they are produced, and monitoring the count rates of the secondary ions of selected elements as a function of depth leads to depth profiles.

A Physical Electronic, Inc. quadrupole SIMS system was used to study the implant and diffusion profiles of the samples respectively before and after annealing. Depth resolution of the system was better than 2 nm at depths less than 1 μm. An energetic primary ion beam is used to sputter atoms from the sample surface. Secondary ions were mass analysed and detected in a quadrupole mass spectrometer [41].

3.3.5.d TEM

In TEM, the wavelike behaviour of an electron is exploited to form an image of a sample of the atomic scale. Basically, the sample is 'irradiated' by accelerated electrons which pass through it to form an image. The sample itself has to be very thin (around 100 nm [12]) so that most of the electrons can pass through it without significant inelastic scattering. Typically, a heated tungsten filament is employed as the source of electrons. The generated electron beam is biased at a voltage as high as hundreds of keV and

accelerated through a condenser lens on to the specimen. The scattered and unscattered electrons from the sample are collected by an objective lens which forms a diffraction pattern and an intermediate image of the object, respectively, in the back focal plane and the image plane. The image produced by the objective lens then can be magnified by intermediate and projector lenses and projected on a screen. Variations in the atomic composition or the thickness of the specimen cause changes in the electron scattering from the main beam. Furthermore, if the sample has a crystalline character then strong Bragg diffraction of the beam will occur in specific directions which can be observed in the electron diffraction patterns.

Transmission electron microscopy (TEM) was performed on a number of samples at 200 keV to observe the Ge nanocrystalline precipitates in the SiO_2 by using a Philips 200 kV system.

3.4 SPARK-PROCESSED Ge

3.4.1 Introduction

Although there has been little work done so far on the visible light emitting Ge nanostructures (in comparison to Si), it has been observed mainly in low dimensional Ge nanocrystals embedded in SiO_2 matrices that they exhibit typical broad PL bands in the visible at 2.1-2.4 eV [20][21], 3 eV [22], and 1.8 eV [38] (see also Chapter 2). Spark-processing has been demonstrated to be one of the methods capable of producing semiconductor nanocrystals. Spark-processed substances are expected to contain nanocrystals (of the substrate material) varying in diameter between 2-10 nm [24], as it was shown for the case of spark processed Si (sp-Si) [42].

In recent years, visible PL from spark-processed Ge (sp-Ge) has also been reported. At room temperature the main PL peak of sp-Ge is typically located at 2.3 eV (520 nm) with two shoulder peaks at around 3.0 and 2.0 eV (410 and 610 nm) [43], as shown in Fig. 3.9. The shoulders at room temperature develop into pronounced peaks at lower temperatures (without any shift in PL position [43]), while the central peak gradually diminishes.

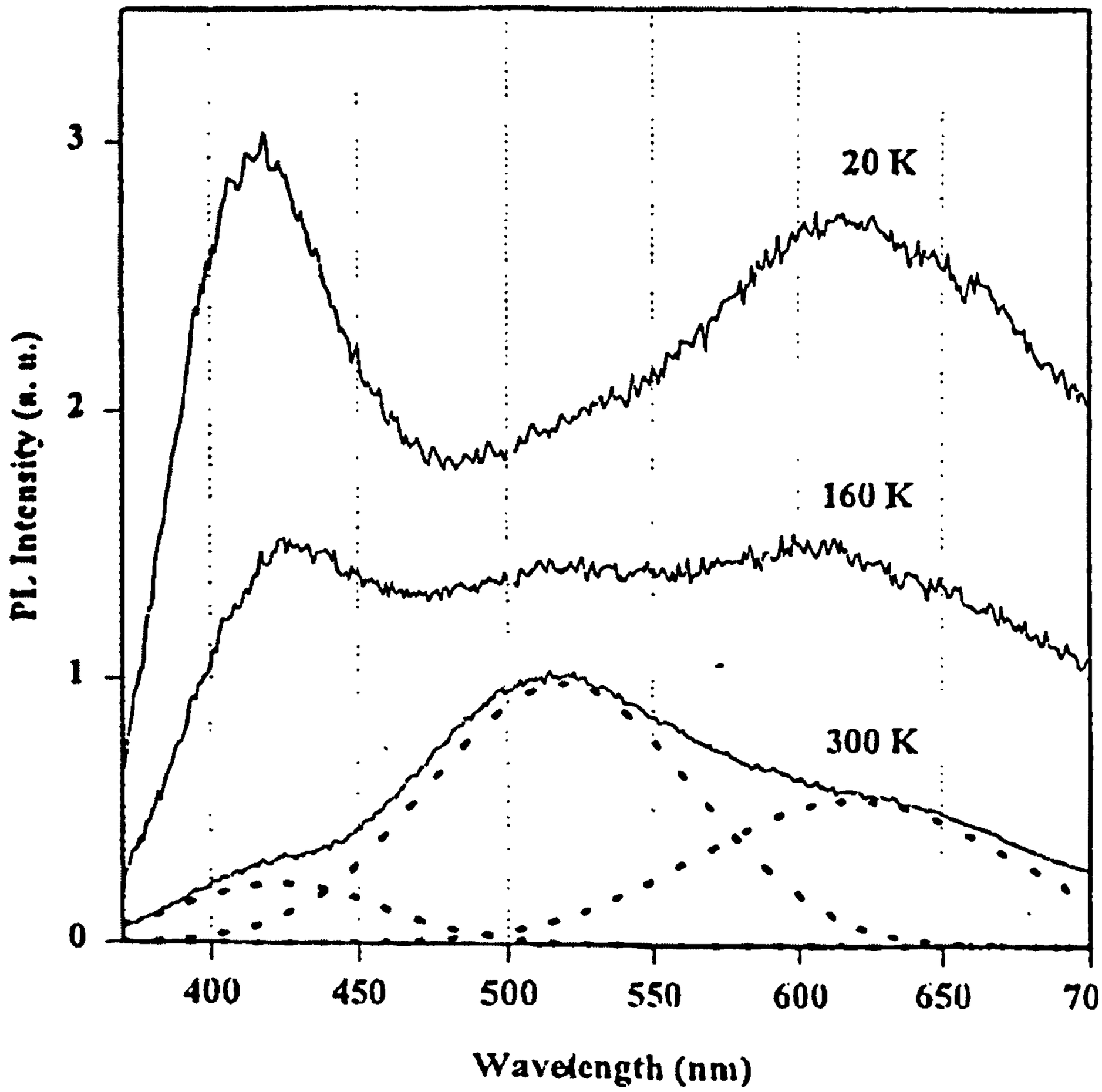

Figure 3.9 PL spectra of sp-Ge at some selected temperatures (300, 160 and 20 K) [43].

However, the origins of PL from sp-Ge are still under discussion. In particular, the debate is as to whether all or any of these PL bands originate due to defects in germanium oxides or nanocrystals, or involve both [43][44]. In addition, the microstructure of sp-Ge has not been studied in detail to date: specifically, no direct link has been made yet between the Ge nanocrystals (or any other chemical species in the films) and the visible PL.

In this study we aimed to investigate the microstructure of visible PL sp-Ge using high-resolution micro-Raman spectroscopy. Specifically, the local chemical compositions, presence of Ge nanocrystals, surface contaminants (such as C) and their contributions to the PL spectra were determined using the simultaneously recorded micro-Raman and micro-PL spectra. Using cross-sectional SEM micrographs the thickness and micro-images of the films were obtained.

3.4.2 Spark Processing

The spark processing was conducted by using an unidirectional pulsed 15 kV source between a tip-shaped tungsten electrode (anode) and undoped c-Ge wafers (cathode). Sparking was performed in stagnant air for 20 min and the repetition frequency and the pulse duration were 16.7 kHz and 10 ns, respectively, as reported earlier in Fig. 3.9 [43]. This generated a greyish-looking, circular-patterned film with a relatively small diameter of about 2-3 mm, which was surrounded by a light brown halo. As the dimension of the films was small several samples were produced under the same conditions described above to examine the consistency of the PL and Raman spectra.

3.4.3 Characterisation

3.4.3.a PL

PL measurements of the sp-Ge samples were carried out at room temperature using the 325 nm line of a He-Cd laser. The detection system consisted of a 0.33 m (focal length) single grating monochromator and a cooled GaAs photomultiplier. The spectra obtained

from the (3) films produced under same conditions were similar to each other and to that room temperature PL in Fig. 3.9 but slightly differed in PL peak energies.

3.4.3.b Micro - Raman & PL

Micro-Raman scattering spectra of the same samples were obtained in back-scattering configuration with a Renishaw RM series Raman microscope (see Fig. 3.1). Spectra were excited with a 514.5 nm Ar^+ laser source at room temperature, using a total laser power of either 4 or 0.4 mW (on the sample). The spectral resolution was 1 cm^{-1}. The beam diameter was 1 μm on the sample surface and scattered light was collected with a CCD camera on the head of the microscope. Micro-optical images of the sample surface enabled positioning of the laser spot on the desired area of the sample.

Micro-Raman spectra of the samples were obtained along with their luminescence backgrounds, i.e. with the micro-PL spectra. The energy range studied with these micro-PL spectra corresponded to the orange band of the visible PL seen in Fig. 3.9. Measurements taken at different spots on each single film were used to check the structural and compositional uniformity (or any non-uniformity) as well as the consistency of the micro-PL spectra across the films or between the films. As the earlier XPS and FTIR data of Chang *et al.* [24][43] indicated the existence of GeO_xs in sp-Ge, we also obtained the Raman spectrum of a commercial c-GeO_2 powder sample in order to compare with those of sp-Ge. The Raman spectrum of bulk Ge was taken from the untreated part of a sample (i.e. on clean substrate) as reference. Spark-processed Ge Raman spectra, however, showed discrepancies in terms of the local microstructure between samples and (even) across a single film.

3.4.3.c SEM

Cross-sectional micro-images of the samples were obtained using a LEO 1530VP field emission gun scanning electron microscope (FEGSEM). The resolution of this system was 2.1 nm at 1 keV accelerating voltage.

3.5 REFERENCES

[1] G. Abstreiter, *Light Emission from Silicon: From Physics to Devices (Editor D.J.Lockwood), Semiconductors and Semimetals*, Vol. 49, Academic Press, San Diego, p.38,39 (1998).

[2] T.P. Pearsall, *Prog. Quant. Opt.*, **18**, 97 (1994).

[3] L.T. Canham, *Appl. Phys. Lett.*, **57**, 1046 (1990).

[4] S. Gardelis, J.S. Rimmer, P. Dawson, B. Hamilton, R.A. Kubiak, T.E. Whall and E.H.C. Parker, *Appl. Phys. Lett.*, **59(17)**, 2118 (1991).

[5] M. Schoisswohl, J.L. Cantin, M. Chamarro, H.J. von Bardeleben, T. Morgenstern, E. Bugiel, W. Kissinger and R.C. Andreu, *Thin Solid Films*, **276**, 92 (1996).

[6] A. Ksendzov, R.W. Fathauer, T. George, W.T. Pike, R.P. Vasquez and A.P. Taylor, *Appl. Phys. Lett.*, **63(2)**, 200 (1993).

[7] A.F. Vyatkin, J. Linnross, N.Lalic and M. Rosler, *Phys. Low-Dim. Struct.*, **5/6**, 89 (1997).

[8] M. Schoisswohl, J.L. Cantin, M. Chamarro, H.J. von Bardeleben, T. Morgenstern, E. Bugiel, W. Kissinger and R.C. Andreu, *Phys. Rev. B*, **52(16)**, 11898 (1995).

[9] B. Unal, M. Parkinson, S.C. Bayliss, T. Naylor and D. Schröder, *J. Porous Mat.*, **7**, 143 (2000).

[10] A. Bsiesy, J.C. Vial, F. Gaspard, R. Herino, M. Ligeon, F. Muller, R. Romenstain, A. Wasiela, A. Halimaou and G. Bomchil, *Surf. Sci.*, **254**, 195 (1991).

[11] S. Takeoka, K. Toshikiyo, M. Fujii, S. Hayashi and K. Yamamoto, *Phys. Rev. B*, **61(23)**, 15988 (2000).

[12] T. E. Jenkins, *Semiconductor Science*, Prentice-Hall (1995).

[13] Dr. Dave Lowe at the National Physical Laboratory (NPL) performed and analysed the X-ray rocking curve measurements on starting $Si_{1-x}Ge_x$ alloy layers and provided us with x=13±1 and thickness ≈ 1050 nm as for the Ge content and the alloy layer thickness, respectively.

[14] K. Inoue, O. Matsuda, K. Maehashi, H. Nakashima and K. Murase, *Jpn. J. Appl. Phys.*, **31(2), No. 8A**, L997 (1992).

[15] H. Richter, Z.P. Wang, and L. Ley, *Solid State Commun.*, **39**, 625 (1981).

[16] I.H. Campbell and P.M. Fauchet, *Solid State Commun.*, **58**, 739 (1986).

[17] Y. Ekinci, *M. Phil thesis*, De Montfort University (2000).

[18] M. Fujii, S. Hayashi, and K. Yamamoto, *Appl. Phys. Lett.*, **57(25)**, 2692 (1990); M. Fujii, S. Hayashi, and K. Yamamoto, *Jpn. J. Appl. Phys.*, **30(4)**, 687 (1991).

[19] Y. Maeda, N. Tsukamoto, Y. Yazawa, Y. Kanemitsu, and Masumoto, *Appl. Phys. Lett.*, **59**, 3168 (1991).

[20] Y. Kanemitsu, H. Uto, Y. Masumoto, and Y. Maeda, *Appl. Phys. Lett.*, **61**, 2187 (1992).

[21] Y. Maeda, *Phys. Rev. B*, **51(3)**,1658 (1995).

[22] M. Zacharias, and P.M. Fauchet, *Appl. Phys.Lett.*, **71(3)**, 380 (1997); M. Zacharias, and P.M. Fauchet, *J. Non-Cryst. Solids*, **227-230**, 1058 (1998).

[23] S. Miyazaki, K. Sakamoto, K. Shiba, and M. Hirose, *Thin Solid Films*, **255**, 99 (1995).

[24] S.S. Chang, and R.E. Hummel, *J. Lumin.*, **86**, 33 (2000).

[25] S. Bayliss, Q. Zhang, and P.Harris, *Appl. Surf. Sci.*, **102**, 390 (1996).

[26] M. Sendova-Vassileva, N. Tzenov, D. Dimova-Malinovska, M. Rosenbauer, M. Stutzman, K.V. Josepovits, *Thin Solid Films*, **255**, 282 (1995).

[27] D.C. Paine, C. Caragianis, T.Y. Kim, Y. Shigesato, and T. Ishakara, *Appl. Phys. Lett.*, **62**, 2842 (1993).

[28] (a) M. Nogami, and Y. Abe, *Appl. Phys. Lett.*, **65**, 2545 (1994); (b) A. Saito, and T. Suemoto, *Phys. Rev. B*, **56(4)**, R1688 (1997).

[29] V. Craciun, C.B. Leborgne, E.J. Nicholls, and I.W. Boyd, *Appl. Phys. Lett.*, **69**, 1506 (1996).

[30] M. Zacharias, R. Weigand, J. Blasing, and J. Christen, EMRS Proceedings, **452**, 117 (1997).

[31] S. Okamoto, and Y. Kanemitsu, *Phys. Rev. B*, **54**, 16421 (1996).

[32] W.K. Choi, S. Kanakaraju, Z.X. Shen, and W.S. Li, *Appl. Surf. Sci.*, **144-145**, 697 (1999).

[33] V.A. Karavanskii, A.A. Lomov, V.A. Bushuev, N.N. Loikho, N.N. Melnik, T.N. Zavaritskaya, G. Kartopu, S.C. Bayliss, and A.V. Sapelkin, *to be submitted.*

[34] L. Pavesi and V. Mulloni, *Societa Italiana di Fisica, Proceedings of the ISP-Course CXLI*, 87, IOS Press (1999).

[35] J.H.Chen, D.Pang, P. Wickboldt, H.M. Cheong, W. Paul, *J. Non-Cryst. Solids*, **198-200**, 128 (1996).

[36] web site: http://srs.dl.ac.uk/xrs/index.html.

[37] Y.H.Ye, J.Y. Zhang, X.M. Bao, X.L. Tan, and L.F. Chen, *Appl. Phys. A*, **67**, 213 (1998).

[38] K.S. Min, K.V. Shcheglov, C.M. Yang, H.A. Atwater, M.L. Brongersma, and A. Polman, *Appl. Phys. Lett.*, **68(18)**, 2511 (1996).

[39] X.L. Wu, T. Gao, X.M. Bao, F. Yan, S.S. Jiang, and D. Feng, *J. Appl. Phys.*, **82(5)**, 2704 (1997), and references 1 and 2 therein.

[40] S.M. Sze, *VLSI Technology*, 2nd Ed., McGraw-Hill Book Company, (1988).

[41] web site: www.eaglabs.com

[42] R.E. Hummel, M.H. Ludwig, *J. Lumin.*, **68**, 69 (1996).

[43] S.S. Chang, and R.E. Hummel, *Mat. Sci. Eng. B*, **76**, 237 (2000).

[44] M.H. Ludwig, R.E. Hummel, and S.S. Chang, *J. Vac. Sci.Technol. B*, **12(5)**, 3023 (1994).

CHAPTER 4. RESULTS AND DISCUSSIONS

4.1 POROUS $Si_{1-x}Ge_x$

4.1.1 Micro-Raman

Raman spectra of the starting c-$Si_{0.87}Ge_{0.13}$ alloy epilayer and of three porous SiGe samples, prepared at the same current density but for different etch times, are given in Fig. 4.1. Optical phonons related to Si-Si vibrations dominate all the spectra as they are responsible for the major peaks located at around 510 cm^{-1}. The corresponding band maximum of the starting alloy occurs at 513.1 cm^{-1} and it has a linewidth (FWHM) of 4.9 cm^{-1}. In the case of pure Si crystal, the Si optic mode peak is at 520 cm^{-1} with a typical linewidth of ~ 5 cm^{-1} [1]. The downshift of the Si-Si peak frequency in bulk $Si_{1-x}Ge_x$ alloys, with respect to c-Si, is explained in the literature as the effect of alloying and sensitivity to the strain in these layers [2,3]. In $Si_{1-x}Ge_x$ alloys, within the neighborhood of larger mass Ge atom, the force constant of the Si-Si bonds decreases and so the optic phonon band of pure Si shifts from 520 cm^{-1} to lower frequencies for $Si_{1-x}Ge_x$ ($x \neq 0$). It is also known that the position of the Si-Si Raman peak is indicative of the composition of $Si_{1-x}Ge_x$ alloys (either bulk [3,4] or nanostructured [5]), as the shift in its frequency is linear with the fractional Ge content x (see below).

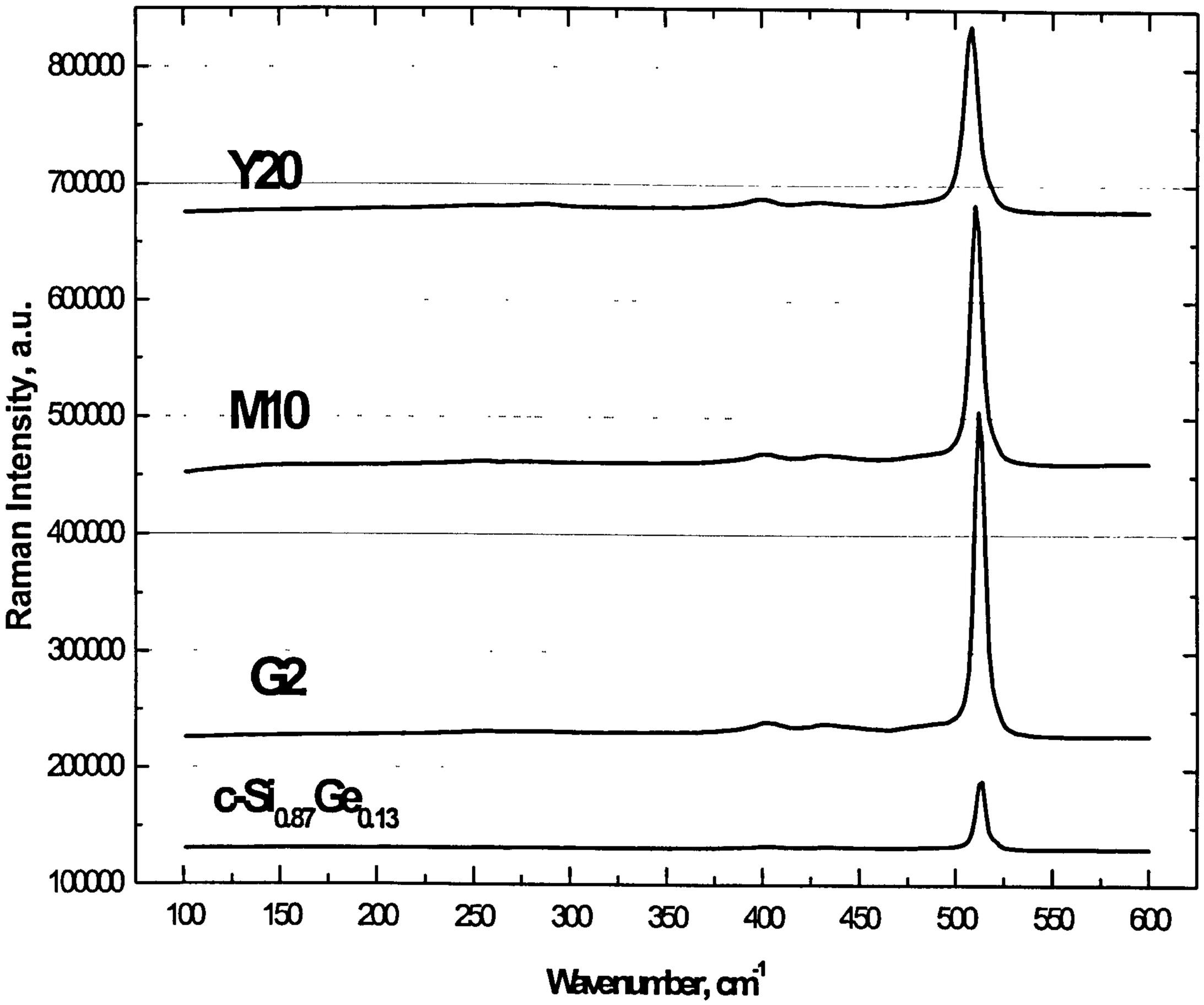

Figure 4.1 Raman spectra of c-SiGe epilayer and 3 counterpart porous SiGe samples. Emission is much more intense for porous samples than for the unetched epilayer, and it decreases with increasing porosity. (The etching time was 2, 10 and 20 minutes for sample G2, M10 and Y20, respectively, at a fixed current density 22 mA cm^{-2}.)

From Fig. 4.1 it is also seen that the Raman intensity from the bulk alloy is approximately 5 times weaker than from porous SiGe samples. A 10 times stronger Raman intensity is observed from porous Si than crystalline Si by Tsu *et al.*, and they attributed this discrepancy to the surface enhancement or resonance effect [6].

Two other fundamental vibrations are observed in Raman spectra of $Si_{1-x}Ge_x$ alloys at ~ 300 cm^{-1} and ~ 400 cm^{-1} due to Ge-Ge and Si-Ge optic phonon modes, respectively [3,7]. There are also other weaker Raman features which have been observed for different compositions of $Si_{1-x}Ge_x$ alloys, though differently prepared, such as in the bulk or in superlattices [3,8]. Figure 4.2, which is a re-plot of the Fig. 4.1 between 200 and 470 cm^{-1}, shows the detail of the weaker features present in our spectra (spectrum of bulk alloy is multiplied by a factor of 5 for the same purpose and to compare quantitatively with the other spectra). As for the present spectra, beside the Ge-Ge (~ 290 cm^{-1}) and Si-Ge (~ 400 cm^{-1}) optic modes, we spot two other extra peaks at ~ 250 cm^{-1} and ~ 430 cm^{-1}, those are generally observed in $Si_{1-x}Ge_x$ alloys with low Ge concentration [3,8,9]. Timbrell *et al.* attributed these two peaks (also seen in their Raman spectra of $Si_{0.82}Ge_{0.18}$ alloys) to vibrational modes of a particular kind of Si-Ge ordering in the alloy [8]. We have therefore assigned these Raman peaks to Si-Ge vibrations as labelled in Fig. 4.2.

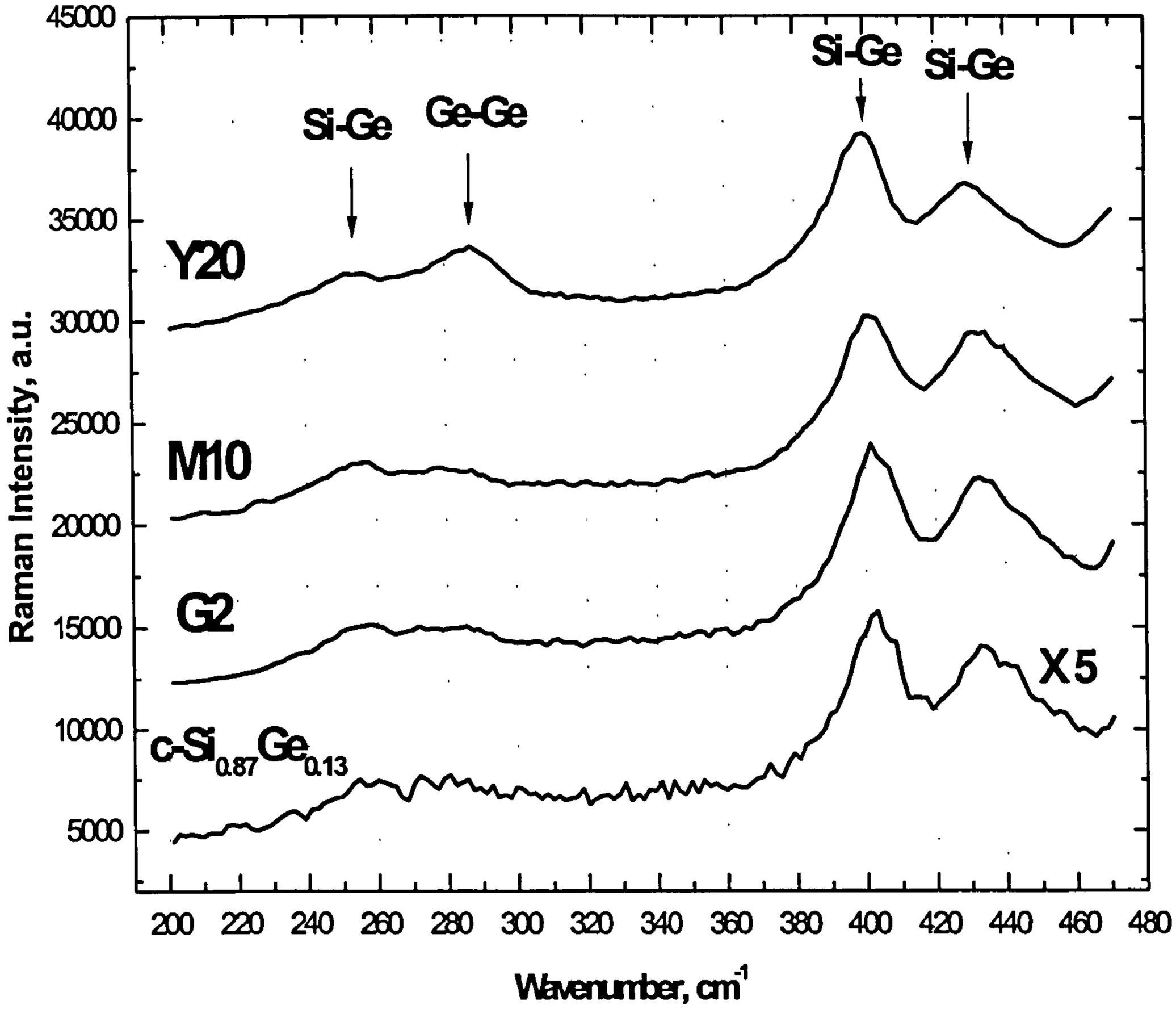

Figure 4.2 Details of the weaker features in Raman spectra of Fig. 4.1. Spectrum of the bulk epilayer is multiplied by a factor of 5 for clarity. Peaks are labelled with assigned vibrations.

All the peak data of the present spectra are given in Table I for the bulk and three porous SiGe samples. The Si-Si peak data (linewidth and peak center) were obtained by a simple lorentzian fitting procedure to the Raman peaks. As can be inferred from the data in Table I, there is an increasing tendency for all the peaks (except the Ge-Ge peak) to shift towards lower frequencies with etch time (or porosity). For example, one of the Si-Ge peaks (at ~ 430 cm^{-1}) shifts by ~ 0.7 cm^{-1}, ~ 1.5 cm^{-1} and ~ 5.3 cm^{-1} to lower frequency respectively for porous samples G2, M10 and Y20 from the peak value of the unetched

alloy (435.05 cm^{-1}). Similar shift values are noticed for the other Si-Ge peaks and the Si-Si peak for increasing porosity. We also note that there is an increase in both intensity and the energy of the Ge-Ge vibration as the etch time increases to 20 min (corresponding peak maxima for sample M10 and Y20 are 277.27 cm^{-1} and 285.83 cm^{-1}, respectively).

Table I. Raman peak data of bulk (c-$Si_{0.87}Ge_{0.13}$) and porous SiGe (samples G2, M10 and Y20). Peak centers and widths are in units of cm^{-1}; etching times for the porous samples are given in brackets. (Spectral resolution = 1cm^{-1}.)

Sample	Si-Si		Si-Ge (~430 cm^{-1}) Center	Si-Ge (~400 cm^{-1}) Center	Si-Ge (~250 cm^{-1}) Center	Ge-Ge Center
	Center	Width				
c-$Si_{0.87}Ge_{0.13}$	513.07	4.92	435.05	402.52	258.06	-
G2 (2 min)	512.62	5.72	434.37	402.91	257.47	278.60
M10 (10 min)	510.85	6.33	433.57	401.98	255.68	277.27
Y20 (20 min)	508.23	8.02	429.76	398.91	254.63	285.83

4.1.1.a Discussion

It might be suggested that the general shift of the Raman peaks in the low frequency direction is due to a progressive change in the film composition with porosity. For the bulk $Si_{1-x}Ge_x$ alloys, an increase in the Ge content results in the shift of the Si-Si peak to lower frequency, and a reduction of its intensity relative to those of Si-Ge and Ge-Ge optic phonon bands [3,5,7]. The linear relationship between the fractional Ge content, x,

and the Si-Si peak position for unstrained (relaxed) $Si_{1-x}Ge_x$ alloys is described in the literature (for example [2-4]) usually as

$$\Omega(x) = 520.0 - 68 * x \tag{4.1}$$

where $\Omega(x)$ represents composition dependent phonon energy, in units of cm^{-1} [2]. For pure Si (x = 0), the frequency is 520 cm^{-1}. If we assume that all the porous SiGe samples are in the fully relaxed state, as well as the initial bulk alloy, according to the linear equation above our bulk alloy and porous SiGe samples G2, M10 and Y20 should contain approximately 11%, 12% 14% and 18% Ge, respectively. Thus, it can be suggested that the Ge content (x) increases with porosity and this increase can be as large as 7% (for sample Y20) relative to the bulk alloy value. However, this picture does not seem quite realistic when we carefully examine the Raman peak lineshapes in comparison with the Raman studies on bulk $Si_{1-x}Ge_x$ alloys and Si nanocrystals. Modifications to the bulk Raman spectral line is expected when particle size (of the same material) is finite.

Figure 4.3.a illustrates the detail of the Si-Si peak for bulk and porous SiGe. The peak linewidth increases and its frequency downshifts progressively with porosity (see Tables I and II). Such an effect, however, is not amongst the observed consequences of compositional variation of $Si_{1-x}Ge_x$ alloys. Holtz *et al.* studied the composition dependence of the Raman spectra for their MBE-grown $Si_{1-x}Ge_x$ alloys and reported that the linewidth of the Si-Si optic band did not change with alloy composition (for $0 \leq x \leq 0.22$) [2]. On the other hand, the phonon confinement model [10] for Si nanocrystals predicts both of the effects observed here, namely the peak broadening and downshifting.

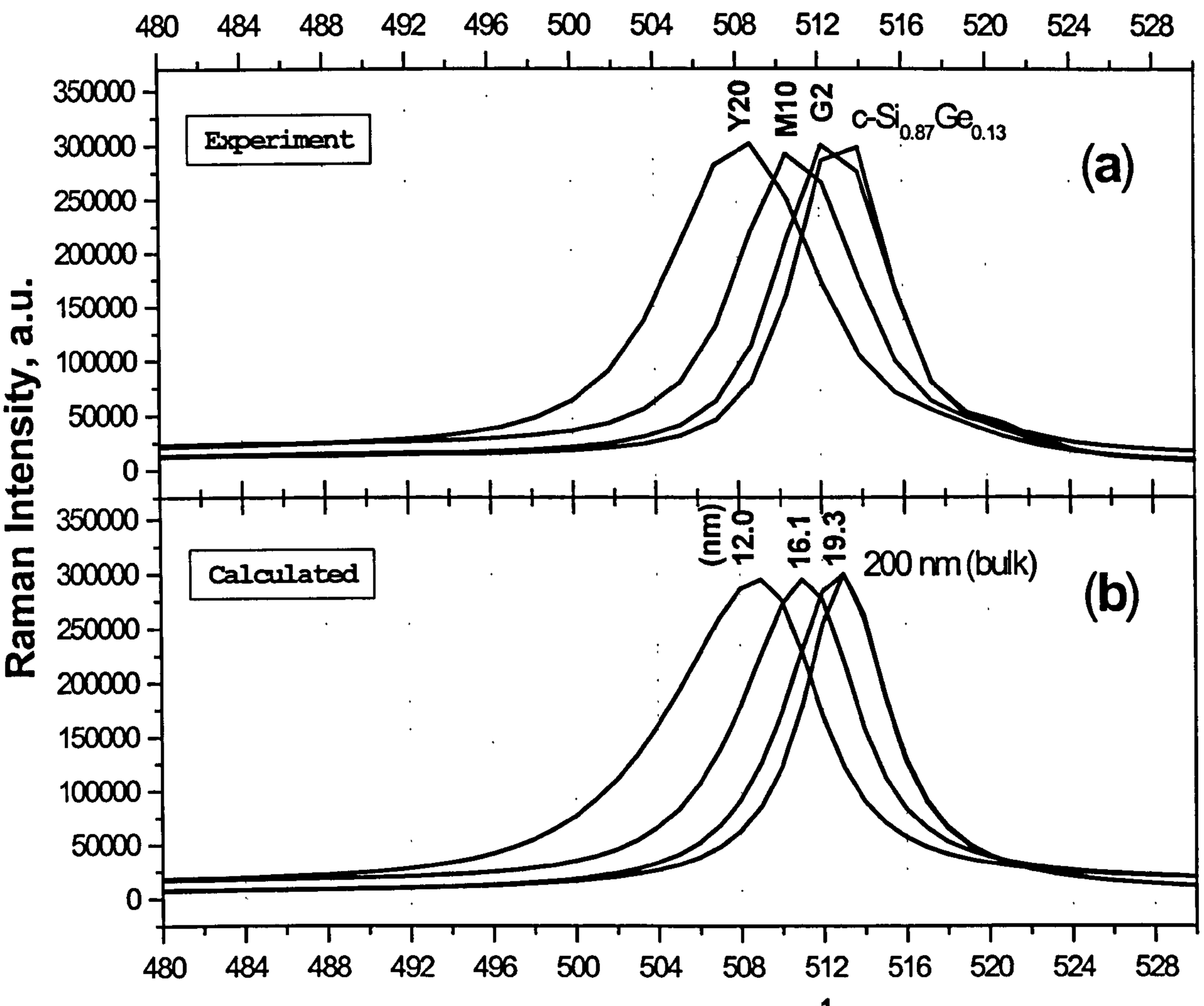

Figure 4.3 (**a**) Detailed experimental Raman spectra around the Si-Si peak for the spectra in Fig. 4.1. (**b**) Raman spectra calculated according to the indicated model [10] for crystal sizes of 12.0 nm, 16.1 nm, 19.3 nm and 200 nm (i.e. corresponding to the bulk). The peak maximum shifts to lower frequency and its linewidth increases with porosity (**a**), or as the crystal size reduces (**b**). Experimental and calculated spectra are given in separate windows for simplicity. Peak intensities in respective windows are normalised for clarity. Peak frequencies of the spectra in (**b**) are arbitrarily moved in order to provide better visual comparison of the theory (**b**) with experiment (**a**) (see Table II).

Comparing only the linewidths of the Si-Si peak of the porous SiGe samples with those calculated (Figure 4.3.b) with the phonon confinement model [10], we estimate an

average nanocrystallite size of 19.3±1 nm, 16.1±1 nm and 12.0±1 nm in samples G2, M10 and Y20, respectively (Table II). For strain-free nanocrystals of Si of these sizes, the position of the Si-Si peak is expected to shift to lower frequency by 0.5 cm^{-1}, 1 cm^{-1} and 2 cm^{-1}, from the bulk c-Si value of 520 cm^{-1} (in this case from 513.1 cm^{-1} for bulk $Si_{0.87}Ge_{0.13}$). However, as can be seen from Table II, the observed peakshifts of the porous samples are increasingly greater than that obtained from their calculated pair values (except for the low porosity sample G2). This suggests that variation of the film composition (i.e. increasing Ge fraction) also takes a role in the observed downshifts of the Si-Si peak.

The degree of compositional variation between samples is calculated using Eq. 4.1 by taking into account the difference between the observed and calculated Si-Si peakshift pairs (Table II). The final Ge fractions were determined for the samples Y20, M10 and G2 as 17%, 15% and 13%, respectively. As the nanocrystal size decreases (or the porosity increases), the Ge content (x) becomes greater, such that the Ge-Ge peak eventually gets clearly visible. Furthermore the intensity of the Si-Ge optic mode (~ 400 cm^{-1}) increases relative to the other Si-Ge peak (~ 430 cm^{-1}) for the sample with the highest porosity, namely sample Y20 (see Fig. 4.2). An increase in the [Ge]/[Si] ratio is also reported by Ksendzov *et al.* in stain-etched MBE-grown SiGe alloys [5].

Table II. Summary of the calculations based on the Si-Si peak data of the spectra in Fig. 4.3. Peak centers, widths and shifts are in units of cm^{-1}. Nanoparticle sizes (d_{ave}) are calculated in accordance with the phonon confinement model [10] (but only the peak width enlargement is taken into consideration). Change in the film composition (in Ge %) is calculated using Eq. 4.1 for the difference in calculated (shift1) and observed (shift2) shifts of the Si-Si peak of porous SiGe from the bulk value.

Sample	Si-Si peak		d_{ave} (nm)	shift1 (calc.)	shift2 (obs.)	∇_{shift} (shift2-shift1)	estimated change in x (%)	final % Ge content
	Center	Width						
Bulk	513.1	4.9	-	0	0	0	0	13.0*
G2	512.6	5.7	19.3	0.5	0.5	0	0	13.0
M10	510.9	6.3	16.1	1	2	1	1.5	14.5
Y20	508.2	8.0	12.0	2	5	3	4.4	17.4

* Ge content in bulk alloy is taken precisely as 13.0% here, although the x-ray data indicated an error of 1% (i.e. 13±1%), since compositional variations in the porous samples are to be calculated relative to a fixed bulk content.

It is possible to suggest that etching takes place selectively on Si atoms as the nanocrystal size decreases, that is the etch selectivity follows a non-uniform path as the dimensions decrease. These results, however, are preliminary and more data is needed to fully comprehend the etch mechanism of SiGe, which in return should yield an understanding of the optical properties of the final porous SiGe material.

Alonso and Winer compared the Raman peak frequencies above 390 cm^{-1} of their fully-relaxed, liquid phase epitaxy (LPE) grown-single crystal $Si_{1-x}Ge_x$ alloys to those of bulk polycrystalline $Si_{1-x}Ge_x$ alloys as a function of Ge content x [14]. Particularly important here, their data for both sets of alloys showed that the position of the Si-Ge optic mode

(~ 400 cm^{-1}) varied slowly with x (for x<~ 0.60) and in an opposite sense to the Si-Si peak and the 430 cm^{-1} Si-Ge peak. These latter two peaks varied linearly with x in the same direction, but with different gradients. In other words, the Si-Ge optic mode shifts to higher frequency for an increase in x, contrary to the other peaks (above 390 cm^{-1}), which shift to lower frequencies. As for the present spectra of porous SiGe, we note that the frequency of the Si-Ge optic band maximum shifts to lower frequencies as the nanocrystal size decreases (Table I), despite the fact that the Ge content, x, slightly increases with porosity (Table II). Therefore, we conclude that the behaviour of this Raman peak indicates distinctively the confinement of Si-Ge optic phonons in several nanometer-sized SiGe crystals, rather than a compositional variation. This observation, to our knowledge, is a first for porous SiGe [11][12] and also for other SiGe alloy microstructures [5][13]. Earlier Raman spectroscopy studies of porous SiGe merely reported a vague downshift of the Si-Si peak by a few cm^{-1} from the bulk value (independent of the sample preparation parameters) [11][12] and attempted to calculate the size of 'Si nanocrystals' in their porous SiGe samples [11].

Lastly, we also note that the sizes of SiGe nanocrystals in our samples are relatively large, for example, compared to those prepared by Takeoka *et al.* in SiO_2 matrices, using a combination of co-sputtering and post-annealing processes [10]. Yet the sizes of SiGe nanocrystals in our samples might be reasonable when it is considered that the production of porous SiGe samples took place from 'undoped' substrates where the density of photo-generated carriers during anodisation may not be so superficial, for example, to reduce the particle dimensions below 10 nm (for the etching times studied). It is suggested for the anodical etching of Si that (intrinsic) holes (h^+) must reach the silicon/electrolyte interface for the etching of Si to carry on, and so the particle size can be further reduced [14].

4.1.2 High-Resolution SEM

Figure 4.4 shows cross-sectional SEM micrographs of porous SiGe sample G2. It was observed that only several hundred nanometers (300-400 nm from the surface) of the SiGe epilayer was rendered nanoporous in this sample (Fig. 4.4.a). The rest of the 1 μm-thick undoped epilayer, as well as the 0.2 μm-thick undoped Si buffer layer underneath, remained intact through the anodisation. Yet it was observed that pores started to form in the n^+-type Si substrate. The depth of the pores was approximately 5 μm from the surface and the pore channels were almost randomly oriented, as seen in Fig. 4.4.b.

Cross-sectional SEM images in Fig. 4.5 reveals clearly the thickness and morphology of the etched and unetched layers in sample M10. Fig. 4.5.b shows, from top to bottom: nanoporous SiGe: ~ 0.2 μm; unetched bulk SiGe: ~ 0.75 μm; unetched Si buffer layer: ~ 0.25 μm. Fig. 4.5.a shows nanoporous Si: ~ 4 μm. It is noticeable that the pore channels in the Si substrate in Fig. 4.4.b develop into a fine-structured porous Si layer after 10 min etching (sample M10, Fig. 4.5.a and b). In addition, a slight decrease (~ 50 nm) in the porous SiGe film thickness is observed for this sample compared to sample G2.

Lastly, in the case of sample Y20, the microstructure was similar to that seen in sample M10, with the only difference being the thickness of porous layers (not shown). While the thickness of the porous Si film was approximately 20 μm, the thickness of the porous SiGe film was not more than 100 nm at most places.

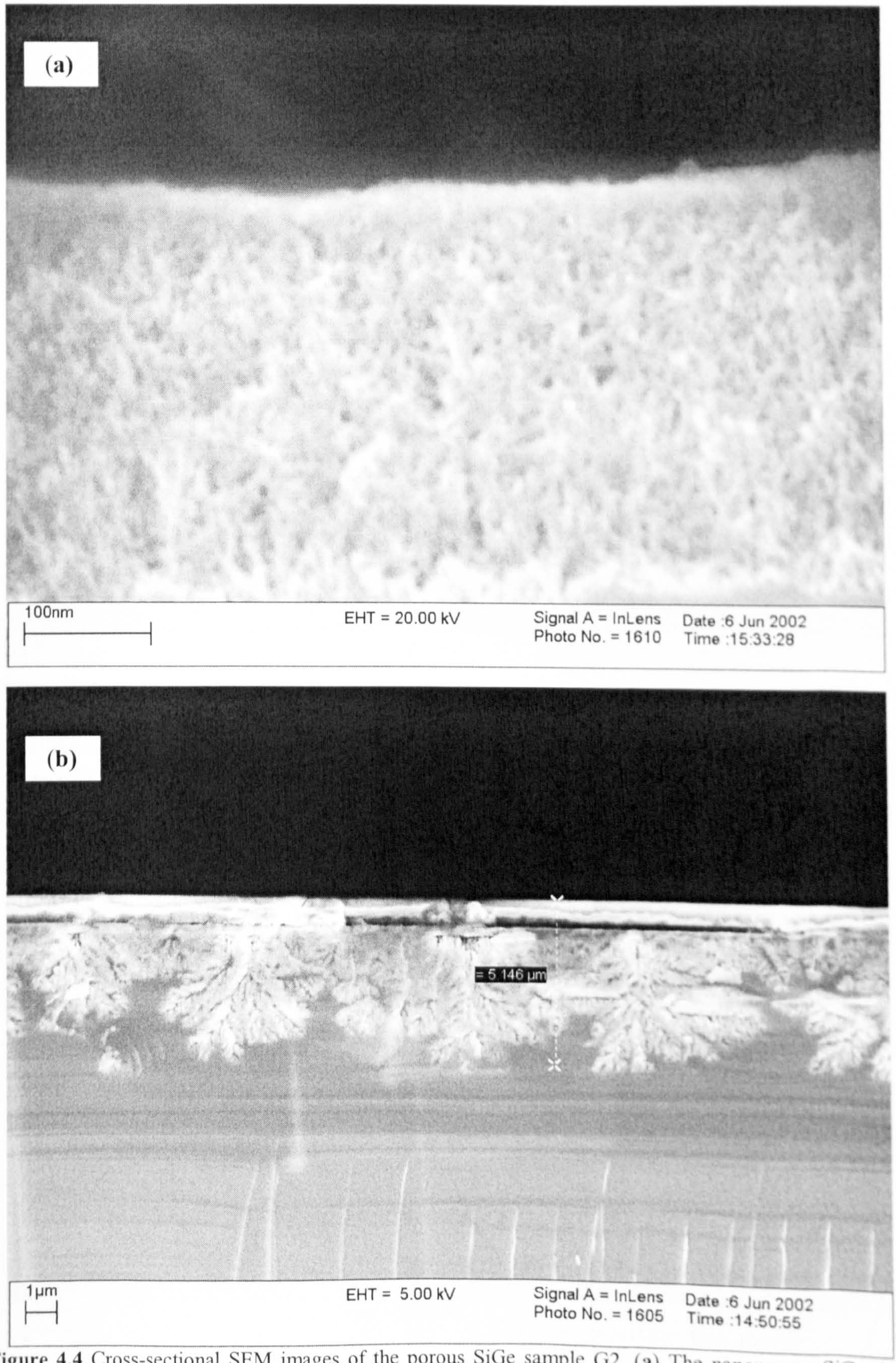

Figure 4.4 Cross-sectional SEM images of the porous SiGe sample G2. (**a**) The nanoporous SiGe film formed in the SiGe epilayer; (**b**) macro-pore channels in the Si substrate which go down to a depth of ~ 5 µm from the surface (internal mark shows 5.146 µm).

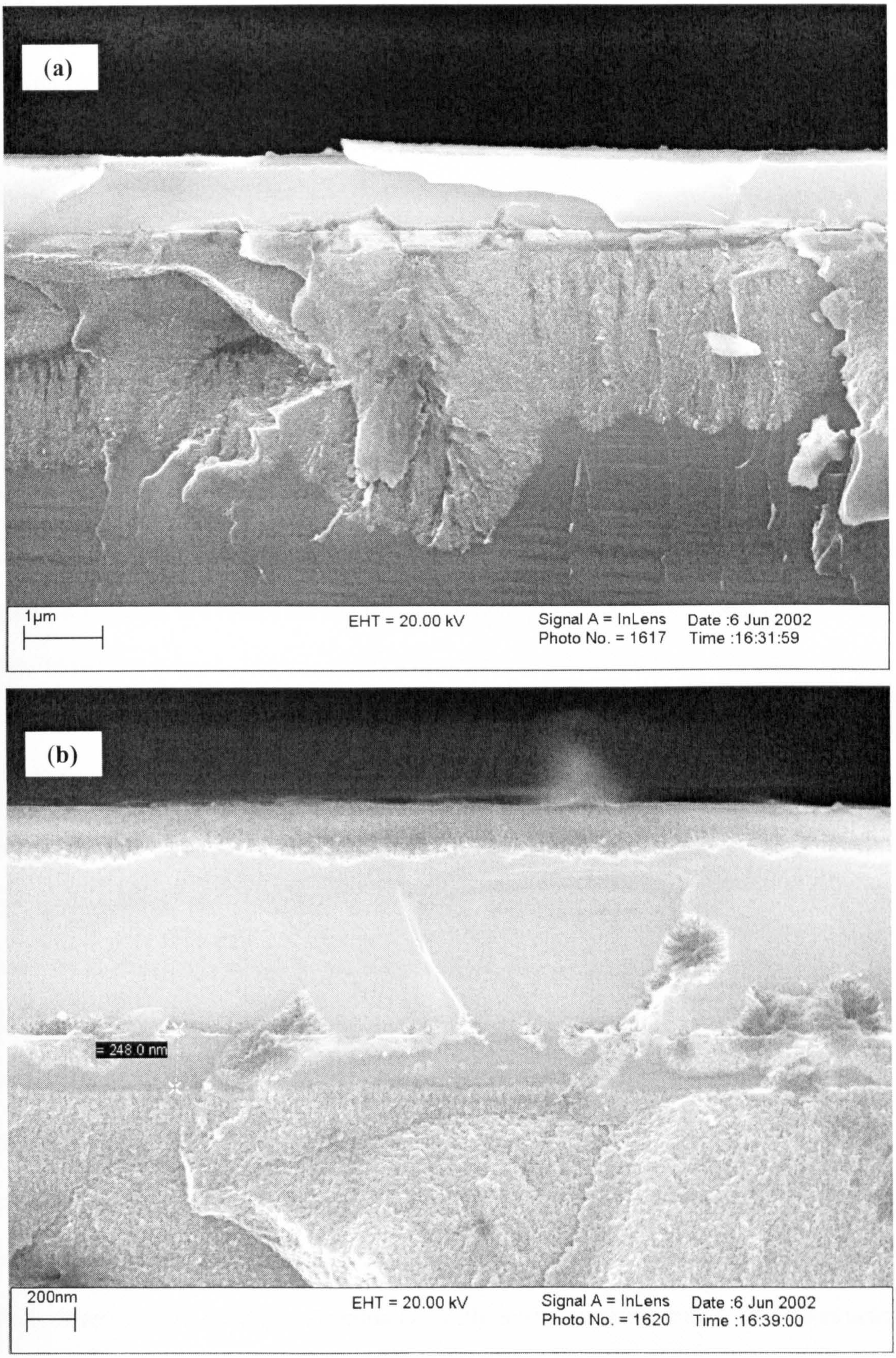

Figure 4.5 Cross sectional SEM images of the porous SiGe sample M10 demonstrating (**a**) the thickness and the fine structure of the porous Si layer; (**b**) the microstructure around the SiGe epilayer.

4.1.2.a Discussion

High-resolution SEM micrographs indicate that SiGe quantum structures are grown, near the surface of the 1 μm-thick bulk SiGe alloy epilayer, in all the samples studied. Although the underlying Si substrate was also etched in all these samples, it was noteworthy that not the entire bulk alloy layer was rendered porous (even after 20 min etching). We suggest that the high resistivity of the (buried) undoped layers, i.e. SiGe alloy and Si buffer layers (see Fig. 4.5.b), precluded them to be etched by anodisation and that only those layers a few hundred nanometers from the surface were etched. A fine porous structure could be formed there with the assistance of light illumination during the anodisation. It is well known that in lightly n-type doped Si substrates the holes necessary must be supplied externally for the etching to take place, and this is usually achieved by light illumination during the anodisation [14][15].

To facilitate the understanding of the etching of the deeper layers (i.e. the Si substrate) beneath the thick, intact layers, we suggest the following mechanism. Channels going all the way through the epilayers, down to Si substrate, were formed rapidly, starting possibly at atomically rough parts of the surface, in an avalanche due to the high voltage biasing and powerful (250 W) light illuminating of the wafer. The atomic structure of the fully-relaxed SiGe epilayer is viable for the growth of such deep channels due to stacking faults in this layer. Then these channels allowed injection and infiltration of the electrolyte through the Si substrate, and the very low resistivity of the (n^+-type) Si substrate permitted the etching to take place, with the macropores in Fig. 4.4.b forming first (after 2 min etching). Eventually, with longer etching times, a fine-structured nanoporous layer was formed (Fig. 4.5), even without the need of light, that is in almost total darkness.

Although cross-sectional high-resolution SEM images provided real-images of SiGe nanowires, a direct size estimation by analysing them did not seem to be easy. Thus, we find it more convenient to use the results obtained by Raman modelling for the corresponding average crystal sizes in our samples. SEM micrographs, nevertheless, supported the Raman results (Fig. 4.3 and Table II) qualitatively. Figure 4.6 illustrates an example SEM image demonstrating the detail of the typical SiGe nanostructures grown in our samples. According to this figure, the diameters of the wire-like SiGe quantum structures in our samples are comparable to ~ 10 nm. However, as quantitative analysis of the sizes does not seem to be easy using SEM images (such as Fig. 4.4 and Fig. 4.6), a numerical comparison between the samples could not be made this way either.

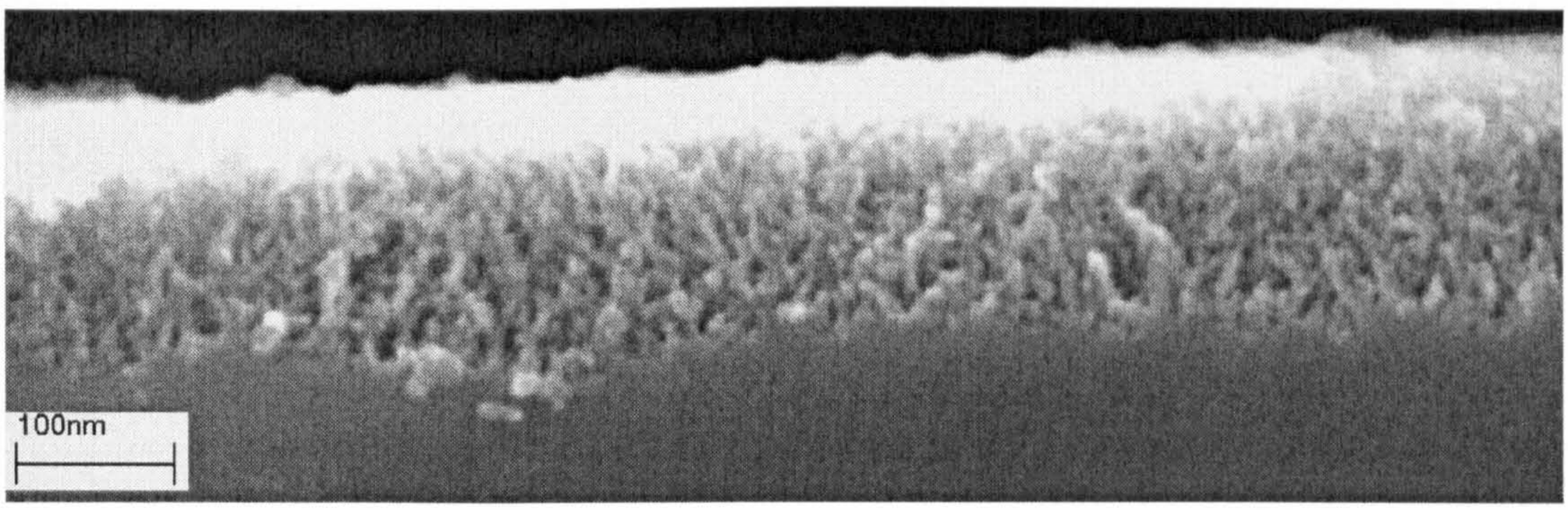

Figure 4.6 Wire-like SiGe quantum structures grown by anodisation (sample M10). Modelling of micro-Raman spectra indicated the average size as 16.1 nm in this sample.

Lastly, we note that the thickness of the porous SiGe layers in our samples decreases with the etching time. The exact mechanism of this effect is presently not clear, but it appears that an etching time of 2 min seems to be enough for the thickness of the porous layer to 'saturate' with the formation of a certain nanostructure. When the etch time is

increased to 10 min the thickness of the already-grown porous film starts to decrease, while the columns of the quantum structure shrinks slowly. The film thickness further reduces when the etch time reaches 20 min. It is then reasonable that the intensity of the first-order Raman spectra in Fig. 4.1 decreases with the etch time, although the spectra of all of the porous samples had approximately 5 times stronger intensity than that of the bulk epilayer.

4.1.3 PL

Figure 4.7 gives the spectra of the PL emission from our porous SiGe samples in the visible region. The intensity of the emission was very weak in all cases. The PL energy is independent of the sample preparation parameters. The energy and spectral shape of the PL are similar to those of the characteristic orange PL emission of PS in air [16]. (Here, we must note that these spectra were recorded when the samples were kept in air for 2 weeks).

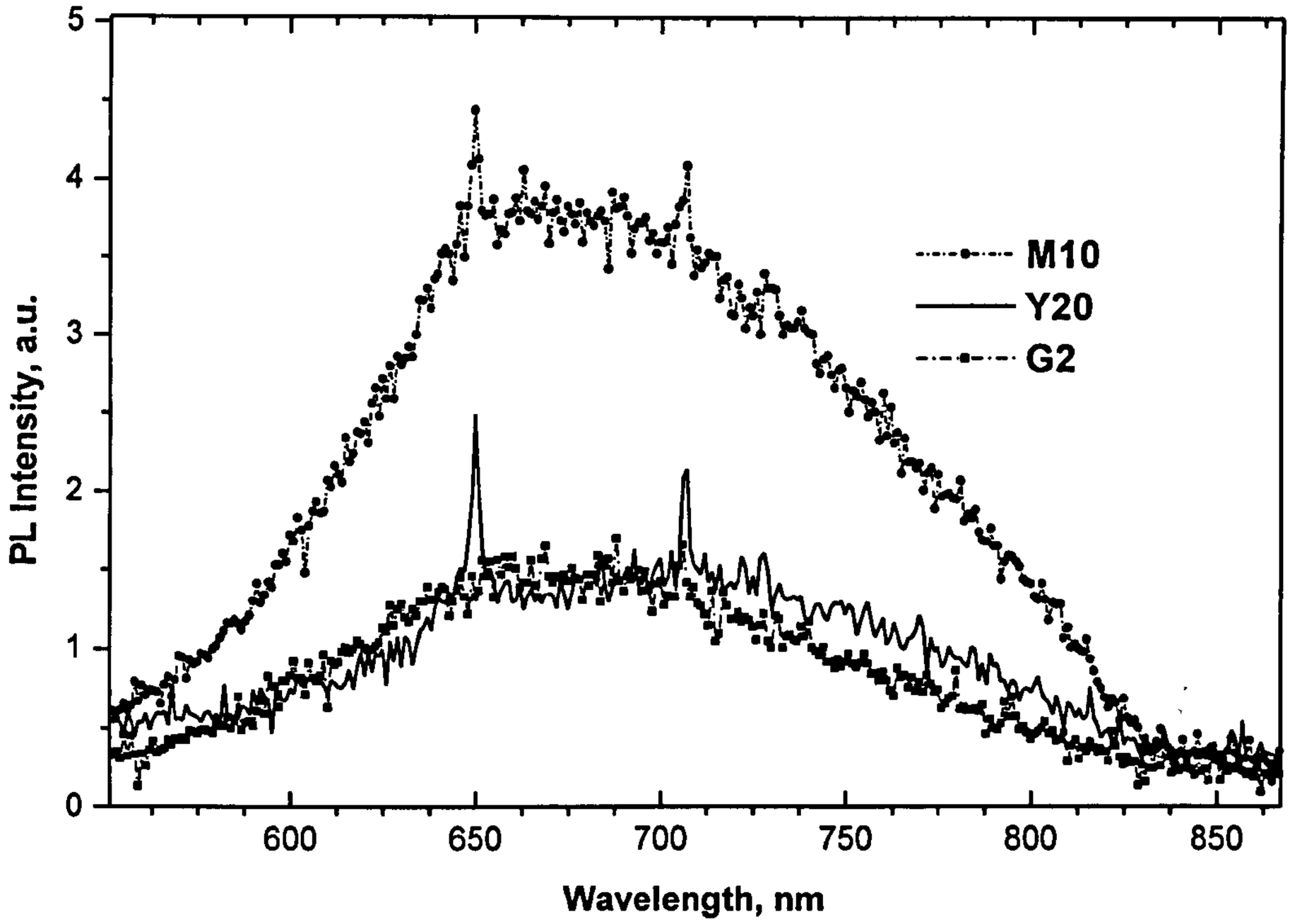

Figure 4.7 Room temperature PL spectra of the porous SiGe samples with 325 nm excitation.

Our porous SiGe samples with average nanocrystal sizes 12.0, 16.1 and 19.3 nm are not expected to emit in the visible if the quantum confinement (QC) is considered as the mechanism of the PL. It is generally accepted that, as a result of QC, the PL will be pushed into the visible for (Si) crystallite sizes below 5 nm, following the widening of the bandgap. However, it is not clear at this stage whether there are a sufficient number of nanoparticles with bandgaps large enough (or sizes small enough) to yield visible light emission in these samples. The similarity of the PL emission to that of PS, however, makes this suggestion somewhat more probable. Still, there is not enough evidence to attribute the visible PL emission to QC effects or to any other particular means.

4.2 STAIN ETCHED Ge

4.2.1 SEM

Figure 4.8 shows typical SEM micrographs obtained from samples prepared in H_2O_2:HF solution (Type I-SG). The layer formed on the substrate shows a high degree of topological uniformity and exhibits two forms (Fig. 4.8.a and b): one has a rounded shape (disk-like) with typical diameters of 100-300 nm, and the other has a cylindrical shape with lengths 100-700 nm and diameters of ~ 20 nm. The layer thickness was a few hundred nanometers, but showed fluctuations even across a single film (Fig. 4.8.c and d). It is also notable from Fig. 4.8.b that there are wide discontinuities present in the film, some possibly going all the way through the substrate (see below).

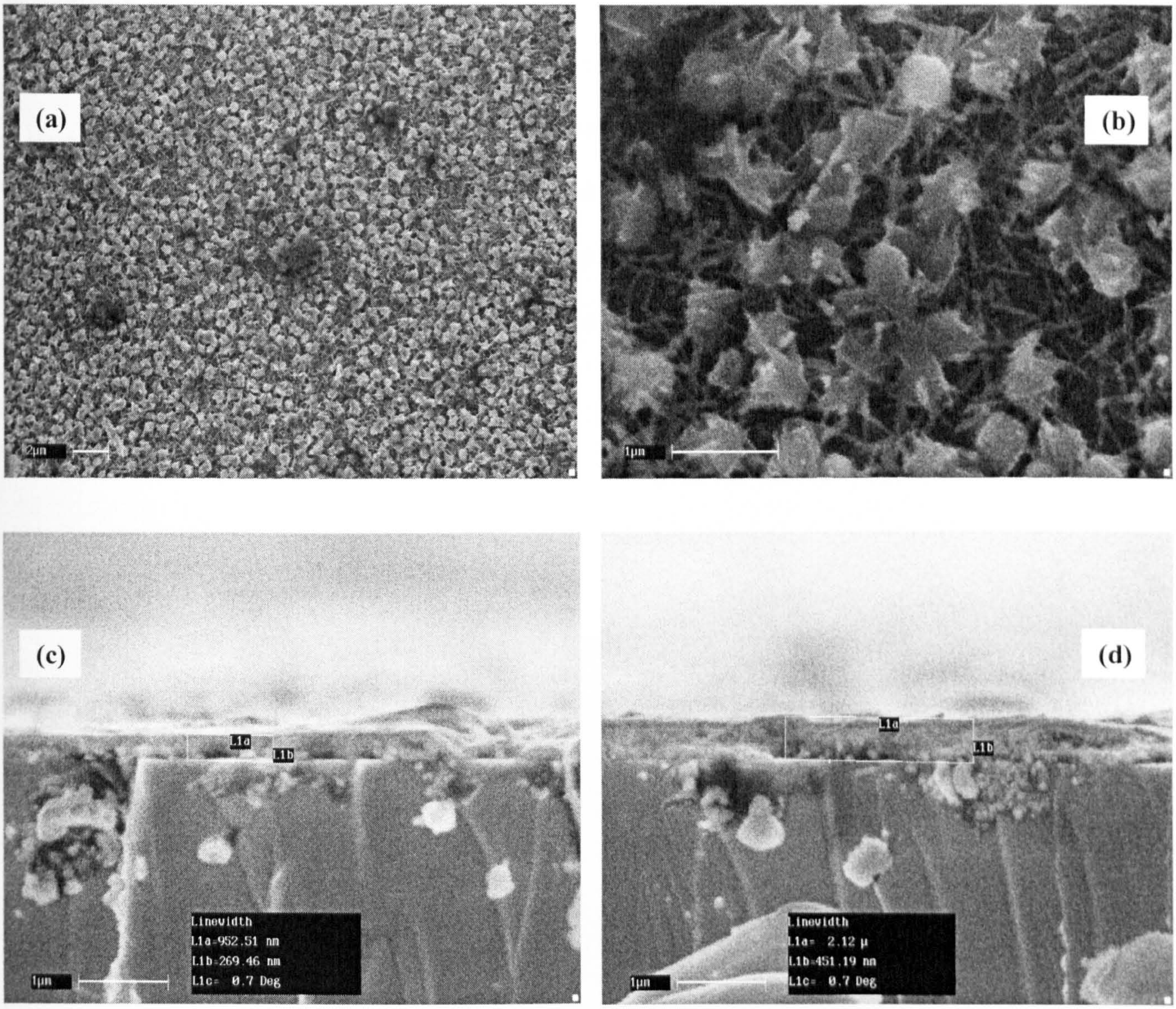

Figure 4.8 Typical SEM micrographs of light-assisted H_2O_2:HF-stain etched Ge (Type I-SG): (**a**) and (**b**) are plan views of the surface features, (**c**) and (**d**) are cross-sectional views from a single film demonstrating variations in film thickness (~ 270 and ~ 450 nm respectively).

4.2.2 EDX

Energy dispersive x-ray (EDX) analysis was used to check the composition of the films. For this purpose, a tiny piece was taken from a sample surface, as shown in Figure 4.9. Care was taken to not include any bulk material from the c-Ge substrate so as not to cause any misinterpretation of the film composition. Contributions from Ge and O were observed and their relative percentages were determined to be 76±5% and 24±5%, respectively.

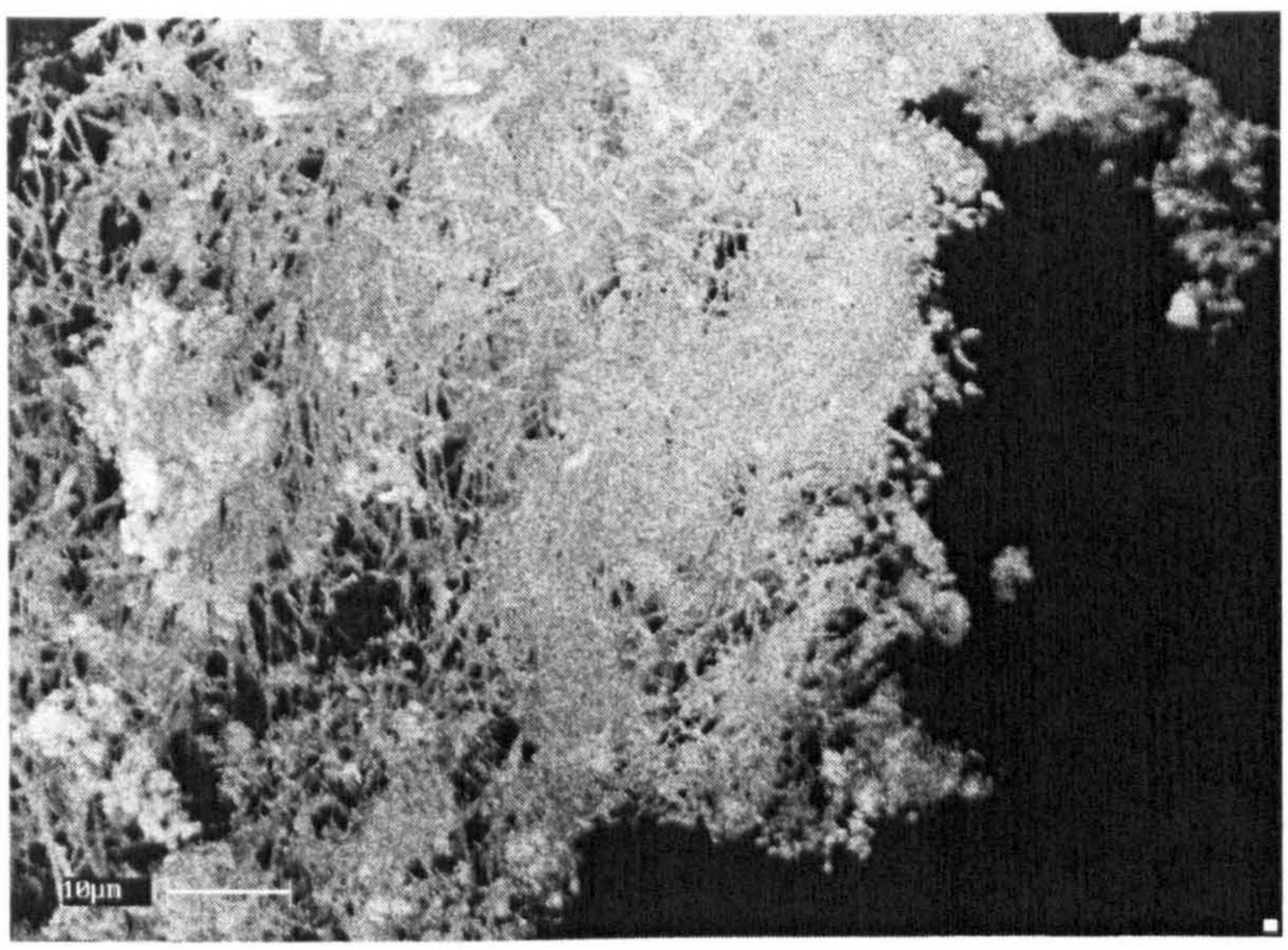

Figure 4.9 A tiny piece from the Type I-SG layer used for EDX analysis (with O=24±5 and Ge=76±5 element %).

4.2.3 FTIR

IR spectra similar to that in [17] were observed for the Type I-SG samples (Fig. 4.10). In addition to the GeO_2 band at 880 cm^{-1} and the broad feature between 3000 and

3650 cm^{-1} due to hydroxyl (-OH) groups and water, another peak ascribed to substoichiometric regions and oxygen-vacancy complexes in GeO_2 [17][18] can be seen at ~ 750 cm^{-1}. However, unlike the observation of Si-H in PS (Fig. 2.3), no Ge-H stretching band appears at 1900-2000 cm^{-1} [19].

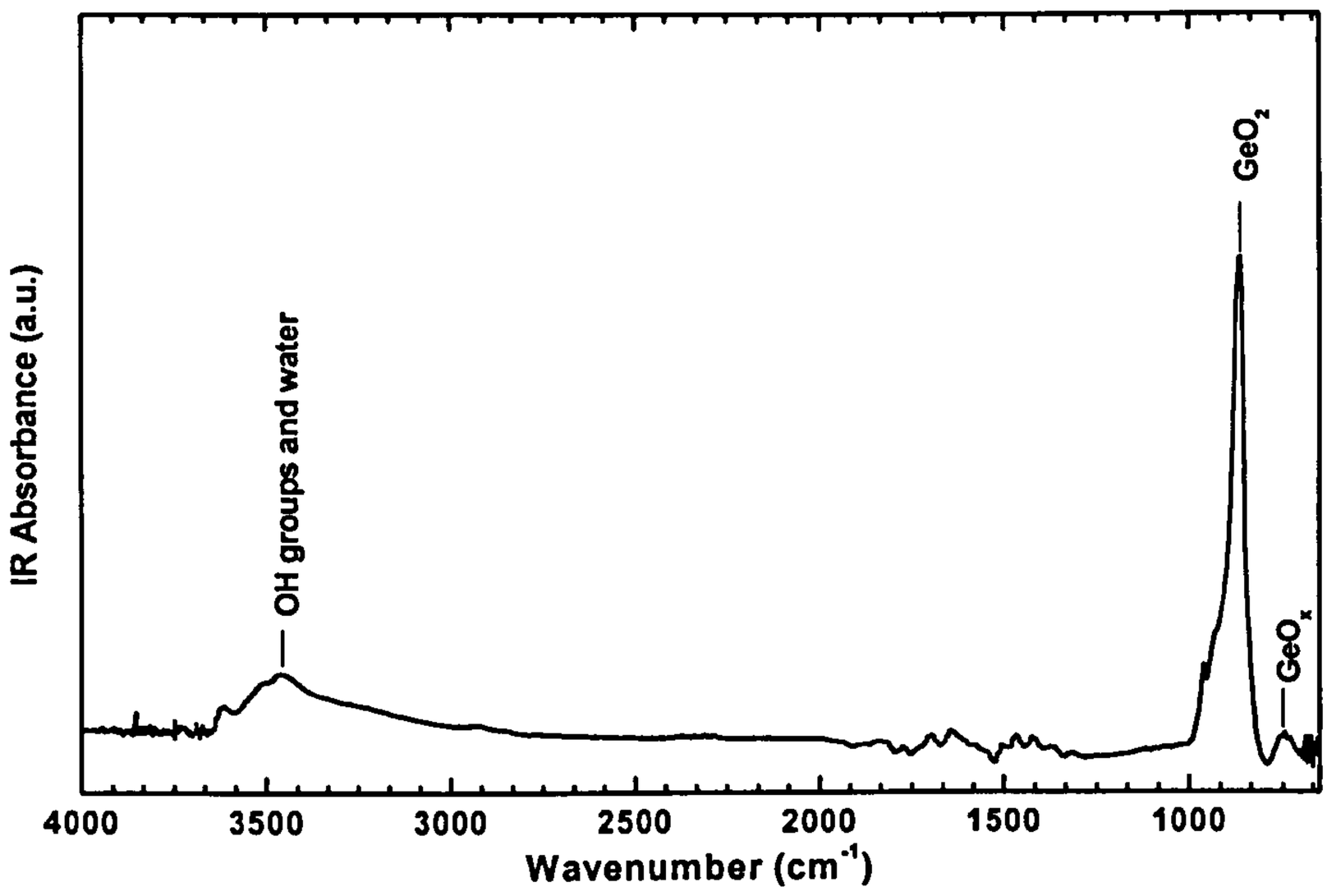

Figure 4.10 Typical FTIR spectrum of Type I-SG.

On the other hand, the IR absorption spectrum given in Fig. 4.11 indicates the presence of hydride bonds, as well as a reduced amount of oxides, on the surface of a fresh Type II-SG film. OH groups were also detected at around 3300-3500 cm^{-1} in extended scans, but the background signal was too high around those frequencies. The scan range is therefore kept shorter here.

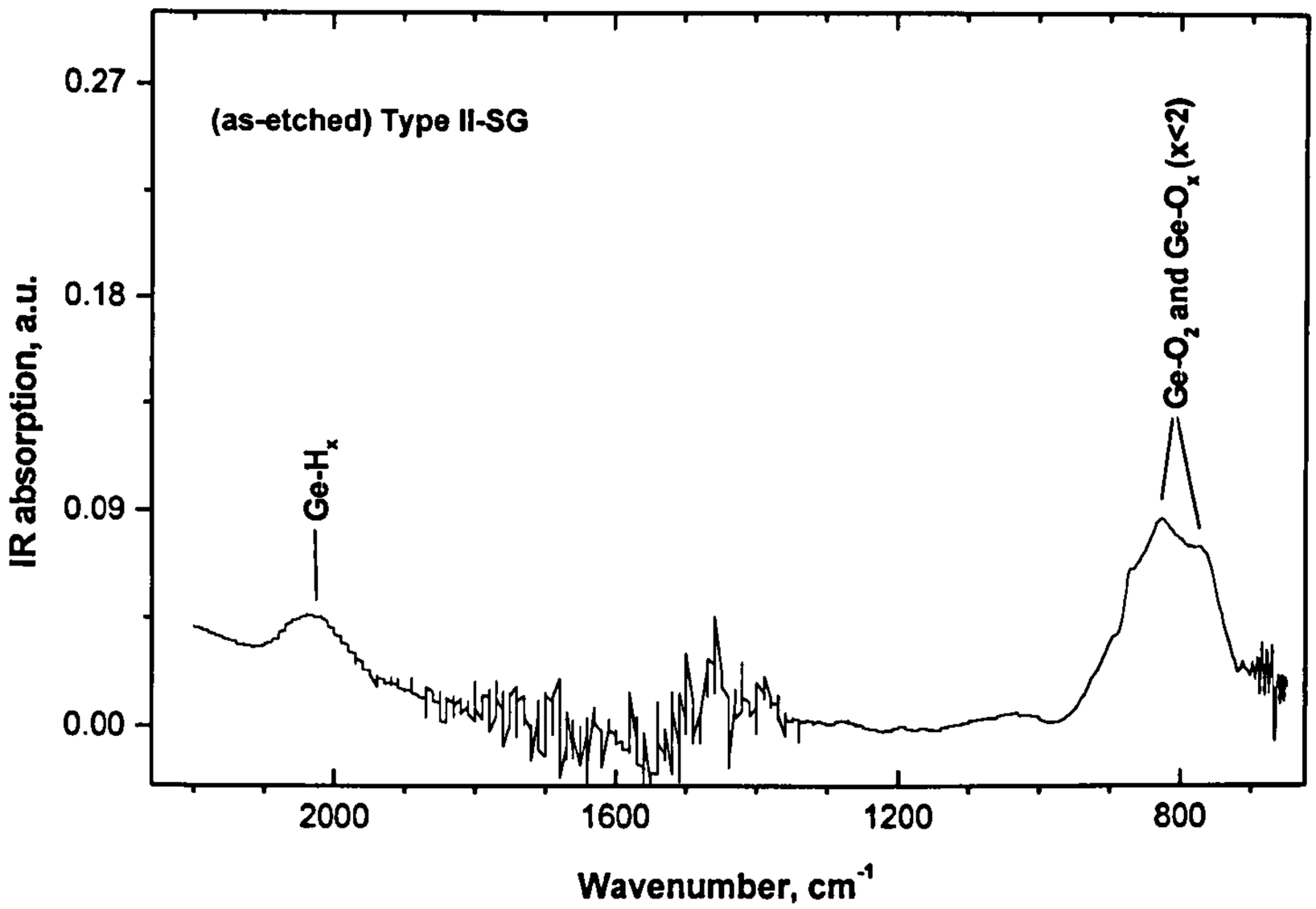

Figure 4.11 IR absorption spectrum of a fresh Type II-SG film. OH groups were also detected at around 3300-3500 cm^{-1} in extended scans. The features around the noisy part (near 1600 cm^{-1}) are related to the presence of CO_2 in the sample window of the spectrometer.

4.2.4 Raman

The one-phonon Raman spectrum of c-Ge is shown in Fig. 4.12.a and clearly indicates the presence of a single peak, at 300 cm^{-1}, which corresponds to Ge optical phonons. In Fig. 4.12.b, however, it is seen that there are two peaks in the Raman spectrum of a Type I-SG sample. The position and FWHM of the Ge peak for Type I-SG at 300 cm^{-1} is practically the same as that seen for c-Ge. The peak at 445 cm^{-1} we attribute to non-stoichiometric Ge oxides because, except for the 442 cm^{-1} peak, Raman peaks typical of c-GeO_2 (Fig. 4.12.c) are not seen here. C-GeO_2 is characterised by peaks at 122, 165, 211, 246, 262, 327, 442, 515, 592, 858, 881, 960, and 972 cm^{-1}, however there is no observable peak at the Ge optic phonon mode position (i.e. 300 cm^{-1}) due to the lack of Ge-Ge bonds. Therefore, we can suggest that the peak at 300 cm^{-1} in the Raman spectrum

of the Type I-SG is due to the c-Ge substrate: the large discontinuities in the film might well have led to a contribution to the spectrum from the substrate. The inset to Fig. 4.12 shows the effect of etch time on the amount of suboxides present: a longer etch time results in a greater oxide fraction.

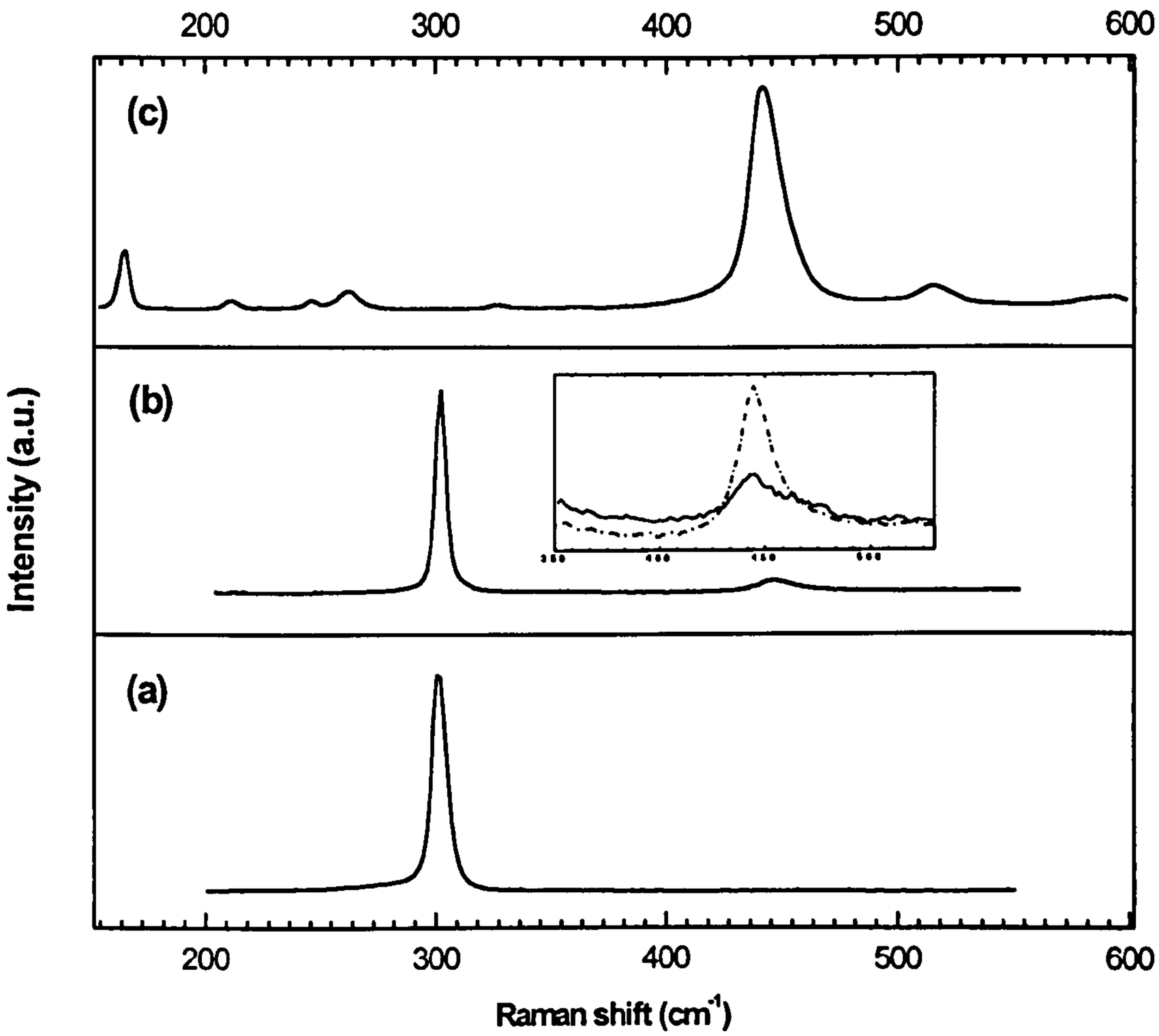

Figure 4.12 Room temperature Raman spectra of (**a**) c-Ge, (**b**) Type I-SG, and (**c**) c-GeO_2. The inset shows 440 cm^{-1} peaks for two SG samples prepared under the same conditions with only etching times different.

These results combined with the FTIR spectroscopy results suggest that Type I-SG films are composed of non-stoichiometric Ge oxides with plenty of oxygen-vacancy complexes, i.e. of various GeO_x ($0<x<2$).

The Raman spectrum from an as-etched Type II-SG film (prepared in $HF:H_3PO_4:H_2O_2$ solution) is shown in Fig. 4.13.a. This spectrum is similar to that of amorphous Ge [20], but it is narrower and shifted slightly to higher frequency. Alternatively 2-3 nm Ge nanocrystals could be responsible for such a spectrum. The Raman spectrum of Type II-SG annealed in air (Fig. 4.13.b) has two clear peaks, at ~ 450 and ~ 170 cm^{-1}, assigned to germanium oxides. With the annealing temperature kept as low as 600 °C, there seems to be a total transformation of the chemically-etched film probed with Raman spectroscopy: that is, Ge-Ge bonded chemically-etched material is completely transformed into GeO_x after annealing in air.

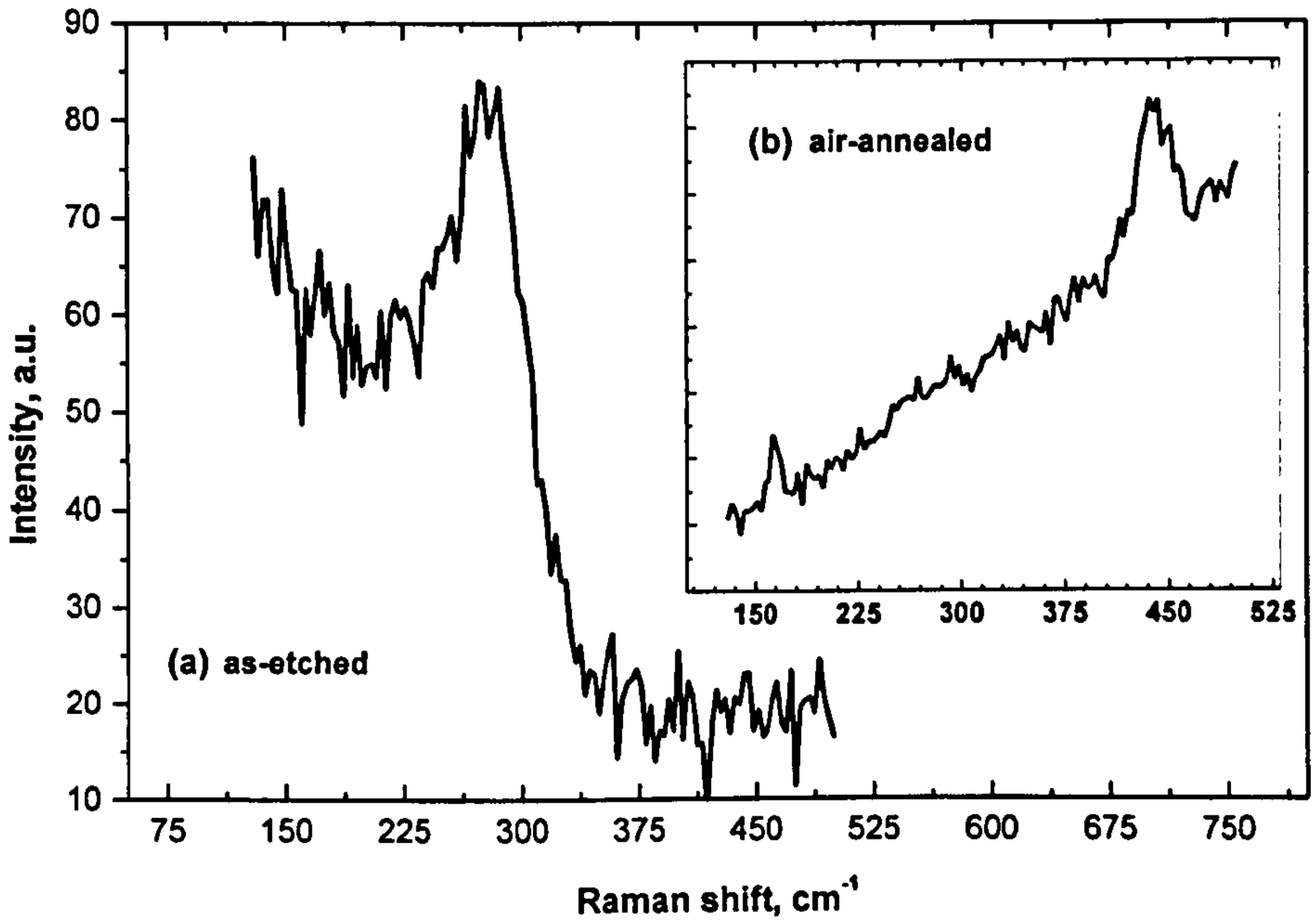

Figure 4.13 Room temperature Raman spectra of $HF:H_3PO_4:H_2O_2$-stain etched Ge (Type II-SG): **(a)** before and **(b)** after annealing in air for 30 min at 600 °C.

Low-temperature annealing of this sample in H_2 has, however, tightened the interpretation of the Raman spectra. A model based on phonon confinement was fitted

to the Raman spectra of H-annealed samples, and nanocrystal sizes at around 8-9 nm were realised (see below) [21].

In Fig. 4.14 it can be seen that the Raman band (curve 1) of an H-annealed film consists of a rather narrow asymmetrical peak at high frequency and a small wide shoulder at low frequency. Thus, the band is expected to consist of more than one component, one of which may be due to c-Ge substrate. Therefore, the processing and interpreting of the spectrum was performed in two stages. First, the contribution of c-Ge was extracted by fitting a Gaussian peak at the known frequency (300.4 cm^{-1}) and width (5.8 cm^{-1}) of c-Ge but with 'freely-varying' intensity [21]. Second, the position and width of the residual spectrum (Fig. 4.14, curve 3) were determined, which gave 297.4±1 cm^{-1} and 10.6±1 cm^{-1} respectively, and a calculated Raman spectrum for 8.7±1 nm Ge nanocrystals using the approach described in [22] was fitted to this peak (Fig. 4.14, curve 2). It can be seen that the correspondence between experimental and model calculated curves is relatively good, which support the existence of Ge nanocrystals in the Type II-SG film. Besides, a small difference in the form of a broad shoulder positioned near 280 cm^{-1} was assigned to the contribution of a fraction of amorphous or very small Ge nanocrystals remaining after annealing [21].

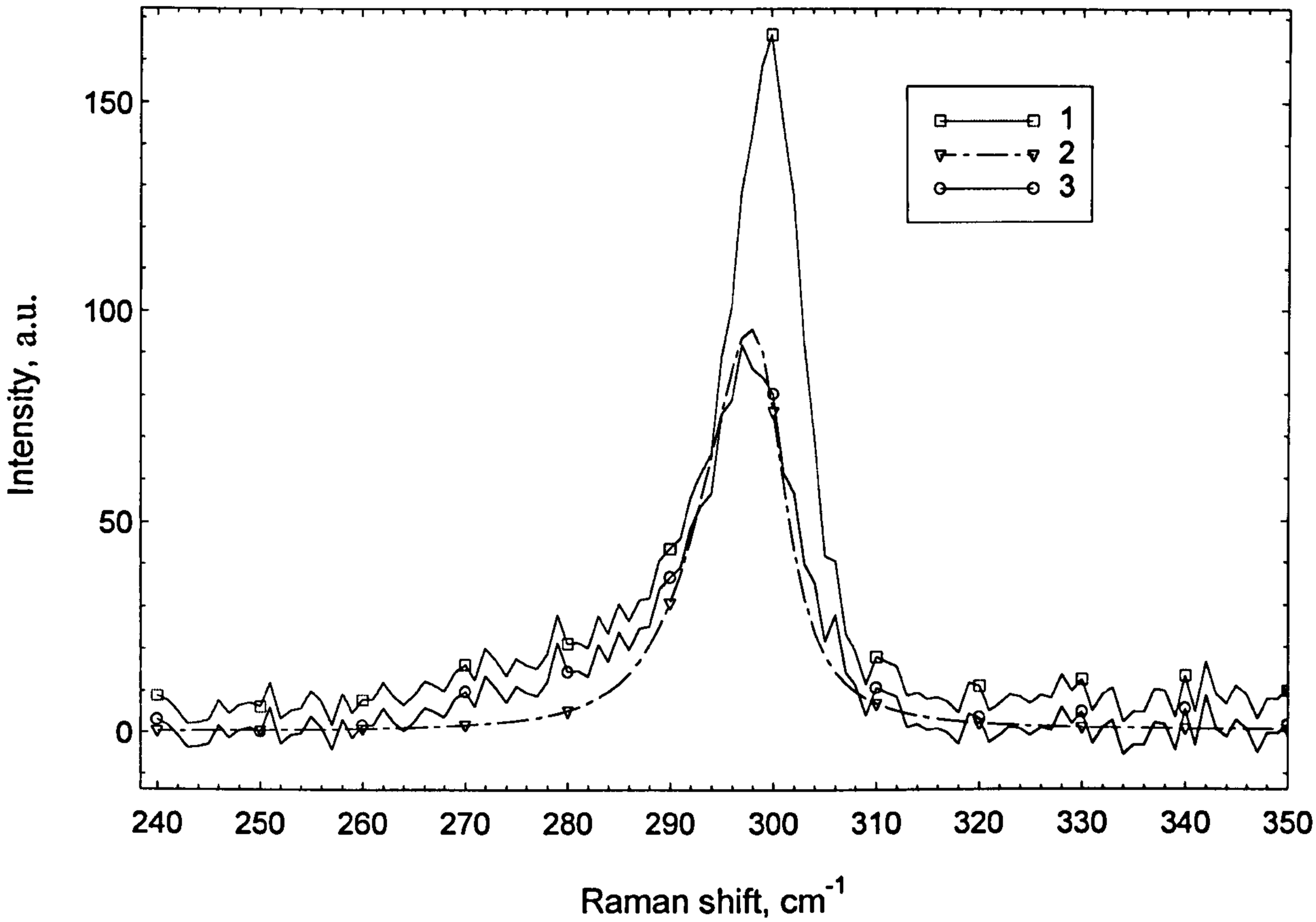

Figure 4.14 **1-** Experimental Raman spectrum of H-annealed Type II-SG; **2-** calculated Raman spectrum assuming phonon confinement for 8.7 nm Ge nanocrystals [21]; **3-** residual spectrum after extracting contribution of c-Ge substrate and background.

4.2.5 XANES

Ge K-edge TEY-XANES raw data of bulk c-Ge and the two types of as-etched SG are shown in Fig. 4.15, along with the transmission-XANES of c-GeO_2. The Ge K-edge is expected to occur at 11104 eV, the small difference in its position in Fig. 4.15 being due to monochromator calibration, and merely a systematic error and which should be adjusted for. In the XANES of c-Ge a feature due to the Ge-Ge environment appears at 11109 eV. In c-GeO_2 since each Ge atom is (tetrahedrally) bonded only to O atoms, its

XANES has only one peak at 11113 eV due to the Ge-O environment. It is clear that Type I-SG does not present as much Ge-Ge bonding character compared to c-Ge or Type II-SG. Although the total yield technique probes only a few tens of nanometers of the material surface [23], scattering from the Ge substrate could be responsible for the Ge-Ge absorption shoulder at ~ 11109 eV for Type I-SG, owing to discontinuities in the film (Fig. 4.8). In addition, there is a peak at ~ 11113 eV for Type I-SG which is ascribed to Ge-O bonds. Indeed we know from EDX (as well as IR and Raman spectroscopy) that Type I-SG mainly consists of Ge and O. Consequently, the XANES of Type I-SG can be viewed as the superposition of the XANES of c-Ge and c-GeO_2 (see Fig. 4.15).

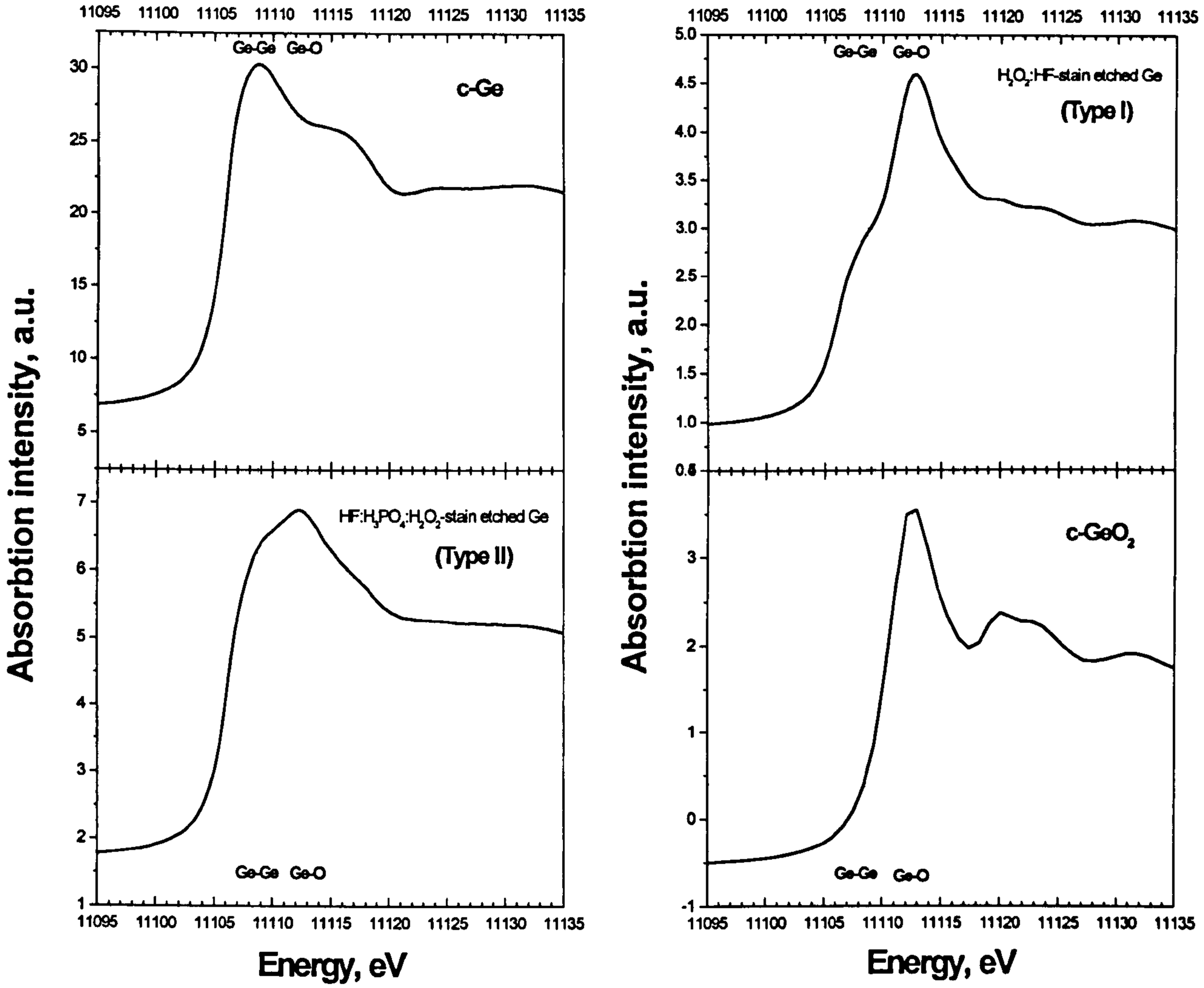

Figure 4.15 XANES of stain-etched PG films, with GeO_2 and Ge crystals for comparison. XAS for Ge crystal and PG samples were measured in TEY mode and for c-GeO_2 in transmission. Ge-Ge and Ge-O absorption peaks are indicated by dashed lines at 11108.8 and 11112.7 eV, respectively.

On the other hand, the average film thickness for the Type II-SG XAS sample is estimated to be between 1 and 2 μm by x-ray reflectometry analysis [21], and thus it is assumed that the entire XAS signal seen in Fig. 4.15 arises from the film, and not from the Ge substrate. As a result, in comparison with the other data in Fig. 4.15 and in accordance with the other spectroscopy data from this sample [21] we interpret the XANES of Type II-SG as due to a nanoporous Ge layer surface-coated with O. In other

words, the feature seen at ~ 11113 eV is attributed to Ge-O surface bonds. Here, we note that as XAS is not a sensitive probe for some light elements (especially H), unlike IR absorption spectroscopy, therefore it cannot alone provide the exact composition in this sample.

4.2.6 PL

Figure 4.16 shows the visible PL spectrum typical of a Type I-SG sample [17], along with the spectrum of commercial c-GeO_2 powder as Type I-SG films appear to have similar composition to GeO_2. Peaks are at 534 and 537 nm (~ 2.3 eV) with peak widths of 76 and 80 nm for Type I-SG and c-GeO_2 respectively. In addition to the visible region, we have also tried to measure PL in the near IR region, up to the bandgap energy of bulk Ge (0.66 eV), using a liquid nitrogen cooled Ge detector. However, no PL signal was detected in the near IR region.

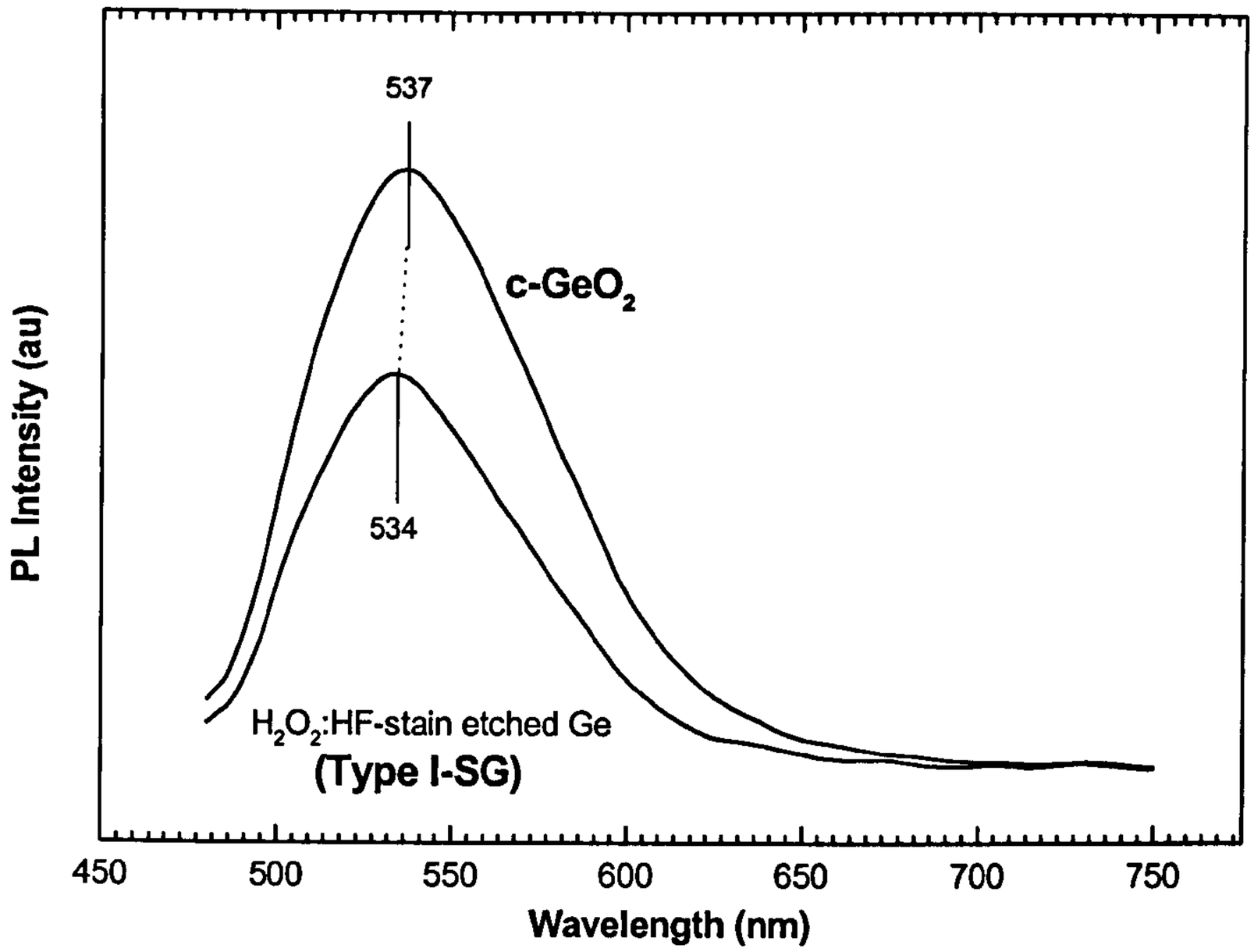

Figure 4.16 Typical room temperature PL from H_2O_2:HF-stain etched Ge (lower curve) and GeO_2 crystal (upper curve).

PL spectra of as-etched and air-annealed Type II-SG are given in Fig. 4.17. Although the shape and energy of the PL from these samples remained identical to each other (as well as to those of c-GeO_2 and Type I-SG, Fig. 4.16), it was noted that the intensity of the PL from the air-annealed sample was at least one order greater (Fig. 4.17). On the other hand, the PL intensity quenched almost completely for H-annealed samples, though the recorded spectra were similar to the others.

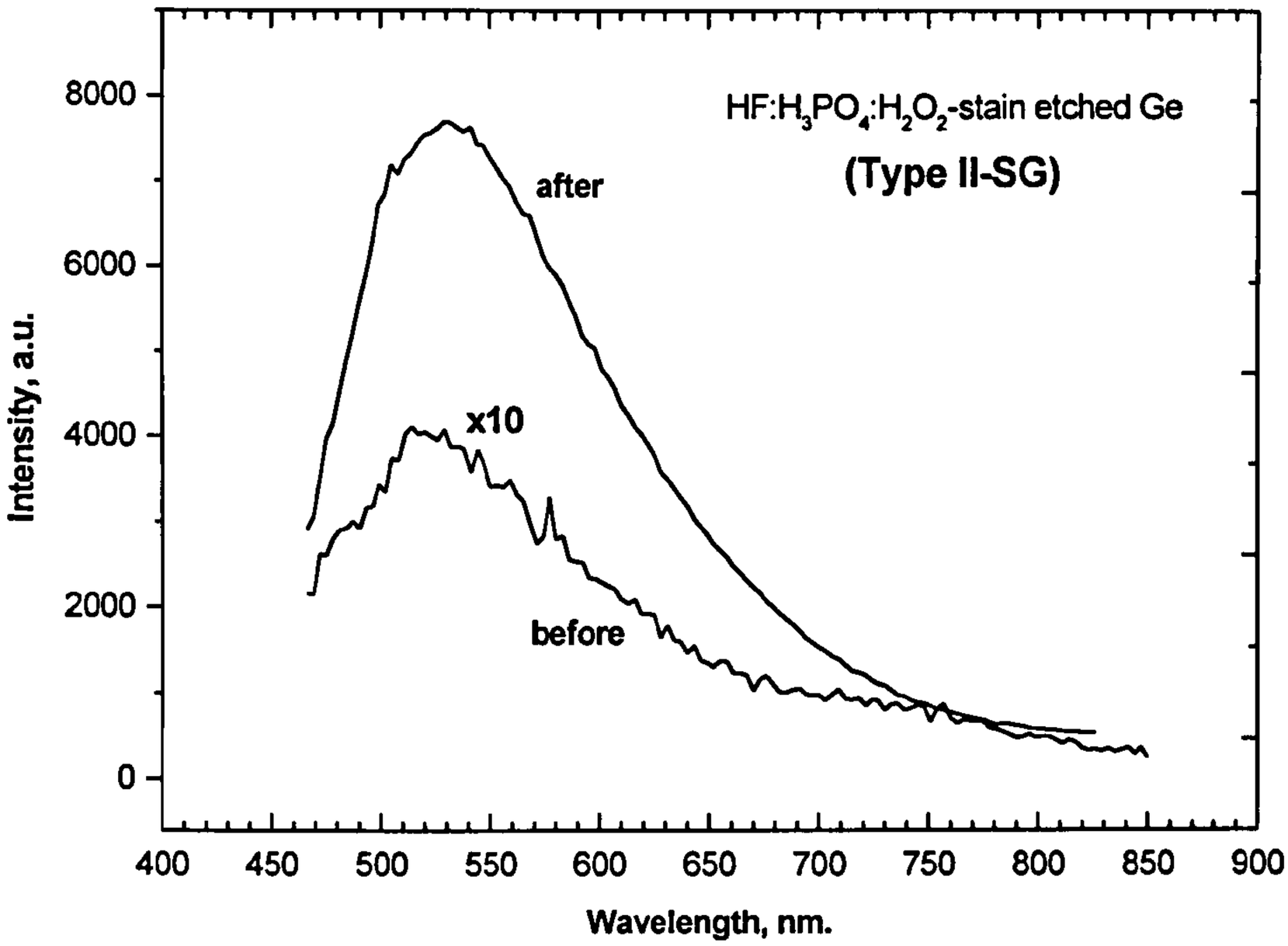

Figure 4.17 Typical room temperature PL from HF:H_3PO_4:H_2O_2-stain etched Ge (Type II-SG): before (lower curve) and after (upper curve) thermal annealing in air.

4.2.7 Discussion

Although the annealing temperature was kept relatively low, Raman spectra of Type II-SG samples suggested that strong modifications occur in the microstructure of the films upon annealing both in air and H. Air-annealing results in a total transformation of the film into Ge oxides; on annealing in H_2 the size of the nanocrystals increases dramatically. The initial Type II-SG is thought to comprise of small nanocrystalline Ge cores (say <2-3 nm) with a rather disordered tissue and surrounding Ge oxides (probably on the order of several monolayers) as well as hydroxyls and Ge hydrides.

Hayashi *et al.* showed that the Raman spectra of isolated (free standing), spherical Ge nanocrystals with a disordered tissue, and having an interface with air, are amorphous-like for sizes <10 nm [24]. Fauchet and Campbell suggested that the boundary conditions of such nanocrystals are important in determining their Raman spectra and that the amorphous-like Raman components produced by the vibrations in the (disordered) shell are enhanced by two mechanisms [25]. First, the (calculated) vibrational amplitudes in the shell are larger than in the core [26]. Second, the electric field (generated by the laser irradiation) is much larger in the shell than in the core when the nanocrystals are isolated and have boundaries with a material that has a very different refractive index (n). A 10 times higher Raman intensity is expected from a shell of thickness ~ 0.8 nm that surrounds a core of diameter 10 nm [27]. Therefore, we also consider it plausible that the contribution from the crystalline phase in the as-etched Type II-SG film is masked by the signal from the shell.

We suggest that the surface tissue (shell) of the nanocrystalline cores crystallise, and further, more elemental Ge (i.e. Ge-Ge bonded material) is reduced from the germanium oxides during the H-annealing. Let us assume that the shape of nanoparticles is wire-like; then for example generation of a 2 nm-thick c-Ge layer on both sides of a nanowire would bring about a total increase of 4 nm in its diameter (i.e. in size). In contrast, in the case of air-annealing the reverse of this reaction takes place, i.e. oxidation, where O atoms replace Ge atoms in the Ge-Ge bonded cores, increasing the oxide thickness. Finally, the whole of the film (or the volume fraction probed by Raman) turns into germanium oxides.

EDX, FTIR and XANES analysis indicated that Type I-SG is composed of mainly Ge and O. Although these samples showed visible PL which peaked at 2.3 eV, similar to that of c-GeO_2, they were found to be free from any Ge nanocrystals (concluded from the Raman spectra). In contrast, Type II-SG samples were characterised as nanocrystalline with an average size of <2-3 nm, as prepared, and 8-9 nm after additional annealing in hydrogen, and they also showed weak visible PL located at 2.3 eV when excited at the same wavelength (442 nm). Moreover, the lineshape of the PL was also quite similar to those of c-GeO_2 and Type I-SG. Further, when Type II-SG samples were annealed in air the PL intensity increased by an order of magnitude despite the depletion of Ge nanoparticles, and when annealed in H_2 it almost quenched, even though the peak wavelength did not change. All these suggest that the PL observed from these materials have a common chemical origin, rather than QC, i.e. the PL originates from GeO_xs ($0<x\leq2$).

The energy dependence of visible luminescence from Ge nanocrystals has not previously been reported. Ge nanocrystals with visible luminescence was first observed in samples prepared by the co-sputtering method [28][29]. XPS and FTIR spectroscopy of samples prepared by RF magnetron sputtering of Ge chips on SiO_2 indicated that a-GeO_2 and a-GeO were formed at the surface of the Ge nanocrystals [30]. Room temperature PL from the SiO_2 films containing Ge nanocrystals showed a broad band around 2.2 eV and 2.3 eV regardless of the Ge nanocrystal sizes (e.g. [29]). In addition to the nanocrystal size independence visible luminescence appears also to be independent of fabrication method when Ge and O atoms are present (e.g. [28,29,31-36]). These samples are mostly reported to exhibit strong visible PL at 2.1-2.3 eV independent of the size of Ge nanocrystals (2-50 nm) and preparation conditions (also see Chapter 2).

The observation concerning the PL peak position is quite similar for chemically-etched Ge samples reported to date [17][37]. Miyazaki *et al.* reported weak PL in the NIR region from their H-terminated nanocrystalline Ge sample which easily quenched even after only 1 min. of thermal oxidation with a new, strong PL band located at 2.2 eV appearing [37]. The above observations give little support to attributing the visible luminescence to QC effects. Our results presented here add weight to the proposal that the origin of the 2.1-2.3 eV visible luminescence is from Ge-O defects [17][38].

4.3 Ge NANOCRYSTALS IN SiO_2

4.3.1 SIMS

The Ge SIMS profile in Fig. 4.18 shows the re-distribution of Ge ions, implanted at a dose of $7x10^{15}$ cm^{-2} in a 200 nm SiO_2 film, on annealing at 1050 °C. Although, initially, the distribution profile of the implanted ions could be described by a simple Gaussian, solid state diffusion of the ions due to high temperature annealing smears this profile. After annealing a fraction of the Ge atoms seem to be diffused out of the oxide (to the vacuum), while most of the atoms remain in the oxide. Furthermore, a fraction of Ge atoms are observed to segregate onto the Si substrate. By calculating the area under each curve in Fig. 4.18 it is possible to work out the density (percentage) of Ge atoms falling in each of such categories. Our calculations give $7.27x10^{22}$ for the total number of ions implanted into the oxide and $7.01x10^{21}$ and $4.09x10^{22}$, respectively, as the number of Ge atoms segregated onto the Si surface and remaining in the oxide after annealing. Thus, the percentage number density of Ge atoms remaining in the oxide, diffused out of the oxide and segregated onto the Si substrate will be 56.26±1%, 34.10±1% and 9.64±1%, respectively, if the initial density of atoms in the as-implanted oxide is taken as 100%.

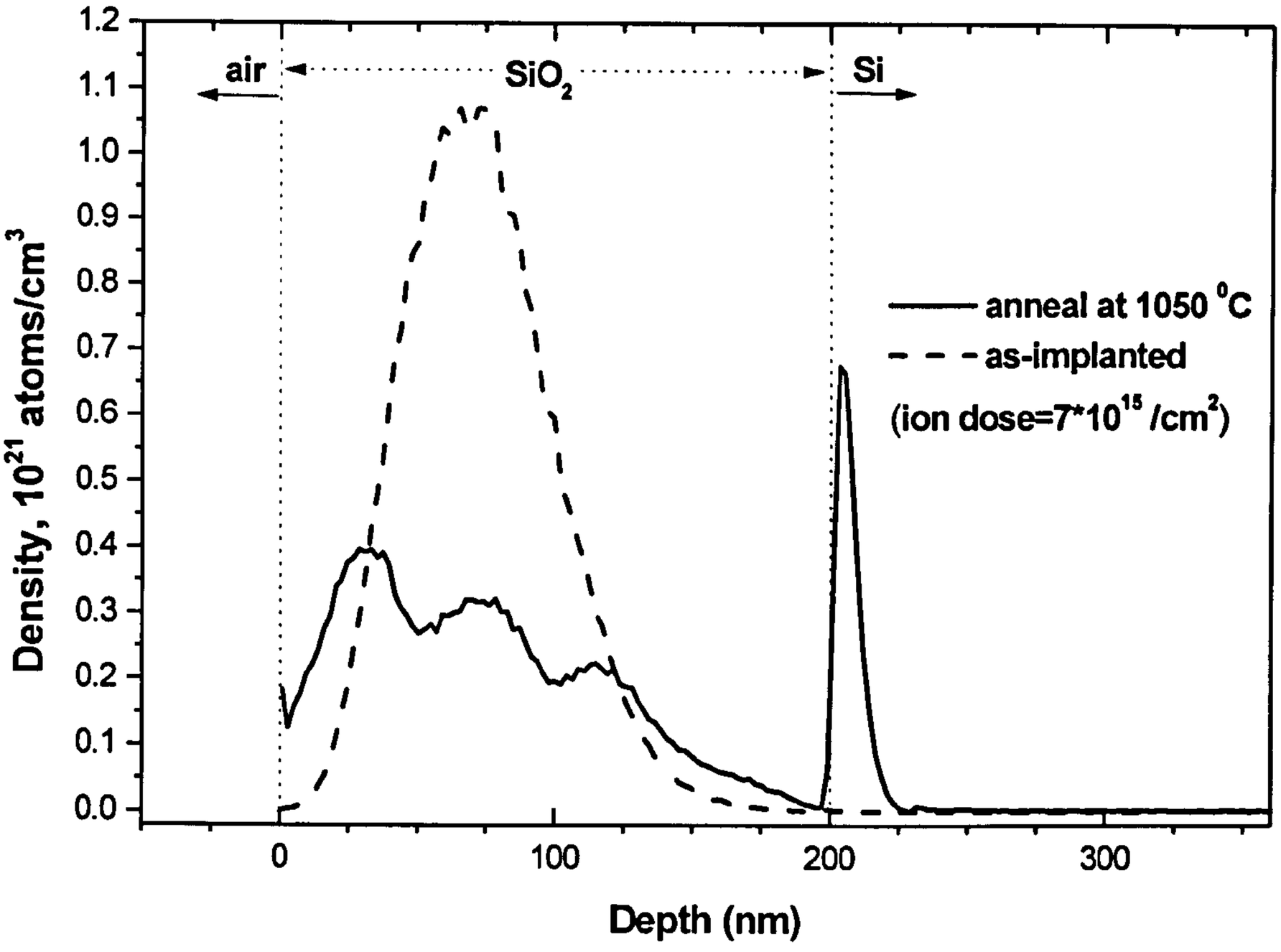

Figure 4.18 Ge SIMS profile before (dashed) and after (line) annealing for a 200 nm-thick SiO_2 film grown on a c-Si substrate and implanted with $7x10^{15}$ cm^{-2} Ge^+ at 100 keV. Compared to the initial density of ions implanted into the film the calculated fractions of Ge atoms remaining in the oxide, diffused out of the oxide, and segregated onto the Si substrate after annealing are 56.26±1%, 34.10±1% and 9.64±1%, respectively.

4.3.2 TEM

TEM analysis of the films implanted with a dose of $7x10^{15}$ ions cm^{-2} did not show formation of any Ge nanoparticles, even though the annealing temperature (T_a) was as high as 1050 °C. This suggests that the Ge atoms that remained in the film after annealing (see the SIMS profile in Fig. 4.18) are either in the form of germanium oxides or dissolved in the SiO_2 film. On the other hand, formation of Ge nanocrystals was clearly observed for the annealed films of SiO_2 implanted with the highest dose of $1x10^{17}$ cm^{-2}, whereas TEM images of the as-implanted films showed no Ge nanoclusters. Figure 4.19

provides the TEM images for a sample annealed at 800 °C for t_a = 60 min. Ge nanoparticles are dispersed uniformly in the oxide as a band that is approximately 60-70 nm wide (Fig. 4.19.a). It appears that the largest precipitates are located near the peak position of the concentration profile, and the smallest in the tails of the band. In addition, the size distribution of the nanocrystals is wide (Fig. 4.19.b); there are particles from 1-2 nm to 8-9 nm. It is also noted that these nanocrystals are randomly oriented. Besides, it is also predicted from the SIMS profile in Fig. 4.18 that a thin Ge-rich layer might also have formed near the SiO_2-Si substrate interface in this sample. We will discuss this later with the Raman results.

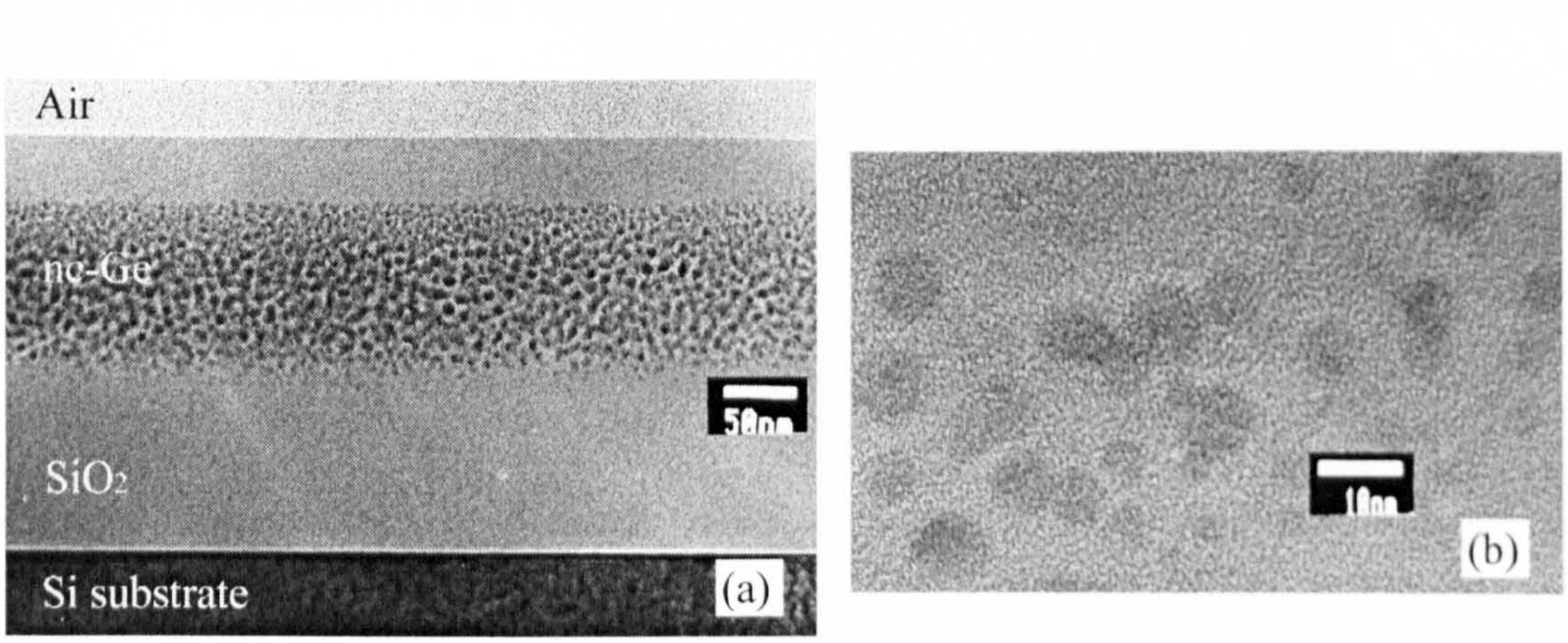

Figure 4.19 TEM images of a film implanted with $1x10^{17}$ cm^{-2} Ge^+ and annealed at 800 °C for 60 min showing (**a**) the distribution of the Ge nanocrystals (the band denoted as 'nc-Ge') within the oxide and (**b**) the size and crystallinity of the spherical nanocrystals dispersed in an amorphous matrix.

4.3.3 Raman

Raman spectra of the samples implanted with Ge^+ of dose $7x10^{15}$ cm^{-2} did not provide any strong evidence which indicate the formation of nanoparticles. However, a very weak Raman signal was seen near the c-Ge peak position (300 cm^{-1}) both for as-implanted and annealed films. Measurements were repeated after removing the oxide layers by wet etching, but a similar peak with a comparable intensity was still observable at ~ 300 cm^{-1}. It is expected that the weak, two-phonon peak coming from the c-Si substrate [39] will occur exactly at the same location as the c-Ge peak. Furthermore, it was observed by the Ge SIMS profile in Fig. 4.18 that a thin Ge-rich layer was formed at the Si-SiO_2 interface after annealing for this sample. Although TEM analysis did not show any Ge nanoparticle formation, we cannot still rule out the possibility that a few Ge nanocrystals might have formed in this film. To summarize, the Raman results for the $7x10^{15}$ cm^{-2} Ge^+-implanted films were inconclusive as to whether the origin of the signal was due to a scattering from Ge nanoparticles or a thin Ge-rich layer or c-Si substrate or a combination of two or three.

Figure 4.20 shows the Raman spectra of the films implanted with $1x10^{17}$ cm^{-2} Ge^+. The annealed film in this figure is similar to the one for which the TEM image was given in Fig. 4.19, except the T_a was 100 °C higher and the t_a was 15 min shorter in this case. The Raman spectrum of the as-implanted film (Fig. 4.20.a) is similar to that of a-Ge [20][40]. In the case of disordered semiconductors, such as amorphous and nanocrystalline, the $\mathbf{q} = 0$ selection rule that determines the Raman spectra of the bulk crystal is either fully or partially violated (relaxed) so that phonons other than the zone-centred phonons can also be observed in their Raman spectra. On the other hand, the spectrum of the annealed film exhibits a sharp peak near 300 cm^{-1} indicating the crystallisation of Ge in the film. The

width and spectral shape of this peak are different from those of bulk Ge but similar to those of nanocrystalline Ge [41]. In these measurements, the zone-centred Ge optical phonons peaked at 303.3 cm^{-1} with a FWHM of 5.8 cm^{-1} in the spectrum of bulk Ge (Fig. 4.20.c); whereas the peak in the spectrum of nanocrystalline Ge (Fig. 4.20.b) is downshifted to 301.5 cm^{-1} and asymmetrically broadened towards the lower frequency with respect to the bulk Ge peak.

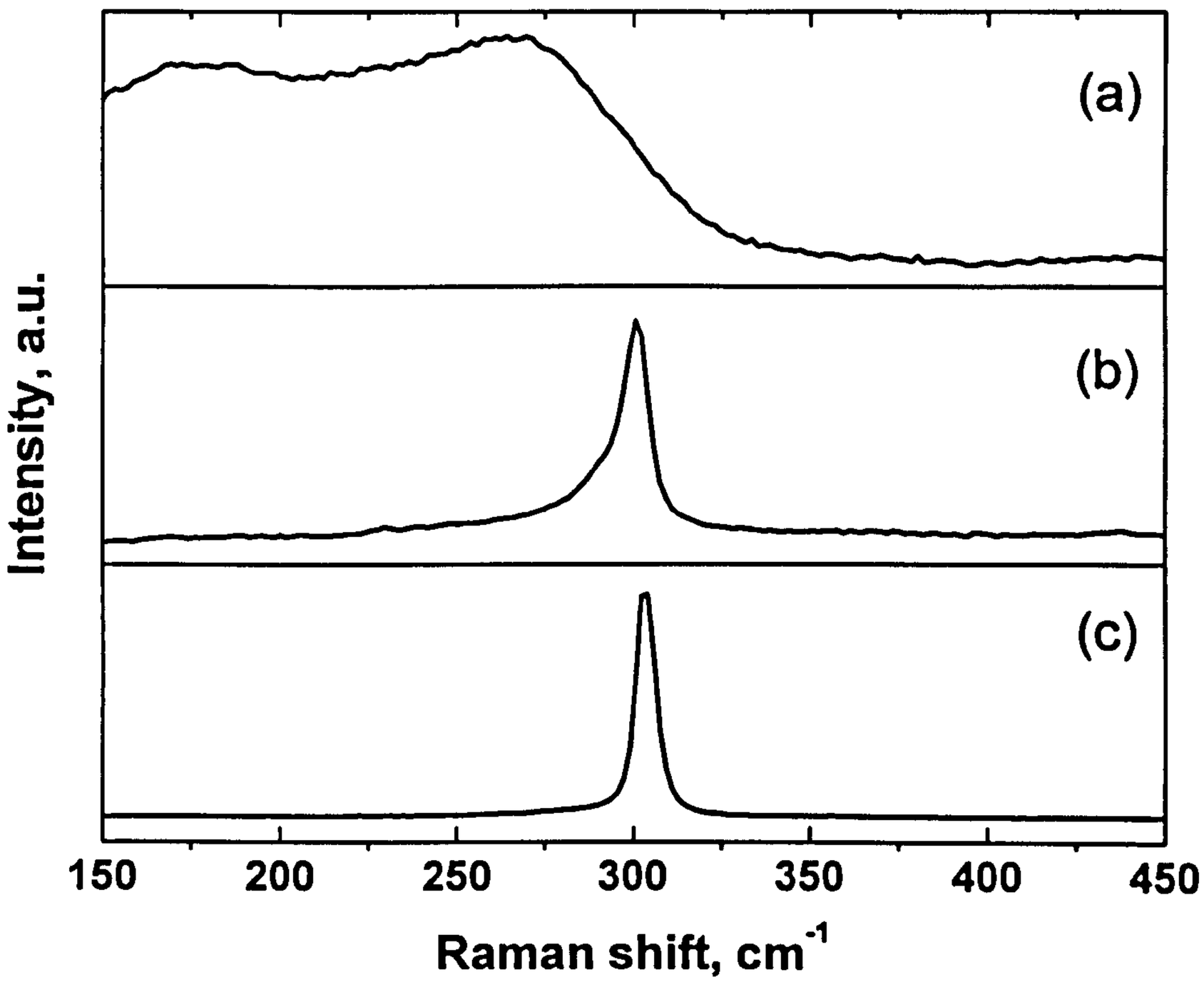

Figure 4.20 Raman spectra for a $1x10^{17}$ cm^{-2} Ge^{+}-implanted SiO_2 film (**a**) before and (**b**) after annealing (T_a = 900 °C) and (**c**) bulk Ge.

We also note that silicon, which was used as the substrate material in this study, also possesses a peak near 300 cm^{-1} and two weaker features at 229 and 435 cm^{-1} (besides the

main peak at 520 cm^{-1}) in its Raman spectrum. Kolobov *et al.* argued that most studies on the Raman scattering from Ge nanostructures grown on Si substrates have actually reached incorrect conclusions by totally ignoring this point and attributed this peak to the formation of Ge nanocrystals [42]. In Fig. 4.21, the contribution of the scattering from the Si substrate to our Raman spectrum (Fig. 4.20.b) has been eliminated by subtracting the normalised Raman spectrum of c-Si (curve 2) from that of nanocrystalline Ge (curve 1). As can be seen from the difference of the two spectra (curve 3), the contribution of the scattering from the Si substrate is almost negligible in the Raman spectra of our samples. We also acquired Raman spectra from the substrate after removing the SiO_2 film by wet etching (in a 20% diluted HF) in order check whether a thin Ge rich-layer had been grown at the Si-SiO_2 interface and contributed to the Raman signal in Fig. 4.20.b. However, no traces of Ge were found on the Si surface (instead we determined that a-C was formed on the Si substrate (see below), which is probably caused by one of the diffusion pumps in the ion-implanter system). These show that formation of the Ge nanocrystals inside the oxide is responsible for the peak observed at around 300 cm^{-1}.

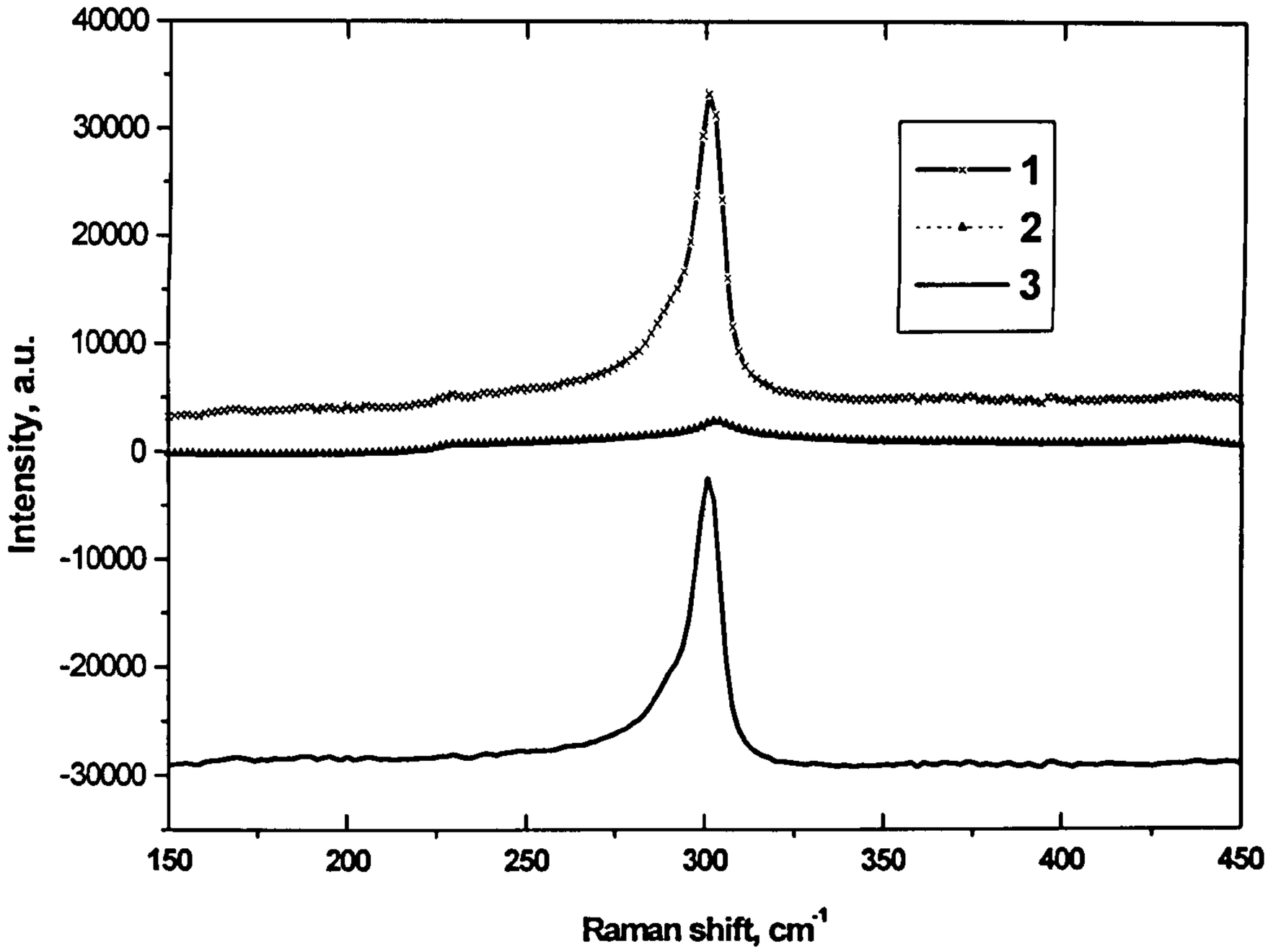

Figure 4.21 Raman spectra for a SiO_2 film implanted with $1x10^{17}$ cm^{-2} Ge^+ and annealed at 900 °C (curve 1) and bulk Si (curve 2) and their difference (curve 3).

4.3.3.a Raman Modelling

For semiconductor nanocrystals, spatial confinement of phonons in a finite volume (on the order of a few hundred angstroms [25]) is expected to partially relax the wavevector selection rules and hence cause modifications in the bulk Raman peak such as peak-frequency shifting, peak broadening, and increase in peak asymmetry. These effects are observable in our case. To calculate the mean Ge crystallite size in our ion-implanted films we adopted the phonon confinement model developed for Si nanocrystals by Campbell and Fauchet [10] (see Chapter 3) using the phonon dispersion relation given in [22] for Ge. In our model we assume spherical crystals. This has been confirmed by TEM (Fig. 4.19). Using the experimental bulk value 5.8 cm^{-1} as the

natural linewidth and a_{Ge} = 0.565 nm for diamond structure as the Ge lattice constant, the calculated peak frequency and linewidth as a function of crystallite size (d_{ave}) are plotted in Fig. 4.22. For Ge nanocrystals, it can be seen from both curves that significant changes to the Raman spectra must become observable below a critical diameter of about 20 nm. Therefore, it is expected for stress-free Ge nanocrystals that as d_{ave} decreases the peak frequency should shift to lower frequency (i.e. redshift), while the linewidth of the peak increases for d_{ave}<20 nm.

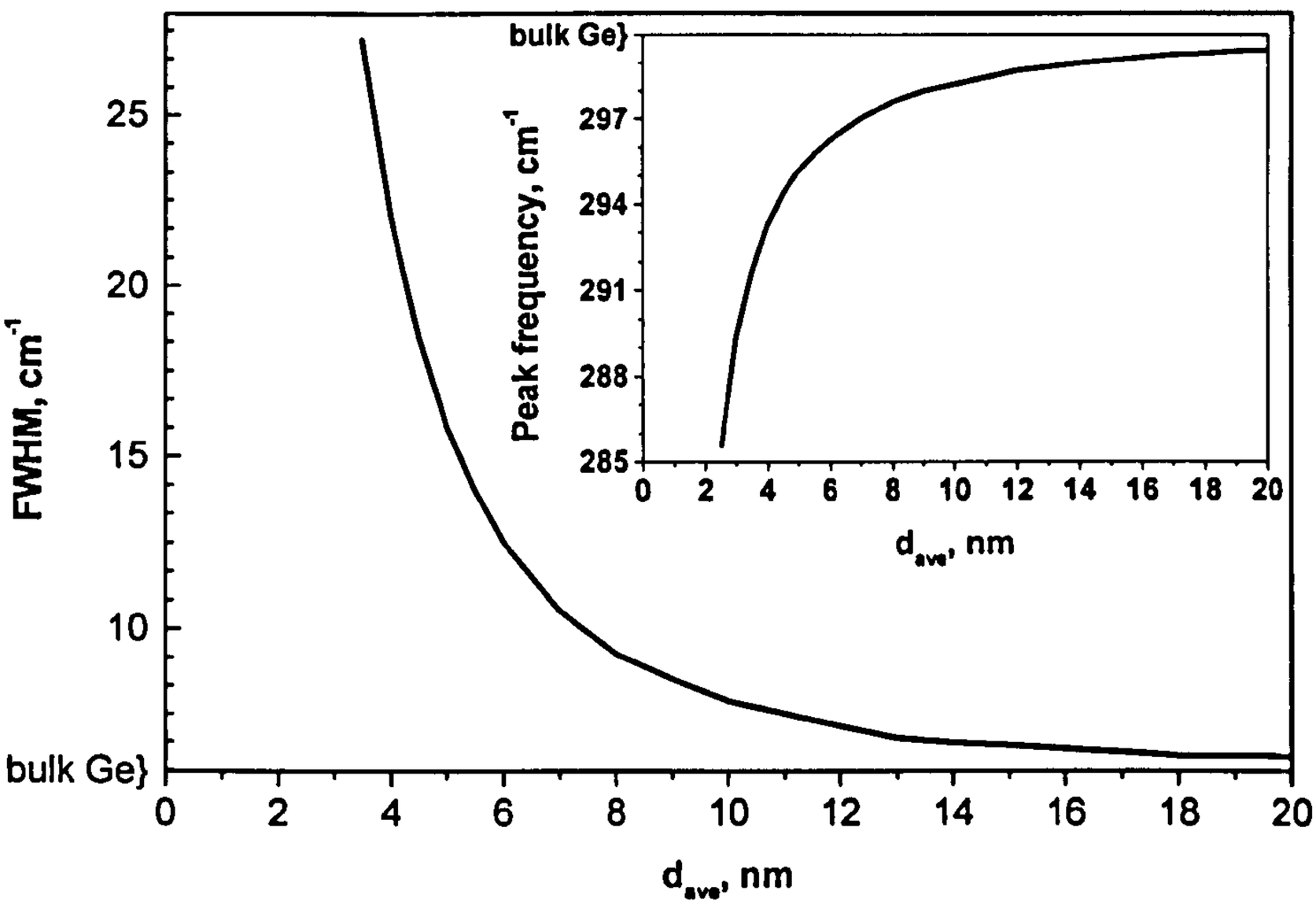

Figure 4.22 Calculated linewidth (FWHM) and peak frequency as a function of average crystal size (d_{ave}) for spherical Ge particles.

For the background-subtracted optical phonon peak in Fig. 4.21 (curve 3) a lineshape fit is made in Fig. 4.23, using the calculated spectrum for d_{ave} = 7.5 nm. The linewidth of 9.9 cm^{-1} for the calculated spectrum is large compared to the bulk value 5.8 cm^{-1}. It

can be seen that the agreement of the lineshapes around the peak is fairly good. However, there exists an extra intensity below 290 cm^{-1} for the experimental spectrum. This difference is attributed to the contribution of a fraction of very small Ge nanocrystals in the film. This point deserves further investigation. Moreover, for the respective crystal size the peak frequency is expected to redshift by 2.7 cm^{-1} from the corresponding value for bulk (300.0 cm^{-1}). This shift is about 1.8 cm^{-1} in the case of experimental spectra. Although the experimental resolution was 1 cm^{-1}, the small difference in the expected value of the redshift can be, alternatively, due to a compressive stress on the nanocrystals; compressive stress is well known to cause the Raman spectrum to blueshift (e.g. [43]). Fujii *et al.* prepared Ge nanocrystals embedded in SiO_2 matrices by annealing co-sputtered Ge-SiO_2 films and studied the size dependence of their Raman spectra [41]. They reported that, despite the fact that the linewidth broadens as the average crystal size decreases (from 15 to 6.1 nm) in good agreement with the expectations (i.e. with their phonon confinement model), the peak frequency did not shift appreciably (even a small blueshift was observed for the smaller sizes). They attributed the latter effect to a compressive stress exerted on the Ge nanocrystals by the surrounding SiO_2 medium. Since the nearest-neighbor distances are 0.24 nm and 0.16 nm for Ge and SiO_2, respectively, it is considered that the lattice mismatch yields a compressive stress on the Ge nanocrystals [22][41].

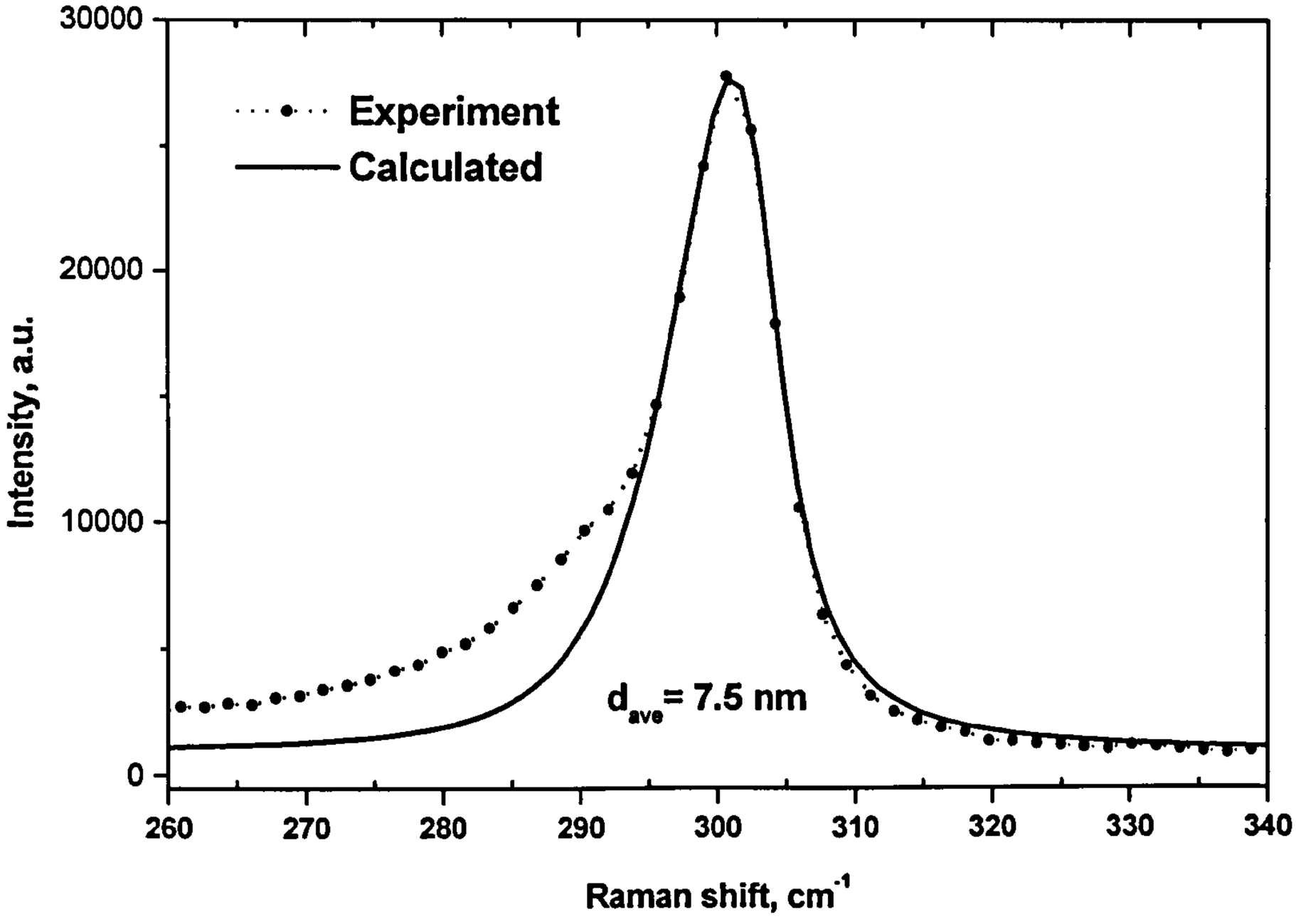

Figure 4.23 Experimental background-subtracted Raman spectrum (curve 3, Fig. 4.21) of Ge nanocrystals compared to theoretical Raman spectrum calculated for d_{ave} = 7.5 nm using a phonon confinement model.

Figure 4.24 gives the Raman spectra of the films implanted with $3x10^{16}$ cm^{-2} Ge^+ before and after annealing (for T_a = 700, 900, 1050 °C). The spectrum of the as-implanted film is similar to that in Fig. 4.20.a and shows that the Ge in the film is in an amorphous phase. The Raman spectra for all of the annealed films, on the other hand, are characterised by a peak near the optical phonon mode of c-Ge, i.e. ~ 300 cm^{-1}, indicating the crystallisation of Ge and formation of nanoparticles. The presence of higher intensity shoulders on both sides of this peak are attributed to the amorphous phase or to very small Ge nanoclusters. By fitting of the Ge peak around 300 cm^{-1} with calculated Raman spectra appropriate to their lineshapes, we estimate the d_{ave} as 4.5±1, 5.0±1 and 5.6±1 nm in the films annealed at 700, 900 and 1050 °C, respectively. The FWHM of the calculated spectra are 18.5, 15.9 and 13.7 cm^{-1}, respectively. It is not surprising that the d_{ave}

increases with the T_a. Moreover, it is also clear from Fig. 4.24 that the peak frequency of experimental spectra do not show any appreciable systematic redshift, whereas it is expected that the peak should redshift by 5.7, 4.9 and 4.1 cm^{-1}, respectively, from 300 cm^{-1}. In fact, as the d_{ave} (or T_a) decreases the peak slowly blueshifts: the peak frequency is 302.9, 303.6, and 304.4 cm^{-1} for the films with T_a = 1050, 900, and 700 °C, respectively (the measured bulk value is 303.3 cm^{-1}). This observation is in line with the report of Fujii *et al.* [41], adding more weight to the proposal that a compressive stress is exerted onto the Ge nanocrystals by the surrounding oxide.

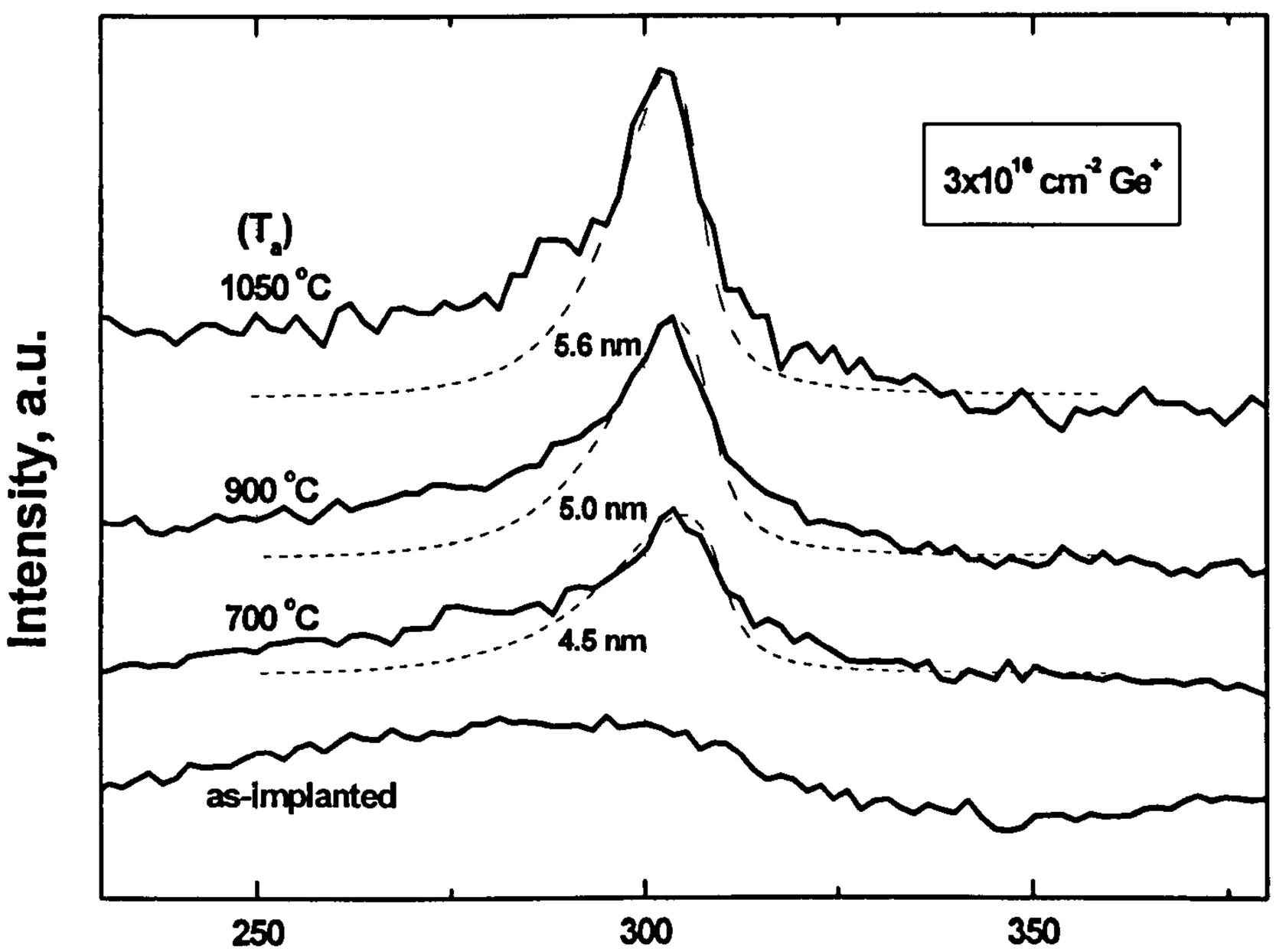

Figure 4.24 Raman spectra for the films implanted with $3x10^{16}$ cm^{-2} Ge^+. The spectrum of the as-implanted film is amorphous Ge-like. The crystalline Ge peaks in the spectrum of annealed films are fitted using a phonon confinement model considering spherical nanocrystals and the calculated average crystal sizes are indicated near the theoretical curves.

4.3.4 PL

We observed visible PL emission from all of the samples, (non-annealed (as-implanted) or annealed, nanocrystalline or not), peaking between the green-yellow and having a shoulder towards red wavelengths, but only when excited using a high laser power (~ 1 W). Fig. 4.25 shows a typical PL spectrum for a $7x10^{15}$ cm^{-2} Ge^{+}-implanted film before and after annealing. It is apparent that the energy, intensity and lineshape of these spectra are very similar to each other. Thus, this might suggest that the origin of both spectra must be the same. Since no strong evidence was found (by TEM or Raman analysis) for the presence of any Ge nanostructures in these films one cannot relate this luminescence to Ge nanocrystals. Instead, we can attribute it to some kind of defects in the oxide, generated by the ion-implantation, that might act as recombination centres. These alone suggest that there is no necessity for the presence of Ge nanocrystals to observe visible PL emission similar to those in Fig. 2.25. However, it is expected that a high temperature annealing at 1050 °C must reduce the amount of such defects in the oxide and hence the PL intensity. This point needs further investigation.

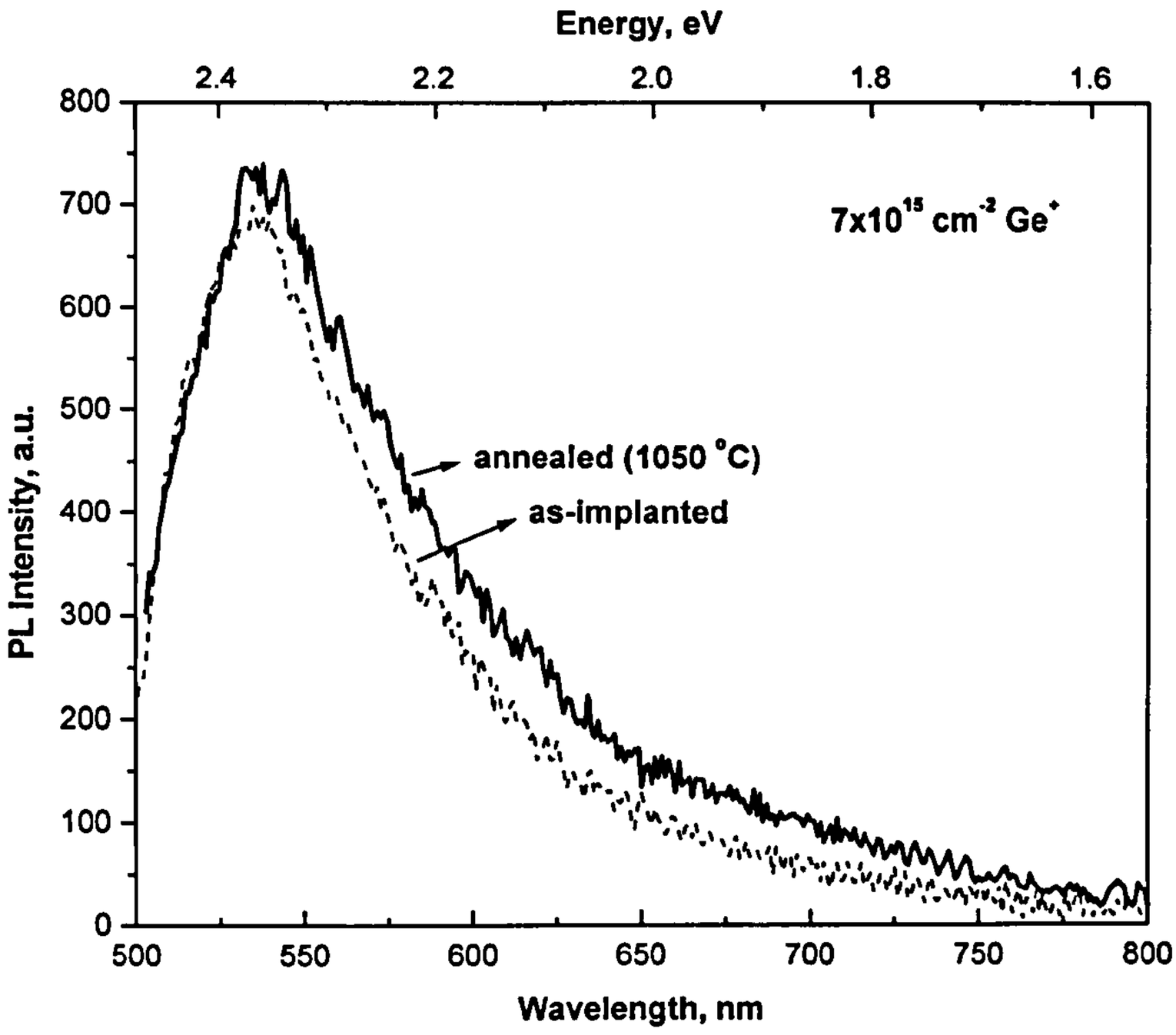

Figure 4.25 Visible PL spectra for a $7x10^{15}$ cm^{-2} Ge^{+}-implanted 200 nm thick SiO_2 film before and after annealing. (The spectra were excited with a 488 nm Ar^{+} laser operating at 1 W.)

We also note that a sharp PL band in the IR (at ~ 0.8 eV) was recordable at 100 K (not shown) from the annealed $7x10^{15}$ cm^{-2} Ge^{+}-implanted films with only 100 nm thick oxide. Combined with the Ge SIMS profile analysis, this PL is considered to originate from the Ge-rich ($Ge_{1-x}Si_x$) layer formed at the Si-SiO_2 interface, having a bandgap very close to that of bulk Ge.

Different from the observation in Fig. 4.25, the PL behaviour of the other films implanted with higher doses and containing Ge nanocrystals indicated that formation of nanocrystals cause an appreciable increasing of the PL intensity without changing the spectral shape very much. To show this we removed the oxide films from a series of nanocrystalline samples and monitored the evolution of the PL spectra (along with the

Raman spectra). Given in Fig. 4.26 are the 514.5 nm (2.408 eV)-excited micro-PL (and Raman) spectra for the $1x10^{17}$ cm^{-2} Ge^{+}-implanted samples before and after annealing (curves 1 and 2) and after removal of the oxide layers (curves 1-b and 2-b). Also given in the same figure is the spectrum of a non-treated SiO_2 film grown on Si (same oxide thickness). Since these spectra were excited with a slightly lower excitation energy than the spectra in Fig. 4.25 (by 0.29 eV), the PL energy is shifted to ~ 2 eV in this case (with higher energy excitation the PL band peaks at 2.25 eV for these samples, not shown). It is clear that the PL is greatest from the sample containing Ge nanocrystals (curve 2). The SiO_2 film on Si does not luminesce on its own (curve 3). As noted earlier, for the series of $1x10^{17}$ cm^{-2} Ge^{+}-implanted samples, an a-C film was grown on the Si substrate during ion-implantation. It can be seen from Fig. 4.26 that there is a broad Raman band at ~ 1500 cm^{-1} in curve 1 and 1-b associated with the a-C. Besides it has several other weaker (Raman or PL) features in the same region where the PL is observed from these samples (see the Fig. 4.26.inset). The as-implanted film show a weak PL emission located near 2.0 eV with the a-C related features superimposed on it (curve 1). These features sharpen somewhat and the single broad a-C band splits into its graphite (G) and diamond-like (D) bands at 1350 and 1610 cm^{-1} [44], respectively, following the annealing (see curve 2-b), but they do not cause an increase in the PL emission (compare curve 2 and 2-b). Therefore, the strong PL emission from the nanocrystalline sample can be assigned to the presence of Ge nanocrystals. Such an intensity increase for the 2.2-2.3 eV PL was earlier reported by Maeda *et al.* after annealing of their Ge-SiO_2 co-sputtered films (formation of Ge nanocrystals was observed by high-resolution TEM images) [35].

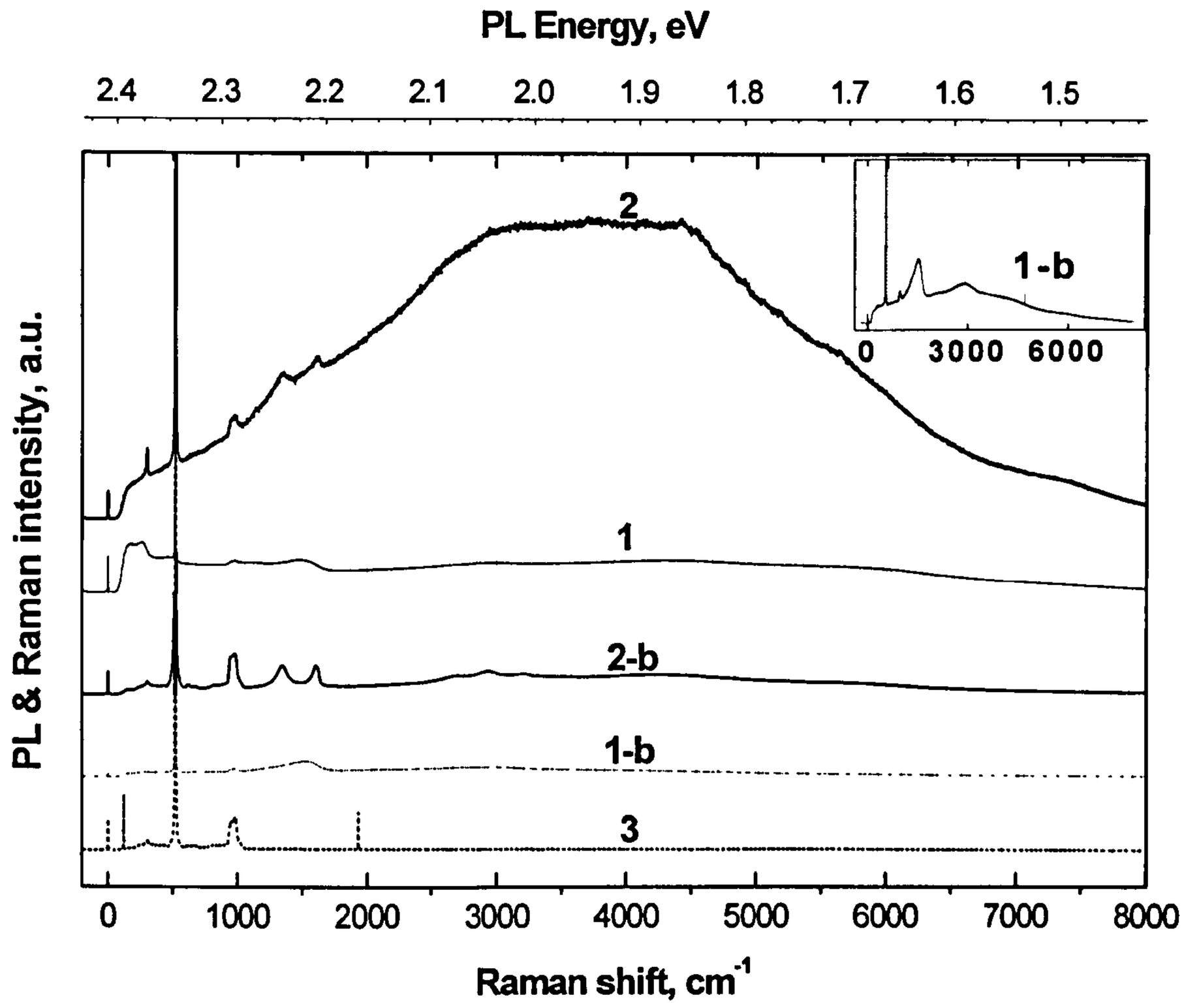

Figure 4.26 Micro-PL and Raman spectra for **1-** as-implanted ($1x10^{17}$ cm^{-2} Ge^{+}) 200 nm SiO_2 film on Si, **1-b-** as-implanted and oxide removed, **2-** annealed (T_a= 900 °C, t_a = 45 min), **2-b-** annealed and oxide removed, **3-** a 200 nm SiO_2 film on Si. Inset gives the detail of the a-C related features in the spectrum of 1-b.

As a result, we cannot totally rule out the possibility that Ge nanocrystals might themselves emit (or take a role) in the visible luminescence occurring in the region 2.0-2.3 eV. Calculations indicated that the PL energy would shift from 2.6 to 1.2 eV as the Ge nanocrystal size increases from 4 to 8 nm [45]. It is considered that recombination of photo-excited carriers in small Ge nanocrystals can take place on the surface of nanocrystals where luminescent defect-centres were probably formed. More data are needed to elucidate the mechanism(s) of the PL from our samples.

4.4 SPARK PROCESSED Ge

4.4.1 SEM

Figure 4.27 depicts a series of cross-sectional SEM images of sp-Ge. The film thickness is expected to be from a few to a couple of hundred of microns for spark processed materials. As seen from Fig. 4.27.a the thickness of the film is not uniform. The thickness of the sp-Ge film is nearly comparable to that of the c-Ge wafer used for sparking, reaching ~ 450 μm at near its maximum point (i.e. near the middle of the Figure), and the diameter of the circular film is about 2 mm. Moreover, the sp-Ge film is not flat either near the surface (notice the upward curvature) or near the bottom of the film where it is separated from the untreated substrate. The film, as being circular-shaped near the bottom, resembles a small portion of a sphere.

The sp-Ge microstructure represents a rough character. There are large voids (discontinuities) running across the film, leaving very large columnar structures in between. Furthermore, there are plenty of spherical cavities of various sizes embedded in the film (Fig. 4.27.b). It is also noticeable that there are small, ball-shaped micro-granules in-between and on the surface of the large features of the film. Fig. 4.27.c and d show the detail of such micro-granules near the (sp-Ge)–(c-Ge) interface. The size of these particles ranges between a few tens of nanometers to a few hundred nanometers.

Although it is not easy to suggest how all these rough features in sp-Ge film are produced, it can be conjectured from location of the particles seen in Fig. 4.27.c and d (near the untreated substrate) that such small particles are produced at the initial stage of

the spark process. These then grow up to become larger particles or large columnar structures of the film repeating the coalescence. Observation of similarly shaped larger particles between and at the surface of the film further supports this suggestion. Cavities, on the other hand, might be produced during coalescence of the particles due to the energetic nature of the spark treatment.

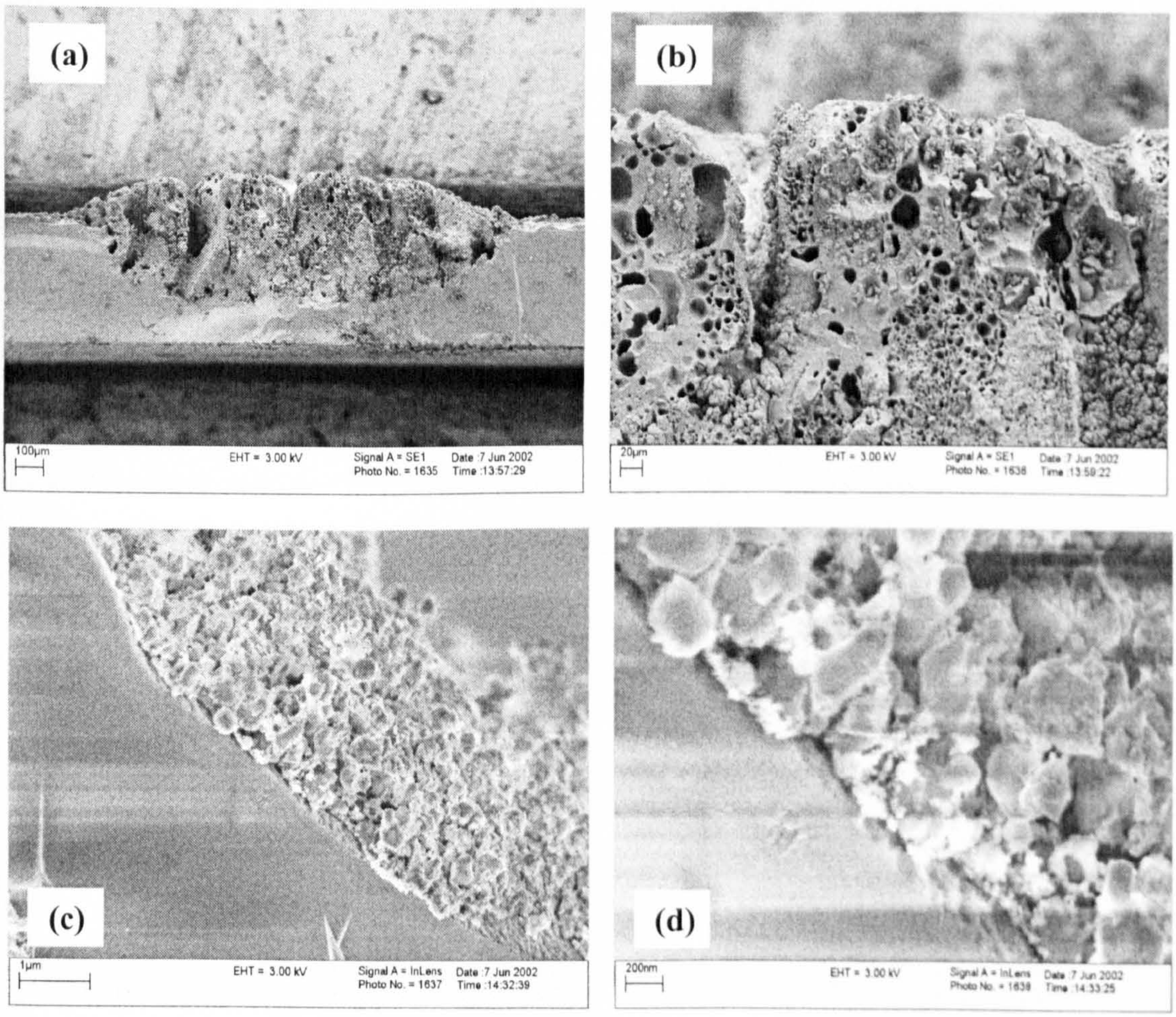

Figure 4.27 A series of cross-sectional SEM micrographs of sp-Ge.

Lastly, it was noted during SEM measurements that the sp-Ge film was not so stable against highly energetic beams (comparable or to higher than 5 kV). Such beams were observed to cause modifications of the film by distorting its microstructure. This suggests that the sp-Ge film is not composed of purely Ge-Ge bonded material, which is stable to such beams, but also of other form(s) of material(s) of different chemistry.

4.4.2 PL

Visible PL spectra of the sp-Ge samples were obtained using the 325 nm line of a He-Cd laser, prior to the micro-PL and Raman measurements. According to the PL data in Fig. 4.28 from 3 sp-Ge samples prepared under equivalent conditions, the PL of sp-Ge can be viewed as a combination of a blue band peaking near 420 nm (3 eV) and a yellowish-green band at ~ 530 nm ± 20 nm (2.2-2.4 eV) with a shoulder in the orange-red (around 1.9 eV). These values are in good agreement with those reported for sp-Ge prepared under similar conditions (i.e. in stagnant air and for 20 min) [46][47].

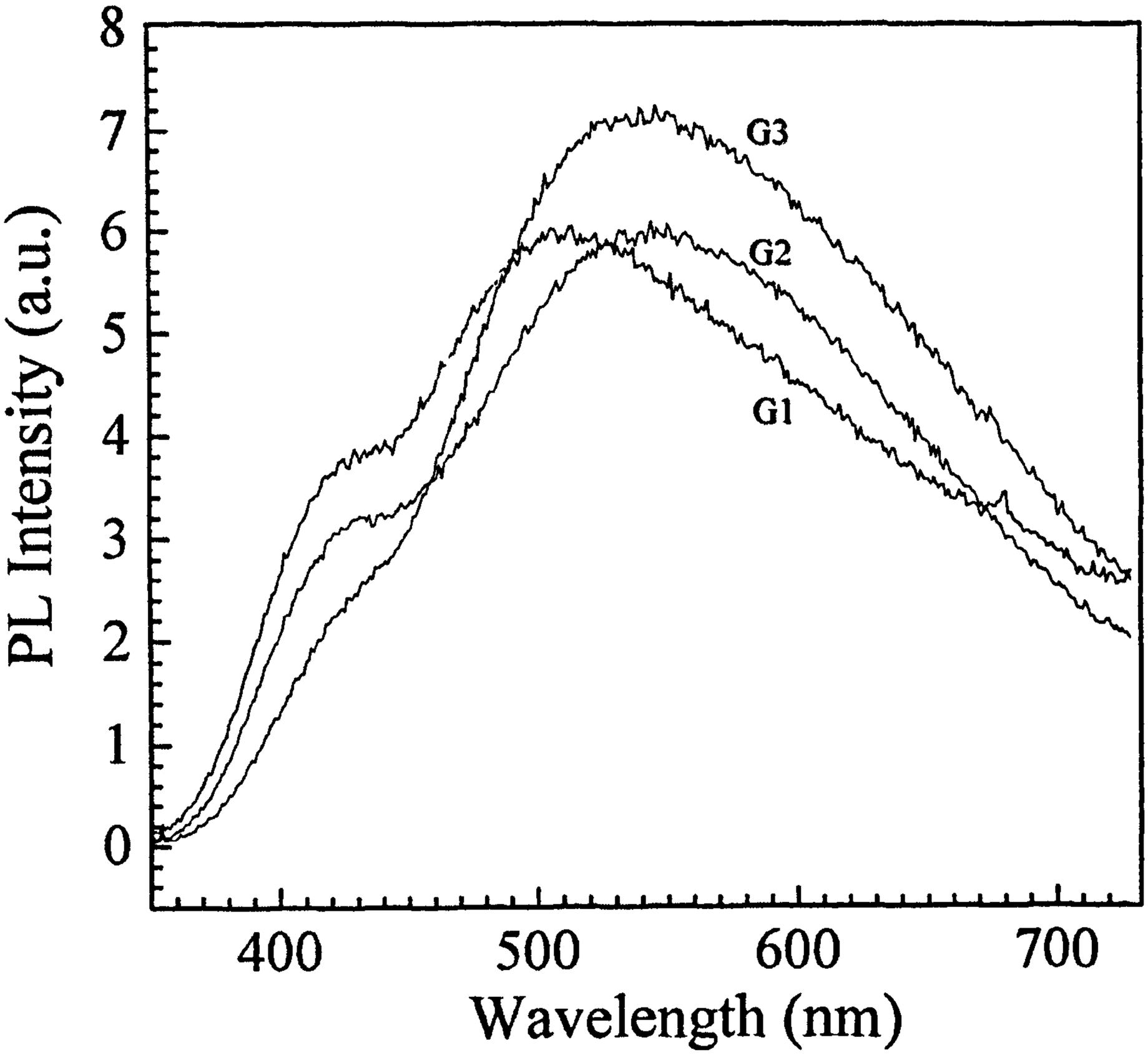

Figure 4.28 Room temperature PL spectra of sp-Ge (3) prepared by sparking undoped c-Ge for 20 min in stagnant air. Samples are marked as G1, G2 and G3.

4.4.3 Micro - Raman & PL

Fig. 4.29 illustrates the Raman spectra of c-Ge and c-GeO_2. In these measurements, the zone-centred optic phonons peaked at 300.9 cm^{-1} with a full width at half maximum (FWHM) of 4.6 cm^{-1} in the spectrum of c-Ge. The GeO_2 spectrum is characterised by several peaks at 122, 165, 211, 246, 262, 327, 442, 515, 583, 592, 858, 881, 960, and 972 cm^{-1}; however, due to the lack of Ge-Ge bonding there is no appearance of a Ge peak at ~ 300 cm^{-1}, as can be expected.

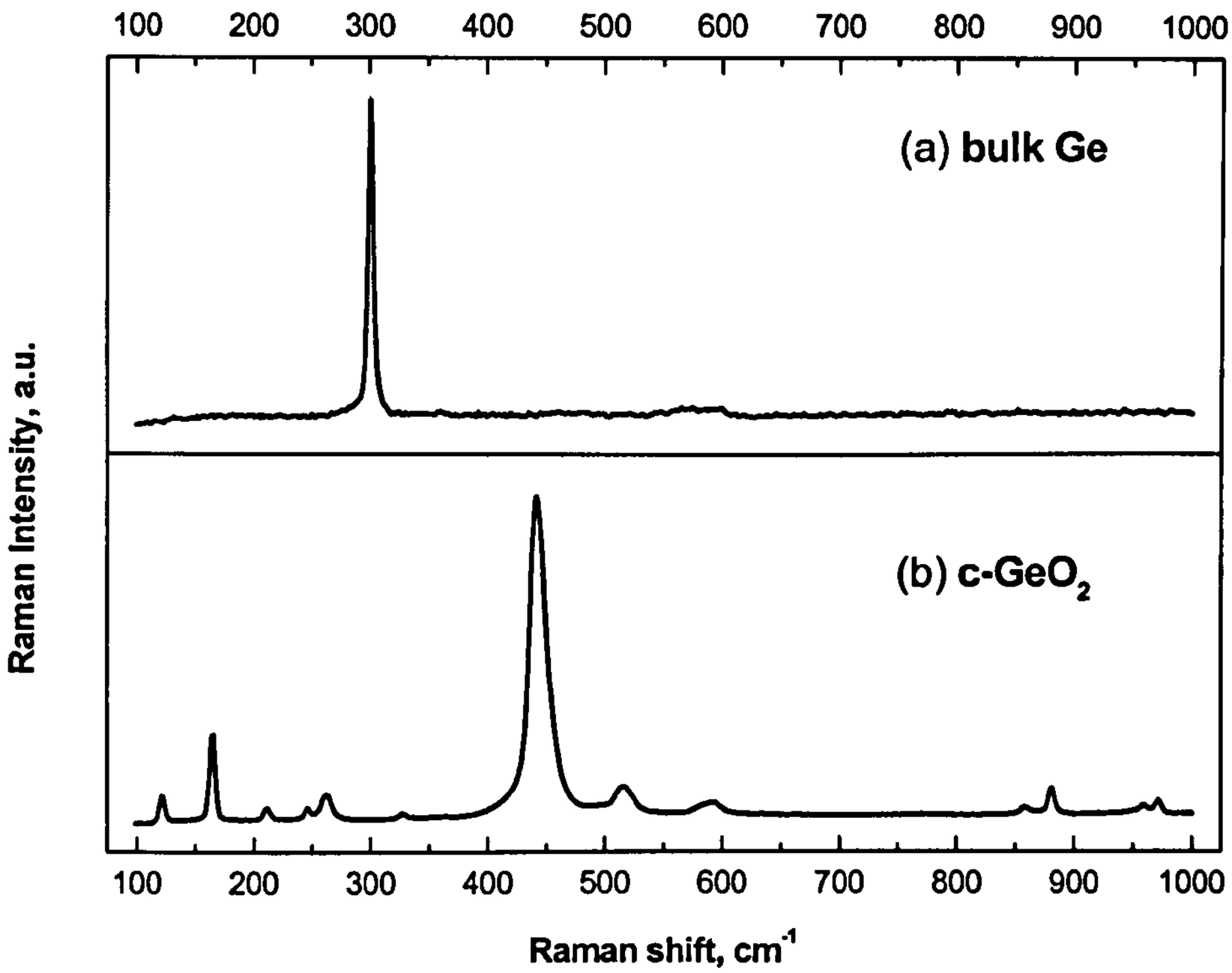

Figure 4.29 Raman spectra of **(a)** bulk Ge and **(b)** commercial crystalline GeO_2 powder. One-phonon spectrum of bulk Ge is characterised with a peak at 300.9 cm^{-1}; whereas no Ge peak, but several other peaks due to Ge-O vibrations (given in the text), are observable in the spectrum of GeO_2.

Figure 4.30 shows a micro-PL and Raman spectrum taken from sp-Ge sample G1 using a 514.5 nm (2.41 eV)-excitation source. Two PL bands are clearly observable near 1.9 eV and 1.7 eV; these energies correspond to the energy range of the orange PL band (seen as a shoulder to the yellow-green band) in Fig. 4.28 where the spectra were excited at 325 nm (3.81 eV). Moreover, there is possibly a third band around the Raman features peaking near 2.2-2.3 eV, corresponding to the yellow-green band in Fig. 4.28, with an attenuated intensity.

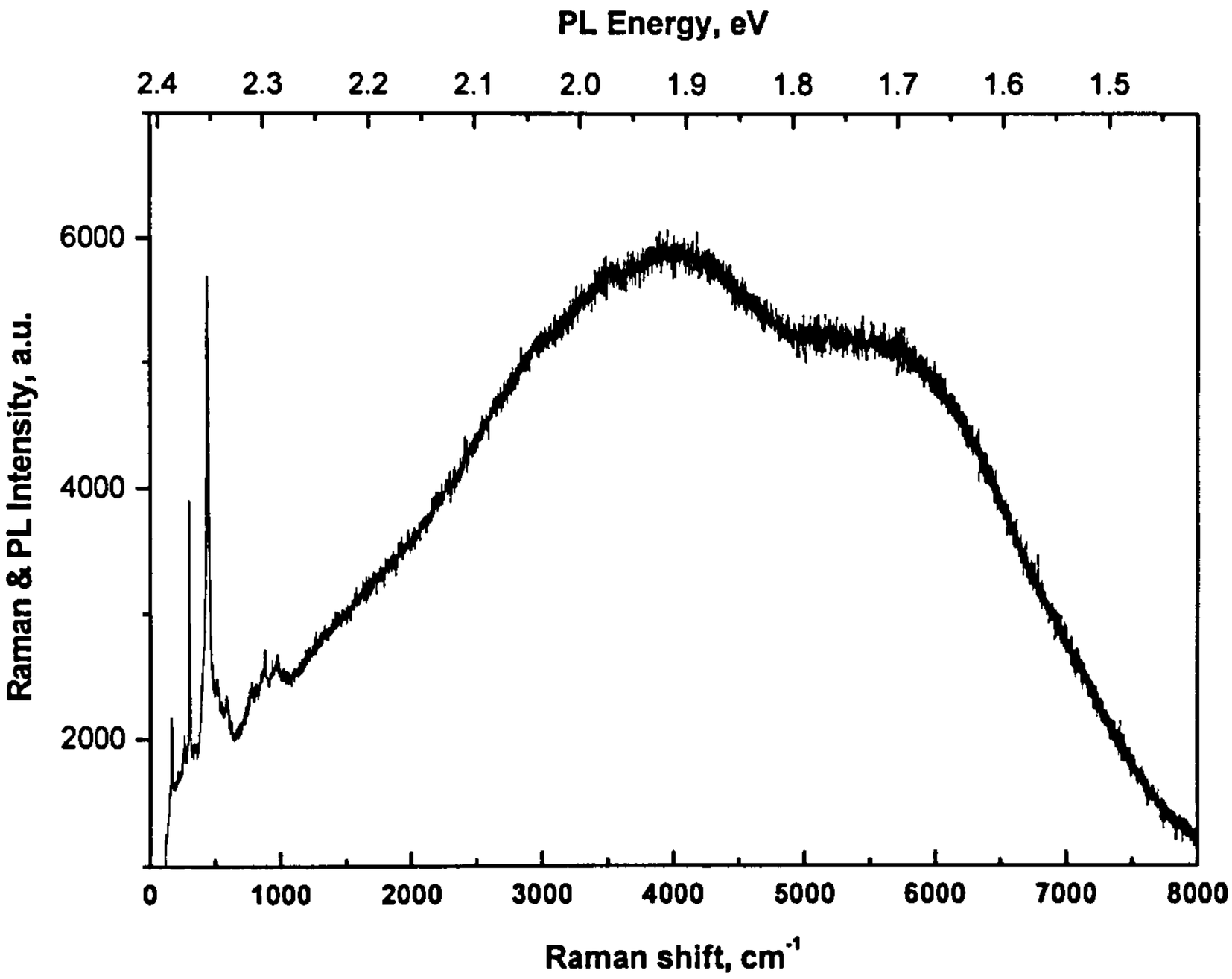

Figure 4.30 Room temperature micro-Raman & PL spectrum of sp-Ge (G1).

Figure 4.31 gives the detail of the Raman spectrum in Fig. 4.30 and compares it to that of GeO_2 crystal. According to these spectra it can be suggested that the sp-Ge film consists of Ge-Ge bonded material (elemental Ge) and Ge-O bonded material (GeO_xs). The Ge peak in sp-Ge spectrum is situated at 299.7 cm^{-1} and has a FWHM of 6.0 cm^{-1}, that is it is 1.2 cm^{-1} redshifted and 1.4 cm^{-1} broadened compared to the bulk Ge peak. Formation of Ge nanocrystals, around 12-13 nm in size, by spark treatment might be responsible for these differences. On the other hand, though somewhat less resolved most of the Raman-active lines of c-GeO_2 are also realised for the sp-Ge sample (G1). For example, the broad band at ~ 965 cm^{-1} in G1 spectrum seems to correspond to a combination of the two sharp peaks at 960 cm^{-1} and 972 cm^{-1} in GeO_2 spectrum. Another difference between the two spectra is the existence of an extra feature at ~ 760 cm^{-1} in the sp-Ge spectrum; we attribute this new mode to O-vacancy complexes in GeO_2.

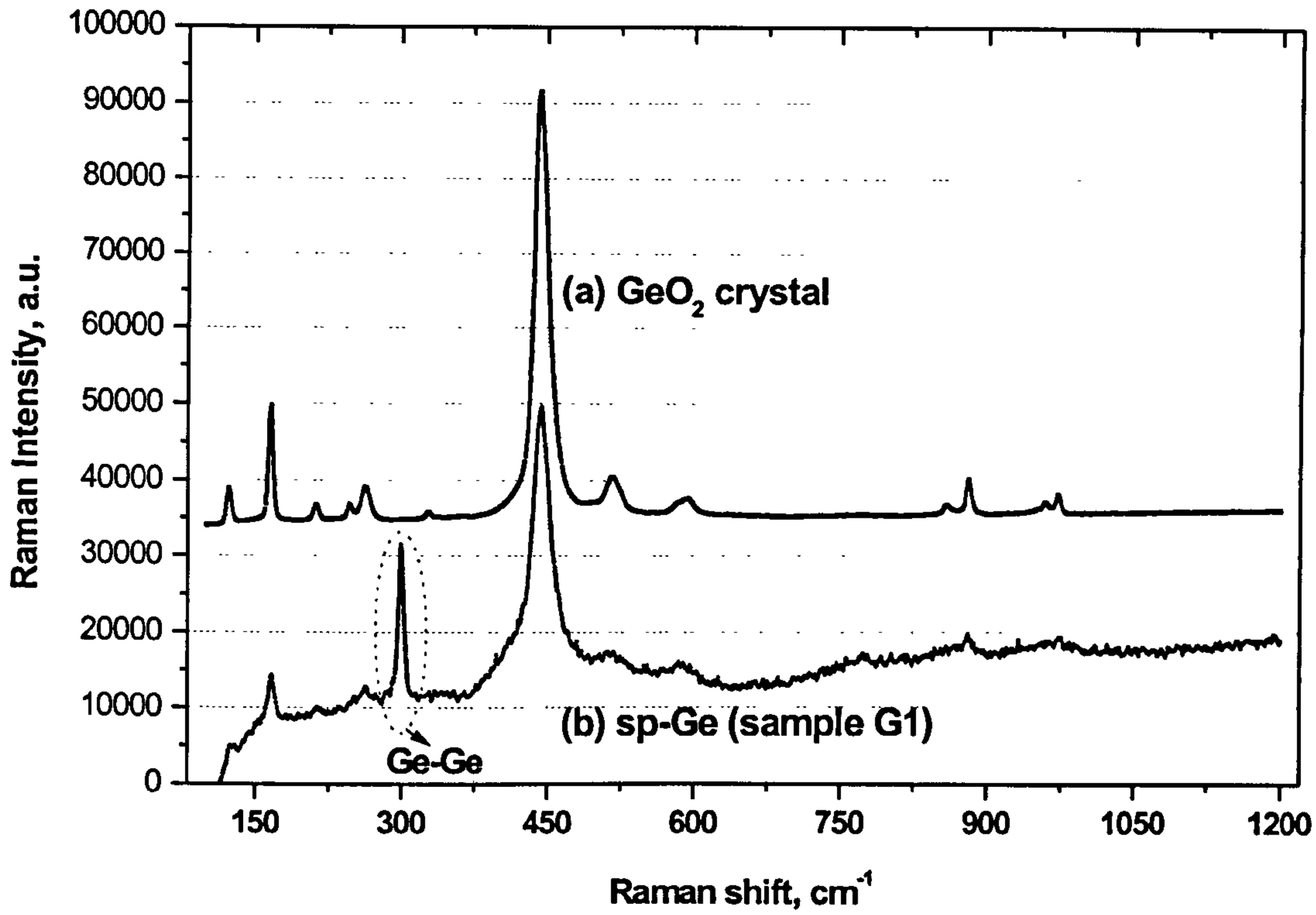

Figure 4.31 Normalised room-temperature Raman spectra of (a) c-GeO_2 and (b) sp-Ge sample G1. Ge-Ge bonding character seen in G1, different from that of GeO_2, is indicated.

Figure 4.32 compares two micro-PL and Raman spectra obtained at two different spots on a single sp-Ge film (sample G2). Both PL spectra are similar to that in Fig. 4.30 taken from sample G1, however, there is a clearly pronounced extra feature near ~ 3000 cm^{-1} superimposed on the 1.9 eV PL band for the present spectra. The origin of this feature will be discussed later.

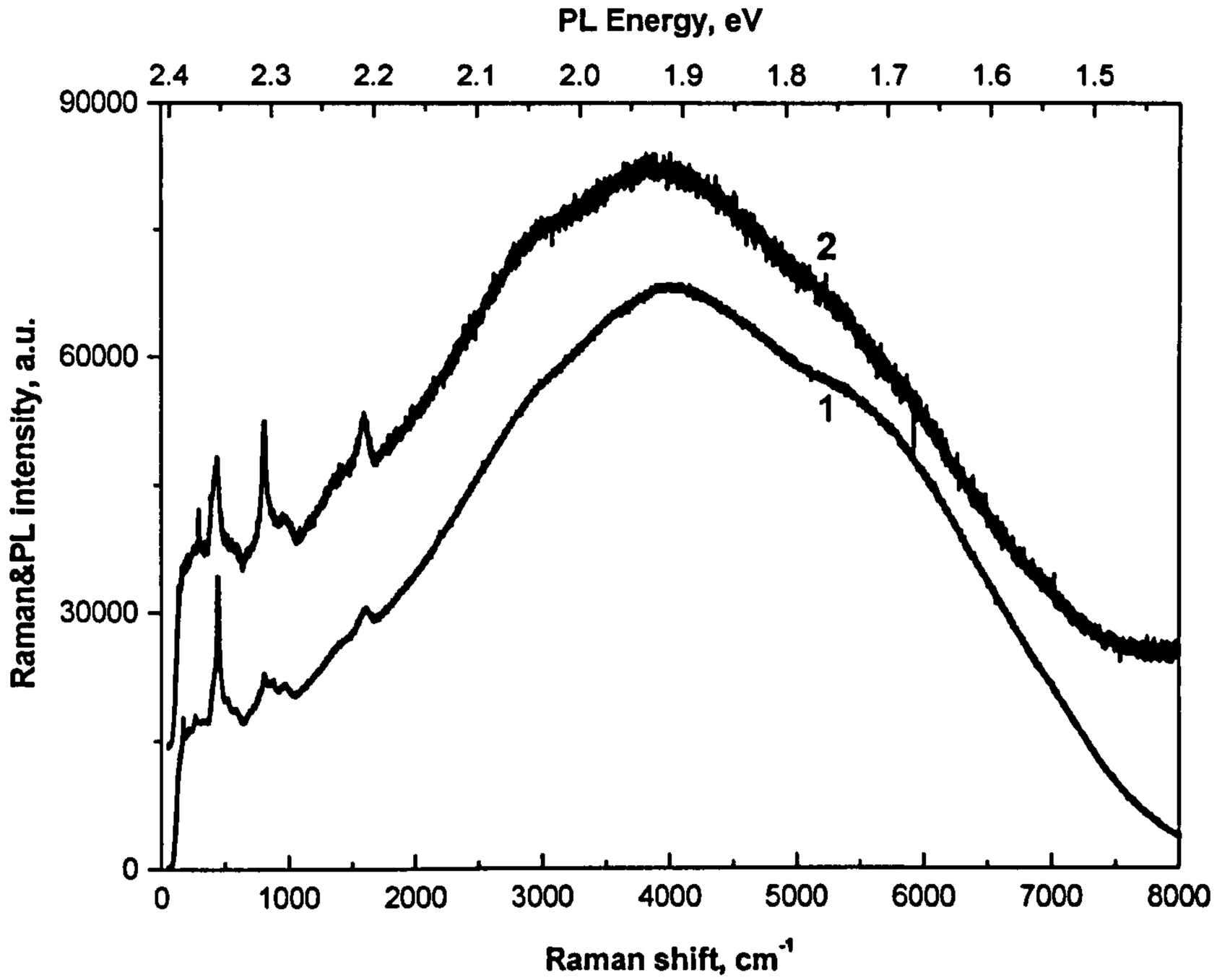

Figure 4.32 Comparison of two micro-Raman and PL spectra taken from different spots on the same sp-Ge film (G2).

Figure 4.33 gives detail of the Raman spectra in Fig. 4.32. Different from that of the spectrum in Fig. 4.31 taken from sample G1, the present spectra clearly indicates the presence of a-C in the film, probably as a contaminant (considering that the sparking was performed in stagnant air); peaks seen at around 1400 cm^{-1} and 1600 cm^{-1} in both curves 1 and 2 are assigned to the graphite (G) and diamond-like (D) peaks bands of a-C [44][48,49]. Beside, Lockwood *et al.* interpreted a Raman band near 3000 cm^{-1} as second-order scattering from a-C in their a-C containing samples [49]. It can also be seen in Fig. 4.33 that there are certain differences between the Ge-O lines of the two spectra. Whereas curve 1 represents most of the characteristic Ge-O lines, most of these fine details are lost in curve 2. For example, in curve 2, the main line peculiar to the crystalline

GeO_2 structure at around 440 cm^{-1} appears to soften and lose its sharpness. This is probably, also in comparison to curve 1, due to an increased disorder in the present GeO_2 signature. On the other hand, in curve 2, a new, sharp peak grows at 813 cm^{-1} on a background hump between ~ 750 and ~ 1000 cm^{-1} that is also observed in the other Raman spectra. This new line and the broad hump are absent in the Raman spectrum of c-GeO_2 (see Fig. 4.29 or Fig. 4.31), but they are near to the position of the main IR-active band of GeO_2 (see the inset to Fig. 4.33). Therefore, we suggest that a relaxation in the selection rules for the Raman and IR spectra [50] results in the observation of these disorder-induced features in the Raman spectrum. It is also possible to assume that a different, uniquely-configured GeO_x structures might form locally, as a result of the energetic spark-treatment.

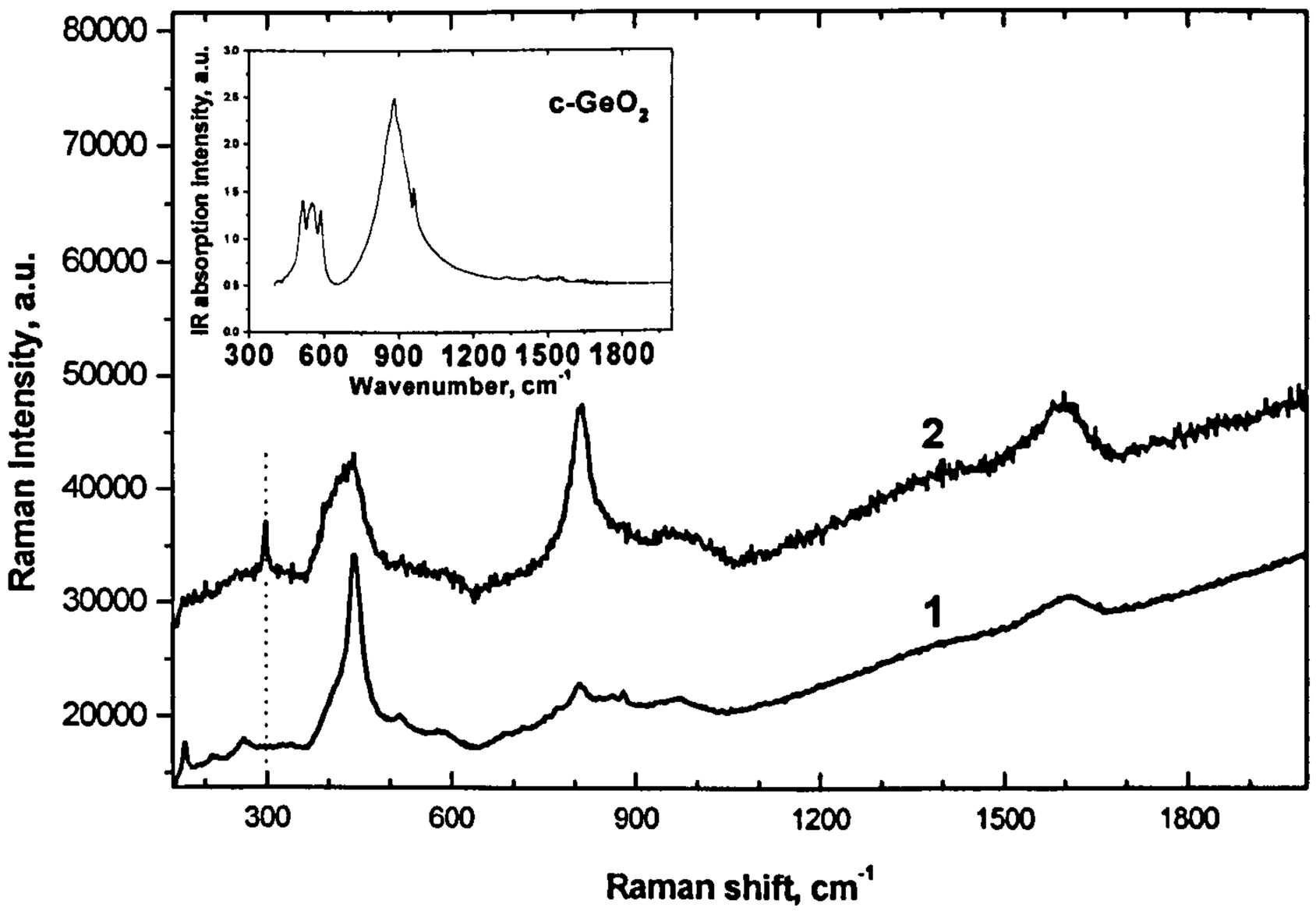

Figure 4.33 Two representative micro-Raman spectra from sample G2 (detail of Fig. 4.32). The dotted line at 300 cm^{-1} is drawn to emphasise that there is no Ge peak in curve 1, but in curve 2. The inset gives the IR absorption spectrum of c-GeO_2.

We also note that there is a striking difference between the two spectra in Fig. 4.33 as there is no contribution from crystalline Ge (either nanometer-sized or bulk) in curve 1, but there is in curve 2, though the simultaneously-obtained PL spectra were very similar for the same spots of the film (see Fig. 4.32). On the other hand, the crystalline Ge peak in curve 2 occurs at 300.0 cm^{-1} with a FWHM of 4.7 cm^{-1}, i.e. only 0.9 cm^{-1} downshifted and 0.1 cm^{-1} broadened in comparison to the bulk Ge peak. This might correspond to a crystal size comparable to 20 nm or simply to bulk Ge.

Micro-PL spectra observed from sp-Ge sample G3 (not shown) were similar to those from the other samples. However, in one particular Raman spectrum taken from the film of sample G3 (Fig. 4.34) it was noticeable that the Ge peak was remarkably different from the others observed in this study since it resembled those of relatively small (<10 nm) Ge nanocrystals [41]. The intensity of the crystalline Ge peak is, however, relatively small when it is compared to those of the weak Ge-O lines in Fig. 4.34.

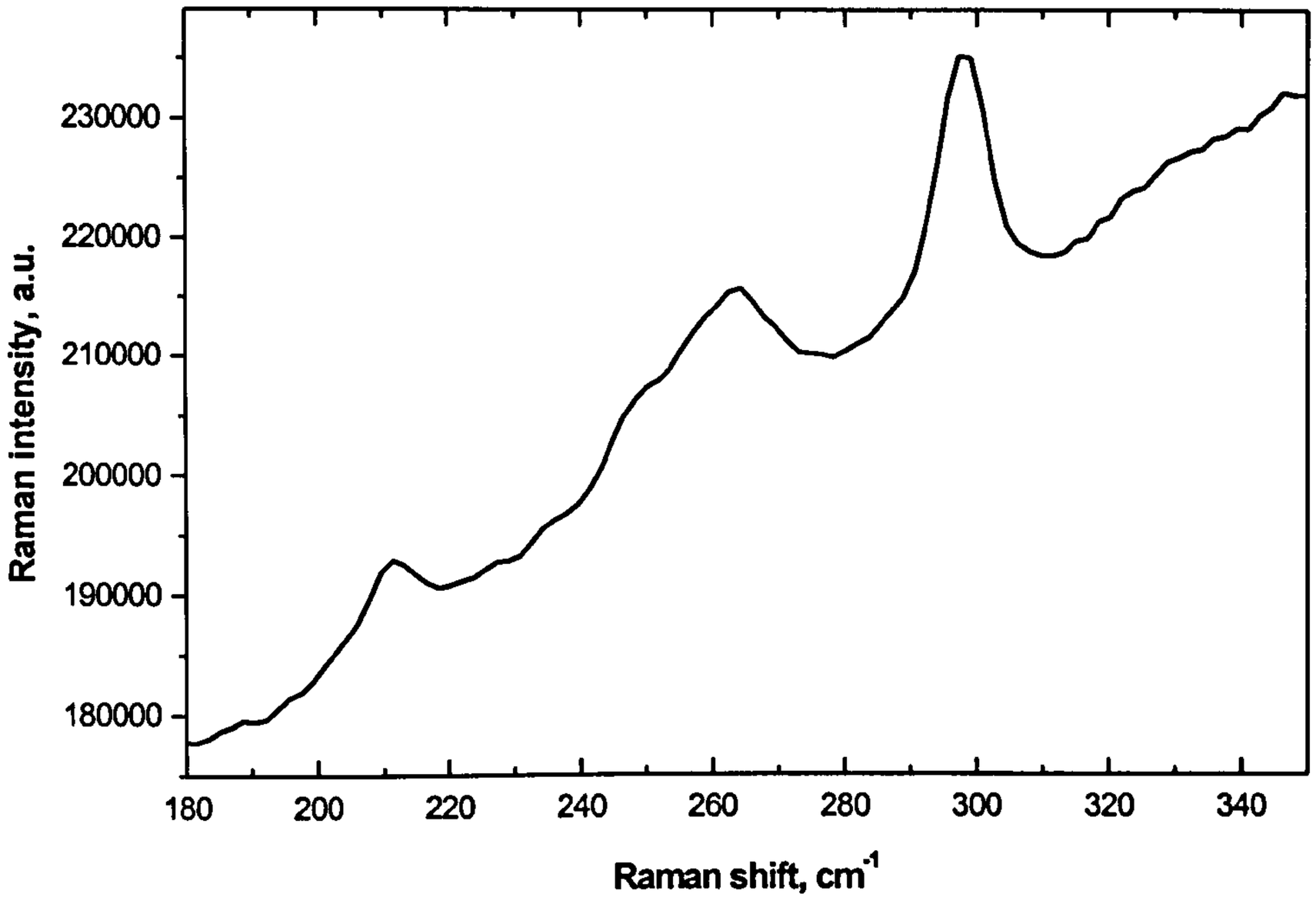

Figure 4.34 A micro-Raman spectrum from sample G3 between 180-350 cm^{-1}. Relative intensity of the Ge peak is comparable to those of the (weak) GeO_2 lines.

In Fig. 4.35 the crystalline Ge peak in Fig. 4.34 is compared to the normalised bulk Ge peak after background subtraction. The sp-Ge peak is at 297.6 cm^{-1} and has a width of 7.6 cm^{-1}, which corresponds to a downshift of 3.3 cm^{-1} and a broadening of 3.0 cm^{-1} compared to those of the bulk (300.9 and 4.6 cm^{-1}, respectively). An average nanocrystal size of 6-7 nm can be predicted when the peak frequency downshifting and peak linewidth broadening effects are taken into consideration. Also given in the same figure is a calculated spectrum for a crystal size of 6.6 nm. The quality of the illustrative fitting between this curve and the sp-Ge curve is, however, not quite satisfactory. The experimental curve does not represent as much asymmetry in its lineshape as that of the calculated one. Instead, its lineshape resembles a Gaussian curve. Therefore, effects (or perhaps mechanisms) other than the relaxation of wavevector-selection rules must be considered here, such as local laser heating, lattice expansion or strain in the films.

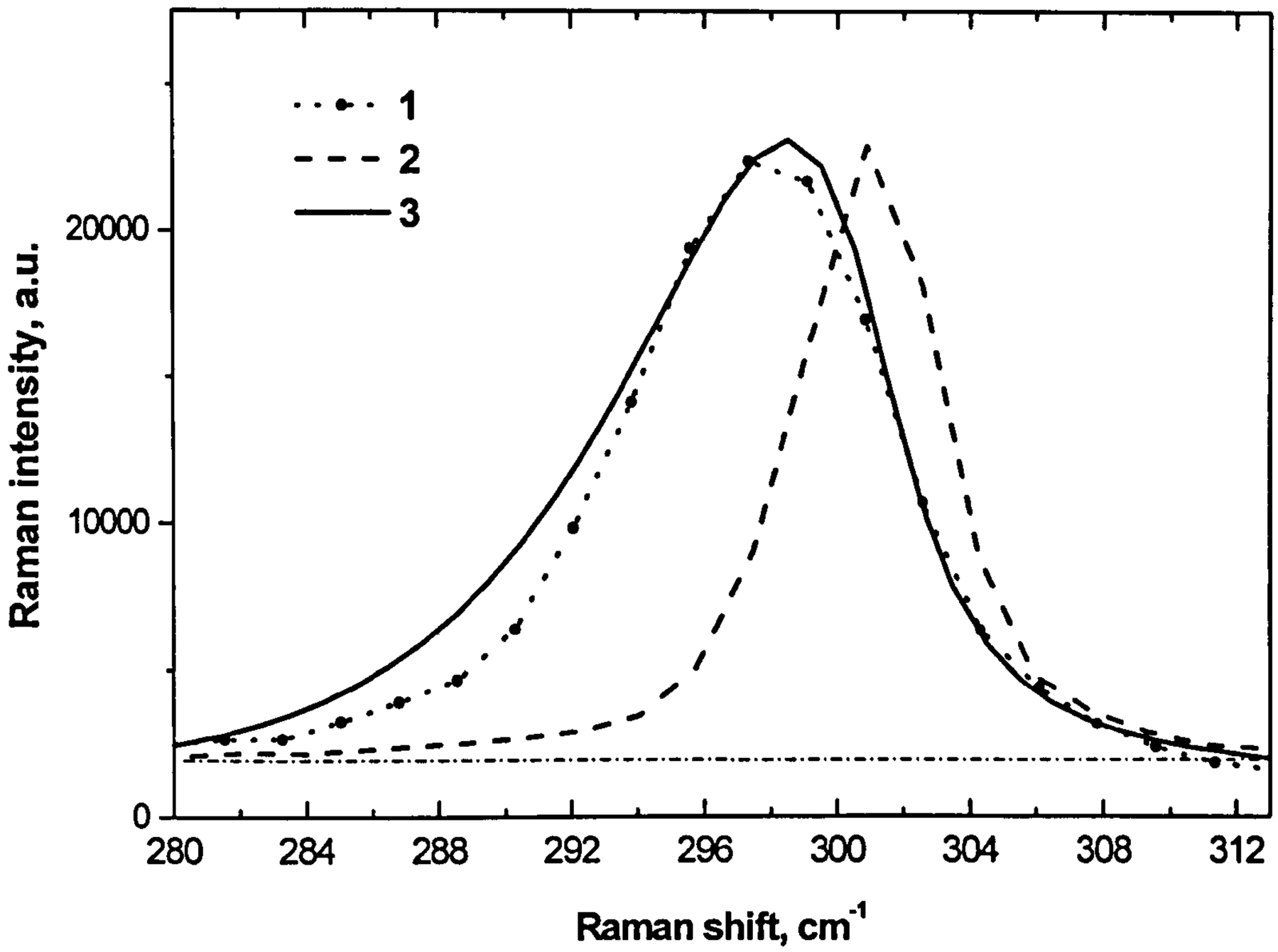

Figure 4.35 1- Background-subtracted Raman spectrum of sp-Ge (G3), **2-** Normalised spectrum of bulk Ge, **3-** a calculated spectrum for a crystal size of 6.6 nm using a phonon confinement model considering a spherical shape. The calculated spectrum is shifted by 0.6 cm^{-1} to higher frequency to provide a better visual fit to the sp-Ge curve.

4.4.4 Discussion

We will first discuss the micro-structure of the films. As can be seen from most of the Raman spectra (e.g. Fig. 4.33, Fig. 4.34), the intensity of the crystalline Ge signal was small compared to that of the GeO_2 signal. For example, in Fig. 4.34, even the intensity of the weak Ge-O Raman lines between 200-300 cm^{-1} is comparable to that of the c-Ge peak. In addition to this, it was observed in a few cases that there was even no Ge signal discernible at all in the Raman spectra (e.g. Fig. 4.33, curve 1). Based on the XPS data from sp-Ge samples S.S. Chang *et al.* [47] suggested that the Ge nanocrystals might be

embedded into GeO_2 layers. The present Raman and SEM results can also be explained using this model. For instance, the Raman signal due to elemental Ge regions might well be attenuated if they are surrounded by thick GeO_x layers. Further it is also possible to think that only a minor volume fraction of the material probed by the laser might consist of elemental Ge (in the form of small nanocrystals or 'microcrystals'). The instability of the sp-Ge layers to energetic electron beams during SEM measurements must be due to the low stability of the (thick) GeO_xs.

Therefore the present experiments suggest that the sp-Ge films are composed of crystalline Ge and GeO_xs. Further, it seems possible that Ge nanocrystals, as small as 6-7 nm in diameter, can be formed by spark treatment of c-Ge wafers. If there are Ge nanocrystals present in these films they are expected to be buried into thick GeO_x layers. The (local) Raman signal coming from the GeO_x layers, on the other hand, showed large variations between samples (compare Fig. 4.31 to Fig. 4.33) and even across a single film (compare curve 1 to curve 2 in Fig. 4.33), suggesting the existence of different structural configurations in these films. Therefore, it can be argued that the micro-structural uniformity of sp-Ge is 'poor'.

Now we discuss the luminescent properties of sp-Ge. Micro-PL measurements in the orange PL band of sp-Ge indicated (different from those in [46][47]) that this band actually consists of a finer structure, showing two clearly distinguished peaks at around 1.9 eV and 1.7 eV. Moreover, our simultaneously taken micro-Raman and PL spectra demonstrated unambiguously that there is, however, no need for Ge-Ge bonded material to realise PL from sp-Ge in this region, hence suggesting that the observed PL must be associated with Ge-O bonded material only. However, it is desirable to know the types of

the defects present in these oxide layers to elaborate the nature of the two PL bands at 1.9 eV and 1.7 eV.

Nevertheless, similar micro-PL and Raman measurements for the other two PL bands of sp-Ge (i.e. blue and yellow-green) using different excitation energies (> 2.41 eV) would probably be very helpful to determine the exact (simple) chemistry and physics responsible for the PL emission.

4.5 REFERENCES

[1] On the same Raman day for example it was 520.7 cm^{-1} with a FWHM of 4.7 cm^{-1}, for a laser power of 4 mW on the sample of c-Si.

[2] M. Holtz, W.M. Duncan, S.Zollner and R. Liu, *J. Appl. Phys.*, **88(5)**, 2523 (2000).

[3] M.I. Alonso and K. Winer, *Phys. Rev. B*, **39(14)**, 10056 (1989).

[4] F.Lu, C.H. Perry, F. Navamar, N.L. Rowell and R.A. Soref, *Appl. Phys. Lett.*, **63(9)**, 1243 (1993).

[5] S. Takeoka, K. Toshikiyo, M. Fujii, S. Hayashi and K. Yamamoto, *Phys. Rev. B*, **61(23)**, 15988 (2000).

[6] R. Tsu, H. Shen and M. Dutta, *Appl. Phys. Lett.*, **60(1)**, 112 (1992), and refs. 5 and 6 therein.

[7] E.V. Jelenkovic, K.Y. Tong, Z. Sun, C.L. Mak and W.Y. Cheung, *J. Vac. Sci. Technol. A*, **15(6)**, 2836 (1997).

[8] P.Y. Timbrell, J.M. Baribeau, D.J. Lockwood and J.P. McCaffrey, *J. Appl. Phys.*, **67(10)**, 6297 (1990).

[9] J.S. Lannin, *Phys. Rev. B*, **16**, 1510 (1977).

[10] I.H. Campbell and P.M. Fauchet, *Solid State Commun*, **58**, 739 (1986).

[11] M. Schoisswohl, M. Rosenbauer, J.L. Cantin, S. Lebib, H.J. von Bardeleben, J.L. Fave, J. Cernegora, G. Amato and A. Rossi, *J. Appl. Phys.*, **79(12)**, 9301 (1996).

[12] G. Amato, A.M. Rossi, L. Boarino and N. Brunetto, *Phil. Mag. B-Physics*, **76(3)**, 395 (1997).

[13] G. Ganguly, T. Ikeda, T. Nishimiya, K. Saitoh, M. Kondo and A. Matsuda, *Appl. Phys. Lett.*, **69(27)**, 4224 (1996).

[14] V. Lehmann and U. Gösele, *Appl. Phys. Lett.*, **58**, 856 (1991).

[15] L. Pavesi and V. Mulloni, *Societa Italiana di Fisica, Proceedings of the ISP-Course CXLI*, 87, IOS Press (1999), p. 102, 103.

[16] M.V. Wolkin, J. Jorne, P.M. Fauchet, G. Allan and C. Deleure, *Phys. Rev. Lett*, **82**, 197 (1999).

[17] M. Sendova-Vassileva, N. Tzenov, D. Dimova-Malinovska, M. Rosenbauer, M. Stutzman, K.V. Josepovits, *Thin Solid Films*, **255**, 282 (1995).

[18] Y. Takano, and H. Ozaki, *J. Non-Cryst. Solids*, **57**, 119 (1983).

[19] K. Kolic, E. Borne, M.A.G. Perez, A. Sibai, R. Gauthier, and A. Laugier, *Thin Solid Films*, **255**, 279 (1995).

[20] A. Czachor, *Phys. Rev. B*, **32**, 5628 (1985).

[21] V.A. Karavanskii, A.A. Lomov, V.A. Bushuev, N.N. Loikho, N.N. Melnik, T.N. Zavaritskaya, G. Kartopu, S.C. Bayliss, and A.V. Sapelkin, *to be submitted.*

[22] X. L. Wu, T. Gao, X. M. Bao, F. Yan, S. S. Jiang, and D. Feng, *J. Appl. Phys.*, **82(5)**, 2704 (1997).

[23] A. Eroil, G.S. Cargill, R. Frahm, and R.F. Boehme, *Phys. Rev. B*, **37**, 2450 (1988).

[24] S. Hayashi, M. Ito, and H. Kanamori, *Solid State Commun.*, **44(1)**, 75 (1982).

[25] P.M. Fauchet, and I.H. Campbell, *Critical Rev. Solid State Mat. Sci.*, **14 (Suplement 1)**, S79 (1988).

[26] T. Hama, and T. Matsubara, *Prog. Theor. Phys.*, **59**, 1407 (1978).

[27] S. Hayashi, and K. Yamamoto, *Superlattices and Microstructures*, **2**, 581 (1986).

[28] Y. Maeda, N. Tsukamoto, Y. Yazawa, Y. Kanemitsu, and Masumoto, *Appl. Phys. Lett.*, **59**, 3168 (1991).

[29] Y. Kanemitsu, H. Uto, Y. Masumoto, and Y. Maeda, *Appl. Phys. Lett.*, **61**, 2187 (1992).

[30] (a) Y. Kanemitsu, in D.J. Lockwood (Ed.), *Light Emission in Silicon, Semiconductors and Semimetals*, Vol. 49, Academic, New York (1997); (b) H.B. Kim, K.H. Chae, C.N. Wang, J.Y. Jeong, M.S. Oh, S. Im, and J.H. Song, *J. Lumin.*, **80**, 281 (1999).

[31] D.C. Paine, C. Caragianis, T.Y. Kim, Y. Shigesato, and T. Ishakara, *Appl. Phys. Lett.*, **62**, 2842 (1993).

[32] (a) M. Nogami, and Y. Abe, *Appl. Phys. Lett.*, **65**, 2545 (1994); (b) A. Saito, and T. Suemoto, *Phys. Rev. B*, **56(4)**, R1688 (1997).

[33] V. Craciun, C.B. Leborgne, E.J. Nicholls, and I.W. Boyd, *Appl. Phys. Lett.*, **69**, 1506 (1996).

[34] M. Zacharias, R. Weigand, J. Blasing, and J. Christen, EMRS Proceedings, **452**, 117 (1997).

[35] Y. Maeda, *Phys. Rev. B*, **51**, 1658 (1995).

[36] S. Okamoto, and Y. Kanemitsu, *Phys. Rev. B*, **54**, 16421 (1996).

[37] S. Miyazaki, K. Sakamoto, K. Shiba, and M. Hirose, *Thin Solid Films*, **255**, 99 (1995).

[38] M. Zacharias, P.M. Fauchet, *J. Non-Cryst. Solids*, **227-230**, 1058 (1998).

[39] K. Uchinokura, T. Sekine, and E. Matsuura, *J. Phys. Chem. Solids*, **25**, 171 (1974).

[40] D. Bermejo, and M. Cardona, *J. Non-Cryst. Solids*, **32**, 405 (1979).

[41] M. Fujii, S. Hayashi, and K. Yamamoto, *Appl. Phys. Lett.*, **57(25)**, 2692 (1990); M. Fujii, S. Hayashi, and K. Yamamoto, *Jpn. J. Appl. Phys.*, **30(4)**, 687 (1991).

[42] A.V. Kolobov, *J. Appl. Phys.*, **87(6)**, 2926 (2000).

[43] M. Kawata, S. Nadahara, J. Shiozawa, M. Watanabe, and T. Katoda, *J. Elec. Mater.*, **19(5)**, 407 (1990).

[44] M. Sendova-Vassileva, N. Tzenov, D. Dimova-Malinovska, Ts. Marinova, and V. Krastev, *Thin Solid Films*, **276**, 318 (1996).

[45] W.K. Choi, S. Kanakaraju, Z.X. Shen, and W.S. Li, *Appl. Surf. Sci.*, **144-145**, 697 (1999), and reference therein.

[46] S. Chang, and R.E. Hummel, *Mat. Sci. Eng. B*, **76**, 237 (2000).

[47] S.S. Chang and R.E. Hummel, *J. Lumin.*, **86**, 33 (2000).

[48] L.G. Jacobsen, Jr. F.L. Freire, G. Mariotto, *Diamond and Rel. Mater.*, **7**, 440 (1998).

[49] D.J. Lockwood, H.J. Labbe, R. Siegele, and H.K. Haugen, *J. Appl. Phys.*, **78(10)**, 6185 (1995).

[50] J.R. Ferraro, K. Nakamoto, *Introductory Raman Spectroscopy*, Academic Press, San Diego (1995).

CHAPTER 5. CONCLUSIONS AND FUTURE WORK

5.1 POROUS $Si_{1-x}Ge_x$

5.1.1 Conclusion

We characterised the microstructure of porous $Si_{1-x}Ge_x$ films using Raman spectroscopy and HRSEM. Porous samples were prepared from undoped $Si_{0.87}Ge_{0.13}$ films with different etch times, but at the same current density. It is found that as the film porosity increases the sizes of $Si_{1-x}Ge_x$ nanocrystals decrease, and also the film composition slightly modifies in favor of Ge. We have shown for the first time the confinement of phonons in SiGe nanocrystals and estimated quantitatively their sizes along with the compositional variations, whilst taking into consideration the parameters of the sample preparation.

5.1.2 Future Work

It is seen by this study that Raman spectroscopy is, as it has always been for bulk $Si_{1-x}Ge_x$ alloys, a very useful technique for characterising the structure of porous $Si_{1-x}Ge_x$ films. However, we believe that the results presented here are preliminary. The average crystal sizes studied were relatively large (between 10-20 nm) and they cannot be taken as responsible for the observation of a visible PL. Much smaller SiGe nanocrystals that could be obtained from highly doped substrates would also show more interesting Raman spectra. Besides, as the initial Ge content of the alloys used for anodisation was very low

(<15%) the estimated compositional variations in the porous films were not so significant. Therefore, it would be particularly interesting to study the structure of a wider range of porous SiGe samples by Raman spectroscopy, as a function of starting substrate composition and nanocrystal size, in order to establish a general relation between the optical properties of porous SiGe [1][2] and the size and/or composition of the SiGe nanocrystals present.

5.2 STAIN ETCHED Ge

5.2.1 Conclusion

The PL at ~ 2.2-2.3 eV from Ge-based nanocrystalline materials is described in the literature usually as nanocrystal size-independent. We observed visible luminescence from c-GeO_2 and two different types of chemically-etched Ge – one being nanocrystalline, the other not – near ~ 2.3 eV. Energy dispersive x-ray analysis (EDX), Raman and FTIR spectroscopy, and the near edge x-ray absorption structure (XANES), indicated that the Ge layers chemically-etched in H_2O_2:HF solution [3] are composed of GeO_xs ($0<x\leq2$) and free from any Ge nanoconstructions. It is also suggested from Raman spectra, XANES and FTIR analysis that the stain-etched Ge prepared in HF:H_3PO_4:H_2O_2 solution [4] was nanocrystalline, comprising 8-9 nm nanocrystals of Ge, and its surface was covered mainly with O, as well as H and OH. Photoluminescence occurred at ~ 2.3 eV in the visible when excited by higher energy photons for all samples. The PL behavior of the latter type of chemically-etched Ge through annealing in different chemical environments (air or H) made it not possible to attribute the visible PL to quantum confinement effects in Ge nanocrystals. Consequently, our results from chemically-etched Ge samples suggest that the origin of the 2.2-2.3 eV PL from these materials, as well as from those Ge-based nanocrystalline materials reported in the literature, is due to GeO_xs.

In other words, by comparison with the other studies of Ge nanocrystals, we propose that regardless of the nature of the material, that is with or without Ge nanocrystals, there

will be an observable PL at 2.2-2.3 eV in the visible region of the electromagnetic spectrum where Ge and O atoms are nearest-neighbors.

5.2.2 Future Work

Any information on the size dependence of the PL spectra is indispensable for further understanding of the quantum size effects of Ge nanocrystals. One way to achieve this would be the preparation of 'oxide-free' Ge nanocrystals (either stand-alone or in insulating matrices) and avoidance of the oxidation of the samples (preferably kept under high vacuum) during analysis.

It is proposed that by varying the etching parameters (e.g. time, illumination) nanocrystalline Ge samples with nanocrystals of different sizes (preferably < 5 nm for the visible PL) and having good crystallinity can be prepared, for the 'first' time, using the novel $HF:H_3PO_4:H_2O_2$ solution for etching Ge wafers. Such a study, undoubtedly, would also help in understanding the etch mechanism of Ge with this solution. As the next step, bandgap and PL measurements can be carried out from near UV, through visible and near IR, up to the c-Ge bandgap (0.67 eV) to comprehensively monitor and characterise the size dependence of the spectra. Moreover, nanocrystals of Ge can be preferably passivated by layers other than GeO_xs to study the visible PL. In this way, the size dependence of the bandgap and PL of Ge nanocrystals prepared by chemical etching could be studied comprehensively.

5.3 Ge NANOCRYSTALS IN SiO_2

5.3.1 Conclusion

Growth of Ge nanocrystals by ion-implantation and subsequent annealing in thermal SiO_2 films has been studied using SIMS, TEM and Raman spectroscopy. TEM and Raman analysis showed that no Ge nanocrystals were formed in films implanted with the lowest doses of Ge ions studied ($7x10^{15}$ cm^{-2}) and it was established by Ge SIMS profile analysis that non-negligible fractions Ge atoms either diffused out of the oxide or segregated onto the Si substrate surface during annealing for these samples. The rest of the Ge atoms remaining in the film were considered to be dissolved in the SiO_2 or have formed germanium oxides. On the other hand, especially in the films implanted with the highest doses ($1x10^{17}$ cm^{-2}), well-formed Ge nanocrystals were observed after annealing by TEM and Raman spectroscopy analysis. TEM images of these samples showed relatively broad distributions of nanocrystal sizes with the largest precipitates located near the peak position of the concentration profile, and the smallest in the tails of the band. The observation of such a broad size distribution was supported by the Raman results. Particle diameters in the other films implanted with a medium dose ($3x10^{16}$ cm^{-2}) and annealed at various temperatures were estimated indirectly from modelling the Raman lineshapes (direct TEM measurements are not yet available for this series of samples). The dependence of the nanocrystal size on temperature was established by this way. However, we did not observe appreciable shifts in the Raman peak frequency as expected by the phonon confinement theory. The discrepancy was explained with a compressive stress exerted on the nanocrystals by the surrounding SiO_2 medium [5].

A yellowish-green PL band with a shoulder in the red wavelengths was observed for all the samples (as-implanted or annealed, nanocrystalline or not). The PL emission was thus attributed to the luminescent defect-centres in the oxide. However, this alone could not explain the observation that the PL intensity was almost the same for as-implanted and high-temperature annealed films containing no (or a few) nanocrystals. On the other hand, it has been well-demonstrated by micro-PL analysis that the annealed films containing Ge nanocrystals show much stronger PL compared to their as-implanted or oxide-removed counterparts. Therefore, it is also plausible as an alternative mechanism that the Ge nanocrystals take a role in the visible PL emission where, for example, the photo-excited carriers in the small Ge nanocrystals might recombine via the localised surface defect states.

5.3.2 Future Work

It is possible that Ge nanocrystals grown in various other matrices, such as Al_2O_3 and Si_3N_4 (rather than SiO_2), can be used to study, for example, the effect of stress on the size dependence of the Raman peak frequency as well as the effect of different defect centres (that will be generated by ion-implantation in different matrices) on the PL properties. For example, it was earlier demonstrated [6] that the growth of Ge nanocrystals in an Al_2O_3 film provides minimisation of stress effects and matrix perturbation on the peak frequency of the Raman spectra. Moreover, the use of a matrix like Si_3N_4, would also enable one to study the photo-absorption and -emission processes in 'oxide-free' Ge nanocrystals provided that enough measures are taken during preparation and characterisation of the samples. It is expected that the PL energy would shift from 2.6 to 1.2 eV as the Ge nanocrystal size increases from 4 to 8 nm [7]. Therefore, it would be,

again, worthwhile to monitor the PL also in the near infrared, especially from those samples containing large nanocrystals (> 5 nm).

5.4 SPARK PROCESSED Ge

5.4.1 Conclusion

Microstructure and luminescent properties of spark processed Ge (sp-Ge) films emitting PL in the visible were studied using SEM, micro-Raman and micro-PL spectroscopy. The PL of sp-Ge consist of three 'colors', blue, yellow-green and orange, when excited in the near UV. Cross-sectional SEM images revealed that the thickness of the films were almost comparable to that of the substrates used for sparking. Instability of these layers to energetic electron beams suggested that their chemistry is different from that of pure crystalline Ge (i.e. different from Ge-Ge bonded material). Local chemistry of the films was examined by micro-Raman spectra and it was found that the films are composed of mainly sub-stoichometric germanium oxides, i.e. GeO_xs, and elemental Ge (in the form of nano- or micro-crystals). It is suggested that the Ge crystals were embedded into thick germanium oxide layers, which showed substantial structural inhomogeneities in terms of local structural configuration and stoichometry, across a single film or between the similarly prepared samples. The micro-PL spectra, simultaneously taken with the micro-Raman spectra, in the orange PL band enabled us to determine unambiguously that this PL band does not involve any kind of Ge-Ge bonded material, i.e. Ge nanocrystals, but presumably Ge-O bonded material. Finally, it is foreseen that the control of the stoichometry of GeO_xs or of the size of Ge nanocrystals in sp-Ge, for example, by changing spark conditions, seem to be desperate tasks, since the material has been found highly inhomogeneous, even across a single sparked Ge film, and with the method being more or less uncontrollable.

5.4.2 Future Work

It has been established by this study that simultaneous micro-Raman and micro-PL spectroscopy pose great advantages in determining the material type (or the simple chemistry) responsible for the PL, provided that the nature of the material let show differences between such spectra. Since the sp-Ge films showed such a behavior indeed, it is favourable to propose that the microstructure of sp-Ge films would enable one also to study the origin of the other PL bands (blue and yellow-green) using the same methods but different excitation energies.

5.5 SUMMARY

We have studied the structural properties of visible luminescent Group IV nanostructures (SiGe and Ge) that have been rather much less studied in the literature, for example, in comparison to Si nanocrystals in porous Si. The confinement of phonons in SiGe nanocrystals has been shown, for the first time, in anodised porous SiGe films, utilising micro-Raman spectroscopy. Several methods, such as chemical etching, ion-implantation and subsequent annealing, and spark processing, were employed to synthesise Ge nanostructures. Properties of 2-10 nm Ge nanostructures, ranging in structure from partially amorphous to crystalline, and in various environments e.g. oxide matrices were studied. They showed PL between 2.0 to 2.3 eV in the visible at room temperature. It has been demonstrated that the visible luminescence from these materials can originate from other chemical origins, such as defects in GeO_xs or defects in host matrices, as well as from Ge nanocrystals. It is strongly recommended that nanocrystalline samples with a wider range of particle sizes must be prepared, preferably as oxide-free, using the first two methods and characterised optically throughout (such as with PL and bandgap measurements) between near IR and near UV, in order to establish a global relation between the particle size and the PL emission from Ge nanocrystals that is unambiguous and comprehensive.

5.6 REFERENCES

[1] M. Schoisswohl, J.L. Cantin, M. Chamarro, H.J. von Bardeleben, T. Morgenstern, E. Bugiel, W. Kissinger and R.C. Andreu, *Phys. Rev. B*, **52(16)**, 11898 (1995).

[2] B. Unal, M. Parkinson, S.C. Bayliss, T. Naylor and D. Schröder, *J. Porous Mat.*, **7**, 143 (2000).

[3] M. Sendova-Vassileva, N. Tzenov, D. Dimova-Malinovska, M. Rosenbauer, M. Stutzman, K.V. Josepovits, *Thin Solid Films*, **255**, 282 (1995).

[4] V.A. Karavanskii, A.A. Lomov, V.A. Bushuev, N.N. Loikho, N.N. Melnik, T.N. Zavaritskaya, G. Kartopu, S.C. Bayliss, and A.V. Sapelkin, *to be submitted.*

[5] M. Fujii, S. Hayashi, and K. Yamamoto, *Jpn. J. Appl. Phys.*, **30(4)**, 687 (1991).

[6] C.E. Bottani, C. Mantini, P. Milani, M. Manfredini, A. Stella, P. Tognini, P. Cheyssac, and R. Kofman, *Appl. Phys. Lett.*, **69 (16)**, 2409 (1996).

[7] W.K. Choi, S. Kanakaraju, Z.X. Shen, and W.S. Li, *Appl.Surf. Sci.*, **144-145**, 697 (1999), and reference therein.

APPENDIX

List of Publications

Papers

1. G. Kartopu, S.C. Bayliss, Y. Ekinci, E.H.C. Parker, T. Naylor, "Observation of Phonon Confinement in SiGe Nanocrystals and Preferential Etching of Si in Porous $Si_{1-x}Ge_x$ Films", *Physica Status Solidi (a)*, **Vol. 197, No. 1**, 263-268 (2003).

2. G. Kartopu, S. C. Bayliss, V. A. Karavanskii, R. J. Curry, R. Turan, and A. V. Sapelkin, "On the Origin of the 2.2-2.3 eV Photoluminescence from Chemically-Etched Germanium", *J. Lumin.*, **Vol. 101, Issue (4)**, 275-283 (2003).

3. V.A. Karavanskii, A.A. Lomov, V.A. Bushuev, N.N. Loikho, N.N. Melnik, T.N. Zavaritskaya, G. Kartopu, S.C. Bayliss, and A.V. Sapelkin, "Observation of Germanium Nanocrystals in Porous Stain-Etched Germanium ", *to be submitted.*

Conference Presentations

1. G. Kartopu, S.C. Bayliss, Y. Ekinci, E.H.C. Parker, T. Naylor, "Observation of Phonon Confinement in SiGe Nanocrystals and Preferential Etching of Si in Porous $Si_{1-x}Ge_x$ Films". A poster presentation in the *3rd International Porous Semiconductors Science and Technology (PSST)-2002 Conference*, Tenerife, Spain, (10-15 Mar 2002).

2. R. Turan, T.G. Finstad, U. Serincan, A.E. Gunnæs, E.S. Marstein, A. Olsen and G. Kartopu, "Evolution of Ge Nanostructures Formed by Ion Implantation in SiO_2". A poster presentation in the *2nd Workshop on Nanomaterials: Fundamentals and Applications Conference (COST)*, Seville, Spain, (3-4 Oct. 2002).